The birth of cosmic structures as revealed by observations in the (sub-)mm bands

Characterizing the first galaxies and galaxy clusters

Joshiwa van Marrewijk

München 2024

The birth of cosmic structures as revealed by observations in the (sub-)mm bands

Characterizing the first galaxies and galaxy clusters

Joshiwa van Marrewijk

Dissertation
der Fakultät für Physik
der Ludwig-Maximilians-Universität
München

vorgelegt von
Joshiwa van Marrewijk
aus Vlaardingen, Niederlande

München, den August 26, 2024

First corrector: Prof. Dr. Eiichiro Komatsu
Second corrector: Prof Dr. Bruno Leibundgut
Day of the Defense: October, 7^{th}, 2024

Contents

List of Figures

List of Tables

List of Abbreviations

ACA	Atacama Compact (Morita) Array
ACF	Autocorrelation Function
ACT	Atacama Cosmology Telescope
ALMA	Atacama Large Millimeter/Submillimeter Array
APEX	Atacama Pathfinder EXperiment
AtLAST	Atacama Large Aperture Submillimeter Telescope
AGN	Active Galactic Nuclei
BCG	Brightest Cluster Galaxy
CARMA	Combined ARray for Millimeter-wave Astronomy
CASA	Common Astronomy Software Applications
CDF	Cumulative Distribution Function
CDM	Cold Dark Matter
COBE	Cosmic Background Explorer
CMB	Cosmic Microwave Background
DDT	Director's Discretionary Time
Dec	Declination
EoR	Epoch of Reionization
eROSITA	Extended ROentgen Survey with an Imaging Telescope Array
eRASS	eROSITA All-Sky Survey
FLRW	Friedmann, Lemaître, Robertson, and Walker
FIR	Far-Infrared
FIRST	Faint Images of the Radio Sky at Twenty-Centimeters
FLRW	Friedmann, Lemaître, Robertson, and Walker
FoV	Field of View
FWHM	Full Width Half Maximum

GBT	Green Bank Telescope
GMC	Giant Molecular Cloud
gNFW	Generalized Navarro-Frenk-White
HST	Hubble Space Telescope
ICM	Intracluster Medium
ISM	Interstellar Medium
JWST	James Web Space Telescope
NIR	Near-Infrared
MUSTANG	MUltiplexed SQUID TES Array for Ninety Gigahertz
PCA	Principle Component Analysis
PDF	Probability Density Function
PWV	Precipitable Water Vapor
RA	Right Ascension
ReCESS	Representative Cluster Evolution Sunyaev-Zeldovich Survey
REXCESS	Representative XMM-Newton Cluster Structure Survey
RMS	Root Mean Square
SKA	Squared Kilometer Array
SKA	Squared Kilometer Array
SAT	Small Aperture Telescope
SPT	South Pole Telescope
SZ	Sunyaev-Zeldovich
TES	Transition-Edge Sensor
TOD	Time-Ordered Data
UPP	Universal Pressure Profile
VLA	Very Large Array
VLASS	Very Large Array Sky Survey
WMAP	Wilkinson Microwave Anisotropy Probe
XMM-Newton	X-ray Multi-Mirror Mission Newton

Zusammenfassung

Die Physik der Gravitationsinstabilität—die primordiale Dichtefluktuationen mit der Bildung kosmischer Strukturen verknüpft—bildet die Grundlage für die Theorie der Galaxien- und Haufenevolution. Die genaue Beschreibung des Schicksals der Baryonen, die sich innerhalb großer Gravitationspotentiale befinden, hat sich jedoch als herausfordernd erwiesen. Mit dieser Dissertation trage ich zum Verständnis des Wachstums großräumiger Strukturen bei, indem ich mich auf (sub-)mm-Beobachtungen der massereichsten gravitativ gebundenen Objekte konzentriere, die in zwei verschiedenen Epochen entstanden sind. Die Arbeit ist in drei Teile unterteilt, deren Ergebnisse wie folgt lauten:

1) Im Rahmen meiner Arbeit zu Galaxien in der Epoche der Reionisierung habe ich eine neuartige Methode entwickelt, die Rauschrealisierungen aus interferometrischen Daten erstellt, um eine angemessene Quantifizierung der Wahrscheinlichkeit von Fehlentdeckungen zu ermöglichen. Basierend auf dieser Analyse habe ich jedoch keine robuste Entdeckung einer Linie in einem der $z > 10$ Galaxienkandidaten gefunden, die mit dem Atacama Large Millimeter/Sub-millimeter Array (ALMA) beobachtet wurden.

2) Im Rahmen meiner Arbeit zur Entstehung von Galaxienhaufen habe ich durch Vorwärtsmodellierung parametrischer Druckprofile auf ALMA- und Atacama Cosmology Telescope (ACT)-Daten das sich bildende Intracluster-Medium (ICM) vom Kern bis zum Virialradius im am weitesten entfernten Galaxienhaufen—XLSSC 122—kartiert, der in SZ-Durchmusterungsdaten mit großem Gesichtsfeld entdeckt wurde. XLSSC 122 zeigt einen Überschuss an SZ-Fluss im Süden des Haufens (wo keine Röntgenstrahlung nachgewiesen wurde). Dieser Fluss kann auf eine einfallende Gruppe oder eine filamentartige Struktur zurückgeführt werden, die das Gas beschleunigt und thermalisiert, während die Dichte noch gering ist.

3) In Bezug auf die letzte Arbeit, die ich während meiner Promotion durchgeführt habe, habe ich ein neuartiges Simulationswerkzeug namens `maria` entwickelt, das zur Vorhersage bolometrischer Einzelteleskopbeobachtungen verwendet wird. Das Werkzeug ist entscheidend für die Analyse, wie verschiedene Instrumenten- und Teleskopdesigns die Fähigkeit beeinflussen, atmosphärische Störungen und Filtereffekte zu mindern, die diese Art von Beobachtungen erschweren. Darüber hinaus habe ich `maria` verwendet, um realistische Vorhersagen des ICM in Galaxienhaufen für aktuelle und zukünftige Einrichtungen zu erstellen, um zu bestimmen, wie gut wir Kalorimetrie untersuchen können.

Meine Arbeit zeigt, dass es eine Herausforderung darstellt, (sub-)mm-Beobachtungen von Galaxien und Haufen auf die Rotverschiebungen zu erweitern, in denen sie sich bilden. Alle ALMA-Beobachtungen, die auf $z > 10$ Galaxienkandidaten abzielen, führten zu Nicht-Nachweisen, was Schätzungen der Bedingungen im lokalen interstellaren Medium und der Anzahl ionisierender Photonen unbestimmt lässt. Darüber hinaus liefert die Analyse von XLSSC 122 wertvolle Einblicke in den Mechanismus, der die Thermalisation dieses Haufens antreibt, jedoch ist dieser Haufen selbst ziemlich einzigartig; es ist der einzige SZ-ausgewählte und optisch bestätigte Haufen, der bei $z \simeq 2$ entdeckt wurde. Außerdem zeigt meine Arbeit keine signifikante Radio- oder (sub-)mm-Kontamination des SZ-Effekts, sodass dieser Haufen möglicherweise kein guter Repräsentant für andere Haufen bei ähnlich hohen Rotverschiebungen ist. Dennoch demonstriert

die hier präsentierte Arbeit wichtige erste Schritte in der anfänglichen Charakterisierung der ersten Galaxien und Galaxienhaufen und verbessert das Set an Werkzeugen, die zur Untersuchung dieser Objekte zur Verfügung stehen, sowohl aus Beobachtungs- als auch aus Simulationsperspektive. In Bezug auf Letzteres wird `maria` für zukünftige (sub-)mm-Experimente wie AtLAST entscheidend sein, um Vorhersagen zu SZ-Messungen mit hoher Auflösung und optisch unverzerrten Liniensurveys für Galaxien bei hohen z zu treffen. Diese Vorhersagen können dann direkt mit den Spezifikationen für Instrumenten- und Teleskopdesigns verknüpft werden, um die Grundlage für die Zukunft der (sub-)mm-Beobachtungen zum Wachstum kosmischer Strukturen zu legen.

Abstract

The physics of gravitational instability—which links primordial density fluctuations to the formation of cosmic structures—provides the foundations for the theory of galaxy and cluster evolution. However, providing a sound description of the fate of baryons that reside within large gravitational potential wells has proven challenging. With this thesis, I contribute to the field of large-scale structure growth by focusing on (sub-)mm observations of the most massive gravitationally bound objects formed at two distinct epochs. The work is divided into three parts, of which the following are the results:

1) Regarding my work on the epoch of reionization galaxies, I developed a novel method that creates noise realizations from interferometric data, enabling a proper quantification of the likelihood of false detection. Based on this analysis, I however found no robust detection of a line in any of the $z > 10$ galaxy candidates observed with the Atacama Large Millimeter/Submillimeter Array (ALMA).

2) Regarding my work on the birth of galaxy clusters, by forward modeling parametric pressure profiles to ALMA and Atacama Cosmology Telescope (ACT) data, I mapped the forming intracluster medium (ICM) from the core to the virial radius in the most distant galaxy cluster—XLSSC 122—detected in wide-field SZ survey data. XLSSC 122 exhibits an excess of SZ flux in the south of the cluster (where no X-ray emission is detected). This flux can be attributed to an infalling group or filamentary-like structure that is believed to boost and thermalize the gas while the density is still low.

3) Regarding the last work I conducted during my PhD, I developed a novel simulation tool named `maria` used for forecasting bolometric single-dish observations. The tool is key to analyzing how different instrument and telescope designs impact the ability to mitigate atmospheric corruption and filtering effects that challenge these types of observations. Furthermore, I used `maria` to make realistic forecasts of the ICM in galaxy clusters for current and future facilities to determine how well we can study calorimetry.

My work highlights that pushing (sub-)mm observations of galaxies and clusters to the redshifts where they form is challenging. All ALMA observations targeting $z > 10$ galaxy candidates resulted in non-detections, leaving estimates of the local interstellar medium conditions and the number density of ionizing photons unconstrained. Furthermore, while the analysis of XLSSC 122 provides valuable insights into the mechanism driving the thermalization of this cluster, this cluster itself is rather unique; it is the only SZ-selected and optically confirmed cluster detected at $z \simeq 2$. Additionally, my work shows no significant radio or (sub-)mm contamination to the SZ effect, so it may not be a good representative for other clusters at similarly high redshifts. Nevertheless, the work I present here demonstrates important first steps in the initial characterization of the first galaxies and galaxy clusters and improves upon the set of tools available to study them, both from an observational and simulation perspective. Regarding the latter, `maria` will be crucial for next-generation (sub-)mm experiments, like AtLAST, to forecast resolved SZ measurements and optically unbiased line surveys to find high-z galaxies. These forecasts can then be directly linked to instrument and telescope design specifications, setting the stage for the future of (sub-)mm observations on cosmic structure growth.

Chapter 1,

Cosmic structure growth as seen in the (sub-)mm regime

“You know those aren’t fish, right?
Of course they are.
Come with me.
This is a telescope.
Old man Bernardi lets me use it.
It makes faraway things seem close. Look.
See any fish?
Then what are all those?
Stars. Like the sun.
Giant, raging balls of fire!
And stars are circled by planets.
Look.
That’s Saturno. It’s my favorite.
It’s the lightest of the planets.
They say if there was an ocean big enough to hold it, it would float in it!
Whoa!
Wow!”

- Luca, Disney Pixar (2021)

This dissertation presents a collection of four works that cover three topics: 1) The search and confirmation of galaxy candidates at $z > 10$ targeted with the Atacama Large Millimeter/Submillimeter Array (ALMA). 2) A detailed analysis of ALMA and Atacama Cosmology Telescope (ACT) observations on a forming galaxy cluster at $z = 2$. 3) The development of a novel simulation tool named `maria` for forecasting bolometric single-dish observations. Although these topics may seem disconnected, they share a common theme: All observations target the largest objects forming within a given epoch and are conducted in the (sub-)mm bands. The characteristics of these objects are highly sensitive to the underlying cosmology and will, in the future, be used to constrain the growth of cosmic structures, provided that the systematics of their formation are well understood.

In this introduction, I will guide you through the cosmological context of my work (Section 1.1). Next, I will describe how overdensities deviate from the expansion of the Universe and gravitationally collapse (Section 1.2). The objects that then form within these overdensities, namely the first galaxies (Section 1.3) and galaxy clusters (Section 1.4), will be discussed thereafter. The latter two sections directly set up their respective science chapters (Chapters 2 and 3, respectively). Then, I will describe the (sub-)mm facilities I used throughout my work (Section 1.5), which will also introduce my final science chapter (Chapter 4). Finally, I conclude with a slightly more in-depth description of the remainder of my work (Section 1.6). I hope you will thoroughly enjoy reading the thesis. I certainly did while writing it and studying the work.

1.1 Cosmology

Cosmology is the study of the Universe—the cosmos—in its entirety. However, the Universe is a complex and constantly evolving system. Astronomers have for centuries challenged themselves to find causality between physics at the smallest of scales, from quantum fluctuations and the physics that govern the movement of light to the largest of scales: planets orbiting stars, stars within galaxies, galaxies bound together into clusters, and clusters interconnected through the cosmic web. Understanding the Universe as a whole thus faces problems with a dynamic range of 61 orders of magnitude; from the Planck length, $\ell_p = 1.6 \times 10^{-35}$ meters, to the size of the observable Universe, approximately 14 Gpc $\approx 4 \times 10^{26}$ meters. Dealing with such a large dynamic range requires some form of imagination and creativity. However, do not be fooled; cosmology is a study that relies on observations and precise measurements.

There has always been an interplay between theory and observation. In times of limited data—something unthinkable these days—the study of cosmology tended to be driven by theory. This was the case in the early 1800s, when modern cosmology was born. In the Astronomisches Jahrbuch (1823)[1], Olbers wrote a scientific article that posed the question: *If the Universe is full of stars, how come the night sky is dark?* This seemingly simple question is actually quite difficult to answer. Olbers, unaware that extragalactic objects existed at the time, suggested that one or more of the following three assumptions might not hold. First, the Universe was assumed to be infinite, both in size and in age (something I will further discuss in Section 1.1.1). Second, the

[1]The book is currently on display in the *Deutsche Museum* in München, Germany.

Universe was assumed to be transparent so that light would propagate freely (I will further touch upon this in Section 1.4.2). And finally, the Universe was assumed to be static, the model no one doubted in the 1800s.

It was a century later that astronomers could first test these assumptions. In the early 1900s, marking the start of the era of observational cosmology, Hubble (1922) measured distances to faraway nebulae (which later turned out to be galaxies) using various standard candles. Then, with Slipher (1917)'s positive radial velocity measurements of emission lines, interpreted as a Doppler shift, which is expressed in terms of redshift,

$$z \equiv \frac{\lambda_{\rm ob} - \lambda_{\rm em}}{\lambda_{\rm em}} = \frac{\nu_{\rm em} - \nu_{\rm ob}}{\nu_{\rm ob}} \,, \tag{1.1}$$

which is a function of wavelengths λ or frequencies ν, at the time of emitting (subscribed with *em*) and at the time of observations (subscribed with *ob*), which are related through,

$$\lambda = \frac{c}{\nu} \,, \tag{1.2}$$

with c being the speed of light, Hubble came to the conclusion in 1929 that the local bubble was expanding (Hubble, 1929). To come to that conclusion, he used the Copernican principle (Copernicus, 1543), which is the basic assumption that matter in the Universe is isotropically and homogeneously distributed, meaning that we observers do not occupy a privileged position to observe the Universe from. But, it was Lemaître that, through this principle and the new observations, found a set of dynamical solutions to Einstein's fundamental equations of general relativity (Einstein, 1916) that provided the mathematical proof that the whole Universe is expanding, not only the local bubble. From the theory of relativity, he derived the velocity-distance relationship of $v = H(t) \cdot d$, which fitted Hubble (1922)'s distances and Slipher (1917)'s redshifts (Lemaître, 1927).[2] Here, $H(t)$ is the Hubble constant, which sets the rate of the expansion of the Universe at a certain time t and is often expressed in terms of the scale factor $a(t)$, such that,

$$H(t) = \frac{\dot{a}(t)}{a(t)} \,. \tag{1.3}$$

The scale factor is defined such that a proper distance $d(t)$ is expressed in terms of $a(t)$, times the distance in comoving coordinates, $d(t) = a(t) \cdot d_0$. The important finding of Lemaître (but also de Sitter, 1917, Friedmann, 1922) was that the measured redshifts of Slipher (1917) using Einstein's laws of relativity could be attributed to the expansion of the Universe;

$$1 + z = \frac{a_{\rm obs}}{a_{\rm em}} \,, \tag{1.4}$$

and are thus not simply a Doppler effect due to peculiar velocities but a cosmological effect. Hence, Olbers' third assumption that the Universe is static was proven false.

[2]For a detailed account on who discovered the expanding Universe, please read Nussbaumer & Bieri (2011). The article is thoroughly enjoyable to read.

The discovery of the expanding Universe created a paradigm shift in cosmology and led to a mathematical formalism of the Universe's evolution, a formalism built by many great scientists/mathematicians (see, e.g., Einstein, 1916, de Sitter, 1917, Friedmann, 1922, Lemaître, 1927, Robertson, 1933, Walker, 1937). The theory posits that the Universe started in a dense state and has been expanding ever since. In brief, Friedmann, Lemaître, Robertson, and Walker created a framework—known as the FLRW-metric—that describes how the Universe expands and evolves as a whole based on the energy components that govern the Universe. The formalism is set up as,

$$\frac{H(t)^2}{H_0^2} = \frac{\Omega_{\gamma,0}}{a(t)^4} + \frac{\Omega_{\mathrm{m},0}}{a(t)^3} + \frac{1-\Omega_0}{a(t)^2} + \Omega_\Lambda \ , \tag{1.5}$$

with the various components expressed in terms of energy densities; Ω_Λ being the cosmological constant, Ω_m the total matter density, Ω_γ the radiative one, and $1-\Omega_0 = 1-(\Omega_{\gamma,0}+\Omega_{\mathrm{m},0}+\Omega_\Lambda)$ the curvature parameter. The 0-index annotates its value at the time of $z=0$, i.e., today.

Deriving the exact values of the energy densities still drives fundamental research, but remarkable steps have already been made. A century of work led to a single comprehensive, data-driven model that is known under various names, such as the concordance model and ΛCDM. This model includes the cosmological constant, Λ, which is often referred to as dark energy. It also includes a cold dark matter component (CDM, or Ω_DM), which is a type of matter with low velocities ($v << c$) that only interacts through gravity. When combined with the baryonic matter, Ω_bar, these components add up to the total matter density of the Universe, Ω_m. The origins of this model stem from observations of the first light ever emitted, the cosmic microwave background (CMB), a topic I will further discuss in the next section.

1.1.1 Cosmic microwave background

As the Universe expands, assuming it is well-described by some isotropic density field, it cools adiabatically. When reversing time, contraction heats it up, indicating the Universe must have started in a hot, dense state. At temperatures $T \gg 10^4$ K, $k_b\mathrm{T} \gg 1$ eV,[3] photons and matter are coupled and in thermal equilibrium, meaning that the Universe in its early phase consisted of an ionized, optically thick plasma that emitted radiation with a blackbody spectrum. As the Universe expanded and the plasma cooled to $T \approx 3000$ K, electrons and ions combined to form neutral atoms and eventually decoupled from the photons, allowing them to travel freely without scattering. Alpher & Herman (1948) postulated that the remnants, or *afterglow*, of this transition—known as *the moment of last scattering*—should be detectable as microwave radiation today.

Using a microwave antenna, Penzias & Wilson (1965) detected an excess noise component, later attributed to an isotropic cosmic background of microwave radiation, the CMB (Dicke et al., 1965). But it was only 30 years later, in 1996, that observations by the *Cosmic Background Explorer (COBE)* satellite characterized the full spectrum of this emission, revealing a perfect blackbody spectrum with a current average temperature $T_0 = 2.7255 \pm 0.0006$ K (Fixsen et al., 1996), confirming the predicted afterglow. Thus, if Heinrich Olbers could look at the microwave

[3] with k_b the Boltzmann constant and eV standing for *electron Volts*

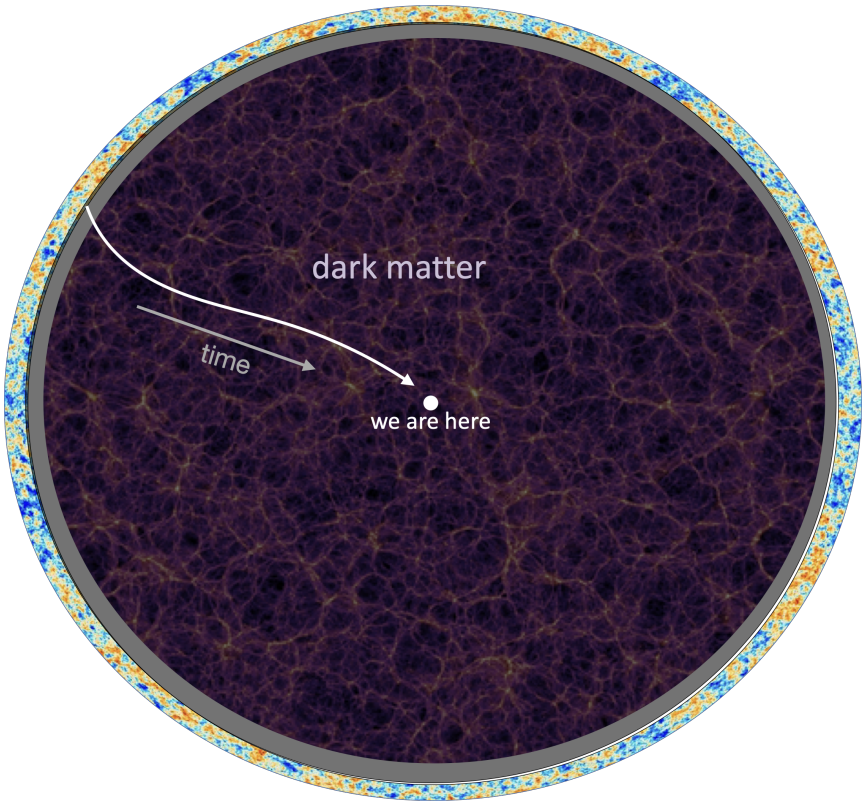

Figure 1.1: Sketch of the observable Universe. Light escapes at the event of the last scattering and travels the Universe till it is captured by one of our telescopes and converted to a voltage. I obtained the figure as a courtesy from Prof. Dr. Blake Sherwin.

sky (ignoring the atmosphere), he would have seen a uniformly bright night sky in every direction he looked, as also illustrated in Figure 1.1.[4]

These first CMB results were crucial for cosmology. They confirmed the Big Bang Theory and robustly rejected the Steady State Universe, a model unable to predict the isotropic background radiation that emits at a temperature of $T \simeq 2.7\,\mathrm{K}$. The CMB also provides the absolute reference coordinate frame of the observable Universe and functions as an isotropic thermal density field, demonstrating that the Universe is indeed isotropic on large scales.

1.1.2 Temperature anisotropies

Following the initial success of *COBE*, multiple probes were launched to map the millimeter-wave (mm) sky at higher angular resolutions, such as the *Balloon Observations Of Millimetric Extragalactic Radiation And Geophysics* (BOOMERanG), the *Wilkinson Microwave Anisotropy Probe* (WMAP; Spergel et al., 2003) and the *Planck* satellite (Planck Collaboration et al., 2014).

[4]With this statement, I assume that Olbers has an incredible sense of motion and would need to be able to correct for the Doppler shift caused the motion of the Earth around the Sun, the Sun's orbital motion in the Galaxy, the Galaxy's velocity by the local group, and the Group's velocity that orientates towards the Virgo supercluster.

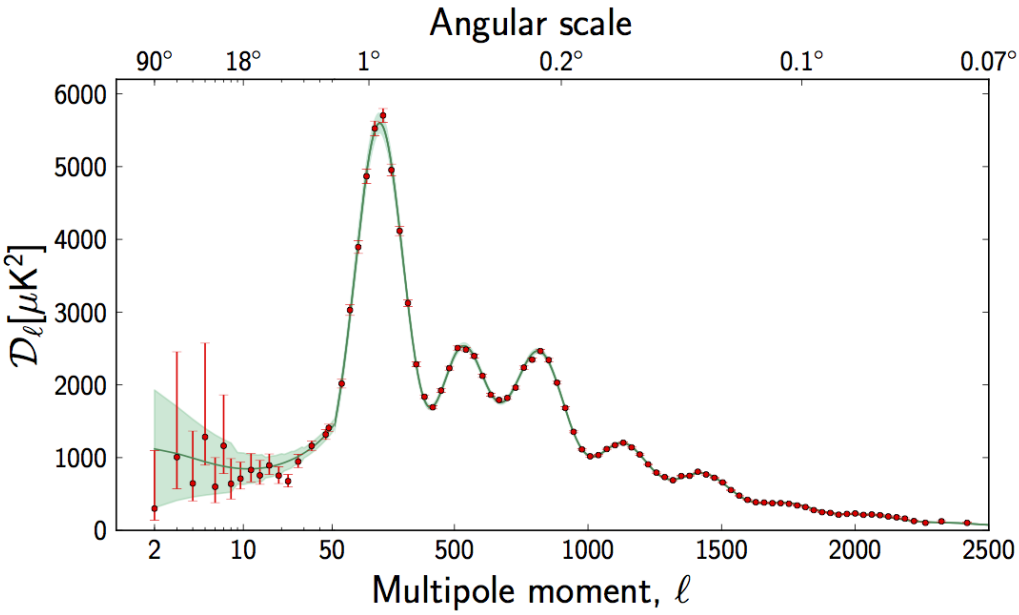

Figure 1.2: Temperature fluctuations of the CMB, as observed by *Planck*. The green line is the best-fit solution of the ΛCDM model. The figure is obtained from Planck Collaboration et al. (2014).

Although *COBE* was the first to detect temperature fluctuations in the CMB—known as *temperature anisotropies*, a discovery that earned the Nobel Prize in 2006—it had limited angular resolution ($\simeq 7^\circ$), preventing it from observing beyond the horizon scale ($\ell \approx 160$). It was BOOMERanG, a balloon experiment as the name suggests, that first fully mapped beyond the sound horizon scale, enabling the constraint that the geometry of the Universe is close to flat (de Bernardis et al., 2000). Observing the CMB at even higher resolutions through WMAP and *Planck* enabled another groundbreaking measurement that contributed to the development of the ΛCDM model; the detection of "acoustic oscillations" in the power spectrum of the CMB's temperature anisotropies (Figure 1.2).

The geometry of the Universe (see, e.g., Eisenstein & Hu, 1998), along with gravitational (see, e.g., Sachs & Wolfe, 1967) and hydrodynamical processes (see, e.g., Peebles & Yu, 1970, Sunyaev & Zeldovich, 1970, Komatsu et al., 2009) caused by small-scale inhomogeneities in the matter distribution at the moment of last scattering and left distinct imprints on the observed temperature fluctuations. Importantly, the relative amplitude of peaks in the temperature power spectrum, which translates to the relative strength of the different hydrodynamical and gravitational effects, indicates a stronger contribution of the gravitational interaction of matter than what was expected from measurements of the acoustic oscillations. This suggests the presence of a type of matter that does not interact with electromagnetic fields, a type of matter already posited in the 1930s based on mass estimates of galaxy clusters (Zwicky, 1933). Adding a dark matter component to the energy density distributions that compose the Universe provided a perfect fit to the data (Figure 1.2).

Throughout the thesis, I will assume the cosmology based on the Planck Collaboration et al. (2014) results. The following parameters are derived based on the fit shown in Figure 1.2 and describes a spatially flat ($\Omega_0 = 1$), ΛCDM model with $H_0 = 67.7$ kms^{-1}Mpc^{-1}, $\Omega_{\mathrm{m},0} = \Omega_{\mathrm{DM}} + \Omega_{\mathrm{bar}} \simeq 0.258 + 0.049 = 0.307$, and Ω_γ negligibly small ($\Omega_\gamma = 9.24 \times 10^{-5}$). Linking back to Olbers's initial question, solving the differential FLRW-metric, Eq. (1.5), provides a formalism for measuring the overall evolution, age, and size of the Universe. Thus, this disproves Olbers' first assumption that the observable Universe is infinitely large and old.

Even though these parameters are derived from measurements at the surface of the last scattering, they remain remarkably consistent with observations across different epochs and spatial scales. These include the gravitational lensing of light (Eddington, 1919), the ability of dark matter to explain the rotation curves of stars in the outskirts of galaxies (Rubin et al., 1980, van Albada et al., 1985), and the distribution of various types of matter within galaxy clusters (Zwicky, 1933, 1937). However, the FLRW-metric, Eq. (1.5), assumes complete homogeneity and isotropy throughout the Universe. While this assumption holds on large scales, as evidenced by the CMB, the Universe is not entirely homogeneous on smaller scales. We know this to be the case since we, planets, galaxies, and galaxy clusters exist. These "small" inhomogeneities originate from initial density fluctuations that perturbed the smooth density field of the early Universe. The following section will introduce the formalism that describes how these initial perturbations developed into the large-scale structures we observe today.[5]

1.2 Hierarchical structure growth

Given that $\approx 80\%$ of the matter in the Universe consists of dark matter — a non-collisional, low-velocity type of matter that interacts only through gravity — it is reasonable to postulate that *gravitational collapse* drives the formation of cosmic structures, ultimately leading to the galaxies and clusters we observe today. It started with the idea from Peebles (1965, 1972) that the development of larger structures through gravitational collapse may have been sequential and that statistical randomness induces the growth of larger gravitationally bound objects over time. This self-similar nature led to the mathematical prescription of what is now known as the hierarchical growth model. Without delving into the exact mathematical build-up of linear perturbation growth, spherical collapse, and Jeans (in)stability that are woven into the hierarchical growth model, this section will conceptually describe the importance and formulation of hierarchical structure growth and how it fits the cosmological context outlined previously.

Let's start small. Given an initial field of random density fluctuations, the fractional density

[5]What large-scale structures are is fairly ambiguous. Some might say that everything larger than a galaxy falls under the nomenclature of large-scale structures. However, I disagree. If we assume a "structure" is something that has detached from the Hubble flow, the largest structures to form at the early, $z > 10$, Universe are, in fact, galaxies. Therefore, I adopt a definition of large-scale structures as the largest objects to form at any given epoch that are gravitationally bound (i.e., matter having a peculiar velocity smaller than the escape velocity set by the gravitational potential well). Thus, this definition includes the earliest galaxies at high-z as well as superclusters and the cosmic web in the local Universe.

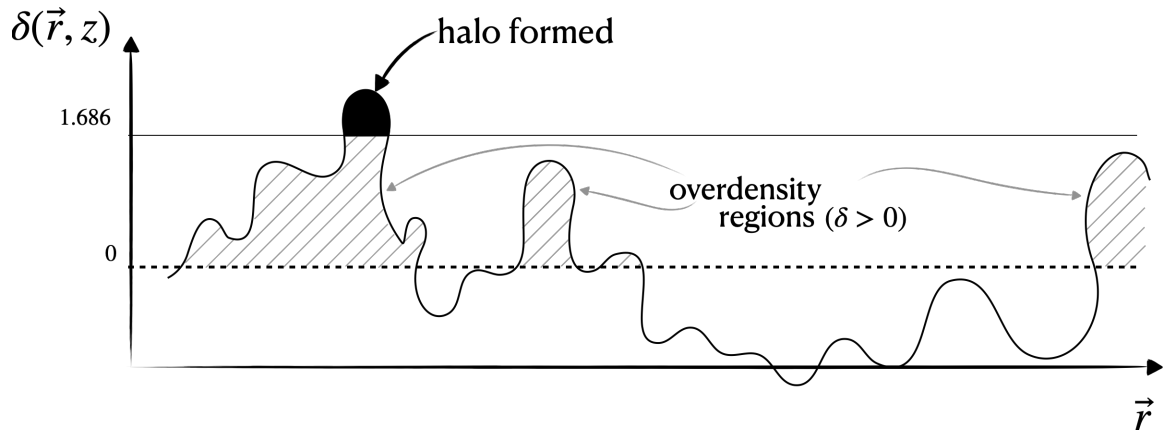

Figure 1.3: Schematic of how structures form through hierarchical growth. The small-scale fluctuations superimposed on large-scale overdensity regions first exceed the linear density threshold $\delta_c = 1.686$. As a result, they collapse and begin forming gravitationally bound objects, such as dark matter haloes in which galaxies and clusters of galaxies reside.

contrast, referred to as the overdensity, is defined as,

$$\delta(\vec{r}, z) = \frac{\rho(\vec{r}) - \bar{\rho}(z)}{\bar{\rho}(z)}, \tag{1.6}$$

where $\bar{\rho}(z)$ is the average matter density of the Universe at a time z, and $\rho(\vec{r})$ the density at a comoving location $\vec{r} = (r, \theta, \phi)$.

How these overdensities grow depends on the balance between the expanding Universe, which stretches space, causing matter to drift apart, and the attractive force of gravity. At an overdensity of $\delta_{\rm ta} \simeq 1.062$ (in terms of the linearly extrapolated growth of $\delta(z)$, while the actual overdensity would be $\delta_{\rm ta} \simeq 4.55$), gravitational collapse balances the Universe's expansion rate when $\Omega_m(z)$ dominates the FLRW-metric (Gunn & Gott, 1972). Therefore, any overdensity with $\delta_{\rm ta} > 1.062$ will "deviate" from the expansion of the Universe and become dynamically dominated by gravitational motion. This mechanism is often referred to as *detaching from the Hubble flow*. At $\delta_{\rm c} \simeq 1.686$ (again, in the linear growth regime), the overdensity will have already virialized and begun gravitational collapse, thus starting to form haloes. As illustrated schematically in Figure 1.3,[6] small-scale density fluctuations on top of large-scale overdensities will be the first to exceed δ_c and thus implode on themselves. The smaller overdensities that collapse first will merge with others, eventually forming larger structures, providing the hierarchical growth pattern in structure formation.

In the late 1970s, around the same time as the introduction of the Press-Schechter formalism (Section 1.2.1), there were significant developments in computing facilities, which enabled

[6] I first encountered a similar sketch to Figure 1.3 during my master's course on *large-scale structures*, taught by Koenraad Kuijken in 2020. However, I believe the sketch originates from the review books by Peebles (1980, 1993), which depict a Gaussian $1/f$ random field that this sketch attempts to encapsulate. Further, some of the aesthetics in Figure 1.3 are inspired by the sketches from Eiichiro Komatsu's class on *Non-Gaussianity*.

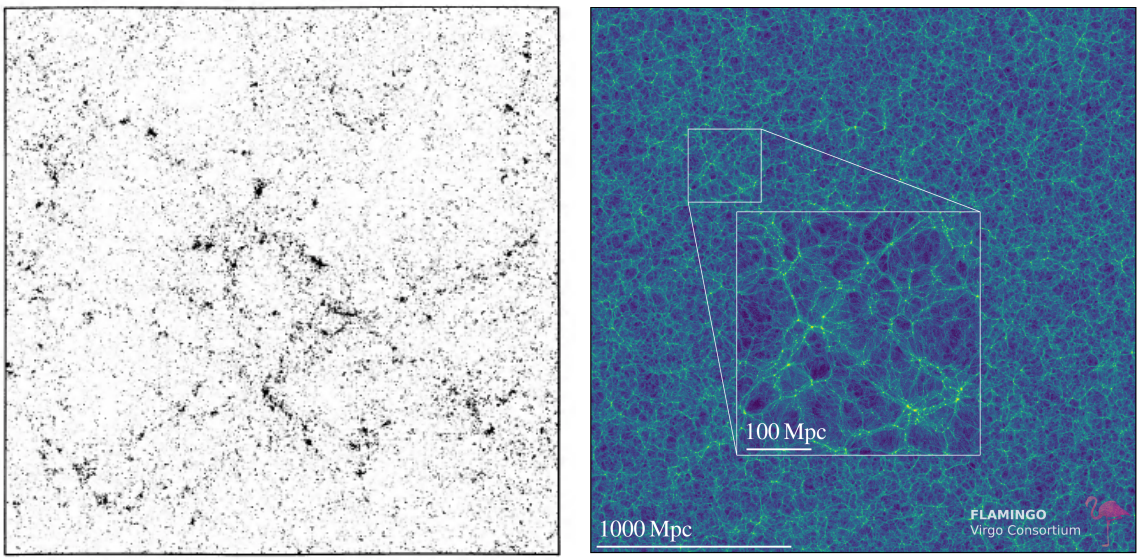

Figure 1.4: The simulated cosmic web. On the left, we show the early numerical simulations of Davis et al. (1985), and on the right, the latest hydrodynamical work of Schaye et al. (2023). The two figures are not to scale. Davis et al. (1985) uses a box size of $L = 32.5\ h^{-1}$ comoving Mpc, while the Flamingo simulations suit is $L = 2.8$ comoving Gpc.

cosmologists to start utilizing more powerful computers. This enabled a wide range of science, including the computation of nonlinear gravitational clustering effects of "particles" that solely interacted through gravity. Numerical models were run with a wide variety of initial conditions covering the uncertainty in the cosmological framework (i.e., Ω_m was thought to be something between $0.2 < \Omega_m < 1$) and showed that over time, particles started to cluster in a hierarchical manner, forming haloes such as described in the Press-Schechter formalism, which were interpreted as the formation of galaxies and galaxy clusters (see, e.g., Davis et al., 1985, Bond et al., 1996, for some early works). Interestingly, the hierarchical growth manifested itself as a web-like structure, which is now famously referred to as the *cosmic web* (Figure 1.4).

To validate the structure growth model, a particularly powerful test would involve: 1) fitting a ΛCDM model to the CMB power spectrum measurements at $z \sim 1100$, 2) using this model to predict the amplitude of density fluctuations at low and intermediate redshifts based on the standard hierarchical growth formalism, and 3) comparing these predictions with direct, high-precision measurements at those redshifts. Qu et al. (2024) provided this test by utilizing CMB lensing measurements. CMB lensing occurs when matter along the line of sight gravitationally lenses CMB photons as they travel from the last scattering surface to our telescopes. The lensing power spectrum is most sensitive to structures at $z \sim 1 - 5$ and is a linear function of the underlying matter power spectrum integrated along the line of sight. The lensing measurements from ACT are independent (e.g., having different systematic uncertainties) from the ΛCDM model fit obtained from *Planck* measurements. The results comparing the predicted amplitude and spectral shape of the density fluctuations at $z \sim 1 - 5$ based on temperature anisotropy

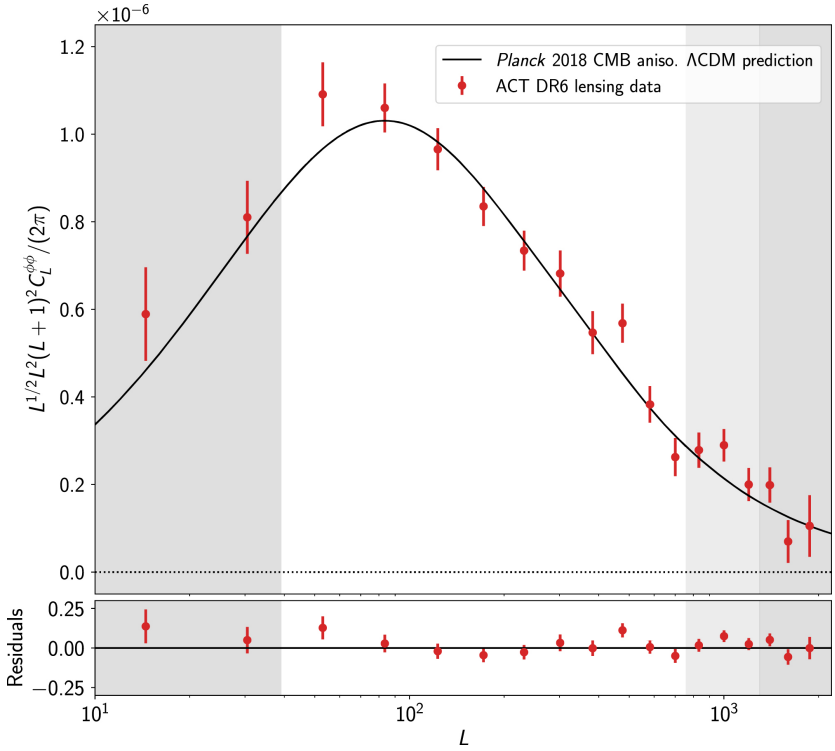

Figure 1.5: Proof of the hierarchical structure growth model. It compares the CMB lensing power spectrum measured by ACT with the predictions from initial temperature anisotropies in the CMB measured by *Planck*. The results provide a $\chi^2_r = 1$, without the need to fit one to the other.

measurements at $z \sim 1100$ with ACT CMB lensing measurements are shown in Figure 1.5. They demonstrate a perfect fit between measurements at both epochs and are thus a strong proof of the hierarchical structure growth model.

1.2.1 Press-Schechter formalism

Given the hierarchical structure growth model, we can use the Press-Schechter formalism to determine how many haloes form at a given redshift (Press & Schechter, 1974). The number of structures forming at any given epoch depends on the shape and amplitude of the matter power spectrum. For example, if there had been more power in fluctuations on larger scales, less matter would have collapsed early on. If the Universe is more clumpy, there would be more structure at later stages. Mathematically, the amplitude of the matter power spectrum measured within a comoving volume V is defined as,

$$\sigma_\delta^2 = \frac{V}{(2\pi)^3} \int P(k) d^3k \ , \tag{1.7}$$

where k is the wavenumber and $P(k)$ is the matter power spectrum, so that,

$$\langle \delta_{\vec{k}} \delta^*_{\vec{k}'} \rangle = (2\pi)^3 \delta_D(\vec{k} - \vec{k}') P(k) \ , \tag{1.8}$$

with δ_D the Dirac-delta function, and,

$$\delta_{\vec{k}} = \frac{1}{V} \int \delta(\vec{r}) \, \mathrm{e}^{i\vec{k}\cdot\vec{r}} d^3r \ , \tag{1.9}$$

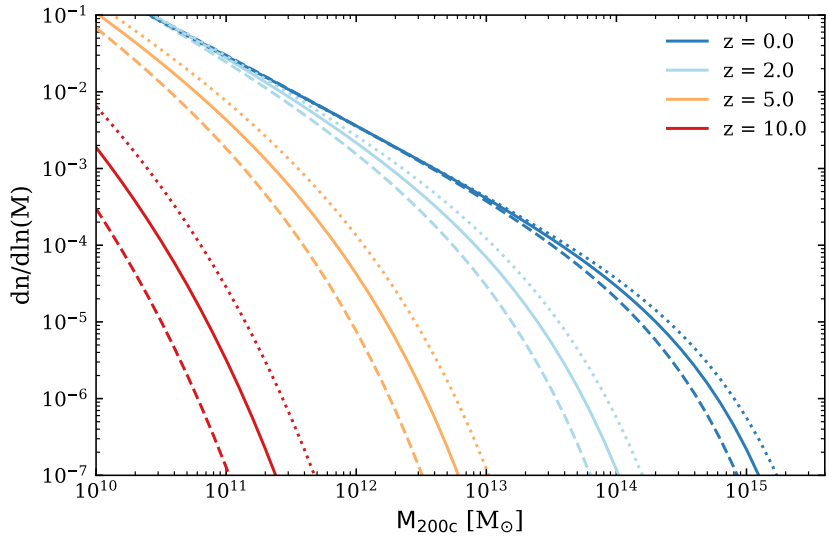

Figure 1.6: Tinker et al. (2008) halo mass function for various redshifts and values of σ_8. We plot $\sigma_8 = 0.7$ (dashed), $\sigma_8 = 0.8$ (solid), and $\sigma_8 = 0.9$ (dotted).

with,

$$\delta(\vec{r}) = \frac{V}{(2\pi)^3} \int \delta_{\vec{k}}\, \mathrm{e}^{-i\vec{k}\cdot\vec{r}} d^3k \,. \tag{1.10}$$

To estimate how many structures form in a given mass bin, Press & Schechter (1974) made use of the fundamental cosmological principle that the Universe is homogeneous and isotropic, making the phases of the different Fourier modes uncorrelated; therefore, the initial $\delta(\vec{r})$ can be approximated as a Gaussian random field with $P(k) \propto k^n$, with $n \approx 1$ (Harrison, 1970, Zeldovich, 1972, as well as the sketch shown in Fig. 1.3). This formalism is rather convenient since all statistical moments of a Gaussian field are zero (assuming a zero mean) or expressed in terms of the variance, Eq. (1.7). Furthermore, the probability that an overdensity with an enclosed mass M within a volume V exceeds the density threshold δ_c is thus also only a function of σ_δ and can be expressed in terms of the error function.

Over the years, several functional forms have been proposed that slightly deviate from the initial Gaussian probability function, which determines the number of overdensities $\delta(\vec{r})$ exceeding δ_c (Bond et al., 1991, Bower, 1991, Lacey & Cole, 1993, Tinker et al., 2008). However, the formalism that describes how many objects form at each epoch at a given mass interval, $dn/d\ln M$, remained and is defined as,

$$\frac{dn}{d\ln M} = f(x)\frac{\bar{\rho}(z)}{M}\left|\frac{d\ln \sigma_\delta^{-1}}{d\ln M}\right|, \tag{1.11}$$

where $f(x)$ is the adjusted functional form, parameterized as

$$f(x) = A\left[\left(\frac{\sigma_\delta}{b}\right)^{-1} + 1\right] e^{-c/\sigma_\delta^2}. \tag{1.12}$$

To summarize, by assuming that the initial distribution of overdensities, $\delta(\vec{r})$, is close to an isotropic Gaussian random field, the entire formalism of hierarchical structure growth can be

reduced to a single tunable parameter σ_δ, which, in turn, only depends on the shape of the matter power spectrum $P(k)$ according to Eq. (1.7).

σ_δ is often expressed as the value measured at a scale of $8\ h^{-1}$ Mpc, since a sphere with a radius of $8h^{-1}$ comoving Mpc contains about the right amount of material to form a cluster (Peebles, 1980). The most precise fit to the data, which comes from the CMB anisotropies, found $\sigma_8 = 0.811 \pm 0.006$ (Planck Collaboration et al., 2014). The resulting functional form of Equation (1.11) using the Planck Collaboration et al. (2014) derived cosmological parameters is shown in Figure 1.6 as a function of redshift and σ_8 to indicate how a different cosmology affects the distribution of haloes at various epochs in the Universe.

Despite the success of the above-described formalism, we need to address the elephant in the room: baryonic physics. The early numerical simulations and the hierarchical growth model, as well as the CMB lesning measurement, do not include baryonic physics, while baryons play a significant role in the formation of large-scale processes. However, baryonic processes are too diverse and complex to provide a single statistical prescription of how baryons evolve over time. Further, new cosmological simulations (Schaye et al., 2023, Nelson et al., 2024, with the first also shown in Fig. 1.4) include hydrodynamical prescriptions but need to be calibrated to local observables, often leading to problems in reproducing observations of the more distant Universe.

With this thesis, I contribute to the study of large-scale structure formation, focusing on observations of the most massive objects to form at any given epoch. By definition, these objects are limited to low-number counts and additionally are heavily impacted by the physics of baryons. In particular, I will describe two types of astronomical objects and discuss how they sparked phase transitions of the baryons that permeate the Universe. Following the order of hierarchical growth, I will first introduce the object earliest to form, namely the first galaxies at $z > 10$ (Section 1.3). The next structures I will discuss are clusters of galaxies — and their progenitors, named protoclusters — representing the end of cosmic structure formation (Section 1.4).

1.3 Galaxies at the epoch of reionization

From a baryonic perspective, the first few million years after the release of the CMB were rather uneventful. During what is known as the cosmic "Dark Ages", small perturbations in the matter field gradually collapsed, detached from the Hubble flow (Peebles, 1980), and coalesced to form larger structures (Bond et al., 1996) while the Universe expanded and cooled adiabatically. It is during this period that baryons, through gravitational collapse, first clumped together and began forming stars (Larson, 1972, White & Rees, 1978).

The basic idea is that dark matter halos collapse first, followed by baryons condensing into the pre-existing potential wells as they dissipate energy (see Dayal & Ferrara, 2018, for a recent review). Since this gas was mainly composed of primordial neutral hydrogen, the main radiative cooling channels were through the rotational-vibrational transitions of molecular hydrogen and the collisional excitation of the Lyα line (Bromm et al., 1999). This cooling causes a loss of pressure, leading the gas to collapse toward the center and form giant molecular clouds (GMCs). These GMCs consist of dense cores and filamentary structures embedded in a more diffuse gas component, spanning a wide range of gas densities (see, e.g., Larson, 2003, for pioneering work

on GMC formation). However, understanding how these clumps of dense, metal-free gas form stars is challenging and remains an active field of research (Dayal & Ferrara, 2018). What is known, however, is that the first stars (referred to as Population III stars) must have had a different composition, intially metal-free, than those we observe today.

The photons emitted by the first stars that formed had enough energy to ionize the neutral hydrogen that permeated the Universe, initiating the "Epoch of Reionization" (EoR). This patchy reionization left an imprint on the small-scale temperature fluctuations in the CMB (Gruzinov & Hu, 1998, Knox et al., 1998) at $\ell \gtrsim 6000$, beyond the axes shown in Figures 1.2 & 1.5 (see, e.g., Park et al., 2013, Smith & Ferraro, 2016). When the hot electrons in the ionized bubbles propagated outward, they Doppler-shifted the CMB photons, a phenomenon known as the kinetic Sunyaev-Zeldovich effect (kSZ; Sunyaev & Zeldovich 1980. We will further touch upon the SZ effect and its many variations in Section 1.4.2). Current CMB survey facilities have not yet been able to directly detect the "patchy kSZ signal" at the EoR due to confusion with other kSZ signals from late-time galaxies, CMB lensing effects, contamination from dust from interlopers (see, e.g., the discussion in Reichardt et al., 2021), and in some cases, the limited resolution of the CMB surveys themselves (e.g., ACT cannot probe beyond $\ell \gtrsim 4000$). Hence, the exact redshift range at which the EoR occurred is not tightly constrained, but the bulk of reionization can be narrowed down to $7 \lesssim z_{\rm EoR} \lesssim 12$ (Park et al., 2013, Smith & Ferraro, 2016).

Consistent with the kSZ predictions that constrain the redshift of the EoR, the first galaxies to form, which drive the universal reionization, seem to appear at similar redshifts ($z \gtrsim 10$). The main photometric method to find potential EoR galaxies has been to search for galaxies with a "break" (or "drop") in emission blueward of the Lyα line, resulting from the absorption of UV photons by the neutral hydrogen in the early Universe (e.g., Oesch et al., 2016). Using the *Hubble Space Telescope (HST)*, many such Lyman break candidates have been discovered (Oesch et al., 2014, Calvi et al., 2016, Stefanon et al., 2019), including the long-held highest-redshift galaxy GN-z11 (Oesch et al., 2014, 2016, Jiang et al., 2021). However, it is the JWST that has revolutionized this field of research. Sensitive near- and mid-infrared observations provide access to the rest-frame ultraviolet (UV) and optical wavelengths at the early stage of the EoR. Using the Lyman break technique, hundreds of $z > 10$ galaxy candidates are identified (see, e.g., Castellano et al., 2022, Harikane et al., 2023, Finkelstein et al., 2023, Donnan et al., 2023), of which over ≈ 20 and counting are now spectroscopically confirmed (see, e.g., Curtis-Lake et al., 2023, Castellano et al., 2022, Zavala et al., 2024, Harikane et al., 2024b) with a current record holder of $z = 14.32^{+0.08}_{-0.20}$ (Carniani et al., 2024, also shown in Figure 1.7).

The rest-frame optical spectroscopy from NIRSpec and MIRI provided fairly robust constraints on the stellar mass, their metal buildup, star formation history, ionizing photon escape fraction, and in some cases, even the presence of an AGN (in GN-z11, Maiolino et al., 2024). These observations have led to the emerging picture of a fast stellar buildup in the early Universe. This rapid buildup challenges our understanding of star formation and baryonic physics (see, e.g., Adamo et al., 2024); even so much so that the cosmological paradigm was brought into question.

As outlined in Section 1.2, the distribution of dark matter halo masses can be accurately predicted in the ΛCDM framework. Therefore, by assuming some total dark matter to stellar mass ratio, a single galaxy (or halo) at a particular redshift can be used to validate the cosmological framework. Using extreme value statistics, there has been tentative (3σ) evidence for a tension

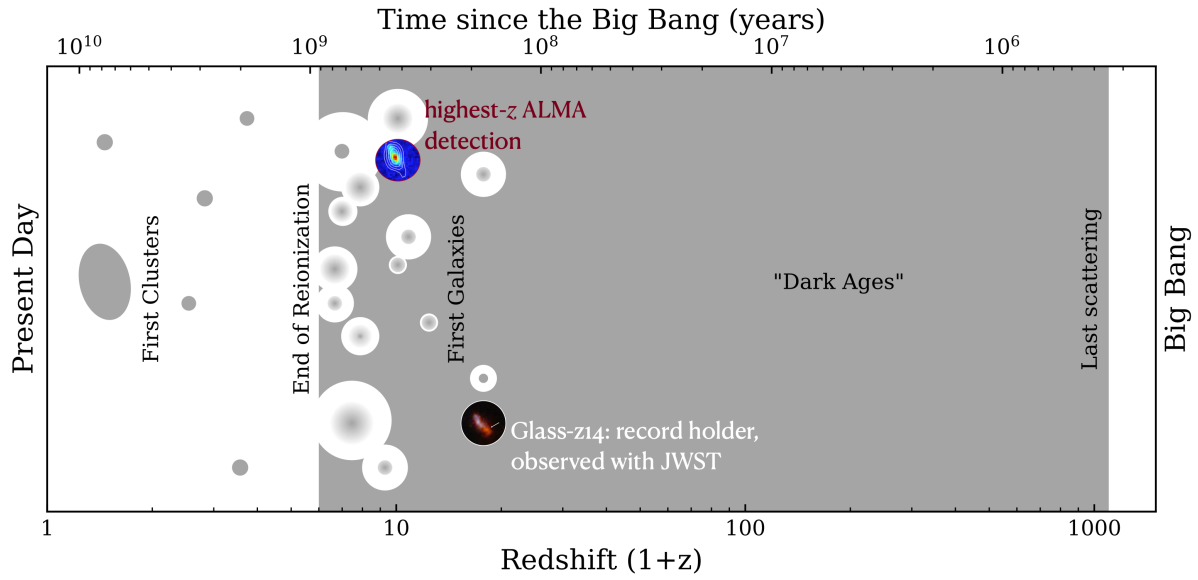

Figure 1.7: Schematic overview of the epoch of reionization. The gray of the "Dark Ages" represents neutral gas, while the white is gas that is ionized by the galaxies within. I highlight the current highest-z galaxy detected by JWST (Carniani et al., 2024) and ALMA (Hashimoto et al., 2018). The figure is inspired by Fig. 12.2 of Ryden (2003).

between recent observational determinations of galaxy masses at high$-z$ (see, e.g., Lovell et al., 2023). However, given the complexity of the observations and our limited understanding of how galaxies are formed, the tension can likely be explained with a better understanding of star formation and baryonic physics. For instance, observations of the interstellar medium (ISM) – the dense gas from which stars form – are still lacking. Since elements produced in stars are returned to the ISM, the metal gas properties traced by fine-structure lines serve as powerful probes of the star formation history and efficiency (see, e.g., Maiolino & Mannucci, 2019).

Observations of the ISM at the early phases of the EoR are missing primarily because the major cooling channels of a more matured ISM are the rest-frame far-infrared (FIR) lines [C II] 158 µm and [O III] 88 µm , which fall outside the wavelength coverage of JWST. Observations with ALMA (see Section 1.5.3)—which cover the observed wavelength range $\lambda = 0.3-8.6$ mm—can complement the new rest-frame UV and optical studies by following up JWST pre-identified galaxies targeting the ISM with ALMA's high-frequency bands.[7] Measurements of [C II] 158 µm and [O III] 88 µm (also when combined with dust continuum measurements) allow for the study of the physical conditions of the ISM by deriving its temperature, density, ionization, and metal enrichment (Bakx et al., 2020, Killi et al., 2023, Tamura et al., 2023, Fujimoto et al., 2024, Rowland et al., 2024). Recent studies using both JWST and ALMA observations on late

[7] I would like to mention that prior to JWST, ALMA was the go-to machine to confirm the redshifts of high-z galaxy candidates through the detection of these fine structure lines. For instance, a handful of $z \sim 8-9$ galaxies with Spitzer and Hubble photometry have been spectroscopically confirmed with ALMA (Laporte et al., 2017, Hashimoto et al., 2018, Tamura et al., 2019, Bakx et al., 2020) before the launch of JWST.

EoR ($z \approx 8$) galaxies (Killi et al., 2023, Fujimoto et al., 2024) indicate high ISM electron densities, as well as a high ratio of [O III] 88 µm /[C II] 158 µm being > 4 (Inoue et al., 2016, Hashimoto et al., 2019, Carniani et al., 2020, Harikane et al., 2020, Witstok et al., 2022, Ren et al., 2023). The high [O III] 88 µm /[C II] 158 µm ratio might be due to late EoR galaxies showing surprisingly low gas depletion time scales (traced by $L_{[\mathrm{C\,II}]\,158\,\mu\mathrm{m}}/\mathrm{SFR}$) compared to what is found in local dwarfs (De Looze et al., 2014, Ura et al., 2023) and galaxies at $z \sim 6-8$ (Bouwens et al., 2022). These results from FIR observations, along with JWST data on $z \gtrsim 8$ galaxies, indicate very different ISM conditions compared to local galaxies, characterized by a low carbon-to-oxygen abundance ratio (Isobe et al., 2023), high ionization parameter (Saxena et al., 2024), and low gas metallicities (Nakajima et al., 2023, Curti et al., 2023, 2024).

Although these FIR studies are promising, there is still no observational consensus on the ISM properties of galaxies during the early phase of the EoR or at even higher redshifts. However, current simulations predict that [O III] 88 µm and [C II] 158 µm in emission (Kohandel et al., 2023, Yang et al., 2023, Nakazato et al., 2023), as well as dust continuum measurements (De Rossi & Bromm, 2023, Mauerhofer & Dayal, 2023, Ziparo et al., 2023, Zhao & Furlanetto, 2024), should be detectable with ALMA at $z > 10$. New (sub-)mm observations are necessary to advance our understanding of the early stages of galaxy evolution and, consequently, its impact on the reionization of the Universe.

1.4 Thermal history of the Universe

The gravitational collapse driven by non-baryonic dark matter sparked a phase transition of the baryonic component in the Universe. The baryons in the Universe transitioned from being completely neutral ($T < 10^4$ K) in the cosmic dark ages to becoming primarily ionized ($> 99.99\%$; Gunn & Peterson, 1965) at a temperature of $T \approx 10^4$ K. Following the evolutionary path of hierarchical structure growth, the small overdensities that collapsed and formed the first galaxies underwent sequential mergers and constant accretion of matter from the cosmic web, deepening the gravitational potential (Bond et al., 1996, Kravtsov & Borgani, 2012). This deepening of the potential well effectively converts gravitational energy to kinetic energy, virializing the whole system. The warm $T \sim 10^4$ K gas that permeates the space between the galaxies then becomes locally thermalized, reaching temperatures of $T \sim 10^6 - 10^8$ K through collisions, such as shocks driven by mergers or accretion, and adiabatic compression (Sunyaev & Zeldovich, 1972b, Kravtsov & Borgani, 2012). Interestingly, the hierarchical nature of the Universe thus sparked another phase transition, leading to $\approx 85\%$ of the total baryonic content being thermalized (Cen & Ostriker, 1999, Fukugita & Peebles, 2004, and Figure 1.8).

To understand gravitational heating and consequently the thermalization of the Universe, we first need to describe the virial theorem[8], which is expressed as,

$$2E_{\mathrm{kin}} + E_{\mathrm{grav}} - 3P(r)V = 0\,, \tag{1.13}$$

where E_{kin} is the total kinetic energy of particles in a halo, E_{grav} is the total gravitational potential energy, and $-3P(r)V$, with V being the volume within radius r, accounts for the non-vanishing

[8]The following section is primarily based on the discussion presented in Voit (2021).

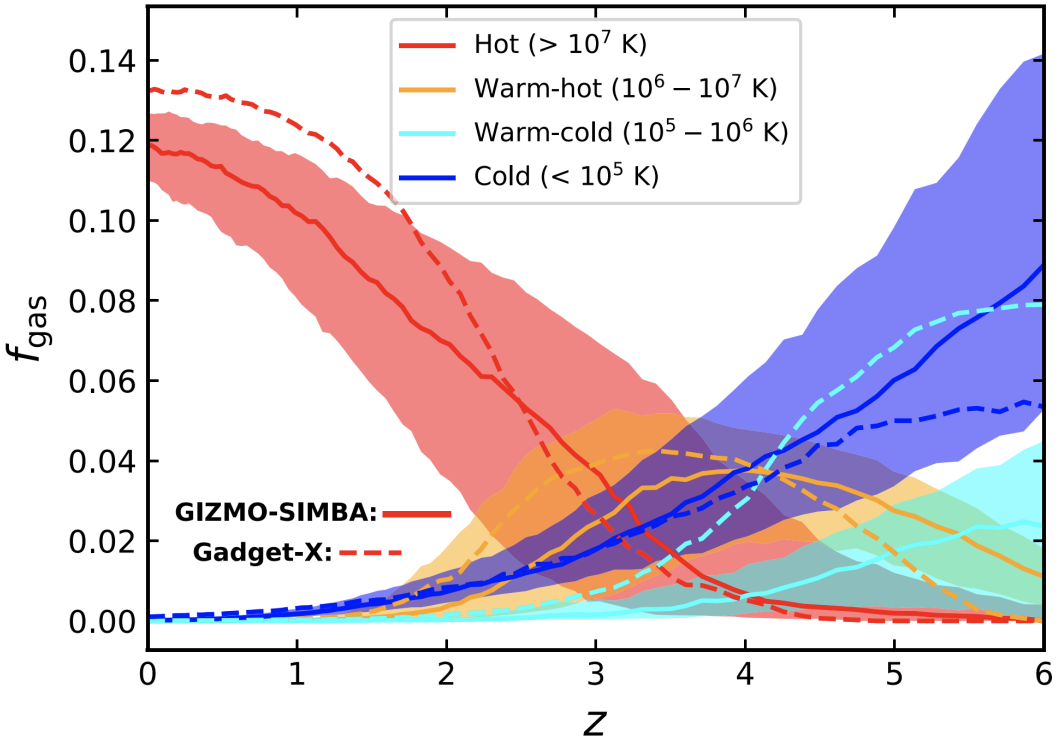

Figure 1.8: Evolution of gas mass fraction at different temperatures for different hydrodynamical code implementations. The figure is obtained from Li et al. (2023).

surface pressure and must be taken into consideration (Mroczkowski, 2011). Eq. (1.13) describes that when a system is virialized, the gravitational energy is converted into kinetic energy, causing the matter within the overdensity to increase its velocity. Assuming that the velocity dispersion in such systems dominates over any peculiar velocities, we can write the total kinetic energy within an arbitrary radius $r_{\rm vir}$ as,

$$E_{\rm kin}(< r_{\rm vir}) = \frac{1}{2} v_{\rm rms}^2 M_{\rm vir}(< r_{\rm vir}) \ , \tag{1.14}$$

where $v_{\rm rms}$ is the root mean square velocity of the matter particles and $M_{\rm vir}(< r_{\rm vir})$ is the virial mass, which is defined as the enclosed mass within the virial radius $r_{\rm vir}$ such that,

$$M_{\rm vir}(< r_{\rm vir}) = \int_0^{r_{\rm vir}} 4\pi r^2 \rho(r)\, dr \ . \tag{1.15}$$

Since $r_{\rm vir}$ is hard to physically define (mathematically, it is the transitional radius at which the accreting matter perturbs the moment of the system enough to break the steady state), one often uses the overdensity convention. In this convention, the mass of a halo is described as the enclosed mass where the average density is a fraction Δ times the critical density of the Universe ρ_c, such that,

$$M_{\Delta,c} = \frac{4}{3}\pi r_{\Delta,c}^3 \Delta \rho_c \ , \tag{1.16}$$

for $\Delta \approx 350$, $M_{350,c} \sim M_{\rm vir}$. A standard convention to use, however, is $\Delta = 200$ or $\Delta = 500$, with $r_{200,c} \approx 2.5 \cdot r_{500,c}$. Furthermore, having expressed the total kinetic energy in terms of its velocity dispersion, we can define a virial temperature so that,

$$\frac{3}{2}\frac{k_b T_{\rm vir}}{\mu m_p} = \frac{v_{\rm rms}^2}{2} = \frac{E_{\rm kin}(< r_{\rm vir})}{M_{\rm vir}(< r_{\rm vir})} \,. \tag{1.17}$$

Importantly, the left-hand side of Eq. (1.17) describes the mean molecular mass per proton, μm_p, or in other words, the gaseous matter (baryons). In contrast, the right-hand side encompasses all matter—including dark matter—as the kinetic energy is defined through Eq. (1.13). Thus, for an overdensity to reach a steady-state configuration, it first needs to virialize, wherein infalling blobs of matter are gravitationally scattered through violent relaxation while maintaining the kinetic energy of the gas (Voit, 2021). The second step is to *thermalize* the gas. Here, the bulk kinetic energy dissipates into thermal energy, which involves small-scale processes that ultimately lead to hydrostatic equilibrium,

$$\frac{1}{\rho(r)}\frac{dP_{\rm th}}{dr} = -\frac{GM(< r)}{r^2} \,, \tag{1.18}$$

with $\rho(r)$ as the gas density, whereas $\rho(r)$ earlier (and in Section 1.2) referred to the total matter density. The hydrostatic equilibrium principle makes the internal thermal pressure of the baryons, $P_{\rm th}$, thus a function of the gravitational potential, enforcing the relationship $E_{\rm kin} = E_{\rm th}$ to hold.

Early works based on hydrodynamical simulations (Springel et al., 2005, Dolag et al., 2009) and observations of massive overdensities (Zwicky, 1933, 1937, Cavaliere & Fusco-Femiano, 1976, Sarazin, 1986) already showed that the average gravitational potential energy, $\langle E_{\rm grav} \rangle$, is efficiently converted to thermal energy, $\langle E_{\rm th} \rangle$, following Eq. (1.18). This means that $\langle E_{\rm th} \rangle$ directly probes structure growth. In addition, precise independent estimates of $\langle E_{\rm grav} \rangle$ and $\langle E_{\rm th} \rangle$ enable us to constrain the amount of nonthermal energy and disentangle gravitational and nongravitational halo heating, with the latter caused by drift motions of gas within the halo and AGN activity (Pandey et al., 2019, Chiang et al., 2020, Chiang et al., 2021, Chen et al., 2024).

Disentangling gravitational heating processes from nonthermal ones is important since the average thermal energy of the Universe at any epoch z is proportional to $\Omega_{\rm m}(z)$ and $\sigma_8(z)$ (Chen et al., 2024), and can thus be used to test the universality of the cosmological parameters. However, hydrodynamical simulations with different AGN feedback implementations deviate in their predictions of what the average Universal thermal energy pressure should be at $z \gtrsim 1.5$, making measurements on the total thermal energy content of the Universe difficult to interpret for cosmological purposes (see, e.g., Li et al., 2023, Chen et al., 2024, and Fig. 1.8). Unfortunately, at $z \gtrsim 1.5$, observations of the average thermal gas energy density are plagued with upper limits, limiting the capabilities to properly constrain simulations to observations. Moreover, at $z > 1.5$, where the global thermal energy is unconstrained, the thermal energy growth is at its maximum (Fakhouri et al., 2010, Dolag et al., 2016), making it the ideal epoch for studying which mechanisms predominantly trigger the *reheating of the Universe*, an epoch in which baryons are converted to have temperatures of $T > 10^6$ K (Figure 1.8). Whether that is through virial shocks and the constant accretion of matter or through high-impact mergers of large-scale overdensities, an open problem I will further study in my thesis.

1.4.1 Galaxy clusters

To study the reheating of the Universe due to gravitational processes, we need to observe the most massive overdensities. According to the virial theorem, Eq. (1.13), which leads to the expression of the virial temperature,

$$T_{\rm vir} \simeq \frac{GM_{\rm vir}(< r_{\rm vir})\mu m_p}{2k_b r} \,, \tag{1.19}$$

the more massive the halo, the higher the temperature of the gas that resides within (Pratt et al., 2019, Voit, 2021). The most massive overdensities are found at the intersections of cosmic web filaments, with total masses at $z = 0$ ranging between $M_{500,c} \sim 10^{14} - 10^{15}\,{\rm M}_\odot$ (see also Fig. 1.6). Despite the tiny stellar component ($\lesssim 5\%$ of the total mass), we refer to these overdensities as *galaxy clusters*, named after their visible constituents, while the dominant baryonic component, also known as the intracluster medium (ICM), is their hot gas ($\approx 15\%$ of the total mass). The remainder can be attributed to the dark matter component, reflecting the total matter content of the Universe, making them, among other reasons, an ideal tool for studying cosmology.

The formation of galaxy clusters takes time, approximately $1 - 2$ Gyr after the Big Bang (Kravtsov & Borgani, 2012, Overzier, 2016). Early theoretical work predicted that hierarchical growth should lead to thermalized gas at redshifts of $z \simeq 3 - 5$ (Sunyaev & Zeldovich, 1972a). This prediction is confirmed by hydrodynamical and numerical simulations, which find small pockets of thermalized gas appearing in cluster progenitors—referred to as *protoclusters*—at similar redshifts (Chiang et al., 2013, Dolag et al., 2016, Remus et al., 2023). The existence of *protoclusters* at these redshifts is confirmed through observations targeting massive galaxies (see, e.g., Schmidt, 1968, Venemans et al., 2007, Miley & De Breuck, 2008), galaxy overdensities (see, e.g., Alberts & Noble, 2022), or Lyα nebulae (Steidel et al., 2000, Daddi et al., 2022). However, these observations are biased tracers of the full baryon population that reside within these halos, probing only $\approx 5\%$ of the total mass. All while observations of the forming ICM at $z \gtrsim 2$ have mainly been elusive.

The traditional means of studying galaxy clusters for cosmology is through observations of their ICM, as seen in the X-rays. X-ray observations of the ICM trace free-free emission (also referred to as bremsstrahlung). In the low redshift universe ($z < 1$), large samples of clusters have been observed with *Chandra* (e.g., Vikhlinin et al., 2009), *XMM-Newton* (e.g., Böhringer et al. 2007 & CHEX-MATE Collaboration et al. 2021), and eROSITA (Bulbul et al., 2024). At $z \gtrsim 1$, however, X-ray detections become more difficult; X-ray flux falls rapidly with increasing z.[9] Hence, X-ray observations of the ICM at redshifts larger than $z \gtrsim 1$ usually comprise a few tens to hundreds of photons in days of integration time (see, e.g., Tozzi et al., 2022). Going even further in redshift space is thus not feasible in the X-ray regime. Hence, observational evidence of the beginning of the thermalization of the Universe has eluded astronomers so far and still needs to be confirmed. The most exciting way forward is through the Sunyaev-Zeldovich effect observations. Di Mascolo et al. (2023) used this phenomenon to obtain the current highest$-z$ detection of the thermalized medium at $z = 2.156$ for an individual object. The next section will go into detail on this phenomenon.

[9] Although it is noteworthy that distant clusters with a given mass are denser and hotter compared to their local counterpart, boosting the restframe X-ray flux, compensating for the redshift dimming (Churazov et al., 2015).

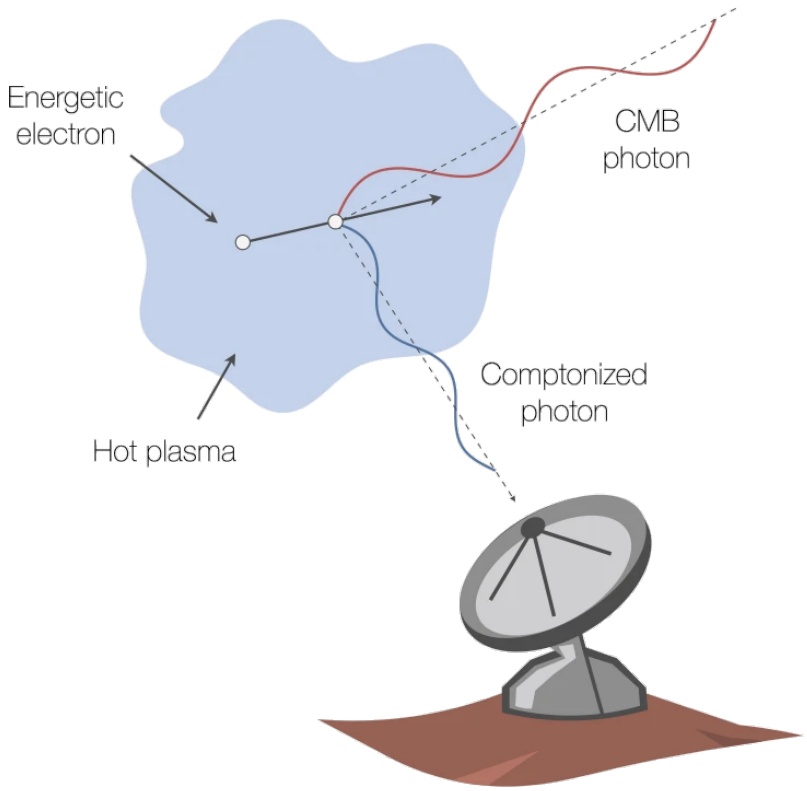

Figure 1.9: Schematic of the tSZ effect. A CMB photon (red) enters the hot ICM (light blue) from an arbitrary angle and, on average, is up-scattered to higher energy (blue) by an electron (black). The figure is obtained from Mroczkowski et al. (2019).

1.4.2 Sunyaev-Zeldovich effect

To study the thermodynamical properties of gas residing in massive gravitational potential wells and link it to observables in the mm-wave regime, I will use the Sunyaev-Zeldovich effect (SZ effect; Zeldovich & Sunyaev, 1969, Sunyaev & Zeldovich, 1970, 1972b). When the freely roaming electrons in the thermalized medium encounter a CMB photon, they distort the initial CMB blackbody spectrum through scattering. Different scattering events manifest differently on the resulting flux measured. In the following subsections, I will discuss the two most prominent types of distortions: the thermal and kinetic ones. These different types of distortions are often referred to as flavors of the SZ effect. Further, I will briefly touch upon general applications of the SZ effect.[10]

The thermal component

Since the CMB photons have much lower energy than the kinetic energy of the individual electrons, the CMB radiation is inversely Compton scattered to higher frequencies, distorting the blackbody spectrum of the CMB (Figure 1.9). This frequency-dependent distortion is the

[10]Most of the information outlined in Section 1.4.2 comes from the review of Mroczkowski et al. (2019).

observable I predominantly exploit in this thesis and is known as the thermal Sunyaev-Zeldovich effect (tSZ effect).

The amplitude of the tSZ effect is a function of the Compton y-parameter:

$$y \equiv \int \frac{k_{\rm B} T_{\rm e}}{m_{\rm e} c^2}\, d\tau_{\rm e} = \int \frac{k_{\rm B} T_{\rm e}}{m_{\rm e} c^2} n_{\rm e} \sigma_{\rm T}\, dl = \frac{\sigma_{\rm T}}{m_{\rm e} c^2} \int P_{\rm e}\, dl\ . \tag{1.20}$$

Here, $\sigma_{\rm T}$ is the Thomson cross section, $n_{\rm e}$ is the number density of the electrons, $T_{\rm e}$ the electron temperature, $m_{\rm e}$ the electron mass, $\tau_{\rm e}$ the optical depth, $P_{\rm e}$ is the thermal pressure due to the electrons following the ideal gas law,

$$P_{\rm e} = n_{\rm e} k_b T_{\rm e}\ , \tag{1.21}$$

and l the path along the line of sight. Thus, the magnitude of the tSZ signal is a direct measure of the integrated line of sight thermal pressure.

The integrated tSZ signal is a direct measure of the total thermal energy of a system. This is often expressed in terms of the spherically integrated Compton $Y_{\rm sph}$-parameter (Mroczkowski et al., 2009),

$$Y_{\rm sph}(R) = \frac{4\pi\sigma_{\rm T}}{m_e c^2} \int_0^R P_e(r') r'^2 dr' = \frac{2}{3} \frac{\sigma_{\rm T}}{m_e c^2} \frac{1}{1+1/\mu_0} E_{\rm th}(R), \tag{1.22}$$

with $P_e(r)$ spherically symmetric and,

$$E_{\rm th}(R) = \frac{3}{2}\left(1+1/\mu_0\right) \int_0^R P_e(r') r'^2 4\pi dr'\ , \tag{1.23}$$

where I used the expression that the volume integral over the thermal pressure of the electrons is equal to the thermal energy, indicating that, indeed, the Compton $Y_{\rm sph}$-parameter is a linear function of it. Furthermore, the spectral shape of the y-distortion is given by;

$$\Delta I_\nu \approx I_0 y \frac{x^4 {\rm e}^x}{\left({\rm e}^x-1\right)^2} \left(x \frac{{\rm e}^x+1}{{\rm e}^x-1} - 4 \right) \equiv I_0 y g(x), \tag{1.24}$$

in terms of the CMB intensity $I_0 \approx 270.33\ \left(T_{\rm CMB,0}/2.7255\ {\rm K}\right)^3$ MJy sr^{-1}, and,

$$x = \frac{h\nu_{\rm obs}}{k_{\rm B} T_{\rm CMB,0}}\ , \tag{1.25}$$

where the CMB temperature is adopted from Fixsen (2009).

An important property of the tSZ effect is that its distortion spectra and, thus, its measured surface brightness distribution are redshift-independent. This is because the redshift dependence in the temperature of the CMB $T_{\rm CMB} = T_{\rm CMB,0}(1+z)$ cancels the redshift dependence on the frequency of the photon according to Eq. (1.1). Since a redshift-independent surface brightness is rather unique, you can also interpret the above as the fractional change in the intensity of the CMB that would be constant for an observer at any given epoch (Mroczkowski et al., 2019).

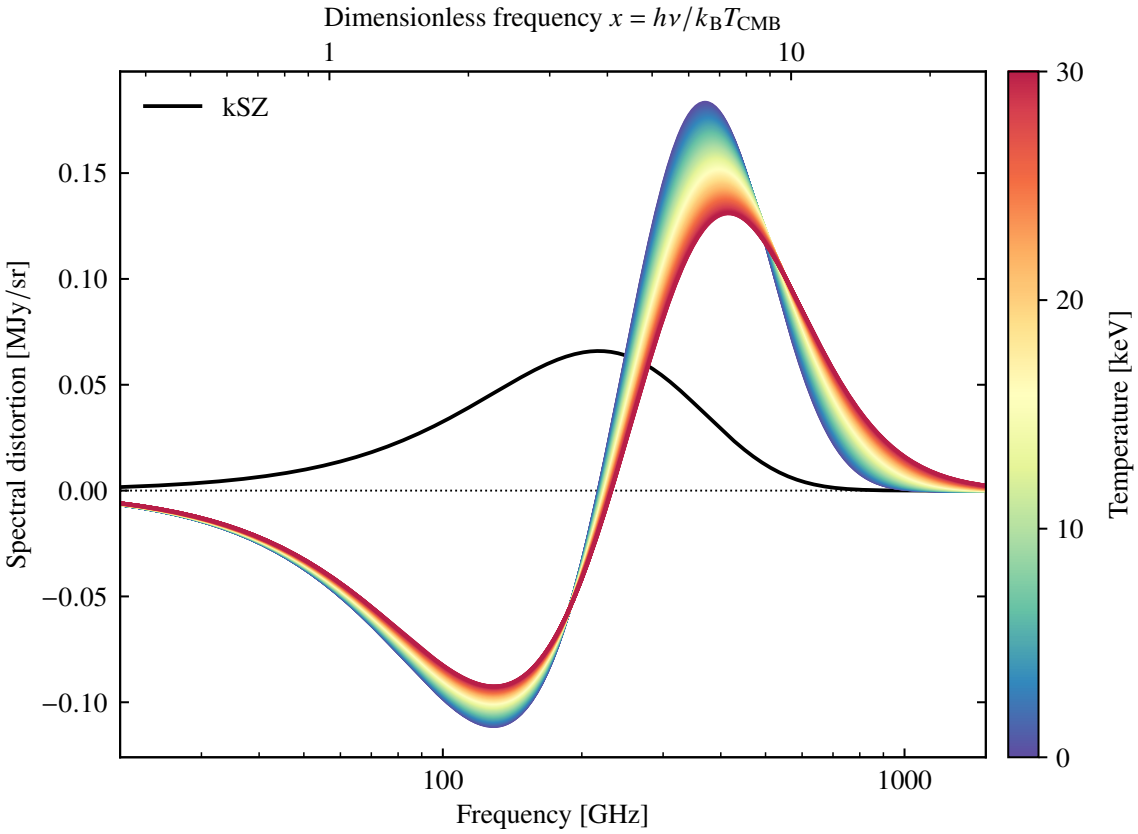

Figure 1.10: Thermal (colored, including relativistic corrections for various temperatures) and kinematic (black) SZ spectra. To generate the kSZ spectra, I used a $\tau_e = 0.01$ and $\beta = 5 \times 10^{-3}$. The tSZ spectrum has $y_c = 10^{-4}$.

The equations above assume the electron number density follows the non-relativistic Maxwell-Boltzmann distribution. However, gas with a mean ICM temperature of $T_e \simeq 4$ keV has dispersion velocities of $\beta \simeq \sqrt{3k_b T_e/m_e c^2} \simeq 0.1-0.2$. Hence, small relativistic corrections must be applied (Itoh et al., 1998, Nozawa et al., 1998, Enßlin & Kaiser, 2000). Figure 1.10 shows the frequency dependence of the tSZ effect for various electron temperatures. In what are often the main SZ-detection bands (~ 90 and 150 GHz), the distortion spectrum becomes negative, manifesting as a negative surface brightness in the continuum maps. The relativistic correction term is on the order of 2.6% at 100 GHz and 2.8% at 150 GHz for gas with $T_e \approx 4$ keV. One could exploit this phenomenon (often referred to as the relativistic rSZ effect) to independently measure the thermal pressure and temperature of the gas. However, measuring the temperature of thermalized gas using relativistic corrections has not come to full fruition yet. To measure this, multiple broadband observations at high angular resolution are needed to disentangle the signal from contaminants such as thermal dust emission from cluster members, as well as other flavors of the SZ effect, such as the kSZ effect (Di Mascolo et al., 2024).

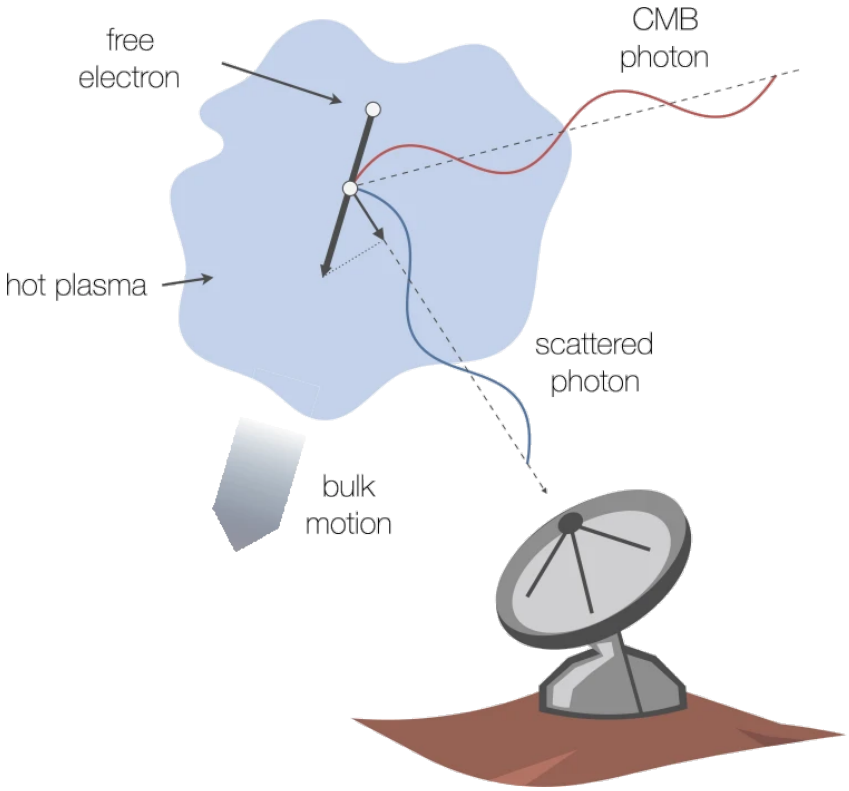

Figure 1.11: Schematic of the kSZ effect. The bulk motion of the gas (blue) creates a Doppler shift to the CMB photons. The figure is obtained from Mroczkowski et al. (2019).

The kinetic component

In contrast to the tSZ, which originates from the velocity dispersion of the electrons in the thermalized medium, the kSZ stems from a Doppler shift caused by the drift, $\beta = v_{\rm peculiar}/c$, velocity of the ICM relative to the CMB rest frame (Fig. 1.11). This Doppler shift induces a shift in the CMB temperature in the direction $\mathbf{n}$ of the thermalized gas, such that

$$\frac{\Delta T_{\rm CMB}}{T_{\rm CMB}} \approx -\int \sigma_{\rm T} n_e \mathbf{n}\cdot\beta dl = -\int \mathbf{n}\cdot\beta d\tau_e \equiv -y_{\rm kSZ}\ , \tag{1.26}$$

or in terms of CMB intensity,

$$\Delta I_\nu = -I_0 \frac{x^4 {\rm e}^x}{\left({\rm e}^x-1\right)^2} y_{\rm kSZ}\ . \tag{1.27}$$

The kSZ effect is indistinguishable from cold and hot spots in the CMB unless prior information on the line-of-sight velocity is exploited. Although hard to detect, resolved kSZ measurements can provide valuable insight into the dynamical properties of the cluster itself. For example, when we introduced the concept of thermalization (Section 1.4) and the hydrostatic equilibrium equation, Eq. (1.18), we assumed that all kinetic energy is converted into thermal energy. However, through kSZ measurements, we can map the kinetic energy in the bulk motion

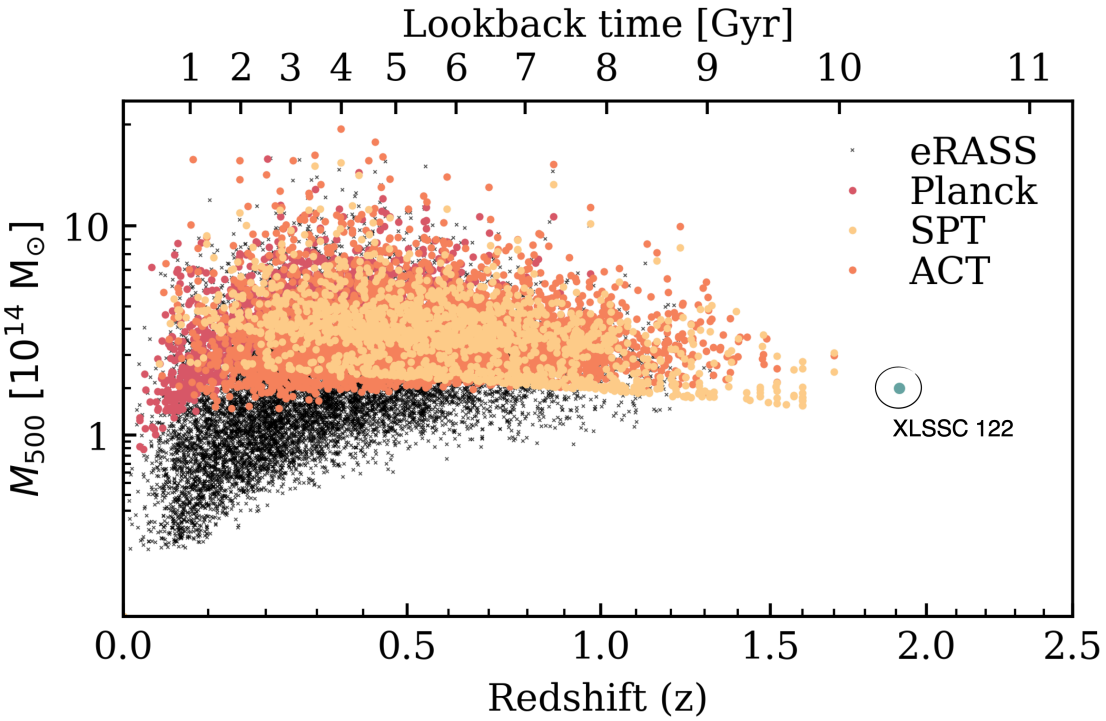

Figure 1.12: Fundamental plane of galaxy clusters. The plot shows the halo mass on the y-axis (M_{500}) vs. redshift (z) on the x-axis for the four largest cosmological surveys: *Planck*, SPT, ACT, and eRASS (obtained from the X-ray mission eROSITA). Binning this figure in redshift space and counting the number of halos leads back to Fig. 1.6. XLSSC 122, the most distant cluster detected in all of these surveys, is highlighted further discussed in Chapter 3.

of the ICM (see, e.g., Sayers et al., 2019, Silich et al., 2024b,a), providing better constraints on the total halo mass, according to the virial theorem, when combined with tSZ measurements (Pratt et al., 2019).

In the remainder of my thesis, the kSZ signal will play a small role compared to the tSZ effect, a small bias in the order of the relativistic corrections. However, since I will use single-band observation (primarily at $\sim$ 90 GHz), the contributions of the various SZ flavors won't be distinguishable from each other. Therefore, for the remainder of the thesis, when referring to the *SZ effect* in general, I will only consider the thermal component.

1.4.3 SZ observations of high-z clusters

The key role the SZ effect plays is that it reveals the gas's thermal energy content. At the low angular (arcmin) resolutions used in SZ surveys, the SZ effect traces a cluster's total thermal energy, serving as an accurate halo mass proxy when the gas is thermalized. At higher resolutions, the SZ effect provides calorimetry, revealing dramatic shocks, mergers, and feedback mechanisms. Ground-based mm-wave CMB surveys have produced large catalogs of galaxy clusters via the SZ effect, containing thousands of members. Figure 1.12 presents the latest cluster catalogs from

three major CMB survey telescopes—*Planck* (Planck Collaboration et al., 2016), SPT (Bleem et al., 2020), and ACT (Hilton et al., 2021)—alongside an X-ray-derived cluster catalog from eROSITA (Bulbul et al., 2024). These catalogs are shown as a function of the redshift (x-axis) and halo mass (y-axis).

Both the redshift and halo mass are fundamental parameters for studying cluster cosmology and are, for instance, needed to reconstruct the halo mass function (Figure 1.6). However, neither parameter is directly measurable from SZ observations. The tSZ effect probes the thermal energy, which serves as a good proxy for the total halo mass, but these measurements require bias corrections, typically done by cross-matching SZ measurements with gravitational lensing ones (Saro et al., 2013, Shirasaki et al., 2024, Singh et al., 2024). In contrast, the redshift of a cluster cannot be inferred from the SZ effect at all and must come from cross-matching optical/NIR galaxy catalogs with wide-field SZ maps (see Table 2 of Hilton et al., 2021). For $z \gtrsim 1$, however, optical confirmation of clusters of galaxies becomes more challenging. At these redshifts, most of the light is redshifted out of the visible bands and into the NIR. Fortunately, NIR observations of galaxy overdensities can be used to derive photometric redshifts since they provide a long-wavelength anchor for color selections intended to separate star-forming galaxies from quiescent populations (Alberts & Noble, 2022). However, follow-up observations targeting the ICM in NIR-selected galaxy overdensities at intermediate $0.7 < z < 1.5$ redshifts more often than not result in non-detections (Orlowski-Scherer et al., 2021). This is mainly caused by the large uncertainties of color-cut-derived redshifts leading to projection effects, which are unaccounted for in current halo-finding algorithms (Thongkham et al., 2024). Therefore, to find high-z clusters of galaxies, one often defers to utilizing single galaxies—such as submillimeter galaxies, luminous radio galaxies, or those embedded within giant Lyα halos—assuming the more massive ones are good tracers of their large-scale surroundings. However, to date, only one system has a robust reported tSZ detection surrounding such a galaxy, namely the Spiderweb (Di Mascolo et al., 2023).

Future photometric surveys (e.g., Euclid and LSST) will push optical/NIR confirmation to higher redshifts by probing larger wavelengths and providing deeper optical surveys. However, current and future CMB surveys such as the Simons Observatory (SO; Ade et al., 2019) and CMB-S4 (Abazajian et al., 2016, 2019, Raghunathan et al., 2022), have or will have limited (arcminute-scale) angular resolutions in their main detection bands, 90 GHz and 150 GHz. Thus, while future surveys might find more clusters at high$-z$, they will still lack the spatial resolution required to study the morphology, dynamical state, and calorimetry of high-z clusters, often blending a merging cluster pair into a single source (e.g., Di Mascolo et al., 2021). Resolved observations are necessary to study the morphology and dynamical structure of clusters to better understand the physical mechanisms that drive the reheating of the Universe. Resolved observations are also needed to map the radial pressure distribution of the thermalized gas and link the measured integrated Compton Y-value to thermodynamical properties.

1.4.4 Importance of pressure profiles

Pressure is the fundamental physical parameter that the SZ effect measures (Section 1.4.2). The shape of the radial pressure profile, a parametric distribution often used to characterize the ICM,

plays a crucial role in linking the thermodynamical properties of the gas to observables. For example:

- The radial pressure profile is used to derive the temperature and density distribution of the gas via the ideal gas law, Eq. (1.21). Variations of the pressure distribution, especially in the core of the cluster, have an impact on the evolution of galaxies that reside within (Donahue & Voit, 2022, Ruppin et al., 2023).

- Pressure profiles enter the expression of the integrated Compton $Y_{\rm sph}$ and corresponding virial mass estimate. The dynamical state of the cluster, often probed by the cuspiness of the core pressure distribution, is important for measuring and interpreting the $Y_{\rm sph} - M_{\rm vir}$ scaling relation used to infer cluster masses, which in turn is crucial for the reliability of cluster counts and cosmological inferences based on those counts (Ruppin et al., 2019, Singh et al., 2024).

- The pressure profile translates to the 2D surface brightness distribution via the SZ effect when assuming line of sight geometry for a cluster. Therefore, the overall profile shape, averaged over a large population, affects the completeness of clusters detected in wide-field tSZ surveys. For example, more peaked profiles concentrate flux in the center, making them easier to detect than flatter distributions. Incorrectly characterizing this completeness introduces biases in derived number counts and thus the cosmological constraints, comparable to the hydrostatic mass bias (Gallo et al., 2024).

- Pressure profiles are used as halo models when cross-correlating unresolved observations of SZ-surveys with large-scale structure tracers at high-z (Pandey et al., 2019, Chen et al., 2024).

Importantly, hydrodynamical simulations predict that the pressure distribution of the ICM should evolve with z (Battaglia et al., 2012, Le Brun et al., 2015, Gupta et al., 2017). However, most SZ studies targeting sources at high$-z$ rely on the "universal" pressure profile (UPP) reported in Arnaud et al. (2010), based on the combination of simulations and X-ray data from the $z \lesssim 0.3$ REXCESS sample. Works at higher redshifts ($0.7 < z < 1.4$, McDonald et al., 2014) rely on stacking X-ray observations and have not utilized resolved SZ observations, which would provide a more direct probe of the electron pressure of the ICM.

Current SZ-only derived pressure profiles based on large samples of clusters are observationally limited to the local Universe because of the limited angular resolution of ACT, SPT, and *Planck* (Planck Collaboration et al., 2013, Pointecouteau et al., 2021). There are current endeavors to extend the sample to higher redshifts, $0.5 < z < 1$, through higher-resolution ($\approx 11''$ and $\approx 17''$ at 150 GHz and 260 GHz, respectively) observations done with NIKA2, an instrument mounted on the 30m-single dish telescope IRAM (Ruppin et al., 2018, Adam et al., 2024), or through ALMA/ACA observations ($\approx 5 - 15''$; Di Mascolo et al., 2020, Kitayama et al., 2023). However, the first results are still limited to low sample sizes ($\approx 5 - 10$ sources) and do not constitute a well-defined selection function. As more and more clusters are discovered at high-z, it becomes increasingly inappropriate to rely on local pressure profile templates to study any of the examples mentioned above.

1.5 (Sub-)mm-wave perspective on the growth of cosmic structurs

The (sub-)mm wavelength range provides a unique window into the electromagnetic spectrum that allows the study of every epoch of the Universe. No other type of telescope can capture light from such a vast range of cosmic history, from the CMB—emitted just a few hundred thousand years after the Big Bang—to the epoch of reionization, the formation of protoclusters, and even the closest astronomical objects like the Sun and its planets. Currently, however, not one (sub-)mm facility has the point source sensitivity combined with a large enough FoV to study all epochs of structure growth at high fidelity on all relevant spatial scales ($\approx 1'' - 10'$). Therefore, I have utilized several different facilities and combined their data to obtain a comprehensive view of the forming structures I study. Although I have also used data from telescopes operating at higher frequencies (NIR, optical, and X-rays), here I will introduce only the (sub-)mm facilities that I have predominantly relied on. The other telescopes will be introduced in the relevant chapters.

Throughout the work presented in this thesis, I have employed three types of (sub-)mm telescopes: CMB survey facilities (Section 1.5.1), large single-dish telescopes (Section 1.5.2), and interferometers (Section 1.5.3). Specifically, I have specialized in using (and observing with) ACT, the Green Bank Telescope (GBT), and ALMA, which will each be discussed in their respective subsections. I am aware that other facilities exist, such as the South Pole Telescope (SPT, similar to ACT), the Large Millimeter Telescope (LMT, similar to the GBT), and the Northern Extended Millimetre Array (NOEMA, similar to ALMA). However, since I worked with data from ACT, GBT, and ALMA, I will focus on these.

1.5.1 Atacama Cosmology Telescope

The goals of ACT (Figure 1.13) were to improve measurements of parameters that describe the very early universe and to study distant clusters of galaxies and their environments. As mentioned earlier in the introduction (Sections 1.2 & 1.4.3), ACT measured the temperature anisotropies of the CMB, enhancing our understanding of the early universe. Additionally, it mapped distortions in the CMB, leading to high-fidelity measurements of CMB lensing and the SZ effect.

To achieve these goals, ACT functioned as a survey facility, scanning the entire southern sky from 2008 to 2022 from Cerro Toco in the Atacama desert at an altitude of 5190 meters. The scientific aim was to map the CMB anisotropies at an angular resolution of approximately an arcminute at around 150 GHz (Swetz et al., 2011), which is approximately five times better than *Planck*. Since the resolution, θ, is set by the dish size, D, through

$$\theta = 1.22 \, \frac{\lambda}{D}, \tag{1.28}$$

with D in meters, ACT was built with a primary mirror of 6 meters in diameter. Furthermore, to optimize mapping speed, it had an off-axis Gregorian design, which provided an unobstructed image of the sky and enabled a large field of view (FoV; $22' \times 26'$, Swetz et al. 2011).

Over its lifetime, the detectors and receiver were modified to cover, at various times, frequency bands centered at approximately 30, 40, 100, 150, 220, and 280 GHz (Swetz et al., 2011,

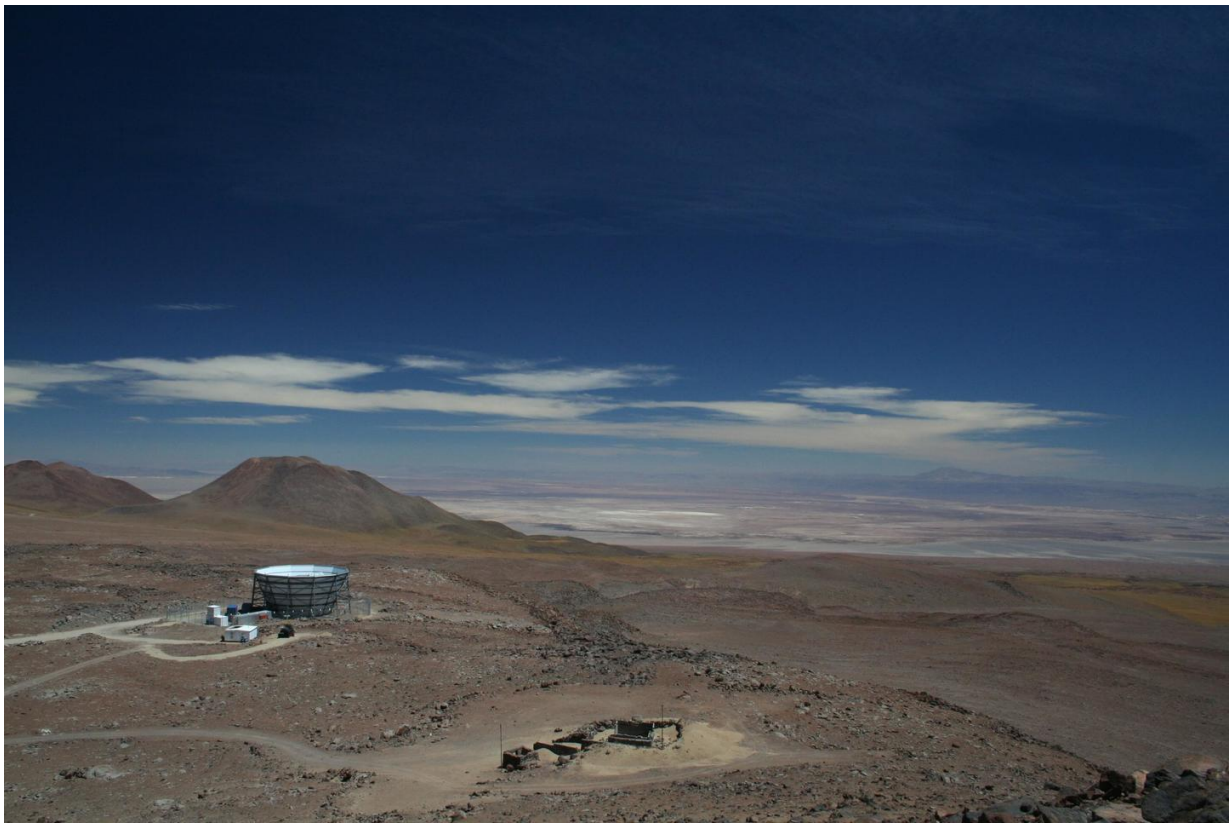

Figure 1.13: Atacama Cosmology Telescope. The figure is obtained from the Atacama Cosmology Telescope website.

Thornton et al., 2016, Henderson et al., 2016). The receiver consisted of three arrays of detectors, each in its own optics tube, positioned differently on the focal plane. For most of the observation period, each array was sensitive to two different frequency bands, allowing for the simultaneous observation of six array-frequency pairs. Each frequency band is imaged by a 32×32 array of transition-edge sensor (TES) bolometric detectors. Bolometers measure temperature variations induced by incoming light; radiation is absorbed by the detector, resulting in a change in temperature that is measured as a change in resistance (Mather, 1982, Low et al., 2007, Wilson et al., 2009). Transition-edge sensors are made from superconducting material. The material is superconducting at low temperatures, but once it heats up, it becomes a regular resistor with higher resistance at higher temperatures. TES detectors take advantage of the narrow interval where the material is at the edge of being a superconductor or regular resistor. Here, the resistance changes very rapidly with even a slight change in the measured surface brightness temperature, making the instrument highly sensitive to small fluctuations.

Figure 1.14: Me, standing in front of the Green Bank Telescope.

1.5.2 Green Bank Telescope

There are two major reasons to build telescopes with larger dish sizes (> 50m). The first is that according to Eq. (1.28), the larger the dish, the better the resolution. For example, to achieve a resolution of $\approx 8''$ at 100 GHz, a 100-meter primary mirror is needed (assuming the beam is diffraction limit). The second reason is the increased collecting area; the larger the dish, the more photons it can collect, resulting in higher point source sensitivity. The GBT (Figure 1.14) is a 100-meter signal dish telescope located in Green Bank, West Virginia, at an elevation of 818 m above sea level. It is the largest steerable object on land. Mounted on top of a rail, it can rotate and observe the full northern sky.

Current optical designs using large single dishes, including the GBT, have a limited focal plane size. This limitation restricts the FoV and the number of detectors that can be placed on the focal plane. MUSTANG-2, the "high-frequency" receiver at the GBT, has an instantaneous

FoV of $4\farcm2$ centered around 93 GHz, with a continuum bandwidth of approximately 30 GHz and 223 TES detectors (Dicker et al., 2014). Due to its limited FoV but large collecting area, the GBT functions more as a user-facility telescope, often targeting individual systems rather than surveying the full sky.

For most observations, the most dominant source of flux in the (sub-)mm wavelength is the atmosphere, being approximately 4-6 orders of magnitude brighter than, for instance, the SZ effect at 90 GHz. Therefore, telescopes using bolometric detectors scan rapidly on and off the source to measure temperature changes as a function of the position in the sky before the atmosphere has time to evolve. The temperature differences are then calibrated to surface brightness units using point sources with known absolute fluxes that are brighter than the atmosphere.

Since MUSTANG-2 consists of 223 TES detectors, it scans requires differential temperature measurements to infer the astrophysical flux of a source. Therefore, the GBT often scans in a daisy-Lissajous scanning pattern, moving with a maximum velocity of $\approx 1'/s$ on and off source before the atmosphere significantly changes. For MUSTANG-2/GBT, the atmosphere is also the biggest noise contributor. Particularly since the GBT is located in "rainy and wet" West Virginia, it only has around 30 nights of observing per year at 100 GHz. More often, the GBT operates in the cm-wave regime, making it not primarily an mm-wave facility. However, to enable high-frequency MUSTANG-2 observations, the GBT is equipped with thousands of actuators that correct for deformations of the primary mirror due to gravity and temperature changes during the night.

1.5.3 Atacama Large Millimeter/Sub-millimeter Array

(Sub-)mm facilities face a major disadvantage compared to optical telescopes in terms of resolution. Following Eq. (1.28), optical telescopes that operate at wavelengths approximately one order of magnitude shorter achieve resolutions an order of magnitude greater with similar mirror/dish sizes. Conversely, achieving a resolution of $\theta = 0\farcs1$ at (sub-)mm wavelengths would require a telescope approximately a kilometer in size. Constructing such a large telescope with the required surface accuracy of the order of a micrometer is not feasible. Therefore, astronomers have turned to the use of interferometers. In the (sub-)mm wave regime, the most powerful interferometer in terms of surface brightness sensitivity is ALMA because of its large total collecting area and long baselines (up to 16 km). However, this capability comes with a trade-off: interferometers like ALMA filter out flux at large spatial scales. Given that ALMA is the facility I used most extensively throughout my thesis (Chapters 2 & 3), I will provide a more in-depth overview of its fundamentals in the following sections, compared to the two previous subsections.

The fundamentals of radio interferometry

Between two antennas in an array that receive light from a coherent wavefront, there is a slight time delay, τ_B, as the light reaches one antenna before the other (Figure 1.16). This time delay is proportional to the baseline length—the distance between the two antennas—and depends on the phase reference point, which is the coordinate where the antennas are pointed. The distance between the two antennas can be expressed in terms of wavenumbers ($k\lambda$), which

Figure 1.15: Atacama Large Millimeter/Sub-millimeter Array. I highlighted the Atacama Compact Array, which is a subarray of ALMA. The figure is obtained from the ALMA webpage.

allows τ_B to be rewritten in terms of a phase delay of the incoming wavefront. The power of the signal is then measured by inferring a sinusoidal pattern of constructive and destructive interference, with the sinusoid's frequency proportional to the baseline length (Remijan et al., 2019). The amplitude of the sinusoid relates to the signal strength. Therefore, in the narrow-field approximation, interferometric arrays fundamentally measure the 2D Fourier transform of the intensity distribution of an astronomical source.

The total power observed at the focal point of an antenna depends on the angle of the incoming wavefront relative to the on-axis pointing. When a plane-parallel wavefront reflects off the parabolic surface of the antenna, it constructively adds at the focal point. However, if the incoming phase front arrives at an angle—meaning the coherent wavefront is rotated relative to the phase reference point—the summed intensity at the focal point experiences destructive interference. This reduces the observed intensity while shifting the flux from the real component to the imaginary. At an off-axis angle of λ/D, where D is the antenna diameter, the path difference maximizes the destructive interference. The central Gaussian-like feature of this Airy pattern is called the *primary beam*, and its width corresponds to the expression given by Eq. (1.28).

The measurements in Fourier space, known as visibilities, are expressed in terms of *uv*-distances, where u and v represent the orthogonal vector bases of Fourier space (Thompson et al., 2017). Since observations are performed with multiple antennas, each visibility has a specific position in the uv-plane. Due to the Earth's rotation relative to the astronomical object, the absolute projected distance between two antennas changes over time, generating additional unique baselines that help populate the uv-plane.

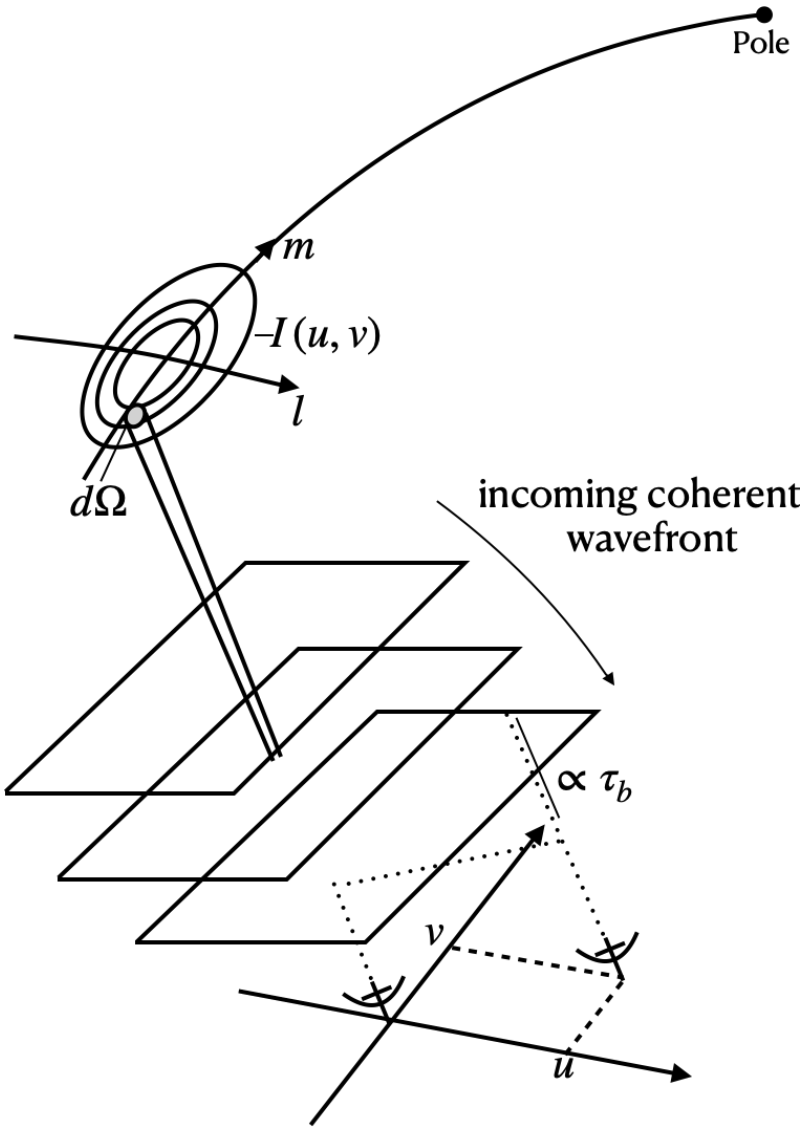

Figure 1.16: Interferometry in a nutshell and its relevant geometries. The source $I(l, m)$ is observed by an interferometer with one antenna pair, where the signal is built from coherent wavefronts. One antenna receives the signal with a time delay of τ_b relative to the other antenna due to the path length difference between the two antennas. The antenna baseline vector, measured in wavelengths, has a length $\sqrt{u^2 + v^2}$. Figure inspired by Fig. 3.2 of Thompson et al. (2017).

Mathematically, each visibility in the narrow-field approximation $\mathcal{V}(u, v)$ is defined as:

$$\mathcal{V}(u, v) = \int_{-\infty}^{\infty} \int_{-\infty}^{\infty} \frac{A_N(l, m)\, I(l, m)}{\sqrt{1 - l^2 - m^2}} e^{-2\pi i(ul+vm)} dl\, dm\,, \tag{1.29}$$

where $A_N(l, m)$ is the normalized primary beam pattern of the antennas, and $I(l, m)$ is the source intensity distribution (Thompson et al., 2017). The infinitesimal terms dl and dm, where l and m are direction cosines measured with respect to the axes u and v, in this equation combine to form a solid angle,

$$d\Omega = \frac{dl\, dm}{\sqrt{1 - l^2 - m^2}}\,, \tag{1.30}$$

such that the power received by each antenna is:

$$P = \int A_N(l, m) I(l, m) \Delta\nu\, d\Omega\,, \tag{1.31}$$

where $\Delta\nu$ is the instrumental bandpass.

Small wavenumbers, corresponding to long baselines, provide high-resolution samples, while short baselines are needed to probe larger spatial scales. The physical distance between an antenna pair is directly proportional to the Fourier mode sampled, which introduces a balance between maximizing the collecting area for each interferometric element and addressing concerns like field of view size and the minimum distance between antennas to avoid collisions. This balance imposes a fundamental constraint on the minimum baseline length, which is close to the diameter of the dish (also known as the shadowing limit), leading to incomplete *uv*-coverage. As described in Eq. (1.29), the signal is a function of the uv-coverage. If a particular mode is not sampled, it inherently means that the interferometer cannot detect the astronomical source at those spatial scales, leading to a missing flux problem. This issue is particularly problematic at zero spacings, where for resolved objects, an interferometer cannot fully measure the total flux of the source, resulting in strong spatial filtering effects. Since the shadowing limit corresponds to the size of the first null of the primary beam, the maximum recoverable scale with an interferometer equals the resolution element of a single-dish telescope, highlighting yet another fundamental difference between interferometric and single-dish (sub-)mm facilities.

Units

Converting the observed power of each visibility to specific intensities,

$$I_\nu = \frac{dP}{d\Omega dA_N \Delta\nu} \,, \tag{1.32}$$

in units of W m^{-2} Hz^{-1}sr^{-1}, we can express the brightness in Rayleigh-Jeans temperatures:

$$I_\nu = \frac{2k\nu^2}{c^2} T_\mathrm{B} \,, \tag{1.33}$$

where T_B is the *brightness temperature* of a blackbody with the same specific intensity at a given frequency in the Rayleigh-Jeans limit (Remijan et al., 2019). Integrating the temperature over the solid angle provides the specific flux density S_ν. Assuming a Gaussian beam, the brightness temperature and the specific flux density can be connected through:

$$\left(\frac{T}{1\mathrm{K}}\right) = \left(\frac{S_\nu}{1\mathrm{Jy}}\right) \left[13.6 \left(\frac{300\mathrm{GHz}}{\nu}\right)^2 \left(\frac{1"}{\theta_\mathrm{max}}\right) \left(\frac{1"}{\theta_\mathrm{min}}\right)\right] , \tag{1.34}$$

where ν is the observing frequency, and $\theta_{\mathrm{max,\ min}}$ are the major and minor axes of the resolution element, often referred to as the synthesized beam. The flux densities observed in astronomy are typically so weak that Janskys (Jy) are used, where 1 Jy $= 10^{-26}$ W m^{-2} Hz^{-1} $= 10^{-23}$ erg s^{-1} cm^{-2} Hz^{-1}. Finally, after Fourier inverting the visibilities, the intensities are given in Janskies per beam or per pixel.[11]

[11] Note that the above equations assume observations of the total intensity and not a single polarization state.

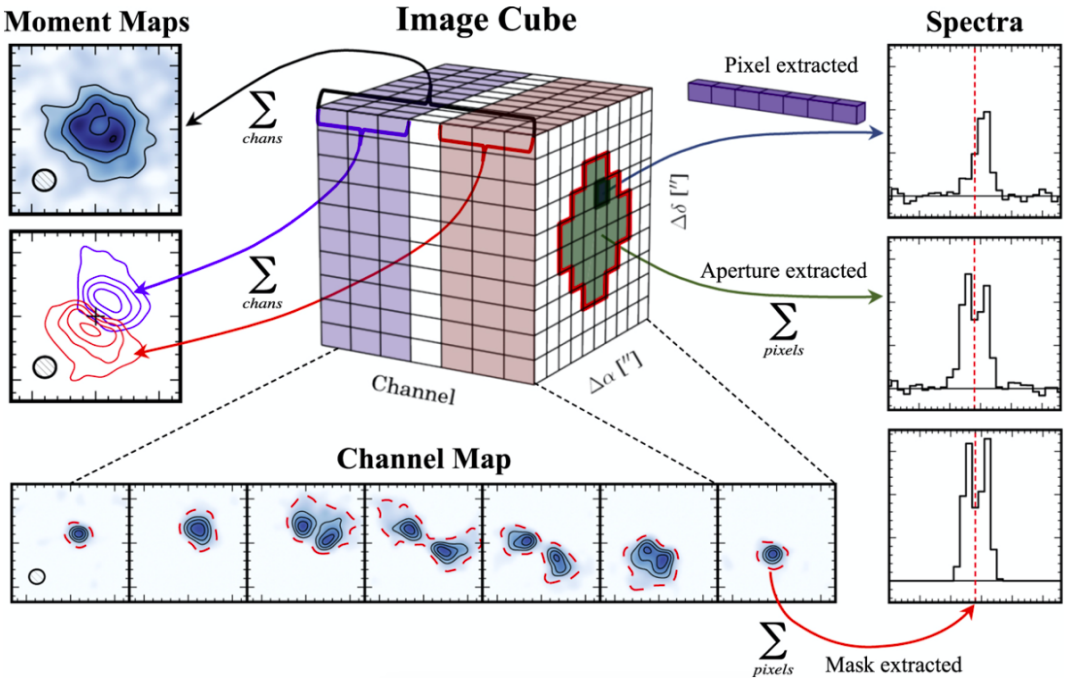

Figure 1.17: Illustration of different analyses applied to an interferometric data cube. Counter-clockwise from top-left: 1) Integrated channels weighted by their frequency, referred to as Moment Maps; 2) Individual Channels; 3) Spectra originating from (top to bottom) a) a single-pixel extraction, b) an aperture-integrated spectrum identical across all channels, and c) a spectral line profile obtained using a matched spatio-kinematic mask (dashed red contours in the Channel Map). The synthesized beam is shown in the lower left of the Moment-0 and Channel maps. The figure is obtained from Loomis et al. (2018).

Generally, the point source sensitivity per visibility in units Jy can be expressed in terms of its rms as:

$$\sigma_{\rm PS} = \frac{2k_{\rm B}T_{\rm sys}}{A_{\rm eff}\sqrt{N_{\rm bl}t_{\rm int}\Delta\nu}}\,, \tag{1.35}$$

where $A_{\rm eff}$ is the effective collecting area of each antenna, $N_{\rm bl}$ is the number of baselines, $t_{\rm int}$ is the integration time, $\Delta\nu$ is the bandwidth, and $T_{\rm sys}$ is the system noise temperature (Thompson et al., 2017). $T_{\rm sys}$ is a linear function of noise terms, such as the receiver and atmospheric contributions (Remijan et al., 2019). Unlike in single-dish data, atmospheric fluctuations on scales accessible by the interferometer are uncorrelated. Importantly, in the Fourier domain, the noise is additive and Gaussian. This occurs because the individual pulses from the electrons are too numerous to distinguish, resulting in a continuous Gaussian random process with a mean of zero (Thompson et al., 2017).

Recovering the spatial distribution of intensities

To obtain the distribution of intensities in the image plane—the native plane of the astronomical source—one must perform an inverse Fourier transform of the visibilities. This transformation,

$$I\left(l,m\right)=\frac{\sqrt{1-l^2-m^2}}{A_N\left(l,m\right)}\int_{-\infty}^{\infty}\int_{-\infty}^{\infty}\mathcal{V}\left(u,v\right)e^{-2\pi i(ul+vm)}du\,dv\,, \tag{1.36}$$

recovers the intensity distribution as a function of angles on the sky (e.g., Jy Beam^{-1} or per sr^{-1}). Since (u,v) depends on the observed frequency, this transformation can be performed per frequency channel, resulting in a data cube that represents the distribution of intensity across RA, Dec, and Frequency (Figure 1.17).

The intensities are convolved with the response function of the interferometer, originating from the incomplete uv-coverage. These interference patterns are referred to as the *dirty beam*. When the intensity of the source is strong (e.g., $S/N > 10$), the side lobes of the dirty beam pattern dominate the noise budget of the cube, creating a strongly correlated spatial distribution. Therefore, deconvolution of the dirty image with the dirty beam is necessary to recover the astronomical signal and accurately infer its significance.

The `clean` algorithm has been the de facto standard in radio astronomy for half a century (e.g., Högbom, 1974, McMullin et al., 2007). `Clean` assumes that the emission distribution is well described by an arbitrary set of point-like or multi-scale Gaussian sources. After Fourier inverting the visibilities, `clean` iteratively deconvolves the intensities through major and minor cycles. In the minor cycle, `clean` matches a delta function or a Gaussian to the brightest emission in the residual image (note that in the first iteration, the residual image is the dirty image). After several iterations of matching components to bright blobs, it removes the model from the visibilities, completing one major cycle. The minor cycle then restarts. This process continues until no signal above a set threshold is found in the residual map. Finally, `clean` convolves the set of matched components with the synthesized beam (i.e., a Gaussian fit to the inner lobe of the dirty beam) and adds this to the residual to create the reconstructed `cleaned` image.

While recovering the spatial distribution of intensities, as outlined above, might provide more intuitive data compared to dealing with its Fourier transform, this process of Fourier inverting the visibility results in several limitations. First of all, a Fast Fourier Transform (FFT) is used to compute the transformation described in Eq. (1.36). By definition, the image plane is therefore a gridded representation of the real data, leading to a loss of information, particularly in terms of sensitivity for underrepresented baselines and baselines at zero spacing (which otherwise could have been recovered by extrapolating from the shadowing limit to $0k\lambda$). Second, due to the FFT, the image domain loses the Gaussian noise properties that characterize the data in the visibility plane, resulting in heavily correlated image plane noise (Vio & Andreani, 2016, Tsukui et al., 2022). Furthermore, to obtain the image reconstruction of the data, `clean` requires a prior to building a model, such as assuming the surface brightness distribution is well described by a set of point sources. In the case of extended emission, such as when observing clusters of galaxies through the SZ effect, this assumption does not hold, leading to a loss of flux on extended scales and inaccurate removal of dirty beam patterns. Noteworthy as well is the Jorsater & van Moorsel effect (JvM effect; Jorsater & van Moorsel 1995). This effect arises from incorrectly quantifying

the proper beam size in a data cube (Czekala et al., 2021), leading to incorrect scaling of the flux after `cleaning`. Overall, the examples provided here suggest that working in the image domain can significantly bias the derived astronomical measurements.

Why I work in the visibility-plane

This final subsection explains why working in the uv-plane not only helps to overcome biases introduced by the FFT and the `clean` algorithm (as outlined previously) but also improves the recovery of astronomical signals. This approach is particularly beneficial when attempting to recover flux on extended scales, such as when probing the SZ effect.

A key advantage of working in the visibility plane is its optimal compatibility with a forward modeling approach when analyzing the data. In this approach, a model is created in the image plane, multiplied by the primary beam, Fourier transformed into the uv-plane to match its exact sampling function, and then compared with the visibility data to compute the likelihood. This method highlights three advantages of working in the visibility plane over the image plane: 1) The noise is less correlated and more Gaussian in the uv-plane (Thompson et al., 2017), which is crucial for accurately estimating the likelihood when comparing the model to the data. 2) Forward modeling allows the usage of the exact sampling function of the interferometer, which is essential for measuring flux at small uv-distances or underrepresented baselines. 3) It also helps overcome problems associated with data deconvolution, such as the JvM effect and incorrect dirty beam removal, which can arise from false assumptions about the surface brightness distribution when creating the model.

Forward modeling in the uv-plane also facilitates a seamless combination of data from different interferometric arrays with varying configurations and antenna sizes (e.g., ACA combined with the 12m array). It also allows for the integration of single-dish and interferometric data through a joint likelihood approach. Furthermore, uv-plane analysis effectively separates the spatial scales of unresolved sources from extended emissions while preserving the spectral behavior of each component without blending them. Overall, working in the uv-plane through forward modeling provides a more robust and versatile framework for analyzing complex datasets, ensuring more accurate and reliable results in astronomical observations than when working in the image domain.

1.6 This thesis

What objects form when overdensities first detach from the Hubble flow and emerge from the cosmic web? What characterizes them? And what impact do they have on the thermodynamical evolution of the Universe? In the introduction, I have sketched the foundation for understanding cosmological structure growth: from the evolution of the Universe to the detachment from the Hubble flow and the initial collapse of overdensities, to the objects that form within them and how they can be observed in the (sub-)mm wavelengths. In my thesis, I examine this evolution within a small sample of objects that are the first to form in their respective epochs and lie at the limit of what is currently observable. I mainly use (sub-)mm facilities to study the first galaxies and

galaxy clusters. I divided my work into three distinct science chapters to provide a comprehensive overview of the research I conducted over the last three years:

Chapter 2 presents a full overview of my work on $z > 10$ galaxy candidates targeted with ALMA. Together with my research group, we wrote an ALMA Director's Discretionary Time (DDT) proposal to observe the [C II] 158 µm line in HD1, a galaxy initially thought to be at $z \approx 13$. The proposal was successful, and the data was published in Kaasinen, **van Marrewijk** et al. (2023). For this study, I developed a novel technique to robustly quantify the likelihood of faint emission lines being real. By jackknifing the visibilities, I create various noise realizations of the observation-specific dataset, thus increasing the sample size of the noise statistics and thereby better sampling the likelihood of false detection. We further applied this technique to all archival ALMA observations targeting galaxy candidates at $z > 10$. The results are part of another academic work, currently submitted as **van Marrewijk** et al. (Sub.), and are presented alongside the work of Kaasinen, **van Marrewijk** et al. (2023) in Chapter 2.

Following the hierarchical structure growth in the Universe, Chapter 3 discusses the work I have done and published as **van Marrewijk** et al. (2023) on the highest redshift galaxy cluster found by wide-field CMB survey telescopes, XLSSC 122. By combining ACT and ALMA observations through a forward modeling routine in the visibility plane, I mapped the radial pressure distribution via the SZ effect from the core to the virial radius at $\sim 5''$ resolution. I also discuss its dynamical implications and the discovery of a sub-component believed to be a smaller halo merging into the larger overdensity, causing shock heating of the gas.

The final science chapter of my thesis, Chapter 4, details the development of a generic simulator for large single-dish facilities. Although GBT/MUSTANG-2 and ALMA observations are ideal for studying the morphology and dynamical state of galaxy clusters, several limitations still exist. These include projection effects along the line of sight, observational sensitivity, and filtering on small and large scales when interpreting results. Moreover, the tools used for modeling the ICM have not been thoroughly validated against extensive hydrodynamical simulations, particularly at high-z. Meanwhile, theoretical work on deriving radial thermodynamical profiles of the ICM typically relies directly on particle data rather than synthetic observations. To address these issues, synthetic observations with realistic atmospheric noise models coming from large cosmological hydrodynamical simulations, analyzed with current observational tools, provide essential insights into the thermal and non-thermal energy growth of the Universe. During my PhD, I developed a generic simulator for single-dish telescopes to address these challenges and facilitate such comparisons. I also used this tool to evaluate science cases and study scanning strategies for future facilities and instruments, such as those detailed in the AtLAST design study (Mroczkowski et al., 2024). The work this chapter presents is also submitted as **van Marrewijk** et al. (2024).

Chapter 5 concludes my thesis with a summary and future outlook section. There, I outline where my own work is heading while also broadening the perspective, providing examples and predictions on the direction this field may take. A significant portion of this chapter is based on the numerous proposals I have written, requesting observation time to study cluster formation and evolution at high redshifts. I particularly highlight a project named *ReCESS* (Representative Cluster Evolution Sunyaev-Zeldovich Survey), which began as a large ALMA program I led in my first year, which, after initial rejection and rebranding eventually secured time on both

the GBT/MUSTANG-2 and ALMA. Through this project, I gained hands-on experience with observations, learning to tune and bias TES detectors, conduct the observations, and reduce data. While most observations were conducted remotely, I also visited the GBT to observe the clusters I proposed. My programs were awarded 80 hours of both MUSTANG-2 and ALMA time, targeting galaxy clusters beyond $z > 1.25$, which are now partially observed. Preliminary results are presented in the future prospects section of Chapter 5.

Chapter 2,

To see or not to see galaxies beyond a redshift of ten

*The content of this chapter is based on two complementary articles. One was published in A&A as Kaasinen, **van Marrewijk**, et al. (2024). The other has been submitted to A&A as **van Marrewijk**, Kaasinen, et al. (Sub.). From the first paper, I have included only the text and analysis that I led or significantly contributed to. Additionally, I note at the beginning of a section if my contribution to that specific section was less prominent.*

“Though it be madness, yet there is method in it”

- William Shakespeare

Determining whether faint astronomical sources are real is critical for many areas in astrophysics. Ever fainter sources are being studied thanks to technological advancements, but even with these advancements, there have always been sources at the limit of detectability that need to be characterized. There is always a reason to push studies to the low S/N regime. Interferometers such as the Atacama Large Millimeter/Submillimeter Array (ALMA) and the Very Large Array (VLA) have enabled the efficient study of faint, distant sources in the mm/cm-wave regime. However, these interferometric data are highly complex; their underlying noise distribution is challenging to quantify, leading to potential biases at low S/N and difficulties in interpreting the data. This can have profound consequences, for example, when determining the existence, redshift, and physical properties of faint galaxies.

Correctly determining the likelihood of faint peaks in interferometric data has become particularly relevant over the last few years as the community has tried to detect the ISM of extremely high-redshift galaxies. Over the past two years, five ALMA Director's Discretionary Time (DDT) programs[1] were approved and executed to follow up $z > 10$ galaxy candidates. These galaxies were initially identified from optical and near-infrared photometry, mostly including data from the JWST. However, modeling the spectral line energy distribution of these photometric data resulted in a wide redshift probability distribution, including several potential solutions. Capitalizing on the broad spectral coverage of ALMA, the DDT programs aimed to confirm the redshifts of the galaxy candidates by targeting the [O III] 88 µm line. But, obtaining robust line detections with an accurate S/N estimate has proven challenging.

So far, ALMA DDT observations of $z > 10$ candidates have resulted in a handful of potential upper limits on the targeted line emission (Popping, 2023) and marginal, low S/N ($3 - 4\sigma$) detections of [O III] 88 µm (see, Harikane et al. 2022, Yoon et al. 2023, Bakx et al. 2023, Fujimoto et al. 2023). Some of these marginal detections have since been proven not to correspond to actual emission lines, with follow-up JWST/MRS and JWST/NIRSpec spectra revealing at least two of these galaxies to be at a different redshift to that implied by the initial false positive [O III] 88 µm detection (Zavala et al., 2024, Harikane et al., 2024a). This highlights a broader issue: false positive identifications of emission lines lead to biases in the derived physical properties. In the case of incorrect redshift solutions, this has profound implications for the number counts of the earliest galaxies, thereby impacting our understanding of both cosmology and galaxy evolution.

In this work, we present a straightforward and effective technique to quantify the detection level and underlying noise distribution in interferometric data sets. By differencing the visibilities, we generate various noise realizations of the observation-specific ALMA measurement set. Then, by applying line-finding algorithms on both the real and source-free image cubes, we sample the likelihood of a marginal detection being real without needing to assume an underlying noise distribution. Because of the increased sample size of the noise statistics compared to only using the distribution of negative peak values, this method does not require the computation of a large four-dimensional auto-correlation function (ACF, see, e.g., Vio & Andreani, 2016, Tsukui et al., 2022). Whereas current ACF implementations have only been developed for 2D data sets, in

[1] Additionally, one 80+ hour NOEMA observation on GN-z11 (Fudamoto et al., 2024) and two other DDTs were executed this year but are yet unpublished.

the case of line searches, the ACF would need to be computed per channel or moment-0 map for cubes made with different channel/line widths. This is computationally expensive, making it more efficient to use our tool in combination with classic matched filter approaches.

We make our technique readily available to the community in the form of the public tool `jackknify`, along with clear, step-by-step tutorials.[2] Although we implement and optimize the tool for ALMA data, `jackknify` is compatible with any type of interferometric observations that use the *Common Astronomy Software Applications for Radio Astronomy* (CASA, CASA Team et al., 2022). For example, this jackknifing technique may be useful for characterizing the faint HI emission from $z > 1$ galaxies using Squared Kilometer Array (SKA; Dewdney et al., 2009) and its precursors (see, e.g., Baker et al., 2024), or quantifying the faint molecular line emission from quiescent galaxies with ALMA. In this work, we apply `jackknify` to the four archival DDT observations targeting $z > 10$ galaxy candidates. We will test two scenarios: one in which no prior knowledge regarding the source's redshift is available and one in which we can use a prior from JWST on the frequency location of the line.

In this chapter, we further perform a more in-depth analysis of one of the four archival DDT observations, HD1. HD1's redshift was tentatively confirmed with ALMA by detecting a [O III] 88 µm line at 3.8σ (Harikane et al., 2022), corresponding to a redshift of $z = 13.27$. However, the tentative line detection and photometric redshift constraints left significant ambiguity, as HD1's spectral energy distribution could also fit a $z \sim 4$ galaxy. To resolve this, we conducted ALMA Band 4 observations targeting [C II] 158 µm emission, which would confirm HD1's redshift. This chapter highlights these observations and their implications.

The chapter is outlined as follows. Section 2.1 describes which interferometric data sets we use highlighting the HD1 data set, Section 2.2 provides the overview of how `jackknify` is built, Section 2.3 describes the performance of the tool via simulated observations, Section 2.4 contains the results of applying `jackknify` to the ALMA observations of $z > 10$ galaxy candidates, and Section 2.6 provides an overview and summary of this work. For all calculations, the assumed cosmology is based on Planck Collaboration et al. (2014), a spatially flat, Λ cold dark matter (ΛCDM) model with $H_0 = 67.7$ kms^{-1} Mpc^{-1} and $\Omega_{\rm m} = 0.307$.

2.1 Archival ALMA observations

We test and validate our jackknifing tool, `jackknify`, on three sets of ALMA DDT observations targeting $z > 10$ galaxy candidates pre-identified from photometry (as presented in Castellano et al., 2022, Naidu et al., 2022, Harikane et al., 2022, 2023). All of these DDT observations (Harikane et al., 2022, Bakx et al., 2023, Yoon et al., 2023, Fujimoto et al., 2023) aimed to detect the [O III] 88 µm emission line over a wide redshift probability range. To maximize the redshift coverage, each spectral setup consisted of four adjacent tunings, covering a large, ≈ 30 GHz bandwidth. A comprehensive overview of the literature results and observational specifics is presented in Table 2.1.

Calibrated measurement sets were provided by the European ALMA Regional Centre network

[2] see https://joshiwavm.github.io/jackknify/

Archival ALMA observations of $z > 10$ galaxy candidates

ID	HD1	GLASS-z12	GLASS-z10	S5-z17-1
RA [deg]	150.463792	3.498985	3.511917	339.015958
DEC [deg]	2.547233	-30.324767	-30.371861	33.904611
ALMA source name	HD1	GLASS-z13	GLz11	S5-z17-1
PI	A. Inoue, G. Popping	T. Bakx	I. Yoon	S. Fujimoto
ALMA Project Code	2019.A.00015.S, 2021.A.00008.S	2021.A.00020.S	2021.A.00023.S	2021.A.00031.S
ALMA Band	6, 4	6	7	7
Beam [″]	$0\farcs51 \times 0\farcs87, 45°$	$0\farcs32 \times 0\farcs29, 46°$	$0\farcs77 \times 0\farcs59, 81°$	$0\farcs78 \times 0\farcs45, 3°$
Channel width [MHz]	39	31	31	31
On source time [h]	2.1, 4.9	8.1	6.9	0.5
Reported tentative detections				
Ref. for initial identification	Harikane et al. (2022)	Castellano et al. (2022),Naidu et al. (2022)	Naidu et al. (2022)	Harikane et al. (2023)
Reference for ALMA data	Harikane et al. (2022)	Bakx et al. (2023), Zavala et al. (2024)†	Yoon et al. (2023)	Fujimoto et al. (2023)
$z_{\rm phot}$	$13.3 - 15.2$ (or 3.9)	12.2 ± 0.2	10.4 ± 0.5	$16.7^{+1.9}_{-0.3}$
Δz covered	$12.6 - 14.3$	$11.9 - 13.5$	$10.1 - 11.1$	$16.1 - 17.3$
S/N ([O III] 88 μm)*	3.8	5.8, 3	4.4	5.1
Offset	–	$0\farcs5$, $0\farcs0$	$0\farcs17$	–
$z_{\rm spec}^{ALMA}$	13.27	12.117 ± 0.001, 12.339 ± 0.002	10.38	16.01
$z_{\rm spec}^{JWST}$	–	12.33 ± 0.02	–	–
Freq [GHz]	237.8	258.7 , 254.35	298.25	338.726
$\Delta\nu$ [km s^{-1}]	400	400 ± 70	225	118

Table 2.1: Candidate coordinates and reported detection significance of the previously reported line searches. †The reported details after precise redshift information became available from JWST observations. * In the case of S5-z17-1, we quote the redshift of the plausible [O III] 52 μm line. The beams are given in terms of major, minor, and position angle. In the case of HD1, wherever applicable, we first note the Band 6 observations than the Band 4.

(Hatziminaoglou et al., 2015) through the calMS service (CalMS; Petry et al., 2020) using CASA v5.4.0. To reduce the data size, we performed two additional operations on the calibrated data, applying a time averaging of 30 seconds and spectral averaging of the visibilities in 30-40 MHz bins. The frequency binning was conducted in a manner that avoided interpolation over the frequency axis. We used `uvcontsub` to manually continuum subtract a first-order polynomial from the measurement sets since interlopers emitting in the continuum could be present. I omitted the frequency channels where tentative features might be present in the data based on the previously reported detections. Finally, we imaged all measurement sets using the TCLEAN task with natural weighting.

2.1.1 In depth look at the ALMA observations of HD1

Rather than detailing all four observations, we will focus on HD1 as an illustrative example to show the data. In the following subsection, we provide a brief overview of the earlier Band 6 (Table 2.1) observations alongside our new Band 4 observations. We then conduct a conventional analysis, including spectral line extraction and the creation of moment-0 maps to reproduce the tentative features observed in Harikane et al. (2022). The conventional analysis highlights the need for a more robust analysis to quantify the likelihood of detection (and non-detection).

New Band 4 observations

To confirm or reject the proposed redshift of HD1, we obtained ALMA Band 4 observations through the ALMA DDT program (Table 2.1), targeting the [C II] 158 µm emission that would correspond to the tentative [O III] 88 µm detection. We used a setup with four spectral windows (SPWs) centered on 131.287 GHz, 133.164 GHz, 143.206 GHz, and 145.087 GHz. All SPWs except the one centered on 133.164 GHz were observed in Time Division Mode (TDM) with a bandwidth of 1.875 GHz (to obtain a continuum measurement), whereas the other one was set up using 240 channels with a 7.812 kHz spectral resolution and 1.875 GHz bandwidth (to target the [C II] 158 µm line). The observations were centered on RA $10^h01^m51.31^s$, Dec $+02^d32^m50.0^s$ and were carried out on March 3 and 6, 2022. The total on-source time was 4.9 hours, with an average PWV of 4.746 mm.

All data processing and calibration were performed with `CASA`, version 6.2 (McMullin et al., 2007). We used the calibrated measurement sets generated by the observatory for the imaging of the observations. Imaging was performed with the `tclean` task, adopting natural weighting. We create both a continuum map (using the SPWs observed in TDM) and spectral cube (using the SPW centered at 133.16 GHz). No continuum emission is detected. The continuum root-mean-square (rms) noise level is 5.2 μJy beam^{-1} (yielding a 3σ upper limit of 15.6 μJy beam^{-1}). For the spectral cube at 133.16 GHz, the rms is 127.3 μJy beam^{-1} per 78 MHz. The continuum and spectral cube image have a beam of $2\farcs78 \times 2\farcs16$ and $2\farcs91 \times 2\farcs27$, respectively. The final data cube used in the analysis reported here spans a frequency range of $132.22 - 134.08$ GHz, corresponding to a redshift range of $z = 13.17 - 13.37$. The CLEANed Band 4 continuum map showed several off-center point sources. For the spectral cube, these were removed through `CASA-imcontsub` (because `CASA-uvcontsub` is less optimized for removing off-centered co-detections).

Revisiting the ALMA Band 6 observations

As stated in Harikane et al. (2022), the ALMA Band 6 DDT observations are observed with a spectral scan setup that should target the [O III] 88 µm emission line for a redshift range of $12.6 < z < 14.3$. For the full observational details, we refer to Harikane et al. (2022). Note that these observations span the frequency range 222 - 250 GHz.

We tested whether manual flagging could significantly alter the tentative [O III] 88 µm like feature visible in the image-plane (Fig 5 in Harikane et al., 2022). Because antenna DA41 had slightly elevated noise levels over the entire time domain, we tested the impact of completely flagging data from this antenna and found no clear difference between the moment-0 maps generated using the initial, `CASA` version 6.3 pipeline reduced and calibrated data and those where we flagged antenna DA41. In this work, we therefore use the calibrated data reinstated using the ALMA pipeline generated scripts provided by the observatory.

We image the data using the `tclean` task, adopting natural weighting and creating cubes with channels of 50 km s^{-1} width. The sensitivity per channel is 0.3 mJy beam^{-1}, where the beam FWHM is $0\farcs51 \times 0\farcs87$. We find no evidence of any continuum emission. For the continuum, the typical rms noise level is 8.0 μJy beam^{-1}, yielding a 3σ upper limit of 24.0 μJy beam^{-1}.

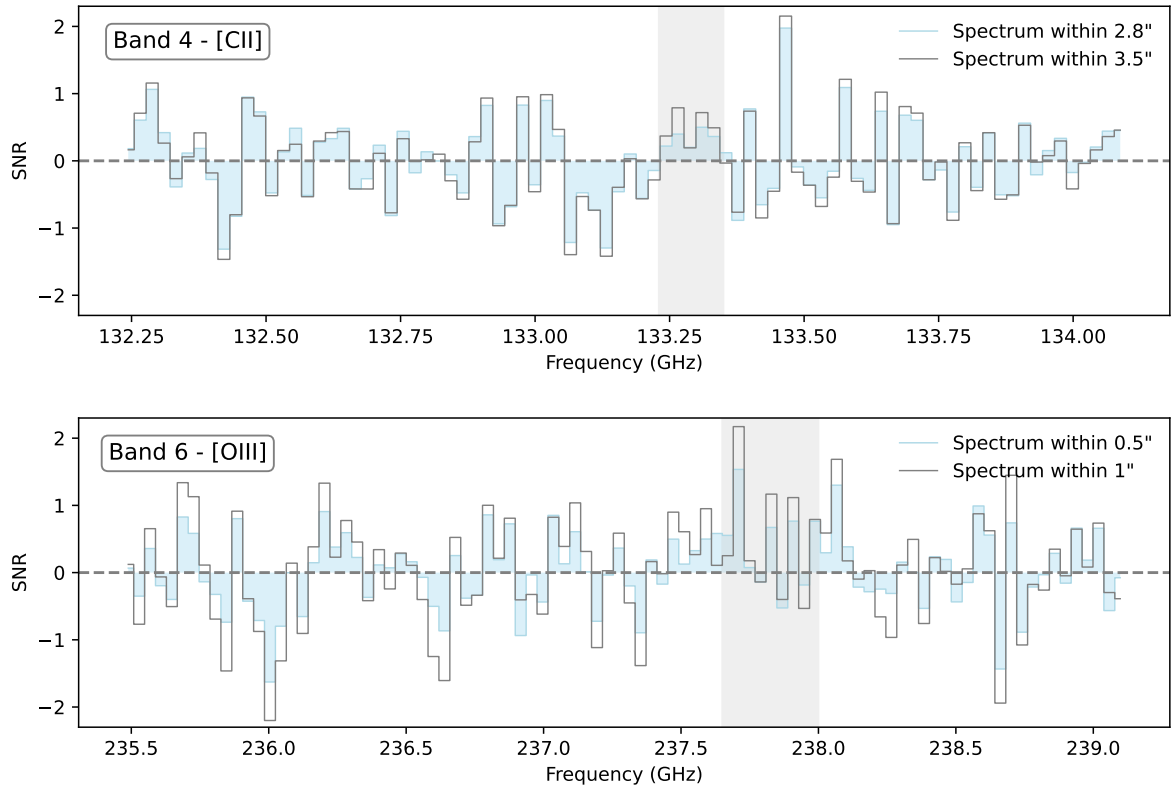

Figure 2.1: Integrated aperture spectra for HD1 around the expected frequency of the [C II] 158 µm (top panel) and [O III] 88 µm (bottom panel) emission lines. To easily compare the spectra extracted within apertures of different size, spectra are presented in terms of signal-to-noise ratio rather than actual flux density. For the [C II] 158 µm emission we adopt apertures of 2.8 and 3.5 arcsec, corresponding to a size close to the beam and 1.25 times the beam of the ALMA band 4 data, respectively. In the bottom panel we adopt an aperture of 0.5 and 1.0 arcsec, corresponding to roughly the beam size and the aperture adopted in Harikane et al. (2022) for the same data, respectively. The grey shaded area marks the tentative [C II] 158 µm feature (top panel), and the location of the [O III] 88 µm line feature presented in Harikane et al. (2022).

Inspecting the ALMA images and spectra

We search for the [C II] 158 µm (and [O III] 88 µm) emission line from HD1, with the aim of securely confirming its spectroscopic redshift. Thus, we create aperture-integrated spectra around the spatial location of HD1, focusing on the spectral range where the [C II] 158 µm and [O III] 88 µm emission lines are expected, given the redshift proposed by Harikane et al. (2022). If HD1 is indeed at $z = 13.27$, the [C II] 158 µm emission line should be located at a frequency of 133.18 GHz. In the top panel of Fig. 2.1, we present the integrated spectrum of HD1 around this frequency within apertures of $2\farcs8$ and $3\farcs5$ diameter (corresponding to approximately the beam size and 1.25 times the beam size). No emission line is visible around 133.18 GHz for either aperture, indicating that the [C II] 158 µm emission line is not detected at the expected frequency

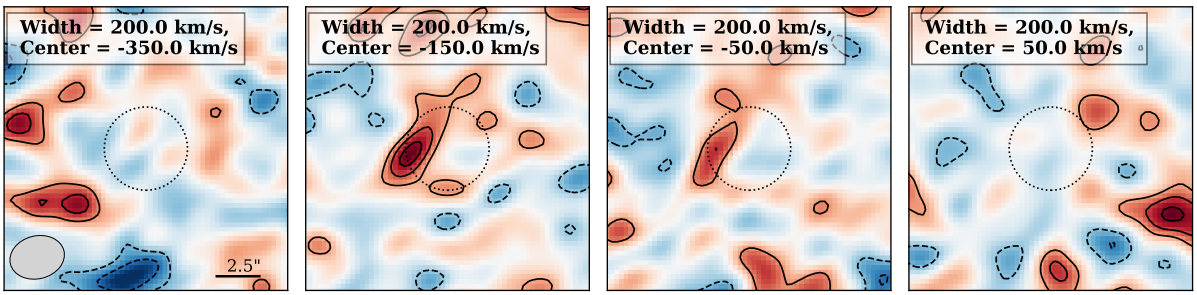

Figure 2.2: ALMA Band 4 continuum-subtracted moment-0 maps of HD1. All maps are based on naturally-weighted data. Each panel shows a moment-0 map collapsed over the same integration width of 200 km s^{-1} but centered at different frequencies, as indicated at the top of each panel. The central frequencies are indicated in km s^{-1} with respect to the reference frequency $\nu = 133.2$ GHz, the frequency of the expected [C II] 158 µm line. For all panels, the contours are drawn at -3.5,-2.5,-1.5, 1.5, 2.5, 3.5-σ and have rms values of 8.32, 8.25, 8.44, and 8.88 mJy $beam^{-1}$ (from left to right). The synthesized beam FWHM is indicated by the ellipse in the lower left, and the image scale is shown on the lower right in the left panel. The dashed circle has a 2″.2 radius.

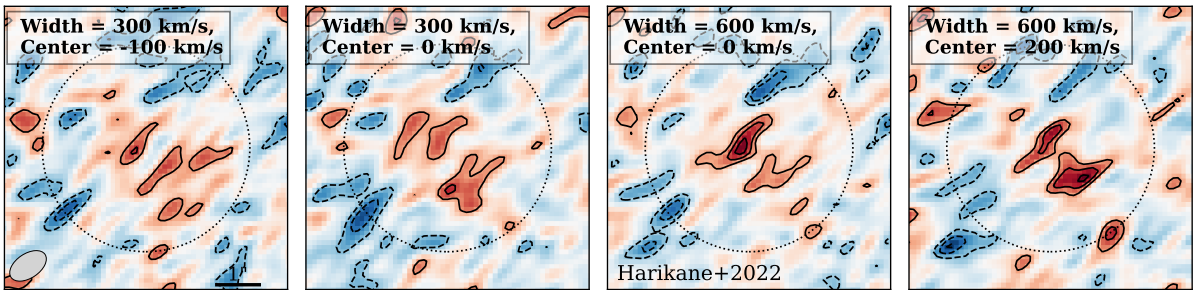

Figure 2.3: ALMA Band 6 moment-0 maps of HD1. All maps are based on naturally-weighted data. Each panel shows a moment-0 map created using a different integration width and central frequency. The integration width and central frequency are provided in km s^{-1} with respect to the reference frequency, $\nu = 237.8$ GHz, as reported in Harikane et al. (2022), at the top of each panel. For each panel, the contours are drawn at -3.5,-2.5,-1.5, 1.5, 2.5, 3.5-σ. From left to right, the moment-0 maps have rms values of 38.3, 37.4, 51.5, and 52.5 mJy $beam^{-1}$. The synthesized beam FWHM is indicated by the ellipse in the lower left, and the scale of the image is shown on the lower right in the left panel. The dashed circle has a 2″.2 radius.

and location. However, there does appear to be a tentative feature centered at a frequency of $\sim$ 133.27 GHz (indicated by the grey shading in Fig. 2.1), particularly for the larger aperture. We refer to this as the "tentative [C II] 158 µm feature" in the remainder of the text and describe it again later in this section.

In the bottom panel of Fig. 2.1, we aim to reproduce the [O III] 88 µm detection reported in Harikane et al. (2022) by presenting the integrated spectrum calculated within multiple apertures

around the location of HD1. We adopt apertures of $0\farcs5$ and $1''$ around HD1, corresponding to about twice the beam size of the data and an aperture identical to the one adopted in Harikane et al. (2022), respectively. We reproduce the feature at ~ 237.8 GHz when adopting an aperture of 1 arcsec (i.e. approximately six consecutive channels with a positive flux, though most of them with SNR < 1). When adopting the $0\farcs5$ aperture, this feature is less pronounced.

To further investigate the tentative features visible in the spectra and test their robustness, we create moment-0 maps focusing on various spectral ranges around the location of the expected emission lines (varying the central frequency and/or the width of the velocity range over which channels are collapsed). Fig. 2.2 shows four, naturally-weighted, continuum-subtracted moment-0 maps integrated over a width of 200 km s^{-1} around the expected [C II] 158 µm redshifted frequency (133.18 GHz) and location of HD1. We find a tantalizing $\sim 4\,\sigma$ feature, offset by $\sim$-150 km s^{-1} from the expected frequency and spatially offset $1\farcs8$ from the location of HD1 reported in Harikane et al. (2022, second panel). However, similar features are found throughout the data cube (see for example the right panel in Fig. 2.2).

We are able to reproduce the findings by Harikane et al. (2022) when following the same procedures to create moment-0 maps (collapsed over 600 km s^{-1}), as shown in the third panel of Fig. 2.3. However, features of similar significance to the one found by Harikane et al. (2022) are present when slightly shifting the central frequency ($\sim$ 200 km s^{-1}) from the original reported central frequency (right panel of Fig. 2.3). Moreover, integrating over a narrower velocity width (the left two panels, consistent with other high-redshift studies, e.g. Hashimoto et al. 2018) yields no clear positive signal at the reported location of HD1.

The multitude of tentative features found in the moment-0 maps of both the Band 4 and 6 data just by shifting the central frequency and/or width over which channels are collapsed illustrates the difficulty in interpreting tentative detections. A more robust analysis of the noise properties of the data is therefore necessary to provide actual meaning to these features.

2.2 Methodology

2.2.1 Jackknifing

In the narrow-field approximation, interferometers measure the 2D Fourier transform of the intensity distribution of an astronomical source over a sparse collection of Fourier modes. Such measurement modes, called visibilities, have units of wavenumbers and are expressed in terms of *uv*-distances, where u and v are the orthogonal vector bases of the Fourier space. In the Fourier domain, unlike the image plane, the noise is additive and Gaussian because the individual pulses from the electrons are too numerous to be distinguishable, resulting in a continuous Gaussian random process with a mean of zero (Thompson et al., 2017).

In this work, we use jackknifing to characterize the noise properties of the data. Jackknifing is a common technique used to retrieve the noise properties from bolometric measurements taken with mm-wave single-dish facilities. It is most commonly employed on Cosmic Microwave Background (CMB)/Single dish experiments (e.g., Weiß et al., 2009, Romero et al., 2018, Naess et al., 2020); however, it has also been used extensively to characterize radio/mm-wave interferometric

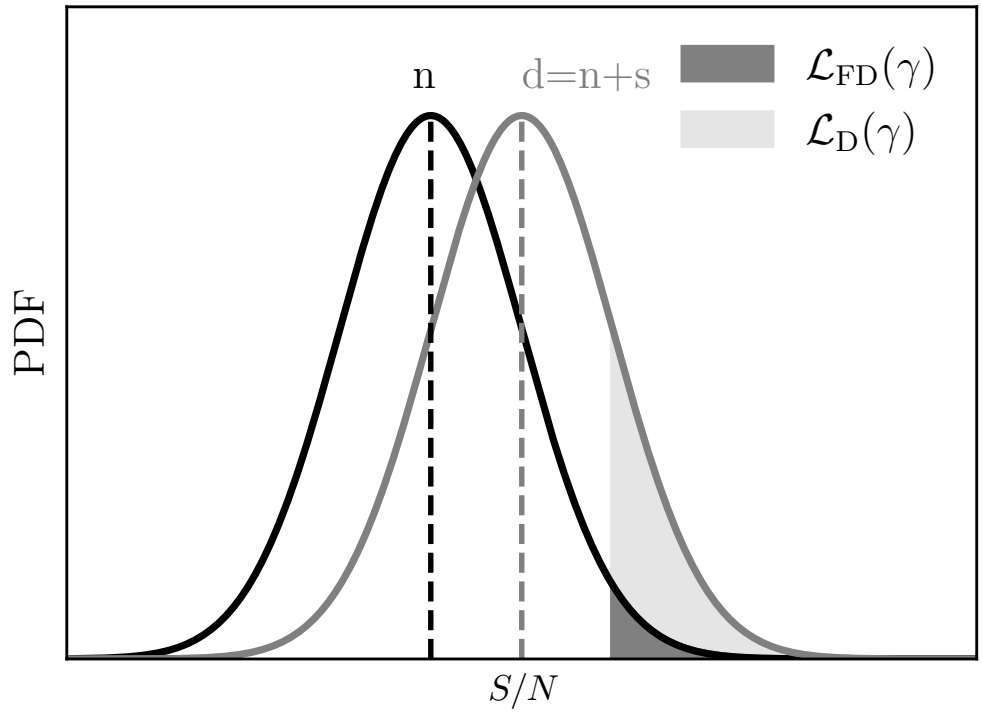

Figure 2.4: Schematic on the detection inference. Given the data d, which is the linear combination of the noise distribution n plus the signal s, we can define the likelihood of detection $\mathcal{L}_{\rm D}(\gamma)$ by setting an arbitrary S/N threshold γ and integrating the probability density function of the S/N for the data d from γ to ∞, as indicated with the shaded area. By nullifying the signal s through jackknifing of the dataset d, we can recover the ideal thermal noise n, and thus compute the likelihood of a false positive detection $\mathcal{L}_{\rm FD}(\gamma)$ as we do for computing $\mathcal{L}_{\rm D}(\gamma)$. The ratio of the two likelihoods provides the significance of detection. This figure is inspired by Fig. 1 of Vio & Andreani (2016).

data (e.g., Padin et al., 2001, Readhead et al., 2004, Sharp et al., 2010, Keating et al., 2015). Assuming proper calibration,[3] interferometric data has uncorrelated, additive, and Gaussian noise with a mean of zero. Therefore, we can retrieve the uncorrelated noise distribution, n, from the data, d, by jackknifing – through randomly multiplying half of the real and imaginary amplitudes of the visibilities by -1 and then rebinning, thereby averaging out the signal, s (see, for instance, Kitayama et al., 2020, González-López et al., 2020, Kaasinen, **van Marrewijk** et al., 2023, Di Mascolo et al., 2023, for an effective implementation).

[3]In the case of incorrect calibration, such as when one of the 44 ALMA antennas has an erroneous gain solution, the noise in the visibility plane becomes multiplicative rather than additive to the signal. The effects of jackknifing in such a situation are not thoroughly tested. However, the assumption of well-calibrated data without antenna calibration errors is reasonable, as it is common practice to check the calibration accuracy before imaging to ensure there are no spurious signals that could result in imaging artifacts.

In interferometric data, rebinning occurs automatically when the visibilities are imaged. All imaging and deconvolution tools, including `tclean`, grid the uv-coordinates before Fourier transforming. Any artifacts caused by the imaging, such as spatially correlated noise, are thus captured by performing the jackknifing in the visibility plane and performing the inference in the image plane. Jackknifing in the visibility plane is thus essential, rather than splitting in the image plane, to avoid removing any correlated noise induced by the Fourier transform present in the data.

To generate various noise realizations, we change the seeding of the randomization process. This allows us to sample the noise distribution, n, until convergence. Once n is adequately sampled, we use the distribution to infer the likelihood of false detection. Figure 2.4 shows schematically how this type of detection inference works. Given that the data d is a linear combination of the noise distribution n plus the signal s, we can define the likelihood of detection $\mathcal{L}_{\rm D}(\gamma)$ by integrating from an arbitrary S/N threshold γ onward, as indicated with the shaded area in Figure 2.4. By nullifying the signal s through jackknifing of the dataset d, we recover the ideal thermal noise n in the visibility plane and thus are able to compute the likelihood of a false positive detection $\mathcal{L}_{\rm FD}(\gamma)$. The ratio of the two likelihoods provides the significance of detection. The next two sections provide a more detailed explanation of the line detection inference process we applied.

2.2.2 Line finding

Traditional empirical methods

To date, most approaches to finding emission-line sources in (sub-)mm interferometric data have been based on determining the significance of an emission line (a positive peak) via the line "fidelity" or "reliability" (e.g., Walter et al., 2016, Pavesi et al., 2018, González-López et al., 2019, Westmeier et al., 2021). The fidelity (or reliability) function is defined as,

$$\mathrm{fidelity}(\gamma) = 1 - \frac{N_{\rm neg}(\gamma)}{N_{\rm pos}(\gamma)}\,, \tag{2.1}$$

where $N_{\rm neg}(\gamma)$ and $N_{\rm pos}(\gamma)$ are the number of negative and positive peaks, respectively, above a given detection threshold γ. The value of γ is usually a function of the S/N but can be arbitrarily chosen.

The fidelity function empirically estimates the likelihood ratio of the false detection, $\mathcal{L}_{\rm FD}(\gamma)$, over the detection, $\mathcal{L}_{\rm D}(\gamma)$ by taking the integral over the Probability Density Functions (PDFs) of their respective probability distributions, $\mathcal{P}_{\rm FD}(x)$ and $\mathcal{P}_{\rm D}(x)$. $\mathcal{P}_{\rm FD}(x)$ and $\mathcal{P}_{\rm D}(x)$ are sampled by searching for negative and positive peaks, respectively. Therefore, the following relation of the likelihood ratio between detection and false detection holds:

$$\Lambda(\gamma) = \frac{N_{\rm pos}(\gamma)}{N_{\rm neg}(\gamma)} = \frac{\mathcal{L}_{\rm D}(\gamma)}{\mathcal{L}_{\rm FD}(\gamma)} = \frac{\int_\gamma^\infty \mathcal{P}_{\rm D}(x|\Delta v)\,{\rm d}x}{\int_\gamma^\infty \mathcal{P}_{\rm FD}(x|\Delta v)\,{\rm d}x}\,. \tag{2.2}$$

This relationship is a function of the kernel width used to determine the line width, Δv. For example, to characterize the line emission in the ALMA Spectroscopic Survey of the Hubble

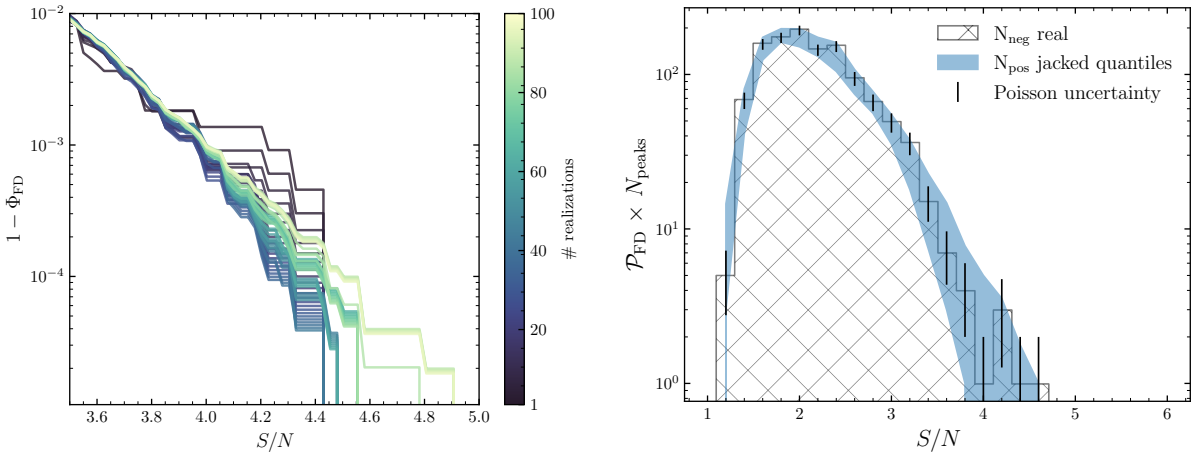

Figure 2.5: *Left:* How an increasing number of jackknife realizations leads to a smoother $\Phi(x)$ that better samples the high-S/N of the probability of false detection, $\mathcal{P}_{\rm FD}(x)$. The probability function is shown as one minus the mean cumulative distributions $\Phi(x)$ of $\mathcal{P}_{\rm FD}(x)$ as a function of the peak S/N for various amounts of jackknife realizations. *Right:* Sampled noise distributions, $\mathcal{P}_{\rm FD}(x)$, as a function of the peak S/N. The grey hatched histogram shows the results from sampling the number of negative peak values of the original data set (shown with corresponding Poisson uncertainty). The blue-filled region represents the 95% confidence interval of the positive peak values from the jackknife observations.

Ultra Deep Field (ASPECS) González-López et al. (2019) chose the detection threshold γ such that $\mathrm{fidelity}(\gamma) = 0.9$. This resulted in $\gamma \simeq 6.4\sigma$ for the ASPECS sample, assuming that Eq. (2.1) is well described by an error function.

The other assumption made while employing the fidelity function is that the flux distribution of negative peak values is a proper estimator for $\mathcal{P}_{\rm FD}(x)$. However, this does not hold when absorption with respect to the CMB or a bright background source leads to negative line fluxes, contaminating the noise statistics. Additionally, since the method is applied in the image domain, any true line or continuum flux will also create a negative signal through the dirty beam patterns. Bright sources can be "cleaned" (if they fall within the imaged part of the sky), but the fainter ones will create correlated spatial noise (Tsukui et al., 2022). Furthermore, ALMA has a limited data volume along the spectral axis; hence, $\mathcal{P}_{\rm FD}(x)$ is not fully sampled over the $\delta\nu$ space, making these empirical approaches inaccurate.

Autocorrelation function implementations

There are several alternatives to empirical approaches in estimating $\mathcal{P}_{\rm FD}(x)$. For example, Vio & Andreani (2016) employed an analytic prescription that depends on the first and second-order derivatives of the autocorrelation function (ACF) of the observation (see Eq. 25 in Vio & Andreani, 2016, and references therein). To compute these derivatives, they fit the ACF with a parametric profile to estimate $\mathcal{P}_{\rm FD}(x)$, which is the flux distribution of positive peaks in a channel

map or spectrum.[4] However, the ACF depends on the observation-specific sensitivity, velocity width of the line, and uv-coverage; For example, a more asymmetric uv-coverage creates more spatially correlated noise (Tsukui et al., 2022). Therefore, there is no unique prescription for the likelihood of false detection in interferometric data.

Another approach is to use Monte Carlo sampling of noise realizations based on the measured ACF, as done in Tsukui et al. (2022). However, both Vio & Andreani (2016) and Tsukui et al. (2022) typically compute the ACF and the corresponding covariance matrix in two dimensions, namely each individual channel map with dimensions of right ascension (RA), and declination (Dec). For blind line searches, the ACF and the corresponding covariance matrix must instead be computed in four dimensions, including the frequency axis and range of line widths. The need to compute the four-dimensional ACF arises for three main reasons. 1) The noise is correlated in frequency space due to the Hanning window being applied to the channels, and there can be correlated noise effects from spectral leakage. 2) The atmospheric transmission varies across the band, especially at higher frequencies. 3) The ACF is a function of the synthesized beam, which also varies with frequency. Since estimating the four-dimensional covariance matrix and ACF for cubes with various channel widths is computationally expensive, we did not employ this method in our analysis. Yet, these types of implementation (e.g., Tsukui et al., 2023) are compatible with our jackknifed approach as the ACF can also be computed on the signal-free cubes.

Line detection inference through jackknifing

Here, we describe how we perform the line detection throughout this work by utilizing the jackknifed data sets. To determine the likelihood of detection, we first quantify the likelihood of false detection, for which we need the underlying PDF. The distribution of false positive detections is set by the distribution of peak values in a data cube that only contains noise (Section 2.2.2). In practice, the distribution of positive or negative peaks is a subset of the pixel-value distribution in the data cube (Vio & Andreani, 2016). The number, location, and amplitude of peak values depend on the realization of the total pixel-value distribution, which for interferometric data in the image plane, can be approximated as a smoothed random Gaussian field. By jackknifing the visibilities, we effectively shuffle the noise distribution, altering the noise realization and creating another subsample of the pixel-value distribution, namely another peak distribution. This allows us to increase the sample statistics of $\mathcal{P}_{\rm FD}(x)$ while using the same data set.

Figure 2.5 shows that for an increasing number of realizations, we probe the tail of the distribution at high S/N better. The cumulative distribution function (CDF) $\Phi_{\rm FD}$ of $\mathcal{P}_{\rm FD}(x)$ is smooth till $S/N \approx 4.5$ and reaches a $S/N = 5$ within a hundred realizations. Specifically, each CDF incrementally includes data from additional jackknife realizations, so, for example, the CDF for $35\times$ jackknife realizations contains all the data from the $34\times$ realization set. Furthermore, the jackknifed data only includes peaks within a $0\farcs6$ aperture of the center of the data cube (chosen so that this test is consistent with the discussion in section 2.4). Figure 2.5 goes up to a hundred realizations in total. Since there is a trade-off between sampling more realizations

[4]We note that the PDF of peaks in a smoothed Gaussian random field is not Gaussian (Vio & Andreani, 2016). This complexity makes obtaining an analytical description of Eq. (2.1) challenging. This is also why Walter et al. (2016) empirically measured Eq. (2.1) and fitted it with an arbitrarily chosen error function.

and computation time, and from ≈ 50 realizations onward, we recover the high-S/N tail of the distribution; we decided to utilize 50 jackknife realizations for our analyses throughout this work.

The difference between the sampled PDF of the false positives, $\mathcal{P}_{\rm FD}(x)$, coming from the negative peak distribution (e.g., one noise realization) in the real data versus that from 50 jackknife realizations is shown in Figure 2.5. For the jackknifed realizations, we show the inner 95% confidence interval per bin. Again, for both the real and jackknifed data, we only consider peaks within a $0\farcs6$ aperture of the center of the data cube. Since we do not expect a negative signal in this data set, in principle, the two distributions should be equivalent. However, our method provides better sampling (as also shown in Figure 2.5) and thus better statistics, particularly at higher S/N. Furthermore, the scatter in the jackknife realizations within the 95% confidence interval is consistent with the Poisson uncertainty in the real data for each bin, except for a potential outlier at $S/N \approx 4$. This indicates that the various realizations are consistent with each other.

As shown in Figure 2.5, jackknifing allows for a more complete sampling of the noise distribution without the need for complex models or computationally intensive four-dimensional covariance estimates. By leveraging this technique, we can obtain a more reliable and efficient measure of the probability of a false detection, $\mathcal{P}_{\rm FD}(x)$, and take the likelihood ratio, $\Lambda(\gamma)$ with $\mathcal{L}_{\rm D}(\gamma)$ according to Eq. (2.2) to estimate a feature being real or not. Then,

- if $\Lambda(\gamma) > 1$, the observed data is more likely to fall under the hypothesis that a signal is present, whereas
- if $\Lambda(\gamma) \leq 1$, the observed data falls under the null hypothesis and is thus better described as being drawn from the underlying noise distribution.

Finally, an excess in the ratio is considered significant if the likelihood ratio exceeds a critical value k, such that:

- if $\Lambda(\gamma) \geq k$, one can reject the null hypothesis that no signal is present in the data, whereas
- if $\Lambda(\gamma) < k$, one cannot reject the null hypothesis.

2.3 Application to simulated ALMA data

To validate our method, we simulated mock ALMA data using `CASA`'s `simobserve` task. We simulated a one-hour-long execution block centered at an RA and Dec of zero degrees. The simulated data contained six channels centered at a frequency of $\nu = 279$ GHz with a channel width of 31 MHz. We created the simulated uv-coverage using configuration 4 from cycle 7, leading to a resolution of $0\farcs6$ when `cleaning` using natural weighting. The setup of the simulations was designed to be similar to the observational setup of GLASS-z12 (Table 2.1). Using this setup, we simulated several datasets containing continuum and line emission from two separate sources with various integrated S/N values. We incremented the flux of the sources, maintaining the same uv-coverage for every observation. The line flux was simulated using a double Gaussian model (i.e., a 1D and 2D Gaussian). The first Gaussian models the spectral flux

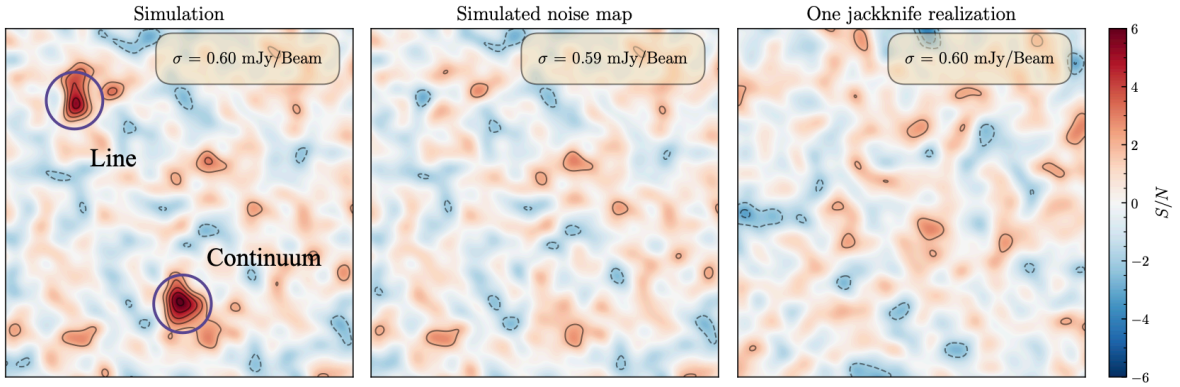

Figure 2.6: Moment-0 maps of simulated ALMA data, generated using `CASA simobserve`. Left: Output of the simulated observation, which contains both a continuum and a line-emitting source with $S/N = 5$. Middle: The corresponding noise map, referred to as the "cleaned" map obtained by subtracting the noiseless output (i.e., filtered sky model) of `simobserve` from the noisy one. Right: The moment-0 map from a single jackknife realization. All contours are drawn at $[\pm 2, \pm 3, \pm 4, \pm 5, \pm 6]\,\sigma$.

distribution; its flux is constrained as described above – so that the integral over the Gaussian equals the respective S/N – and has an FWHM equal to $\sim$ 73 MHz, corresponding to a line width at a full-width half maximum of 80 km s^{-1}. The second Gaussian generates a blob in each channel map, with its amplitude set by the first Gaussian and an FWHM of 2.355 pixels (1 pixel = $0\farcs01$). Hence, the observation is considered unresolved. The same angular size on the sky is used for the continuum source.

Using the simulated data, we checked how well `jackknify` removes the signal. Figure 2.6 shows the moment-0 maps of the $S/N = 5$ observation (*Left*), the corresponding noise map (*Middle*), and the map resulting from jackknifing the visibilities (*Right*). We masked out the sources before computing the standard deviation in the dirty map. We created the noise-only map by subtracting the noise-free dirty map (which is an output of `simobserve`) from the noisy output. Thus, the noise-only map is representative of the noise in a "perfectly `cleaned`" map. The simulated noise map and jackknifed realization exhibit the same noise structure, validating our jackknifing approach.

We tested how well the jackknifing performs as a function of the sources' S/N, as the randomization process might not fully remove the signal, leaving residuals in the generated noise realization. We initially noticed a bias between the standard deviation from the single cleaned map and the mean of the 50 jackknife realizations (see Appendix 2.6). This bias depended on the seeding used in `simobserve`, which is the result of the inherent variance of `simobserve`, combined with the fact that the standard deviation is estimated from maps with a finite size. Due to the limited representation of the chosen image domain, large- and intermediate-scale modes can induce non-negligible biases in the measured noise variance compared to the underlying truth distribution. To explicitly test for this, we create jackknifed realizations over a large set of `simobserve` runs without a source ($S/N = 0$), each assuming a different input random seed

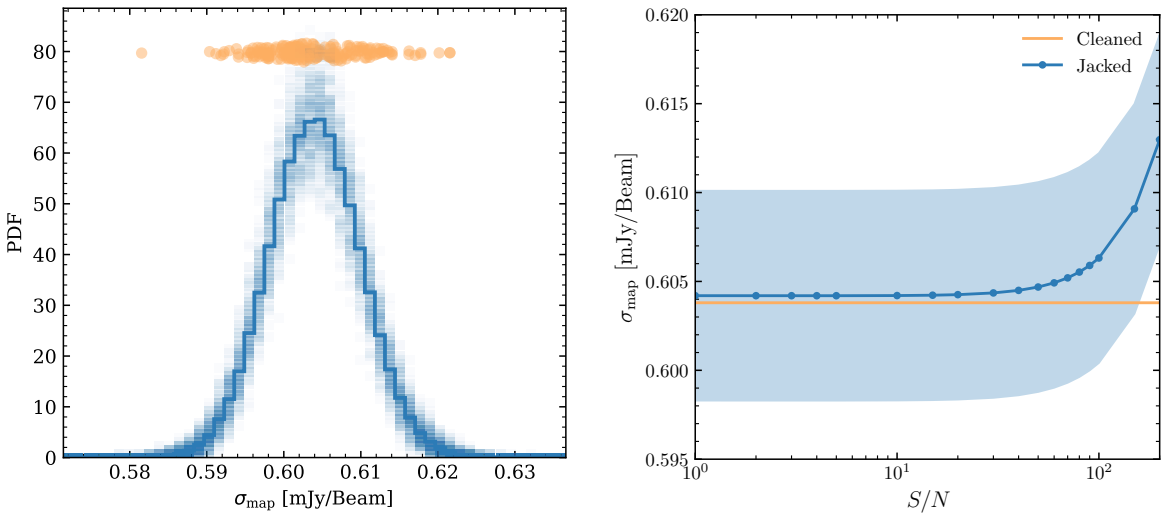

Figure 2.7: *Left:* Comparison of the standard deviation $\sigma_{\rm map}$ measured from different `simobserve` realizations using 200 different random seeds (orange points) and the $\sigma_{\rm map}$ of the jackknifing for each corresponding mock observation (shaded blue squares). The thick blue line traces the total distribution of the derived standard deviations, $\sigma_{\rm map}$ when averaging over all the jackknife realizations for all the different `simobserve` seeds. *Right:* The standard deviation for all maps as a function of the peak S/N of the sources. The blue-shaded region indicates the standard deviation over the various noise estimates from the 50 jackknife realizations for each S/N. The orange-shaded region is the standard deviation over the orange data points in Fig. 2.7. By jackknifing the observations, we retrieve the noise properties of the cleaned map accurately when the sources have $S/N < 50$.

(Figure 2.7). All the resulting marginalized jackknife distributions are found to be consistent with the same normal distribution, which is characteristic of the noise probability function. The `simobserve` variance estimates are, in fact, scattered according to the same distribution, implying that the `simobserve` output itself shows the same statistical properties of the result of an individual jackknifing cycle. Therefore, the jackknifing can be used to better describe the underlying distribution function independent of the noise realization used in `simobserve`.

We test how the measured standard deviations from the jackknife realizations evolve with S/N in Figure 2.7. To this end, we simulated the sources as Gaussians that were off-centered from the phase reference point. This setup allows the signal to leak from the real to the imaginary components, testing the effectiveness of the jackknife routines without assuming the source to be at the phase reference – an assumption often made in interferometric data analysis tools (such as `uvcontsub`). We compare the mean and standard error of the standard deviation values measured for the jackknifed realizations vs the observations simulated with `simobserve`.

We find that our jackknifing approach is perfectly reliable for $S/N \lesssim 50$. That is, the jackknife realizations of simulated observations with sources at $S/N \lesssim 50$ are perfectly consistent with the cleaned noise maps. The observations simulated with a peak $S/N \gtrsim 50$, however, indicate

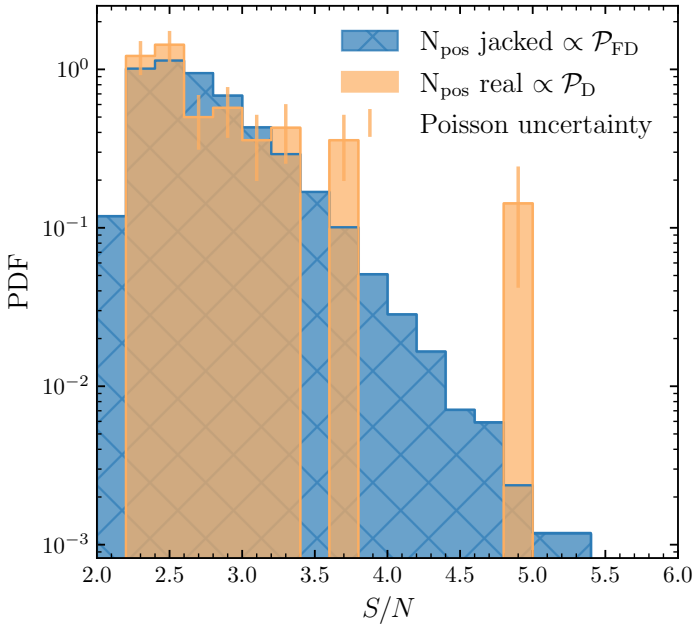

Figure 2.8: Output of the line finding done on the simulated ALMA observation that had an off-centered line and continuum source which was initialized to have an integrated S/N of 5 in the integrated velocity map (see Fig. 2.6). In blue, we show the underlying PDF of a false detection $\mathcal{P}_{\rm FD}(x)$ derived from counting peak values in the jackknifed realizations. In orange, we show the results on the simulated data, which shows a clear detection of the two sources at a $S/N = 5$. The peak at $S/N \approx 3.6$ is consistent with being noise (as explained in the main body of the text)

a stronger deviation from the cleaned noise estimate. We note that this does not manifest as a residual of the source but as an overall larger standard deviation throughout the map. We therefore advise that before applying `jackknify` to the measurement set, one should remove extremely bright continuum and line-emitting sources (e.g., $S/N > 50$) from the data set in the visibility plane, as is common practice with other line-finding methods (e.g., Walter et al., 2016). Overall though, the tests we have performed with simulated data (Figure 2.7), show that jackknifing allows for an accurate estimation of the underlying noise distribution.

The final validation we performed with the simulated data was to test the accuracy of the line-finding method. Since jackknifed data cubes have an output identical to the original dataset, we apply the same tools to the real and noise realizations. Therefore, we use the simulation of which the sources have an integrated $S/N = 5$. We sample the distribution of false positive detections, $\mathcal{P}_{\rm FD}(x)$, by applying the line finding algorithm to the jackknifed data and use the `FindClump` algorithm[5] to search for lines in the jackknifed data cubes (see Section 2.4.1 for a description on how `FindClump` is setup). The average distribution of the peak values in the 50 jackknife realizations is shown by the blue histogram in Figure 2.8. This histogram reveals a smooth peak distribution, declining from $S/N = 2.5$ to $S/N \approx 5.5$.[6] Given the number of peaks `FindClump` detected in a single realization ($N_{\rm peaks} = 70$), and a likelihood of $\mathcal{L}_{\rm FD}(\gamma = 4.5) = 0.0021$, we expect to find on average 0.1 ± 0.4 peaks above $S/N = 4.5$ in the simulated observation. By applying the line-finding algorithm to the real data (orange histogram), we recover the simulated continuum and lines sources, both with a $S/N = 4.9$. Compared to the underlying noise distribution (in blue), the likelihood ratio tests yield $\Lambda(\gamma = 4.0) = 13$. We also find a small

[5] we note that this is an arbitrary choice and other algorithms may be better suited

[6] We note that the drop-off at lower S/N is due to the cropping of peaks and the way *Source Extractor* catalogs its findings.

excess at $S/N \approx 3.6$ and check if our likelihood ratio test indicates this to be real or not (we know it is not). We find that the number of peaks, expected from jackknifing, at the S/N range of $3 < \gamma < 4$ ($3.5 < \gamma < 4$) is 14.6 ± 3.8 (2.1 ± 1.5), while we find 16 ± 4 (5.0 ± 2.2) in the simulated data, resulting in a $\Lambda(3 < \gamma < 4) = 1.1$ ($\Lambda(3.5 < \gamma < 4) = 2.4$). Thus, our statistical tests do indeed find these peaks to be consistent with being noise. Thus, we recover the simulated sources while the noise is correctly characterized as such.

2.4 Application to z>10 galaxy candidates

Our tool, `jackknify`, can be applied to various science cases, including ones involving blind line searches in deep fields (i.e., without known counterparts), targeted searches around candidates identified at other wavelengths (e.g., following up $z > 10$ candidates) and searches for companions around known sources. Here, we apply our method to four sets of ALMA observations targeting the $z > 10$ galaxy candidates GLASS-z12, GLASS-z10, S5-z17-1, and HD1 (Bakx et al. 2023, Yoon et al. 2023, Fujimoto et al. 2023, and Harikane et al. 2022 respectively). In Section 2.4.1, we describe the experimental setups. In Section 2.4.2, we detail the results of the blind line search across the entire spectral axis. In Section 2.4.3, we summarize the line finding results for GLASS-z12, incorporating an additional redshift prior based on spectroscopic JWST/MRS measurements of the Hα line (Zavala et al., 2024). Finally, in Section 2.4.4, we describe the analysis of finding two correlated peaks in two different ALMA bands regarding observations of HD1.

2.4.1 Specific experiment set up

To quantify the detection significance of a line along the full spectral axis, we adopt the following procedure.

1. We jackknife each observation set 50 times, creating 50 different noise realizations.
2. We use `FindClump` (Walter et al., 2016), as implemented in the `interferopy` package (Boogaard et al., 2021), to sample the distribution of positive peak values from both the real and jackknifed data.
3. We mask out features outside a $0\farcs6$ radius of the optically derived center. This corresponds to a physical radius of ≈ 2 kpc at $z = 12$ and is $\approx 2\times$ the size of the beam for all four datasets. We chose a radius of $r = 0\farcs6$ to include the tentative detection previously reported in our analysis (the feature was found at an offset of $0\farcs51$ from the JWST-derived centroid; Bakx et al., 2023), but be able to exclude serendipitous detections of interlopers.
4. We calculate the likelihood ratio of the respective distributions to infer if there is an excess in the peak distribution in the real data compared to the sampled noise distribution.
5. We consider a detection significant if the excess of peaks in the real data with respect to the noise has at least a significance of 2σ based on Poisson statistics. Therefore, we require $\Lambda(\gamma)k$, with $k = 3$.

In step 2, we configure `FindClump` to search for emission lines with widths between $100-500$ km s^{-1}, corresponding to $3-11$ times the channel width. The velocity width varies slightly across different observation sets as we are examining galaxies at various redshifts. With `FindClump`, we identify peaks that exceed a signal-to-noise ratio (S/N) of 0, and we crop "identical" peaks if they are found within $0.2''$ of each other spatially (approximately $1/3$ of the beam width) and within 0.2 GHz spectrally (roughly $4-5$ channels apart). Additionally, we have modified the default settings in `Sextractor` (Bertin & Arnouts, 1996), specifically the analysis and detection thresholds which we both set to 2 to better detect low S/N clumps.

2.4.2 Results on blind line searches

We check for any real signal by comparing the distribution of positive peaks in the real and jackknifed data (Fig. 2.9). According to Eq. (2.2), this comparison translates to the ratio of the probability distribution of a detection, $\mathcal{P}_{\rm D}(x)$, versus a false detection, $\mathcal{P}_{\rm FD}(x)$. Thus, any excess of positive features in the real data relative to the noise distribution indicates a true positive line detection. Table 2.2 provides an overview of the likelihood of previously reported tentative detections being real. In the following section, we will discuss the results for each source, one by one.

For GLASS-z12 (top left panel, Fig. 2.9), we find no excess of positive peaks in the real data compared to the underlying noise distribution. We integrated the probability of a false detection from the detection threshold of $\gamma = 4\sigma$ onward. Considering the total number of peaks in the real data ($\rm N_{peaks} = 1150$), we estimated the expected number of peaks due to noise fluctuations. We found $\mathcal{L}_{\rm FD}(\gamma = 4\sigma) \times \rm N_{peaks} = 0.0011 \times 1150 = 1.3 \pm 1.1$. In the real data, we recover one peak above $S/N > 4$, which is consistent with being noise. This is also indicated by the likelihood ratio test (Eq. 2.2), which results in $\Lambda(4\sigma) = \mathcal{L}_{\rm D}(4\sigma)/\mathcal{L}_{\rm FD}(4\sigma) = 0.80$. We note that the $S/N = 4.2$ peak discussed here is not the same peak found by Bakx et al. (2023). The peak we have recovered is at a frequency of $\nu = 246.6106$ GHz and coordinates RA, Dec $= (3.49895, -30.32469)$, which differs from their reported peak 5.8σ peak over 400 km s^{-1}, offset $0\farcs5$ from the JWST position (Table 2.1). We recover a peak at the same location but at a lower significance of 2.9σ for a linewidth of 280 km s^{-1} (the maximum S/N peak over any linewidth at this position). The difference in S/N and line width is due to the difference in how the data were imaged. Whereas we imaged these data using natural weighting and using a channel width of 46 km s^{-1}, Bakx et al. (2023) tapered the data to $0\farcs3$ and used a channel width of 150 km s^{-1}. This highlights the importance of imaging the jackknifed data in the same way as the real data.

For GLASS-z10 (top right panel, Fig. 2.9), we find a small excess of peaks in the real versus the jackknifed (noise-only) data at $S/N = 4.1 - 4.3$. Given the noise distribution and the total number of peaks in the real data ($\rm N_{peaks} = 271$), we expect to find 1.5 ± 1.2 peaks at $\gamma > 4\sigma$. In the real data, we find two peaks at $\gamma > 4\sigma$. The likelihood ratio resulted in $\Lambda(\gamma = 4\sigma) = 1.4$. This does not exceed our detection threshold of $k = 3$, meaning that the two tentative features[7] are

[7]Both features have a $S/N = 4.3$, a spatial offset of $0\farcs35$ and $0\farcs39$ from the optical counterpart, and are found at $\nu = 291.58$ and $\nu = 296.12$ GHz. Both have a line width of 170 km s^{-1}.

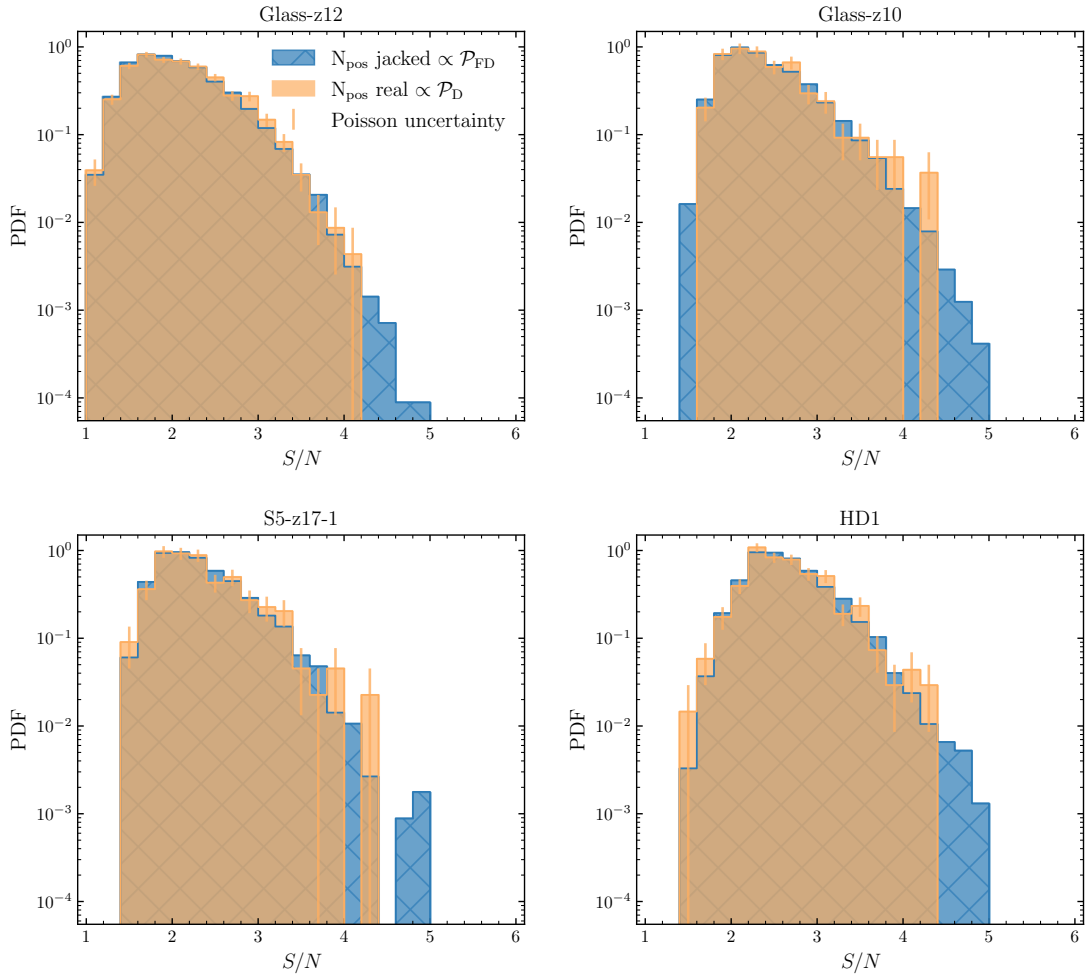

Figure 2.9: Probability distribution of false detections, $\mathcal{P}_{\rm FD}(x)$ noted as $\rm N_{pos}$ jacked, and the peak value distribution of the observations, $\mathcal{P}_{\rm D}(x)$ noted as $\rm N_{pos}$ real. Both distributions are obtained by running `FindClump` on the jackknifed cubes and the real data cube, respectively. From the left to right, we show the four data sets of GLASS-z12, GLASS-z10, S5-z17-1, and HD1 (See Tab. 2.1). An excess of $\mathcal{P}_{\rm D}(x)$ over $\mathcal{P}_{\rm FD}(x)$ is indicative of line detection. However, no such excess is detected.

consistent with being noise at a likelihood of $\mathcal{L}_{\rm FD}(\gamma = 4\sigma) = 0.0054$. Neither peak was previously reported by Yoon et al. (2023). We also recover the previously reported detection at 2.7σ with a line width of 235 km s^{-1}. This line has a false detection likelihood of $\mathcal{L}_{\rm FD}(\gamma = 2.7\sigma) = 0.19$ and a likelihood ratio test resulting in $\Lambda(\gamma = 2.7\sigma) = 0.9$.

For S5-z17-1 (lower left panel, Fig. 2.9),the expected number of peaks is $\mathcal{L}_{\rm FD}(\gamma = 4\sigma) \times \rm N_{peaks} = 0.0032 \times 221 = 0.7 \pm 0.8$. Given that we find one peak above $S/N > 4$ and since $\Lambda(\gamma = 4\sigma) = 1.4$, we conclude that these data are also consistent with being noise. We recover the peak reported in Fujimoto et al. (2023), albeit with a significance of 3.9σ instead of the

Table 2.2: Significances of Detected Peaks

	HD1	GLASS-z12	GLASS-z10	S5-z17-1
Reported significance	3.8σ	5.8σ	4.4σ	5.1σ
Found highest significance†	4.3σ	4.2σ	4.3σ	4.3σ
$\mathcal{L}_{\rm FD}(\gamma = 4)$	0.0095	0.0011	0.0054	0.0032
$\mathcal{L}_{\rm FD}(\gamma = 4) \times {\rm N}_{\rm peaks}$	3.2 ± 1.8	1.3 ± 1.1	1.5 ± 1.2	0.7 ± 0.8
${\rm N}_{\rm peaks}$ found	5 ± 2.2	1	2	1
$\Lambda(\gamma = 4)$	1.5	0.80	1.4	1.4

In this table, we quote the individual likelihoods of false detections for the three DDT-ALMA data sets on $z > 10$ galaxies. Multiplied with the number of peaks in the real dataset (${\rm N}_{\rm peaks}$), this leads to the expected number of peaks above $S/N > 4$ in a purely noisy dataset. We compare this with the found number of peaks in the real data and the likelihood ratio test as defined in Eq. (2.2).† We note that the peaks with the highest found significance are not the same peaks as the ones that correspond to the reported significance (top row). See section 2.4.2 for more detail.

reported 5.1σ. This line has a false detection likelihood of $\mathcal{L}_{\rm FD}(\gamma = 3.9\sigma) = 0.0060$ and a likelihood ratio test resulting in $\Lambda(\gamma = 3.9\sigma) = 2.2$.

For HD1 (lower right panel, Fig. 2.9), the expected number of peaks is $\mathcal{L}_{\rm FD}(\gamma = 4\sigma) \times {\rm N}_{\rm peaks} = 0.0095 \times 342 = 3.2 \pm 1.8$. We find five such peaks in the real data, leading to a $\Lambda(\gamma = 4\sigma) = 1.5$, we conclude the ALMA Band 6 data are completely consistent with noise. We further recover the initial tentative detection at 3.2σ with `FindClumps`.

In conclusion, our analysis of the GLASS-z12, GLASS-z10, and S5-z17-1 datasets reveals no significant detections of any of these (candidate) $z > 10$ galaxies in the ALMA data. All of the peaks identified in the real data are consistent with noise, as indicated by the likelihood ratio tests and comparison with the jackknifed noise distributions. Given the number of peaks per data set, the detection significance does not follow a Gaussian distribution. Since a 4σ detection should reflect that only one in fifteen thousand random draws should be a false detection, we reach a 5σ fluke already within a sample size of $\approx 200 - 1000$ peaks. This highlights again the importance of rigorous noise analysis in confirming potential astronomical signals.

2.4.3 Detection significance with a known redshifts for Glass-z12

So far, we have presented the jackknifing plus line-finding approach for the case of a blind detection experiment and the case where the approximate position of the source is known but where we have no strong prior on the central frequency. We now extend the analysis for cases where the redshift and hence the line frequency are known from other observations. To provide an example, Zavala et al. (2024) detected bright nebular emission lines of GLASS-z12 with JWST, constraining the redshift to be $z_{\rm spec} = 12.33 \pm 0.02$. With this prior knowledge, they reanalyzed the ALMA observations and found a $\sim 3\sigma$ feature in the moment-0 map at the expected location (spatially and spectrally) of the [O III] 88 µm line. Notably, this feature is spectrally and spatially offset from the earlier reported tentative detection of Bakx et al. (2023). However, we recover the

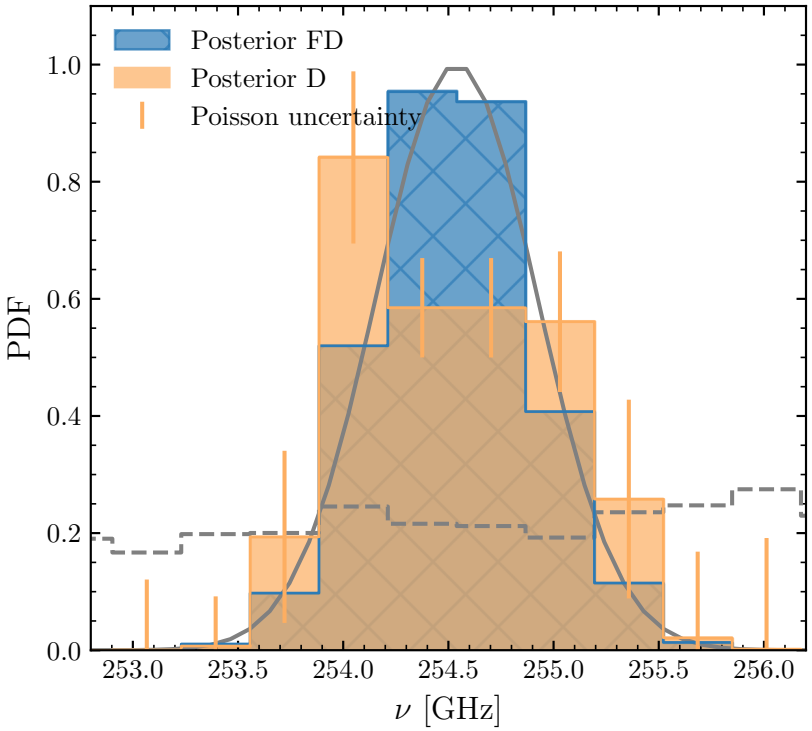

Figure 2.10: Posterior distribution of peaks above $S/N > 2.5$ and within 0.″6 of the JWST derived centroid as a function of frequency for both the real and jackknifed realization. The Gaussian prior derived from JWST/MRS Hα observation of Zavala et al. (2024) is shown as the gray line, and the initial PDF of the probability of false detections is the gray-dashed line.

same feature at 2.7σ.

The redshift uncertainty ($\Delta z = \pm 0.02$) derived from the JWST/MRS spectrum of GLASS-z12 translates to a frequency width of $\Delta\nu_{\rm obs} = \pm 0.4$ GHz at the expected [O III] 88 µm frequency of $\nu_{\rm obs} = 254.54$ GHz. We compute the frequency uncertainty from,

$$\left|\frac{\Delta z}{1+z}\right| = \left|\frac{\Delta\nu_{\rm obs}}{\nu_{\rm obs}}\right| = \left|\frac{\Delta v}{c}\right| , \tag{2.3}$$

where Δz is the redshift range probed, $\Delta\nu_{\rm obs}$ is the corresponding frequency width centered on the frequency $\nu_{\rm obs}$, Δv is the corresponding velocity width, and c is the speed of light. This frequency uncertainty is roughly equivalent to the maximum correlated bandwidth of a single ALMA spectral window. Even with better redshift constraints, astrophysical processes such as outflows could lead to both spatial and spectral offsets, as observed in the [C II] 158 µm and [O III] 88 µm lines reported by Fujimoto et al. (2024). Therefore, the likelihood of false detections, $\mathcal{L}_{\rm FD}(\gamma)$, is still determined by the probability density function similar to the blind search scenario, albeit with the addition of a relatively wide prior of ± 0.4 GHz from the JWST/MRS observations.

To incorporate the redshift prior from auxiliary data sets into our line-finding routine, we adopt a Bayesian approach using Bayes theorem,

$$P(A|B) = \frac{P(B|A)\cdot P(A)}{P(B)} . \tag{2.4}$$

where $P(B|A)$ is the general expression for a probability function—in our case, the probability of a detection,$\mathcal{P}_{\rm D}(x)$, and false detection, $\mathcal{P}_{\rm FD}(x)$—, $P(A)$ is the prior, and $P(B)$ is the Bayesian

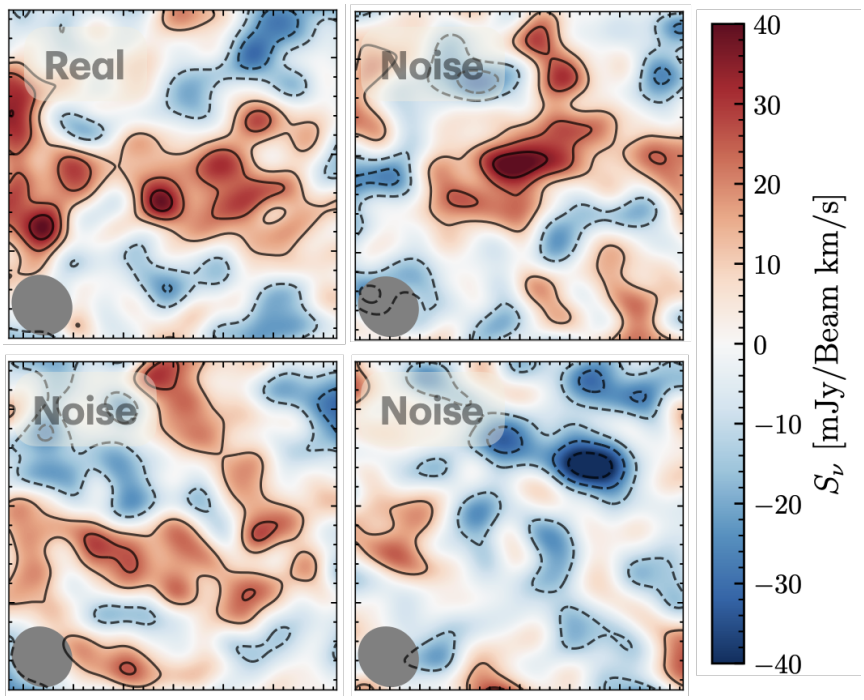

Figure 2.11: Moment-0 maps centered at $\nu = 254.35$ GHz with a line width of 280 km s^{-1} for the real data set (also reported in Zavala et al. 2024) and three jackknife realizations which are imaged identically. In the lower left, we show the beam size. The size of the images is 1.″7 by 1.″7. The contours are drawn at $\pm 1, \pm 2, \pm 3\sigma$.

evidence. For the detection inference of GLASS-z12, we adopt a Gaussian prior on the redshift, $\mathcal{G}(\mu = 12.33, \sigma = 0.02)$. We also use a uniform prior on the radial distance, $\mathcal{U}(0, 0.6'')$, and a uniform prior on the S/N of the peak, $\mathcal{U}(2.5, \infty)$, thereby only counting peaks with $S/N > 2.5$. The latter prior was chosen in order to capture the tentative detection reported by Zavala et al. (2024). After multiplying the probability distribution by the priors to obtain the posterior distribution, we normalize it such that the integral over the bins of S/N, frequency, radial distance equals one.

Unlike techniques such as Markov chain Monte Carlo, where the posterior distribution is directly sampled, we have first sampled the PDFs using `FindClumps` without any priors. We therefore apply Bayes' theorem in post-processing to determine which feature is most likely to correspond to GLASS-z12. This approach assumes that there is no correlation between the S/N of a peak and its location along the RA, Dec, and frequency axes, a reasonable assumption as there should not be any correlation between the different parameters for non-primary-beam-corrected maps.

We visualize our approach to determining the likelihood of a positive peak being real, given the redshift prior, in Figure 2.10. The posterior distributions for both the real and jackknifed observations are shown in the frequency domain. We also show the prior from JWST/MRS observations and the initial PDF of the probability of false detections without applying the prior. The latter indicates that the PDF has a flat distribution with respect to frequency, thus showing the above-stated assumption that there is no correlation between the S/N of a peak and its location along frequency axes. We find a slight excess of detection peaks at a frequency of $\nu = 254.0$ GHz, corresponding to two peaks located at $\mathrm{RA}, \mathrm{Dec}, \nu = 3.49892°, -30.32469°, 253.92$ GHz and

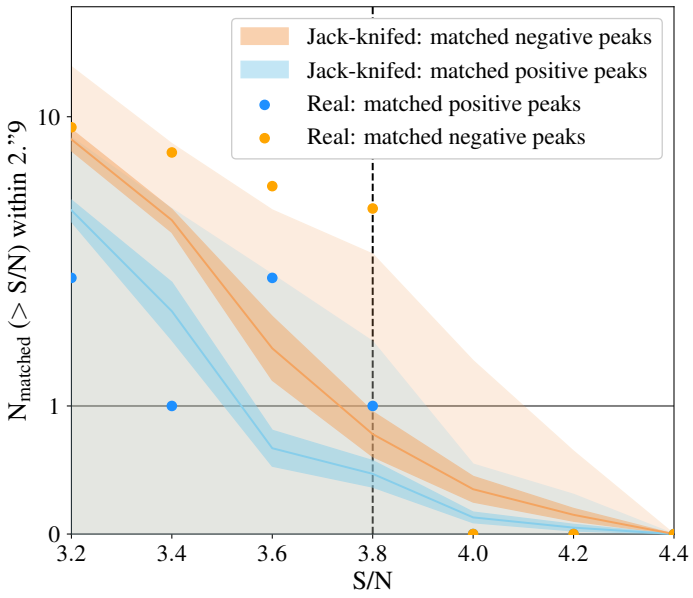

Figure 2.12: Number of matched peaks above a certain S/N within 2.″9 of the expected position of HD1. The filled blue and orange circles correspond to the number of positive and negative matched peaks, respectively, in the real data cubes. The solid line, dark- and light-shaded regions correspond to the mean, standard deviation, and standard error about the mean for the matched pairs of jackknifed data cubes. We find one matched positive pair in the real data (the tentative [O III] 88 µm and [C II] 158 µm features) at $S/N > 3.8$. Given the mean and standard deviation on the matched peaks in the jackknifed data, one set of matched peaks in the real data is perfectly consistent with being noise.

$\mathrm{RA}, \mathrm{Dec}, \nu = 3.49918°, -30.32469°, 253.92\,\mathrm{GHz}$. These peaks have S/N values of 2.7 and 2.6, and line widths of 230 km s^{-1} and 140 km s^{-1}, respectively. Given the probability of false detection and the number of peaks found in the real data, the likelihood ratio test results in $\Lambda(\gamma = 2.5\sigma) = 1.64$. This does not exceed our detection threshold of $k > 3$, set in Section 2.4.1.

Furthermore, we recover the peak reported by Zavala et al. (2024) with `FindClump` at a significance of $S/N = 2.7$. For illustrative purposes, Figure 2.11 shows the moment-0 map that reproduces this feature alongside three jackknife realizations. In one of these realizations, we observe a similar spatial flux distribution as in the real data. The moment-0 maps and the posterior distribution clearly indicate that there is no detection of GLASS-z12 in the ALMA data. Even including a prior from JWST, the ALMA data is statistically consistent with noise.

2.4.4 Detection significance of two correlated noise peaks for HD1

We test the likelihood of finding two tentative detections in each data set in the case that neither corresponds to a real source. In other words - how likely are we to obtain emission-line-like features at the same redshift and location on the sky *if neither are actually line emissions from*

the source? For this test, we ensure that all data cubes have the same spectral resolution of 50 km s^{-1} but keep the spatial resolution of the original imaged cubes (i.e. cell sizes of $0''.1$ and $0''.25$, and beam sizes of $0''.51 \times 0''.87$ and $2''.91 \times 2''.27$, for the Band 6 and 4 data respectively). The frequency ranges of the data are the same as those shown in Figure 2.1; the Band 6 and 4 data sample similar redshift ranges for [O III] 88 µm and [C II] 158 µm emission ($z = 13.19-13.41$ and $z = 13.17-13.37$ respectively). We further adopt a similar approach to that used in Section 2.4.3, but this time we use only flat priors. Specifically, the source is required to be within a $2''.9$ aperture (equivalent to one beam) centered on the optically derived centroid, $\mathcal{U}_{\rm r}\,(0, 2''.9)$, and one peak has to be within a 1000 km/s of the other, according to the frequency difference between the [C II] 158 µm and [O III] 88 µm line, $\mathcal{U}_{\Delta v}\,(0, 1000\ {\rm km/s})$, to account for possible outflow effects.

Using `FindClumps`, we find one positive $\geq 3.8\sigma$ feature within the $2''.9$ aperture in the Band 4 data. We also find five positive $\geq 3.8\sigma$ features in the Band 6 data cube within this aperture. All lists include the line candidates for the proposed $z = 13.27$ source (by design). The higher number of $\geq 3.8\sigma$ features in the Band 6 data is due to the difference in spatial resolution. Cross-matching the real Band 4 and 6 data cubes, we recover one matched pair of positive $\geq 3.8\sigma$ features within 10 kpc and 1000 km s^{-1} of each other, which correspond to the proposed [O III] 88 µm line at $z = 13.27$ (Band 6 cube) and tentative [C II] 158 µm line, offset by ~ 6 kpc and ~ -190 km s^{-1}.

Regarding the jackknifed data, the mean number of corresponding pairs of $\geq 3.8\sigma$ emission features within 10 kpc and 1000 km s^{-1} is 0.5, with a standard error on the mean of 0.1 and standard deviation of 1. The mean number of matched peaks implies that with the data in hand, there is on average, a 50% chance of detecting spatially and spectrally correlated $\geq 3.8\sigma$ noise peaks in both the Band 4 and 6 data and results in a $\Lambda(3.8 < \gamma < 4.2) = 2$.

The mean, standard error on the mean, and standard deviation (overall matched pairs) for various γ are shown in Figure 2.12. We find that the number of matched noise peaks drops sharply with S/N (Figure 2.12). The number of jointly detected noise peaks drops to 0 at a S/N threshold of ~ 4.4. Thus, at $S/N > 4.4$, two matched positive features in the Band 4 and 6 data are certain to be real, whereas at $S/N > 3.8$, they are fully consistent, with both being noise peaks.

2.5 Physical implications of the found upper limits

2.5.1 Exploring the potential redshift solutions

*The following subsection is primarily based on the work of Kaasinen, **van Marrewijk** et al. (2023). Since I did not lead or make a significant contribution to this part of the paper, I will briefly summarize the results rather than discussing the entire work.*

Unfortunately, we found no evidence that any of the line emissions from the four targets are real. This outcome could suggest two possibilities: (1) the emission line is not within the redshift range covered by our observations, or (2) the line exists at this redshift but is too faint to detect.

Regarding the first possibility, the ALMA continuum measurements for these observations are not deep enough to further constrain the redshift solution through SED modeling. For example, we revisited the SED-fitting analysis for HD1, employing alternative SED-fitting codes `MAGPHYS`

and `Bagpipes` to assess the likelihood of different redshift scenarios (see also the discussion in, Fujimoto et al., 2023, Yoon et al., 2023, regarding GLASS-z10 and S5-z17-1). However, we found that the relative likelihood of the $z \sim 4$ and $z \sim 14$ solutions is highly dependent on the assumed star formation history and the priors on stellar ages. Given the range of redshift probability distributions obtained with different prior combinations, we concluded that, with the available photometry, there is no definitive way to identify a single, best-fitting redshift.

At the time of publication (Kaasinen, **van Marrewijk** et al., 2023), we identified three main potential redshift solutions for HD1 that the current data could not distinguish between (1) a dust-rich, low-redshift dwarf galaxy at $z = 0.2 - 0.3$, (2) a passive galaxy at $z = 3.6 - 4.6$, where the photometric break corresponds to the Balmer break, or (3) a galaxy at $z > 13$ with a Lyman break bluewards of 2 μm. It was only recently that HD1 was confirmed to be a passive galaxy at $z = 4.0$ via JWST/NIRSpec observations that revealed a Balmer break (Harikane et al., 2024b).

The following possibility remains for the other sources: the galaxies are positioned at $z > 10$ but are inherently too faint to be detected in the sub-mm. For example, the upper limits for HD1 (even though we now know that HD1 is at $z = 4.0$) on the [O III] 88 µm and [C II] 158 µm line luminosity are 5.2×10^8 K km s^{-1}pc^2 and 4.9×10^8 K km s^{-1}pc^2, respectively. In solar luminosity units, this corresponds to $L_{[\mathrm{OIII}]} < 6.4 \times 10^8$ L$_\odot$ and $L_{[\mathrm{CII}]} < 1.1 \times 10^8$ L$_\odot$. In their Figure 11, Harikane et al. (2020) presented the predicted ratio of the [O III] 88 µm and [C II] 158 µm luminosity as a function of the SFR of galaxies using `cloudy` (Ferland et al., 2017). Based on the SED fitting, the SFR for the $z \sim 13.3$ solution is $\sim 100\,\mathrm{M\,yr^{-1}}$. Thus, the upper limits on these ratios are $\log\,[\mathrm{O\,III}]/\mathrm{SFR} < 6.7$ and $\log\,[\mathrm{C\,II}]/\mathrm{SFR} < 6.0$. This is fully consistent with an ISM metallicity of $\leq 0.2\,\mathrm{Z}_\odot$ and a density of $\sim 10^3\,\mathrm{cm}^{-3}$. Thus, the lack of any significant ALMA Band 4 or 6 detection corresponding to the [C II] 158 µm and [O III] 88 µm emission lines also did not rule out HD1 being a $z \sim 13.3$ galaxy. It could simply imply a low ISM metallicity and/or high gas density, for instance, also found for GLASS-z12 (Popping, 2023, Zavala et al., 2024) and predicted by Kohandel et al. (2023).

2.5.2 Plausible conditions of the ISM in z>10 galaxies

What is the effect of the predicted low ISM metallicity and high electron density on the photon ionization rate? To link this work back to the introduction (Section 1.3), these potential EoR galaxies are the driving force behind the phase transition of the Universe: the reionization of primordial hydrogen. With a back-of-the-envelope estimate, we can calculate the number density of ionizing photons from these galaxies.

The photon ionization rate is often expressed as a dimensionless quantity, U_{ion}, to describe the ionization state of a gas cloud, particularly for H II regions around young stars (referred to as Strömgren spheres, Strömgren 1939). Mathematically, the ionization parameter U_{ion} is defined as,

$$U_{\mathrm{ion}} = \frac{Q_H}{4\pi\ R_s^2\ n_H\ c}\ , \tag{2.5}$$

where n_H is the hydrogen number density in the gas cloud, c is the speed of light, $Q(H)$ is the ionizing stellar luminosity, and r is the distance from the ionizing source to the gas cloud, often

set to the Strömgren radius R_s. The Strömgren radius is defined as,

$$R_s = \left(\frac{3 Q_H}{4\pi \, n_H^2 \, \alpha_H} \right)^{1/3} , \tag{2.6}$$

where α_H is the recombination coefficient (for which we assume $\alpha_H = 2.6 \times 10^{-13}$ cm^{3}s^{-1} at $T = 10^4$ K). Note that by substituting Eq. (2.5) into Eq. (2.6), we find that $U_{\rm ion} \propto (n_H \, Q_H)^{1/3}$.

Since Q_H is the rate of emission of photons with energies greater than 13.6 eV from an inner source (e.g., a set of young stars imbedded within a starcluster), we can link Q_H to the luminosity of such stars as follows,

$$Q_H(Z) = \left(\frac{M_\star}{10^6 \, {\rm M}_\odot} \right) \frac{1}{hc} \int_0^{912\,\text{Å}} \lambda L_\lambda \, (\lambda | Z) \, d\lambda \, , \tag{2.7}$$

where h is the Planck constant, $\lambda_L = 912$ Å is the wavelength of the Lyman limit, and Z is the stellar metallicity. Note that we dropped the Z-dependence in Eq. (2.5) and Eq. (2.6), as only L_λ weakly depends on Z. From now on, we further assume the gas metallicity to be equal to the stellar metallicity, a common assumption for galaxies at $z > 10$ (see, e.g., Harikane et al., 2022, Kohandel et al., 2023, Zavala et al., 2024). Additionally, in Eq. (2.7), the luminosity for a star cluster is normalized to that of a cluster with mass $M_\star = 10^6$ M$_\odot$ and a total bolometric luminosity of $L_{\rm bol} = 1.3 - 1.4 \times 10^9 \, L_\odot$, with the latter slightly varying depending on Z.

To compute $U_{\rm ion}$, we derived the input luminosity using the standard stellar population model from the Binary Population and Spectral Synthesis code (BPASS, Stanway & Eldridge, 2018). We adopted the standard initial mass function (IMF) with a broken power law, a cut-off mass at $M_\star = 300$ M$_\odot$, and an upper slope of 1.35, and let the stellar population evolve for 10^6 Myr before computing Eq. (2.5). Furthermore, the BPASS spectra are already normalized to $M_\star = 10^6$ M$_\odot$ and include binary stellar populations. We varied the solar/gas metallicity $|Z/Z_\odot| = [1 \times 10^{-3}, 1 \times 10^{-2}, 2 \times 10^{-2}]$ and hydrogen number density $\log_{10} n_H = 2.0 - 5.0$ cm^{-3} to compute $U_{\rm ion}$. The results are shown for various star cluster masses (referred to as cloud mass) in Figure 2.13, assuming a linear dependence between Q_H and $M_\star$.

These simple estimates on $U_{\rm ion}$ can give valuable insights into other works that highlighted the importance of $U_{\rm ion}$ on the derived line luminosities using codes such as `cloudy` (see, e.g., Harikane et al., 2022, Wilkins et al., 2023, Kohandel et al., 2023, Zavala et al., 2024). `Cloudy` models the chemical composition and structure of an expanding H II region and uses radiative transfer codes to link these conditions to emission line luminosities. However, `cloudy` uses $U_{\rm ion}$ as an input parameter, which is varied over a broad range (e.g., $\log_{10} \, U_{\rm ion} = [0, -4]$) while keeping L_λ constant. This means that according to Eq. (2.5), Eq. (2.6), and Eq. (2.7), `cloudy` will vary R_s, n_H, and $M_\star$ arbitrarily to obtain such extreme values for $U_{\rm ion}$ as for instance measured in Kohandel et al. (2023) using *single-zone* type of models, thus losing a realistic structure for the simulated Strömgren spheres.

A better approach would be to constrain the chemical compositions and structures of the H II regions and the diffuse gas using the work of Gutkin et al. (2016). By constraining the CLOUDY parameters according to Eq. (2.5), Eq. (2.6), and Eq. (2.7), there would be more control over the initial stellar properties of the star cluster that CLOUDY approximates. From Figure 2.13, we

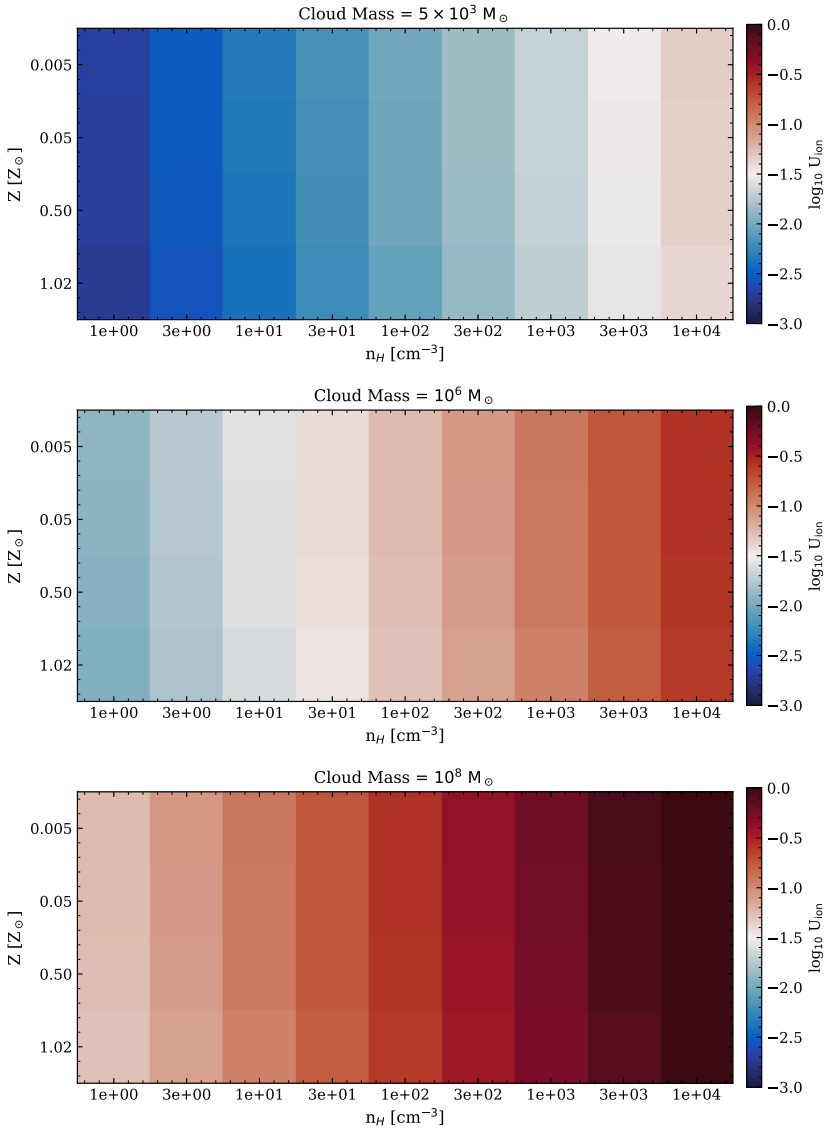

Figure 2.13: Computed ionization parameters $U_{\rm ion}$ for various $n_H - Z$ combinations. The top panel represents a cloud with a mass of $M = 5 \times 10^3$ M$_\odot$, the middle panel a mass of $M = 10^6$ M$_\odot$, and the bottom panel corresponds to a single-zone CLOUDY run with a star cluster mass of $M_\star = 10^8$ M$_\odot$ (see, e.g., Harikane et al., 2022, Kohandel et al., 2023). The grid values are reported in absolute metallicities (*y-axis*) and hydrogen number densities (*x-axis*).

conclude that given the BPASS spectrum, we must probe a low n_H to reach the extremely low $U_{\rm ion}$ parameters derived in Kohandel et al. (2023) when constraining the star cluster to $M_\star = 10^6$ M$_\odot$.

We can also apply this methodology to observations. Of the four galaxies we analyzed, Glass-z12 is the only one confirmed to be at $z > 10$. It has extensive JWST and ALMA data, which are necessary to estimate the metallicity, hydrogen number density, and ionization parameter. Zavala et al. (2024) estimated the gas-phase metallicity to be $Z = 0.05^{+0.12}_{-0.03}$ $Z_\odot$ through the [O III]λ4959,5007 Å /Hβ line ratio, which is consistent with the [Ne III]λ3868 Å /[O II]λ3727 Å measurements taken with JWST/NIRSpec (Castellano et al., 2024, which resulted

in $Z/Z_{\odot} = 0.04^{+0.03}_{-0.02}$). Furthermore, Castellano et al. (2024) found $\log U_{\rm ion} = -1.78 \pm 0.28$, based on the C IV/C III ratio and using the UV-BPT diagram of Mingozzi et al. (2024). The derived values of $U_{\rm ion}$ are broadly consistent with those obtained by Zavala et al. (2024) through SED-fitting the MIRI + ALMA observations. Zavala et al. (2024) reported $\log U_{\rm ion} = -1.4^{+0.2}_{-0.3}$ using `BAGPIPES` and $\log U_{\rm ion} = -2.1^{+0.6}_{-0.3}$ using `CIGALE`. The difference between these two $U_{\rm ion}$ values is likely due to the latter solution also finding four times higher dust attenuation than when using `BAGPIPES`. Additionally, Zavala et al. (2024) found a lower limit on the hydrogen number density n_H through the [O III]λ5007 Å /[O III] 88 µm ratio, resulting in a lower limit of > 250 cm^{-3} using `cloudy` single-zone models, which might go up to 1,000 cm^{-3} when adopting a temperature of $T_e \simeq 10,000$ K instead of $T_e \simeq 4,000$ K.[8] Using the tabulated values shown in Figure 2.13, the reported metallicity and ionization values would only match if we assume an average star cluster mass of $M_{\star} \approx 5 \times 10^3$ M$_{\odot}$. This suggests that these high-z, metal-poor galaxies might be composed of numerous lower-mass star clusters rather than fewer more massive ones. It also implies that the single-zone `cloudy` models used in Harikane et al. (2022), Zavala et al. (2024) might bias the results toward lower ionization states due to the need for higher input bolometric luminosities (which scales linearly with the cloud accoring to Eq. 2.7) to properly model such large clouds. How this impacts the reionization of the Universe is, however, still unknown. It would depend on many factors, such as the underlying correlation functions of these galaxies and their overall UV luminosity function. However, this exercise illustrates that FIR observations targeting the various [O III] lines to obtain a direct constraint on n_H are crucial for estimating the ionizing photon output of these galaxies.

2.6 Summary

In this study, we showed that conventional methods are not robust enough to confirm the presence and characterize the properties of galaxies beyond $z > 10$ with ALMA. We, therefore, introduce an easy-to-use framework for determining the likelihood of faint emission in interferometric data bring real. By jackknifing the visibilities, we generate noise realizations of the measurement set. Line-finding tools can then be applied to both the noise and the original data set to quantify the level of false detections. In this work, we have tested our approach using `FindClumps` (Walter et al., 2016), but there are several other line-finding tools, which may be more appropriate for interferometric data, including `SoFiA` (Serra et al., 2014, Westmeier et al., 2021), `LineSeeker` (González-López et al., 2020) or `MF3D` (Pavesi et al., 2018). Our entire analysis procedure, modulo the user's choice of line-finding algorithm, is publicly available at `https://joshiwavm.github.io/jackknify/`, and the tool, `jackknify`, is installable using pip[9] (**van Marrewijk** & Di Mascolo, 2024).

We applied this methodology to four ALMA-DDT observations targeting galaxy candidates

[8] Here, we used the upper limit value from Zavala et al. (2024) on the [O III] 88 µm line luminosity. We do stress that a small change in the upper limit translates non-linearly to the derived n_H value. For instance, increasing the upper limit from a 3σ to a 5σ value would change the lower limit on n_H from 250 cm^{-3} to 10 cm^{-3} for an electron temperature of $T_e \simeq 4,000$ K.

[9] `https://pypi.org/project/jackknify/`

at $z > 10$ to recover the likelihood of peaks at a certain S/N being real. Given the number of peaks in each dataset and their respective distribution of peak values, the likelihood ratio test using a minimum detection threshold of $\gamma = 4\sigma$—as formalized in Eq. (2.2)— resulted in $\Lambda(\gamma = 4\sigma) = 1.5, 0.80, 1.4, 1.4$, respectively (see Table 2.2). Since we set the detection threshold to $\Lambda(\gamma) > k$ with $k = 3$ (see Section 2.4.1), we conclude that none of the previously reported tentative detections could be distinguished from noise, even when incorporating additional prior information from JWST/MRS slit measurements in the inference.

Our analysis shows that, given the current ALMA data volumes ($N_{\rm peaks} \approx 200 - 1000$), we expect to find approximately 3 ± 2 line features with S/N$\sim 4 - 5$ based on the underlying noise distribution. Ensuring a secure detection is therefore challenging, requiring $> 5\sigma$ detections when performing a blind line search in a cube probing 30 GHz of bandwidth and targeting a single line. Detecting two lines at matching redshifts would strengthen the significance; however, even then, the likelihood of detecting two noise features within a reasonable spatial and frequency offset needs to be accounted for. Even when probing multiple lines in different bandwidths, spurious features arise at a significance of $\approx 4\sigma$ at the right frequency and realistic spatial offset in both data sets.

While the elegance of `jackknify` lies in its straightforward implementation, new approaches are needed to optimize line searches computationally and to increase fidelity. There is currently no publicly available line-finding algorithm implemented in uv-space for extragalactic sources (see, for instance, Loomis et al. 2018 with the code `VISIBLE`, which they used for finding isotopes in protoplanetary disks in high spatial and spectral resolution observations). Operations in uv-space are not affected by side lobes or other sources of correlated noise to which analyses in the image plane are susceptible, but they come at the cost of computational efficiency. Additionally, ongoing ALMA studies – albeit still in the image plane – are exploring the use of unsupervised machine learning to identify faint emission lines (see, e.g., Baronchelli et al., 2021, 2024). Although these methodologies are in the early stages of development, their implementation could drastically increase computation speed and efficiency.

Improving current line-finding methods is important in the context of several upcoming surveys and telescope upgrades. For example, the Wideband Sensitivity Upgrade of ALMA (Carpenter et al. 2023) will increase the bandwidth and sensitivity by a factor of 2–4. This upgrade will greatly increase the efficiency of line-finding experiments, especially at high frequencies, and is, therefore, critical for identifying $z > 7$ galaxies. Looking to the more distant future, significant advances are expected from major new submillimeter-to-centimeter facilities, such as the Atacama Large Aperture Submillimeter Telescope (AtLAST; Booth et al. 2024) and SKA (Dewdney et al., 2009). The proposed 50 m single dish, AtLAST, would enable large, unbiased surveys of cosmological volumes in multiple bands through the use of on-chip spectrometers (e.g., Endo et al., 2012) and its large 2° field of view, providing secure line identifications for large samples of high-z galaxies. At centimeter wavelengths, deep HI surveys are already revealing new HI detections up to $z \sim 0.4$ (e.g., Baker et al. 2024; Xi et al. 2024; Kazemi-Moridani in prep.), with the full SKA likely to push this to $z \sim 1$. With the increase in data volume associated with these new and upgraded facilities comes the increased potential for spurious line detections. Thus, it is crucial that the community accurately identifies the probability of false detections using statistically motivated approaches like the one we have presented here.

Appendix: Further comparison between the simulated noise and jackknifed realizations

Figure 2.14 shows the difference between the standard deviation from the cleaned map of the first, single simulated observation (i.e., one seed used for `simobserve` visualized with the orange point) and the distribution of standard deviations obtained from the various jackknife realizations (blue dotted line). We find that the jackknifed realizations follow the average distribution of standard deviations, obtained with various `simobserve` seeds (solid line, Fig. 2.7), but their median clearly differs from the first single `simobserve` estimate. This shows that jackknifing can be used to better describe the underlying distribution function than a single noise realization used in `simobserve`.

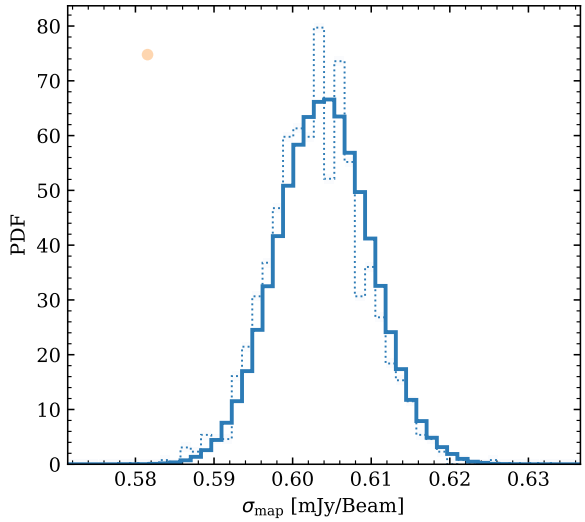

Figure 2.14: Comparison of the standard deviation $\sigma_{\rm map}$ measured from a single `simobserve` simulation (i.e., using one random seed; orange point also shown in Fig 2.7) and the output of jackknifing that single realization (blue dotted line). The latter clearly follows the total distribution of the derived standard deviations (blue solid line of Fig. 2.7) instead of being centered on the single `simobserve` realization.

Chapter 3,

XLSSC 122 caught in the ACT of growing up

The content of this chapter is based on an article that is published in A&A as ***van Marrewijk*** *et al. (2024).*

- The return of the Jedi

Despite being named for their visible galaxy constituents, the main baryonic matter component of a galaxy cluster is the thermalized, low-density plasma found between the galaxies, which is known as the intracluster medium (ICM). The traditional means of studying the ICM is through X-ray observations. In the low redshift universe ($z < 1$), large samples of clusters have been observed with *Chandra* (e.g., Vikhlinin et al., 2009) and *XMM-Newton* (e.g., Böhringer et al. 2007 & CHEX-MATE Collaboration et al. 2021). At $z \gtrsim 1$, however, X-ray detections become more difficult; X-ray flux falls rapidly with increasing z. Hence, X-ray observations of the ICM at redshifts larger than $z \gtrsim 1$ usually comprise a few tens to hundreds of photons.

Fortunately, there are other means to study the ICM. When cosmic microwave background (CMB) photons propagate through the hot plasma, inverse Compton scattering shifts the blackbody spectrum of the CMB to higher frequencies. By measuring the spectral distortion, one has a direct handle on the integrated pressure along the line of sight of the hot electrons in the ICM. This phenomenon is known as the Sunyaev-Zeldovich effect (SZ effect; Sunyaev & Zeldovich 1970) and in contrast to X-ray observations, produces a redshift-independent surface brightness, making it ideal for high-z studies of galaxy clusters.

Ground-based millimeter (mm)-wave CMB surveys have already produced large catalogs of galaxy clusters via the SZ effect containing thousands of members, such as the >4000 optically confirmed clusters of galaxies found in the $\sim 13,000$ deg^2 survey by the Atacama Cosmology Telescope (ACT) survey (Hilton et al., 2021). This catalog alone contains 222 massive ($\gtrsim 1.5 \times 10^{14}\,\mathrm{M}_\odot$) galaxy clusters at $z > 1$. However, current SZ surveys, such as those with *Planck* (Planck Collaboration et al., 2016), ACT, the South Pole Telescope (SPT; Carlstrom et al., 2011, Bleem et al., 2015, 2020), and future CMB surveys such as those with the Simons Observatory (SO; Ade et al., 2019) and CMB-S4 (Abazajian et al., 2016, 2019, Raghunathan et al., 2022), have or will have limited (arcminute-scale) angular resolutions in their main detection bands, 90 GHz and 150 GHz. Thus, while SZ surveys are efficient at finding clusters, they lack the spatial resolution to study the morphology and dynamical state of high-z clusters, often blending a merging cluster pair into a single source (e.g., Di Mascolo et al., 2021).

Characterizing the dynamical state and shapes of clusters of galaxies has been pivotal for cluster cosmology (e.g., Yoshida et al., 2000, Sereno et al., 2018, Ruppin et al., 2019, Lau et al., 2021). For the past two decades, clusters of galaxies have been categorized as cool cores, morphologically disturbed (noncool cores), or simply close to the ensemble average based on their radial pressure distribution in the ICM (i.e., having a pressure distribution that follows some form of self-similar or "universal" pressure profile; Nagai et al. 2007). These pressure profiles are used for measuring and interpreting the scaling relation used for inferring cluster masses. However, most SZ studies still rely on the universal pressure profile (UPP) from Arnaud et al. (2010) which is based entirely on the combination of simulations and X-ray data from the $z \lesssim 0.3$ REXCESS sample. At higher redshifts, profiles are derived by stacking X-ray observations (McDonald et al., 2014). Importantly, since hydrodynamical simulations show that the pressure profile should evolve with redshift (e.g., Battaglia et al., 2012, Le Brun et al., 2015, Gupta et al., 2017), it becomes increasingly inappropriate to rely on these pressure profile templates when probing higher redshifts. As upcoming telescopes such as SO and CMB-S4 are expected to be capable of detecting clusters up to redshifts of $z \sim 3$ (Raghunathan et al., 2022), it becomes particularly urgent to characterize the pressure distribution of high-z galaxy clusters through

resolved imaging of the SZ effect.

In practice, only a few instruments are currently capable of characterizing the ICM morphology through the SZ effect at the relevant scales (tens to a few 100 kpc) to resolve their substructure at $z > 1$. Among them are MUSTANG-2 on the Green Bank Telescope (e.g., Romero et al., 2020, Orlowski-Scherer et al., 2022), the Atacama Compact Array (ACA; also known as the Morita array), the Atacama Large Millimeter/submillimeter Array (ALMA; e.g. Di Mascolo et al. 2021, Kitayama et al. 2023), MISTRAL on the SRT (Battistelli et al., 2023), and NIKA2 on IRAM (e.g., Ruppin et al., 2018, Kéruzoré et al., 2020, Ricci et al., 2020). Observations by these instruments, at four to five times higher resolution than available with the ground-based survey telescopes used to discover SZ clusters, showed that the low-resolution signal could be resolved into separate components in higher resolution follow-up observations (for a recent review on resolved SZ studies, see Mroczkowski et al. 2019).

In the most recent ACT DR5 cluster database (Hilton et al., 2021), there is only one detected cluster with a redshift $z > 1.75$, namely, ACT-CL J0217.7−0345 (at $z = 1.98$, Willis et al., 2020), which was first discovered in the XXL X-ray survey (Pierre et al., 2004) and thus is also known as XLSSC 122 and XLSSU J021744.1−034536. This work focuses on understanding the dynamical state and morphology of the ICM of this cluster, which we refer to as XLSSC 122 henceforth. Earlier measurements of the pressure distribution in the ICM from SZ studies with CARMA were presented in Mantz et al. (2014) and Mantz et al. (2018). Very few other resolved measurements exist for clusters at $z > 1.75$. These include X-ray data on four clusters that were first found in the IR/NIR: JKCS 041 (Andreon et al., 2009, Newman et al., 2014), Cl J1449+0856 (Gobat et al., 2011), IDCS J1426.5+3508 (Zeimann et al., 2012), and IDCS J1433.2+3306 (Stanford et al., 2012). The first three also have follow-up SZ detections: JKCS 041 with the single-dish receiver MUSTANG-2 (Andreon et al., 2023), Cl J1449+0856 with ALMA and ACA (Gobat et al., 2019), and IDCS J1426.5+3508 with CARMA (Brodwin et al., 2012) and MUSTANG-2 (Andreon et al., 2021). Beyond these, only one additional $z > 1.75$ cluster has had a successful follow-up detection of its pressure profile with the SZ effect, namely the Spiderweb protocluster (Di Mascolo et al., 2023) via ALMA+ACA observations. We note that all five of the aforementioned clusters are outside the ACT survey footprint or below the mass limit of the ACT catalog (Hilton et al., 2018, 2021).

Yet achieving high-resolution observations is not the only aspect that needs to be considered when characterizing the pressure distribution of high-z clusters of galaxies. Interferometric arrays fundamentally measure the 2D Fourier transform of the distribution of emission intensities from an astrophysical source. The long baselines provide the high-resolution samples but only short spacings can probe larger scales as the physical distance between an antenna pair is linearly proportional to the Fourier mode sampled. These Fourier modes in units of wavenumbers are thus expressed in terms of *uv*-distances where u and v are the conventional variables for denoting the orthogonal vector basis of the Fourier space. Balancing between maximizing the collecting area for each interferometric element and mitigating concerns like the field of view size and the minimum distance between two antennas to avoid a collision imposes a fundamental constraint on the minimum length a baseline can be, which inevitably leads to an incomplete *uv*-coverage and strong spatial filtering. To address the loss of information at large angular scales ($> 1'$), we can turn to data from bolometer arrays on single-dish telescopes. However, existing single-dish

facilities also do not provide the extent of complete Fourier sampling required for high spatial dynamic range and unbiased image reconstruction (Frayer, 2017, Plunkett et al., 2023). In order to address this missing baseline problem in the ALMA and ACA data, we will also make use of known radial pressure profiles to interpolate over the missing information.

In this chapter, we treat this issue by combining archival SZ observations from both the main ALMA (12m-array) and ACA (7m-array) with single-dish data from ACT. This comprehensive approach enables us to probe the broad range of spatial scales needed to provide the first detailed, sub-arcminute view of the ICM in the highest redshift cluster found in the current generation of SZ survey data. The remainder of this work is outlined as follows: we provide an overview of the measurements used for our analyses and the data reduction details in Section 3.1. Section 3.2 provides the methodology on how the forward modeling is implemented. There are three results sections: The first, Section 3.3, is on how we handle and correct for compact source contamination; Section 3.4 describes the first results on the derived pressure profiles; And finally, Section 3.5 goes into detail on how to recover and model asymmetric surface brightness distributions. The implications of our observations and an exploration of their potential interpretations are provided in the following two sections. Section 3.6 treats the derived halo mass of XLSSC 122 and Section 3.7 the morphological implications of the results obtained from the forward modeling. Finally, we summarize and conclude our work in Sect. 3.8.

For all calculations, the assumed cosmology is based on Planck Collaboration et al. (2014), a spatially flat, Λ cold dark matter (ΛCDM) model with $H_0 = 67.7\ \mathrm{kms^{-1}Mpc^{-1}}$ and $\Omega_\mathrm{m} = 0.307$. Here $1'' = 7.855$ kpc for XLSSC 122 ($z = 1.98$).

3.1 Observations of XLSSC 122

The galaxy cluster XLSSC 122 has not gone unnoticed. It was discovered via its extended X-ray emission in the *XMM-Newton* Large Scale Structure survey (Pierre et al., 2004), and first named and described in Willis et al. (2013), almost a decade later. XLSSC 122 was further followed up with CARMA observations that map the ICM through the SZ decrement at 30 GHz (Mantz et al., 2014) as well as a combined analysis of the CARMA plus short *Chandra* and deeper *XMM-Newton* X-ray follow-up observations (Mantz et al., 2018). At the same time, Hilton et al. (2018) noted that while not meeting the threshold for detection in the ACTpol sample, the data showed a 3.5σ decrement at the location of this cluster, which if verified would correspond approximately to the mass reported in Mantz et al. (2014), namely $M_{500,\mathrm{c}} \simeq 1 \times 10^{14}\ M_\odot$. The cluster can be found at an RA and Dec of $2°17'44''.2128$, $-3°45'31''.68$. The cluster was formally detected at a signal-to-noise ratio $S/N > 5$ in the next ACT cluster catalog (Hilton et al., 2021).

Optical spectroscopy using the *Hubble Space Telescope* (HST) Wide Field Camera 3 established that 37 galaxies are associated with XLSSC 122 (Willis et al., 2020) and found the average spectroscopic redshift to be $z = 1.98$. Since then, studies on the cluster member properties using multiwavelength archival data came to light, finding that $88^{+4}_{-20}\,\%$ of the members of the cluster lying within $0.5\,r_{500,\mathrm{c}}$[1] are quenched and exhibit a larger half-light radius than field galaxies (Noordeh et al., 2021). The presence of quenched galaxies, and thus the existence of a red sequence,

[1] $M_{500,\mathrm{c}}$ is defined as the total mass of the cluster within a radius $r_{500,\mathrm{c}}$ in which the average density is 500 times

plus the detection of the ICM indicates that XLSSC 122 is, in some sense, already a mature cluster.

To this multiwavelength view of XLSSC 122, we add microwave data from ALMA (the main array of 12m antennae), ACA (the 7m-array), and ACT Data Release 6 (DR6; Coulton et al. 2024) to map the SZ decrement from the core to the virial radius at sub-arcminute resolution. These observations will map any asymmetry in the pressure distribution of the ICM and characterize its radial profile; both were previously inaccessible because of the low resolution ($\approx 1'$) and low S/N of the previous data. In the following subsections, we will describe ALMA, ACA, and ACT observations that will determine if this cluster is thus truly relaxed and mature or is still actively forming.

3.1.1 The Atacama Large Millimeter/Submillimeter Array

We rely upon archival yet unpublished ALMA and ACA Band 3 observations (henceforth denoted ALMA+ACA) made on 2016-10-22 and 2017-01-06, respectively, for characterizing the SZ decrement. For both observations with project code 2016.1.00698.S (PI: A. Mantz), calibrated datasets were obtained through the calibrated measurement set service (CalMS; Petry et al., 2020) of the European ALMA Regional Center using CASA 5.4.0. The total on-source time for the ACA and ALMA observations are 3.9 and 0.42 hours, respectively.

Both the 12m-array and 7m-array observations span four spectral windows: 89.51–91.50, 91.45–93.44, 101.51–103.49, and 103.51–105.49 GHz, observed in continuum mode. The spectral windows are set up to exclude any strong molecular emission lines of cluster members (we note, however, that we identified spurious emission lines of other galaxies along the line of sight; see Sec. 3.3 below for details). Both observations were carried out in mosaic mode, with the ACA observations consisting of five pointings and the ALMA observations consisting of 11. The ACA and ALMA observations reach a central continuum sensitivity of 0.24 and 0.037 mJy beam^{-1} per pointing with an angular resolution of $11''$ and $2''$, respectively. The maximum recoverable scales of the ACA and ALMA observations are $77''$ and $23''$ per pointing. The ACA and ALMA continuum maps, as well as a jointly imaged ALMA+ACA map, are shown in Figure 3.1. The maps show dirty images in which the true sky is convolved with the transfer function, which arises from the incomplete uv-coverage of the interferometer. The bottom panel and remaining figures in this paper that show ALMA+ACA observations are tapered[2] to have a beam with an FWHM of $5''$.

Furthermore, we make use of ancillary ALMA Band 4 observations to get better spectral constraints on the contaminating emission from dusty galaxies. These observations, with project code 2018.1.00478.S, were performed on 2019-01-18 and reduced via the standard CASA 5.4.0 pipeline. The Band 4 observations span four spectral windows – 139.7–141.6, 143.0–143.9, 153.1–154.0, and 154.9–155.9 GHz – with a single pointing centered on $\mathrm{RA} = 2^\circ17'42\farcs8$, $\mathrm{Dec} = -3^\circ45'31\farcs2$. It reaches a continuum sensitivity of ~ 0.024 mJy beam^{-1} RMS.

the critical density of the Universe at that redshift.

[2]Tapering is equivalent to smoothing the PSF with a Gaussian. However, tapering in *uv*-space uses a natural weighting scheme that down weights higher spatial frequencies relative to lower spatial frequencies to suppress artifacts arising from poorly sampled areas of the uv-plane.

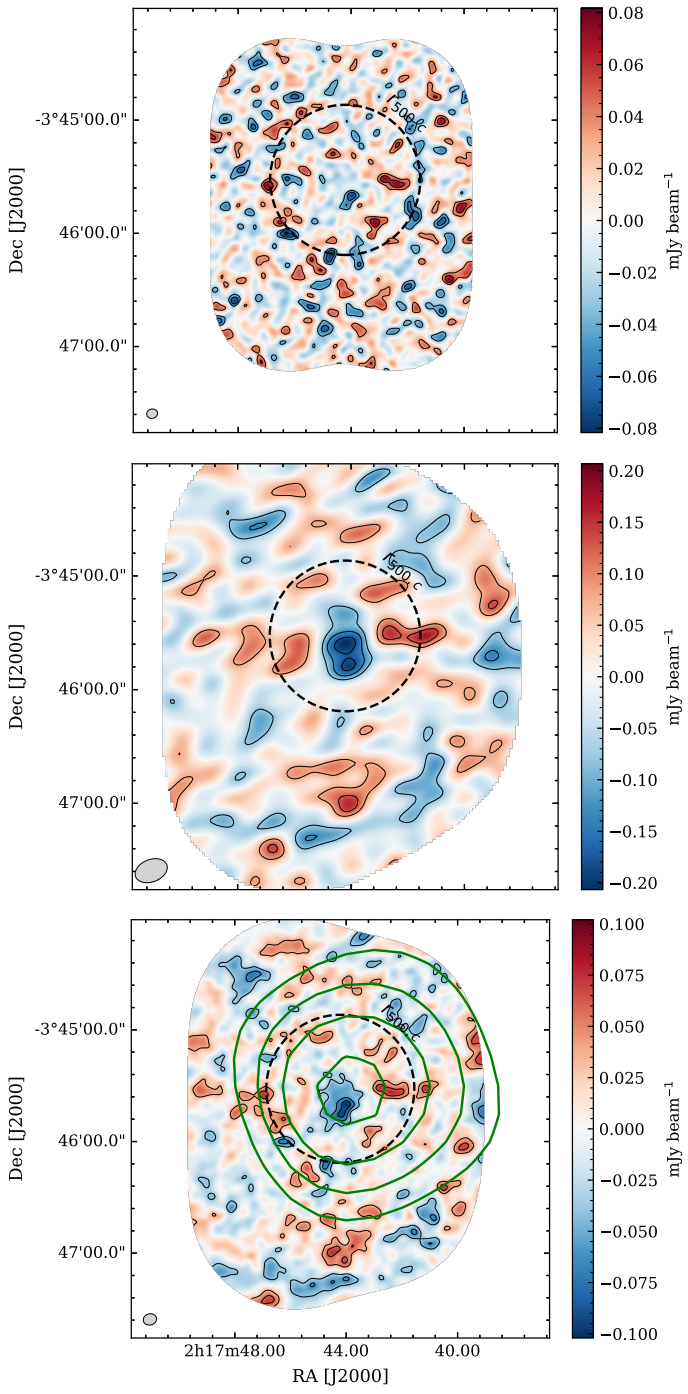

Figure 3.1: ALMA observations of XLSSC 122. From top to bottom, we show the raw (dirty) continuum images of the 12m-array mosaic, ACA mosaic, and the jointly imaged Band 3 observations. The latter image (bottom panel) is tapered with a *uv*-taper of 20 $\mathrm{k}\lambda$. Black contours in each panel are drawn at $[-4.5, -3.5, -2.5, -1.5, 1.5, 2.5, 3.5]-\sigma$ except for the top panel, which excluded the $\pm\ 1.5\sigma$ contours. We find a central noise RMS of $\sigma = 0.051, 0.014, 0.022$ mJy beam^{-1}, respectively. The dashed circles in all panels indicate $\mathrm{r}_{500,\mathrm{c}}$ centered on the BCG. The green contours in the bottom panel indicate the ACT-y map contours and are drawn at [2.5, 3.5, 4.5, 5.5] times the local noise level. The beams of the ACA, ALMA, and jointly imaged ACA+ALMA observations are indicated in the lower-left corner of each panel. We clearly see that the ACT and ALMA+ACA observations align spatially.

3.1.2 The Atacama Cosmology Telescope

To characterize larger angular scales of XLSSC 122, and in particular, to constrain the integrated Compton Y ($= \int y d\Omega$) (see Sec. 3.2.1), we include data from the Atacama Cosmology Telescope (ACT). ACT was a 6-meter, off-axis Gregorian survey telescope that operated from 2008 to 2022

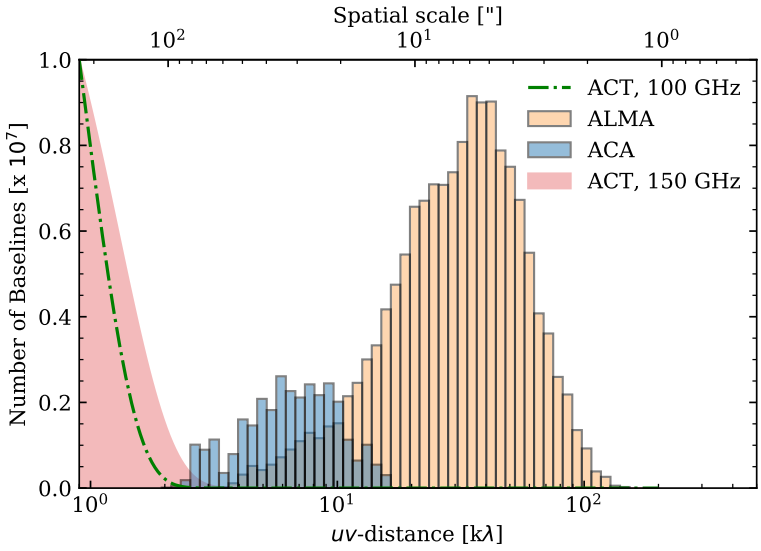

Figure 3.2: Distribution of the number of visibilities as a function of the *uv*-distance sampled with ALMA (yellow) and ACA (blue) Band-3 observations. In red, we overlay the ACT beam at 150 GHz ($\sim 1\farcm4$) and 100 GHz ($\sim 2\farcm0$) as a green dashed line. The y-axis is scaled using arbitrary values regarding the ACT beams.

in the Atacama Desert of Chile. Over its lifetime, the detectors and receiver were modified such that it covered, at various times, frequency bands centered at approximately 30, 40, 100, 150, 220, and 280 GHz; detectors were sensitive to polarization starting in 2013 (Swetz et al., 2011, Thornton et al., 2016, Henderson et al., 2016). The receiver consisted of three arrays of detectors, each in its own optics tube, such that each was located at a different position on the focal plane. For most of the period of observation used in this paper, each array was sensitive to two different frequency bands: thus, at any given time, six array–frequency pairs were observed.

In this paper, we use the ACT maps at 100 and 150 GHz from DR6 with a point-source sensitivity integrated over the beam of 0.5 mJy and 0.8 mJy, respectively. These observations are taken from 2017 to 2022. We note that these are the frequencies that are most sensitive to the SZ effect (see Sec. 3.2.1). ACT provides the larger scales with a FWHM resolution of $\approx 2'$ and $\approx 1.4'$ at 100 and 150 GHz, respectively. The bottom panel in Figure 3.1 overlays the contours of the ACT DR6 S/N map of XLSSC 122 to be included in Hilton et al. (in prep.). The figure shows that XLSSC 122 is largely unresolved by the ACT observations.

Figure 3.2 overlays the baseline distributions for the spatial scales sampled by ALMA and ACA with the ACT beams at 100 and 150 GHz to show which spatial scales we are sensitive to when utilizing both types of observations. Here, angular scales are converted to *uv*-distances through the relation:

$$uv\text{-distance}[\lambda] = \frac{1}{\text{angular scale [radians]}}. \tag{3.1}$$

Thus, the scale probed in radians equals the inverse of the baseline length in wavenumbers.

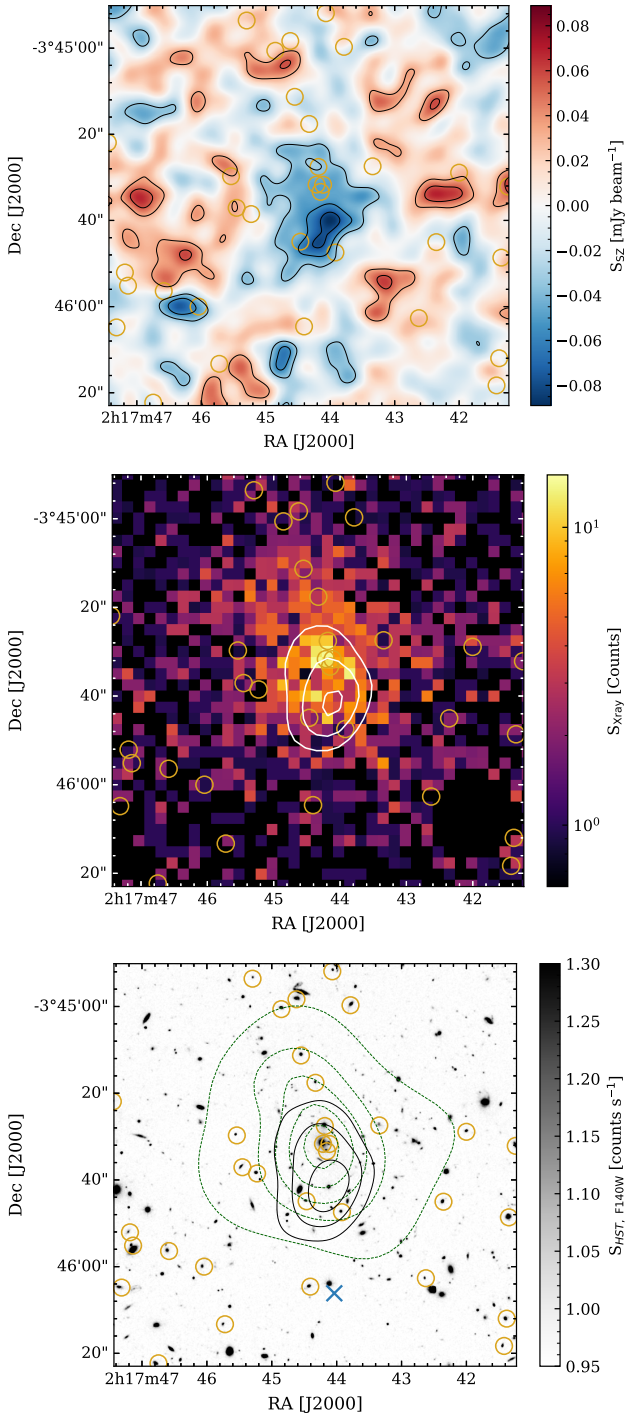

Figure 3.3: Multiwavelegth view of XLSSC 122. *Top:* A dirty map of the joint ALMA+ACA Band 3 observations overlaid with the distribution of member galaxies of the cluster shown as small gold circles, as in all other panels. The black contours are drawn at [-4.5, -3.5, -2.5, -1.5, 1.5, 2.5, 3.5]$-\sigma$. *Middle: XMM-Newton* image of Mantz et al. (2018) overlaid with the directly visible SZ decrement as seen by the ALMA+ACA imaging with a *uv*-taper of 10 kλ. *Bottom:* HST imaging from Willis et al. (2020) used to find the cluster members. Here, we overlay in black the directly visible SZ decrement as seen by the ALMA+ACA observations, and in dark green, we show the adaptively smoothed X-ray contours drawn at [2, 4, 6, 8, 10]$-\sigma$. We further highlight the SZ centroid derived from CARMA measurements (Mantz et al., 2018) with the blue cross. Overall, this figure indicates a coherence between the pressure and density distribution of the ICM seen by ALMA+ACA and X-ray measurements, and the cluster member distribution.

3.1.3 Auxiliary data comparison

Throughout this work, we will compare the results obtained from our analysis of the SZ effect with the X-ray surface brightness distribution. As mentioned above, XLSSC 122 was first discovered

via its extended X-ray emission as seen with *XMM-Newton*. In total, *XMM-Newton* collected ≈ 1096 source photons in an exposure of 106 ksec, while higher-resolution *Chandra* observations only collected ≈ 200 source counts in 182.2 ksec after light curve filtering (deflaring). Here, we use the previously unpublished data from the archive (PI: Noordeh)[3] and applied the standard ACIS reprocessing technique in order to merge the *Chandra* observations into a flux-corrected image using the `ciao` tools. However, the combined *Chandra* data translates to $\lesssim 4$ source photons per hour of observation time, which is not uncommon in high-redshift observations of clusters of galaxies in the X-ray regime. As an example, X-ray observations of the Spiderweb protocluster collected approximately 1 photon per 3.6 ksec (Tozzi et al., 2022). Therefore, to study the diffuse ICM in XLSSC 122 from the X-ray perspective, we henceforth only rely on the *XMM-Newton* observations.

Figure 3.3 compares the SZ decrement (also shown in Figure 3.1) with the observed X-ray emission seen by *XMM-Newton* from Mantz et al. (2014, 2018) and the deep optical HST-imaging from Willis et al. (2020). Our mm-wave observations are in contrast with the findings of Mantz et al. (2018), who reported an offset of $35'' \pm 8''$ (295 ± 64 kpc at $z = 1.98$) between the X-ray emission and the CARMA-measured SZ decrement (its centroid is marked with the blue cross in the bottom panel of Fig. 3.3). However, the CARMA measurements suffer from low signal-to-noise ($\sim 5\sigma$) and low resolution, which makes it difficult to account for and remove contaminating sources. The ALMA+ACA observations, on the other hand, clearly reveal the central SZ decrement, while the higher resolution better allows us to mitigate the impact off-centered point sources have on the overall SZ measurement.

3.2 Methodology

To study the dynamical state and morphology of XLSSC 122, we forward-model the pressure distribution of the ICM to the observations. In this section, we describe how we jointly model interferometric ACA and ALMA measurements with multi-band imaging data from ACT. In brief, the routine flows as follows: (1) From a parametric description of the pressure distribution, we map the ICM on a three-dimensional grid which is then integrated along the line of sight to produce a projected Compton y map (see section 3.2.1). (2) Using the spectral scaling of SZ effect, we convert the Compton y model to a surface brightness distribution for each of the spectral bands of the analyzed data (see section 3.2.1). (3) We Fourier transform the surface brightness map to the visibility space, which is the native space of the ALMA and ACA data. We then apply the ALMA and ACA transfer function to the model to account for the missing baselines and compute the likelihood of the resulting model on the unbinned visibilities assuming Gaussian properties for noise statistics (see section 3.2.2). (4) As the ACT and ACA+ALMA observations probe different spatial scales, we can forward model the same pressure distribution to both observations separately and combine them by adding the log-likelihoods linearly (see section 3.2.2). We use the radial dependency of the parameterized model to fill in the gap in the angular scales where the observations are less sensitive.

[3] *Chandra* Observation IDs 22562, 22563, 22857, 22868, 22869, and 22870.

3.2.1 Parametric descriptions of the ICM

Pressure profiles

Our forward modeling technique Fourier transforms the SZ signal based on a parametric description of the ICM to the *uv*-plane. As a parameterized model, we choose the generalized Navarro-Frenk-White (gNFW) profile proposed by Nagai et al. (2007):

$$P_{\rm e}(r) = P_{\rm e,i} \left(\frac{r}{r_{\rm s}}\right)^{-\gamma} \left[1 + \left(\frac{r}{r_{\rm s}}\right)^{\alpha}\right]^{(\gamma-\beta)/\alpha}, \tag{3.2}$$

where $P_{\rm e,i}$ is the pressure normalization and γ, α, and β the shape parameters of the broken power law. Respectively, they represent the slopes at small, intermediate, and large radii with respect to the characteristic radius $r_{\rm s}$. In this description, the pressure distribution is a function of the radial distance r from the centroid of the cluster ($x_{\rm gNFW}$, $y_{\rm gNFW}$). Eq. (3.2) is often rewritten to break the spherical symmetry and encapsulate a projected eccentricity which we define as

$$e = 1 - \frac{b}{a}, \tag{3.3}$$

with a and b, the major (with $a = r_{\rm s}$) and minor axis of the ellipse, respectively.

Further, the theoretical formalism of Nagai et al. (2007) can be rewritten such that the normalization parameter $P_{\rm e,i}$ is linked to the halo mass of the cluster, $M_{500,\rm c}$, through the self-similarity principle, the local $M_{500,\rm c} - Y_{\rm X}$ relationship based on the REXCESS sample, and the redefinition of $r_{\rm s}$ such that $(r/r_{\rm s})$ is expressed in terms of the concentration parameter $c_{500,\rm c}$, such that

$$\left(\frac{r}{r_{\rm s}}\right) = c_{500,\rm c} x, \tag{3.4}$$

with $x = r/r_{500,\rm c}$ and $c_{500,\rm c} = r_{500,\rm c}/r_{\rm s}$. This way, the amplitude of the pressure profile and also its specific radius is scaled according to an additional self-similar principle and is a function of halo mass ($M_{500,\rm c}$) and redshift (z) via the $c_{500,\rm c} - M_{500,\rm c}$ relationship. This formalism was introduced by Arnaud et al. (2010) and provides additional constraints in the parameter space, simplifying the modeling of the gNFW. All combined, this empirical relation is expressed as

$$P_{\rm self-similar}(M_{500,\rm c}, z) = P_e(r) \times P_{500,c}, \tag{3.5}$$

with $P_e(r)$ as described in Eq. (3.2) but with the substitution provided in Eq. (3.4). Following Arnaud et al. (2010), the mass dependency comes from the $P_{500,c}$ parameter which is defined as

$$P_{500,c}(M_{500,c}, z) = 1.65 \times 10^{-3}\, E(z)^{8/3} \left[\frac{M_{500,c}}{3 \times 10^4 M_\odot}\right]^{2/3 + a_p(r/r_s)} \tag{3.6}$$

in units of keV cm^{-3}. Here, $E(z)$ is the ratio of the Hubble constant at redshift z to its present value H_0 and $a_p(r)$ the parameter that accounts for deviations from self-similarity in the core of galaxy clusters:

$$a_p(r/r_s) = a_0/[1 + 8 \times (c_{500,c}x)^3]. \tag{3.7}$$

Since Arnaud et al. 2010 (hereafter, A10), the A10 profiles have been used throughout the literature as the universal pressure profiles (e.g., Arnaud et al., 2010, McDonald et al., 2014) by estimating averaged values of γ, α, β, and $c_{500,c}$ for different dynamical states, halo masses, and redshifts.

In this work, we will construct models with both the gNFW-formalism as presented in Equation (3.2) and the parameterization described by Arnaud et al. (2010). When we use the formalism of Arnaud et al. (2010), we will freeze the shape parameters (α, β, γ, and c_{500}) of the derived classifications at the averaged values derived from Arnaud et al. (2010) and McDonald et al. (2014). These values are split in subsamples referring to local ($z < 0.2$) and more distant ($0.6 < z < 1.2$) clusters, respectively. In the remainder of this work, we refer to each of these two formalisms as the theoretical formalism (referring to Eq. 3.2) and the empirical formalism (referring to Eq. 3.5), respectively.

Both Arnaud et al. (2010) & McDonald et al. (2014) split their cluster samples into three classifications: the cool cores (CC), the morphologically disturbed (MD, also known as noncool cores), and the ensemble-averaged classification (also known as the universal pressure profiles, abbreviated to UPP). Cool cores are, on average, more relaxed clusters of galaxies with a cusped core, while morphologically disturbed profiles are a direct consequence of merger activity and exhibit a more flattened inner pressure profile. Hence, by modeling pressure profiles that correspond to these different classifications for the two redshift bins, we can classify the dynamical state of XLSSC 122.

The thermal Sunyaev-Zeldovich effect

To model the hydrostatic properties of the ICM and link it to observables in the mm-wave regime, we use the SZ effect (Zeldovich & Sunyaev, 1969, Sunyaev & Zeldovich, 1970, 1972b). When CMB photons propagate through the hot plasma in the ICM, inverse Compton scattering shifts the photons to higher frequencies, distorting the blackbody (BB) spectrum of the CMB. The predominant source of the transformation, called the thermal SZ effect, is caused by the pressure distribution of the hot electrons in the ICM. This frequency-dependent distortion is the observable we exploit in this work and which we henceforth refer to simply as the SZ effect. (For a thorough description of the various types of other SZ effects, we refer the reader to the review paper of Mroczkowski et al. 2019.)

The amplitude of the SZ effect is a function of the Compton-y parameter:

$$y \equiv \int \frac{k_{\rm B} T_{\rm e}}{m_{\rm e} c^2}\, {\rm d}\tau_{\rm e} = \int \frac{k_{\rm B} T_{\rm e}}{m_{\rm e} c^2} n_{\rm e} \sigma_{\rm T}\, {\rm d}l = \frac{\sigma_{\rm T}}{m_{\rm e} c^2} \int P_{\rm e}\, {\rm d}l\ . \tag{3.8}$$

Here, $\sigma_{\rm T}$ is the Thomson cross section, $P_{\rm e} = n_{\rm e} k_{\rm B} T_{\rm e}$ is the thermal pressure due to the electrons, $n_{\rm e}$ is the number density of the electrons, $k_{\rm B}$ is Boltzmann's constant, $T_{\rm e}$ the electron temperature, $m_{\rm e}$ the electron mass, c the speed of light, $\tau_{\rm e}$ the opacity, and l the path along the line of sight. Thus the magnitude of the SZ signal is a direct measure of the integrated line of sight pressure

and can be obtained by integrating along $\mathrm{d}l$ with the radial dependence of P given by Eq. (3.2). Finally, the corresponding distortion signal is given by

$$\Delta I_\nu \approx I_0 y \frac{x^4 \mathrm{e}^x}{\left(\mathrm{e}^x - 1\right)^2} \left(x \frac{\mathrm{e}^x + 1}{\mathrm{e}^x - 1} - 4 \right) \equiv I_0 y g(x), \tag{3.9}$$

in terms of the CMB intensity $I_0 \approx 270.33 \ \left(T_{\text{CMB}}/2.7255 \text{ K}\right)^3$ MJy sr^{-1} and $x = h\nu \left(k_\text{B} T_{\text{CMB}}\right)^{-1} \approx \nu/56.8$ GHz, where the CMB temperature is adopted from Fixsen (2009).

As shown in Eq. (3.9), the SZ distortions are frequency dependent. In ACT and ALMA's main SZ-detection bands (~ 90 and 150 GHz) the distortion spectrum becomes negative, manifesting as a negative surface brightness in the continuum maps. The equations above assume nonrelativistic speeds for the electrons. We note, for instance, that in a galaxy cluster with a mean ICM temperature of 2 keV, the relativistic correction term would change the overall amplitude of the SZ effect at 100 GHz by 1.3%, and at 4 keV by 2.6%. At 150 GHz, the 4 keV correction is 2.8%. Therefore, any relativistic corrections fall within the calibration uncertainty of the ALMA and ACA observations ($\sim 5\%$). As we do not expect the electron temperature in XLSSC 122 to exceed 5 keV (see Mantz et al., 2018, Duffy et al., 2022), we have neglected the temperature-dependent relativistic corrections of the thermal SZ in this work.

3.2.2 Visibility-based modeling of the ICM

The visibility plane

We employ a forward-modeling approach to determine the best-fitting model parameters that describe the ALMA interferometric and ACT map-domain data on XLSSC 122. This involves reconstructing the surface brightness distribution by forward-modeling the pressure distribution of the hot electrons in the ICM to both types of observations. Here, we rely on a *uv*-space Bayesian approach based on the work of Di Mascolo et al. (2019). For details, we refer to the original presentation, discussion, and references therein; here, we provide a brief summary.

The reconstruction method makes use of the native measurement space of interferometric data, which incompletely samples the *uv* (i.e., Fourier)-plane. Interferometric observations measure Fourier transforms of the distribution of emission intensities from an astrophysical source at a given angular scale and spectral resolution. The Fourier-space measurements, called visibilities, have coordinates (u, v) representing the projected baseline distances between two antennas in a plane normal to the direction of the phase reference position (see e.g., Thompson et al., 2017, page 91). Therefore, each visibility $\mathcal{V}\left(u, v\right)$ is defined as

$$\mathcal{V}\left(u, v\right) = \int_{-\infty}^{\infty} \int_{-\infty}^{\infty} \frac{A_N\left(l, m\right) I\left(l, m\right)}{\sqrt{1 - l^2 - m^2}} e^{-2\pi i (ul + vm)} \mathrm{d}l \, \mathrm{d}m, \tag{3.10}$$

with $A_N\left(l, m\right)$ being the normalized primary beam pattern of the antennas (assumed to be the same for each), and $I\left(l, m\right)$ the source intensity distribution. Infinitesimal terms $\mathrm{d}l$ and $\mathrm{d}m$ in this equation combine to form a solid angle, $\mathrm{d}\Omega = \mathrm{d}l \, \mathrm{d}m / \sqrt{1 - l^2 - m^2}$, such that the power received by each antenna is $P = \int A_N(l, m) I(l, m) \Delta\nu \mathrm{d}\Omega$, where $\Delta\nu$ is the instrumental bandpass (and we make the approximation that A_N is the same across the bandpass).

Modeling in the *uv*-plane avoids issues related to the deconvolution of interferometric data (e.g. heavily correlated image-space noise, the filtering of large spatial scales, and the nonuniform weighting of the signal across the baselines); it also takes full advantage of the knowledge of the exact visibility sampling function as we interpolate the Fourier transformed ICM model to match the *uv*-coordinates of the ACA+ALMA observations. Regarding handling the ALMA+ACA mosaic, we model each pointing individually and correct for the primary beam attenuation per field. The fields are combined at the likelihood level of our routine, adopting a Gaussian likelihood. The implementation uses the static nested sampling method implemented in the `dynesty` package (Speagle, 2020).

Joint likelihood modeling of the ICM via ALMA, ACA, and ACT observations

The remainder of this section will describe how we utilize both types of observations to model the SZ effect over a broad range of spatial scales, how we correct for the different covariances between the various data sets, and how we infer the significance of the modeling via the Bayes factor.

Similar to how we combine the separate pointings in the ALMA and ACA mosaics, we also combine the ALMA+ACA interferometric observations with the ACT maps at the likelihood level. Thus, in every iteration, we model the pressure distribution given a set of parameters, project the model to the *uv*-plane, apply the transfer function for each specific set of observations, and compute the Gaussian log-likelihoods of the ACA+ALMA and the ACT observations individually. We treat the ACT and ACA+ALMA observations as independent when computing the final posterior distribution of the model parameters. This is done by adding the log-likelihoods linearly. Hence, we assume no covariance between the ACA+ALMA observations and the ACT maps. This approximation is justified by the minimal overlap in angular scales probed by the two datasets, shown in Figure 3.2.

Even though the covariance between ACT and ALMA+ACA observations can generally be neglected, there can be covariance between the ACT maps from different frequency–array pairs (see Sec. 3.1.2), particularly since the primary CMB anisotropies—which are a source of noise for us—are present in them all.[4] Turbulence in the atmosphere, which produces a contaminating signal for ground-based CMB observations, as well as instrumental noise, are additional sources of covariance between some combinations of the ACT maps. To account for these sources of covariance, we estimate inter-map covariance matrices using similar procedures to Madhavacheril et al. (2020); we refer the reader to this paper and the references therein for a detailed description. In brief, the covariance matrix is constructed by adding a signal covariance *S* and a noise covariance *N*. Both of these components are obtained empirically, as follows. The noise covariance comes from nonstatic sources in time, like the instrument and the atmosphere. It is calculated by taking the difference of various splits of the data that are interleaved in time so that the static celestial signal is removed, leaving only the nonstatic noise terms behind. The signal covariance includes the contributions from components on the sky not included in our cluster model, including the CMB. Both the signal and noise covariances are estimated from 8

[4] We note that any CMB realization near XLSSC 122 plays a negligible role in the noise budget of the ACA+ALMA observations (< 1 μK) when compared to the instrumental noise and calibration uncertainty of ALMA and ACA.

	Parameter	Prior Type	Min – Max		Parameter	Prior Type	Min – Max
Empirical formalism				*Theoretical-formalism*			
	RA [deg]	Uniform	34.425921 – 34.442521		RA [deg]	Uniform	34.425921 – 34.442521
	Dec [deg]	Uniform	-3.768419 – -3.751819		Dec [deg]	Uniform	-3.768419 – -3.751819
	$M_{500,c}$ [$M_\odot$]	Log-Uniform	$10^{13.4} - 10^{14.6}$		P_0 [keV cm^{-3}]	Uniform	0.0001 – 1.0
	eccentricity	Uniform	0.0 – 1.0		r_s [arcsec]	Uniform	1.1772 – 120.024
	Position angle [deg]	Uniform	-90.0 – 90.0		eccentricity	Uniform	0.0 – 1.0
	z	Gaussian	1.977 – 1.979		Position angle [deg]	Uniform	-90.0 90.0
	$\alpha_{\rm ACA,B3}$	Gaussian	0.95 – 1.00		α	Uniform	0.5–10.0
	$\alpha_{\rm ALMA,B3}$	Gaussian	0.95 – 1.00		β	Uniform	0.5–10
Point Source					γ	Uniform	-1.0 – 5.0
	RA [deg]	Uniform	34.42588105 – 34.45717415		z	Gaussian	1.977 – 1.979
	Dec [deg]	Uniform	-3.7905406 – -3.7377484		$\alpha_{\rm ACA,B3}$	Gaussian	0.95 – 1.00
	Amplitude [Jy]	Uniform	0.0 – 1.0		$\alpha_{\rm ALMA,B3}$	Gaussian	0.95 – 1.00
	Spectral slope	Uniform	-5.0 – 10				
	$\alpha_{\rm ACA,B3}$	Gaussian	0.95 – 1.00				
	$\alpha_{\rm ALMA,B3}$	Gaussian	0.95 – 1.05				
	$\alpha_{\rm ALMA,B4}$	Gaussian	0.95 – 1.05				

Table 3.1: Priors used for the forwarded modeling. In the case of a Gaussian prior, we report the range at a $\pm 1\sigma$–level.

patches of the sky adjacent to the field containing XLSSC 122. We assume that both the signal and noise covariances are stationary such that we can calculate the ACT likelihood in Fourier space where the covariance matrices are diagonal.

Furthermore, in our modeling, we mainly use flat priors except for the calibration and redshift uncertainty parameters which we marginalize over. Table 3.1 provides an overview of the priors used in our modeling. As we use a nested sampling implementation, we explore the entire prior volume. Hence, we compute the Bayesian evidence with a simple quadratic integration scheme using trapezoids over the initial samples (see Speagle, 2020, for more details), thus enabling a tool for fair model comparison. Sampling of the posterior distribution continues until the log difference of the Bayesian evidence is less than an arbitrary threshold, in our case set to $\Delta \ln \mathcal{B} = 0.01$. In this work, we normalize the Bayesian evidence by the evidence of a null model to compute the Bayes factor $\mathcal{Z}$. The null evidence is computed by estimating the Gaussian likelihood when the model is set to zero while maintaining the same prior volume. When assuming a multivariate normal distribution for the posterior probability distribution, the Bayes factor can be expressed in terms of σ through[5]

$$\sigma = \mathrm{sgn}\left(\Delta \ln \mathcal{Z}\right) \sqrt{2 \times \left|\Delta \ln \mathcal{Z}\right|} \,. \tag{3.11}$$

3.3 Interloper and cluster member removal

As the SZ effect in our observations is manifested as a decrement, we must account for any emission that would infill the signal. Such emission could arise from background sources, cluster

[5]Assuming that the posterior probability distribution follows a multivariate normal distribution, the process of likelihood marginalization needed to derive the Bayesian evidence is analogous to calculating the cumulative probability function of the underlying normal distribution. When flat priors are applied, this can be readily adjusted by introducing an analytical truncation to the likelihood function. Consequently, it becomes possible to represent the Bayesian evidence as a linear combination of scaled error functions.

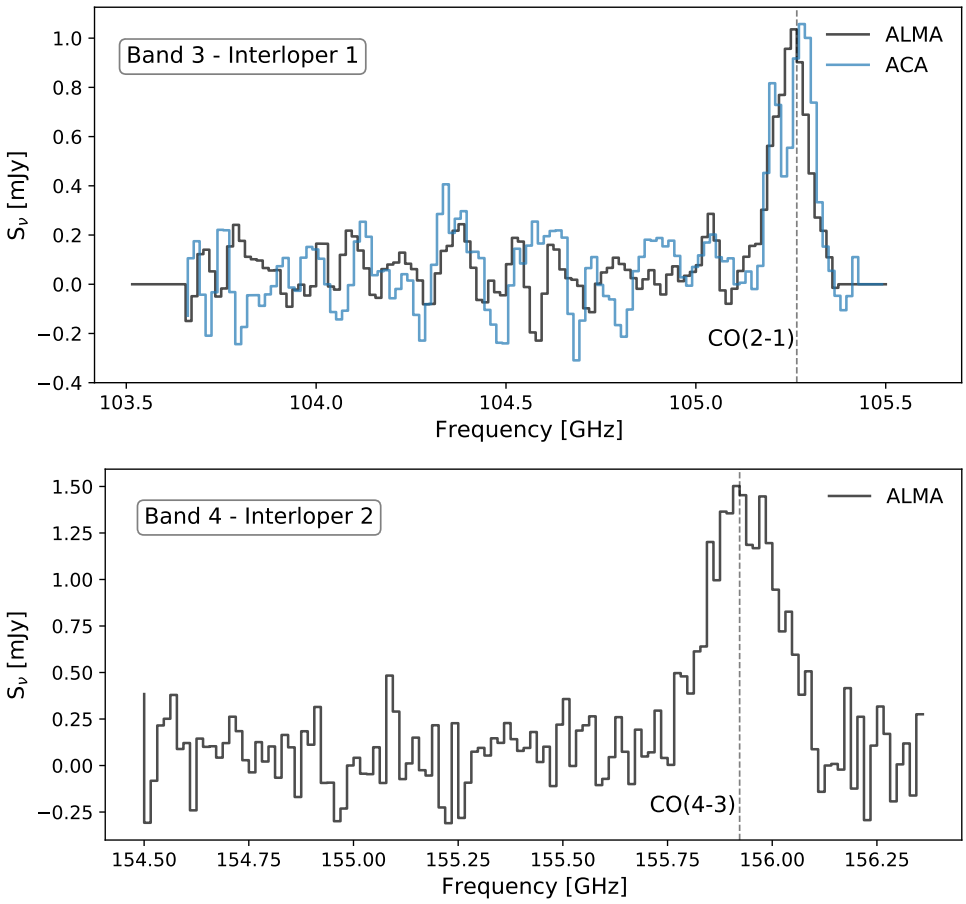

Figure 3.4: Emission lines in the ALMA and ACA observations obtained from a single beam. One in Band 3 and the other in Band 4 at (RA, Dec) coordinates ($2°17'42\overset{''}{.}8101, -3°45'31\overset{''}{.}062$) and ($2°17'41\overset{''}{.}2573$, $-3°45'31\overset{''}{.}799$) respectively. The line emission comes from two galaxies at $z = 1.19$ and z=1.96 which are also detected in optical broadband images.

members, and foreground interlopers such as active galactic nuclei (AGNs) or dusty star-forming galaxies observed at lower redshifts (see e.g., Sayers et al., 2013, 2019, Dicker et al., 2021). Hence, we simultaneously model the extended SZ effect jointly with the more compact sources. Unresolved, compact sources are modeled using point-like (Dirac delta) emission models with a first-order polynomial to describe their spectral behavior. Often, the contaminating source is orders of magnitude brighter than the extended signal from the ICM (unlike the case for XLSSC 122). Therefore, the characterization of the ICM (for instance, the inner slope, γ in Eq. (3.2)) could depend on how the unwanted continuum emission is subtracted from the data. By modeling both the SZ effect and contaminating sources, we have a better handle on removing contamination through Bayesian inference.

At two locations in the ALMA and ACA image, we find evidence for bright spectral line emission, as shown in Figure 3.4. One line is found in Band 3 and the other in Band 4 at an RA and Dec ($2°17'42\overset{''}{.}8101, -3°45'31\overset{''}{.}062$) and ($2°17'41\overset{''}{.}2573, -3°45'31\overset{''}{.}799$) respectively. The

lines correspond to two galaxies at $z = 1.19$ and z=1.96 and are co-spatial with galaxies detected in the optical broad-band images. The galaxies are bright enough to show as point sources in the continuum maps (e.g., see Fig. 3.1). Hence, we removed the higher-frequency half of the corresponding spectral window before continuum modeling the pressure distribution of the ICM.

Furthermore, we detect line emission from two cluster members by visually inspecting the channel maps at the location of their optical counterparts. These sources, however, are too faint to be detected in the continuum image.[6] Hence, these lines represent a negligible contribution to the modeling. Finally, we find no radio source in surveys such as the Very Large Array Sky Survey (VLASS, Lacy et al. 2020) within our field of view, including the brightest cluster galaxy (BCG).

With the removal of the bright emission lines, we find no further $> 4\sigma$-bright point sources in the ALMA+ACA Band 3 continuum maps (e.g., see Fig. 3.3). However, we find a 21σ point source continuum detection in the ALMA Band 4 observations at the location of the bright emission line seen in the Band 3 observations ($2^\circ17'42\farcs8101, -3^\circ45'31\farcs062$). Thus, we utilize Band 4 data to broaden the spectral coverage and remove the dust-continuum emission originating from this interfering source. We did this by modeling the point source using both ALMA Band 3 and 4 observations. We note that this point source is located just beyond r_{500} and is undetected ($< 2\sigma$) in the ACA+ALMA Band 3 map. Nevertheless, we subtracted the model from the observations before modeling the SZ signal, which is described in the next section.

Finally, we ran a point source search with our forward modeling routine using both the ALMA+ACA Band 3 and ALMA Band 4 observations with a lower *uv*-cut of 11 kλ to exclude extended emission. We model any possible emission features with a point source which is described by seven parameters, namely: RA, Dec, Amplitude, spectral slope, and the three calibration uncertainty parameters of the observations. Other than the earlier mentioned two bright sources, we found no other region with a significant detection in the posterior distribution of the modeled parameters, indicating that no further point source contamination is present in the data set, including the sources for which we found tentative line emission in the channel maps. So, by adding the high-resolution ALMA+ACA observations, we find that XLSSC 122 is not significantly contaminated. The only contaminating source present is off-center and can be considered point-like.

3.4 Single component ICM modeling

Here we present our general results regarding the pressure profile modeling. Our baseline assumption is that the surface brightness distribution is well-described by one component, and hence the pressure distribution of the ICM is modeled with a single profile. For this, we will model using both the empirical and theoretical formalism. To assess the impact of adding data from a single-dish telescope to the forward-modeling routine, we first model the ICM using ALMA and ACA observations only. These results are given in Section 3.4.1. The results regarding the joint modeling to the ALMA+ACA+ACT observations are provided in Section 3.4.2. The

[6] We perform additional binning along the frequency axes into a single-frequency bin to decrease computation time while minimizing the *uv*-coverage loss.

ALMA+ACA: Single theoretical-model posterior values

Model Type	$\lvert\Delta \ln\mathcal{Z}\rvert$	$\sigma_{\rm eff}^{\dagger}$	ΔRA	ΔDec	P_0	$r_{\rm s}$	e	PA	α	β	γ
–	–	–	[″]	[″]	[keV cm^{-3}]	[°]	-	[°]	–	–	–
gNFW	59.9	10.9	$-0.5^{+0.9}_{-0.9}$	$11.0^{+1.2}_{-1.2}$	$0.07^{+0.02}_{-0.02}$	$0.011^{+0.003}_{-0.002}$	0.00	0.0	1.0510	5.4905	0.3081
gNFW	59.8	10.9	$-0.9^{+1.0}_{-1.0}$	$10.7^{+1.2}_{-1.2}$	$0.48^{+0.31}_{-0.29}$	$0.007^{+0.002}_{-0.001}$	0.00	0.0	1.0510	5.4905	$-0.51^{+0.44}_{-0.29}$
gNFW	59.5	10.9	$-0.9^{+0.9}_{-1.0}$	$10.7^{+1.2}_{-1.2}$	$0.43^{+0.34}_{-0.26}$	$0.010^{+0.004}_{-0.004}$	0.00	0.0	1.0510	$7.1^{+1.9}_{-2.5}$	$-0.44^{+0.42}_{-0.30}$
gNFW	57.7	10.7	$-0.8^{+1.0}_{-1.0}$	$10.7^{+1.4}_{-1.2}$	$0.18^{+0.38}_{-0.13}$	$0.008^{+0.008}_{-0.004}$	0.00	0.0	$1.3^{+2.1}_{-0.4}$	$5.8^{+2.5}_{-3.0}$	$-0.17^{+0.53}_{-0.42}$
gNFW	62.0	11.1	$-0.4^{+0.8}_{-0.8}$	$10.9^{+1.3}_{-1.3}$	$0.11^{+0.04}_{-0.03}$	$0.014^{+0.003}_{-0.002}$	$0.52^{+0.12}_{-0.15}$	-0.0^{+10}_{-10}	1.0510	5.4905	0.3081
gNFW	60.7	11.0	$-0.8^{+0.9}_{-1.0}$	$10.7^{+1.3}_{-1.4}$	$0.39^{+0.36}_{-0.22}$	$0.009^{+0.003}_{-0.002}$	$0.51^{+0.13}_{-0.16}$	-1.0^{+11}_{-11}	1.0510	5.4905	$-0.25^{+0.39}_{-0.35}$
gNFW	60.8	11.0	$-0.8^{+0.9}_{-1.0}$	$10.6^{+1.4}_{-1.3}$	$0.42^{+0.34}_{-0.24}$	$0.013^{+0.005}_{-0.005}$	$0.50^{+0.12}_{-0.16}$	-1.5^{+11}_{-11}	1.0510	$7.2^{+1.8}_{-2.4}$	$-0.28^{+0.37}_{-0.31}$
gNFW	59.5	10.9	$-0.9^{+0.9}_{-0.9}$	$10.5^{+1.3}_{-1.4}$	$0.17^{+0.28}_{-0.10}$	$0.007^{+0.007}_{-0.003}$	$0.52^{+0.12}_{-0.16}$	-3.0^{+11}_{-11}	$1.8^{+3.5}_{-0.80}$	$5.1^{+2.9}_{-2.7}$	$-0.11^{+0.56}_{-0.48}$

ALMA+ACA: Single empirical-model posterior values

Model Type	$\lvert\Delta \ln\mathcal{Z}\rvert$	$\sigma_{\rm eff}^{\dagger}$	ΔRA	ΔDec	log $M_{500,\rm c}$	e	PA	α	β	γ
–	–	–	[″]	[″]	[M$_\odot$]	–	[°]	–	–	–
A10-UPP	62.3	11.2	$-0.3^{+0.8}_{-0.9}$	$11.0^{+1.3}_{-1.2}$	$14.01^{+0.03}_{-0.03}$	0.00	0.00	1.0510	5.4905	0.3081
A10-MD	62.6	11.2	$-0.8^{+1.0}_{-1.0}$	$11.0^{+1.3}_{-1.3}$	$14.00^{+0.04}_{-0.04}$	0.00	0.00	1.4063	5.4905	0.3798
A10-CC	59.5	10.9	$0.2^{+0.9}_{-0.9}$	$10.9^{+1.5}_{-1.4}$	$13.87^{+0.03}_{-0.04}$	0.00	0.00	1.2223	5.4905	0.7736
M14-UPP	62.5	11.2	$-1.1^{+1.0}_{-1.0}$	$10.7^{+1.3}_{-1.3}$	$14.12^{+0.04}_{-0.04}$	0.00	0.00	2.2700	3.4800	0.1500
M14-MD	62.3	11.2	$-1.2^{+1.0}_{-1.0}$	$10.9^{+1.4}_{-1.3}$	$14.10^{+0.04}_{-0.04}$	0.00	0.00	1.7000	5.7400	0.0500
M14-CC	62.7	11.2	$-0.9^{+1.0}_{-1.0}$	$10.7^{+1.3}_{-1.3}$	$14.11^{+0.04}_{-0.04}$	0.00	0.00	2.3000	3.3400	0.2100
A10-UPP	63.8	11.3	$-0.3^{+0.8}_{-0.8}$	$10.9^{+1.2}_{-1.3}$	$14.17^{+0.10}_{-0.09}$	$0.49^{+0.14}_{-0.18}$	-1.6^{+18}_{-12}	1.0510	5.4905	0.3081
A10-MD	64.3	11.3	$-0.8^{+0.9}_{-0.9}$	$10.9^{+1.4}_{-1.4}$	$14.17^{+0.10}_{-0.09}$	$0.47^{+0.13}_{-0.17}$	0.4^{+16}_{-17}	1.4063	5.4905	0.3798
A10-CC	61.5	11.1	$0.2^{+0.7}_{-0.7}$	$11.0^{+1.3}_{-1.3}$	$14.13^{+0.12}_{-0.12}$	$0.57^{+0.12}_{-0.17}$	-4.3^{+10}_{-17}	1.2223	5.4905	0.7736
M14-UPP	64.1	11.3	$-1.1^{+0.9}_{-0.9}$	$10.6^{+1.3}_{-1.4}$	$14.30^{+0.10}_{-0.09}$	$0.47^{+0.13}_{-0.16}$	-1.3^{+11}_{-11}	2.2700	3.4800	0.1500
M14-MD	64.0	11.3	$-1.3^{+0.9}_{-0.9}$	$10.7^{+1.4}_{-1.4}$	$14.29^{+0.10}_{-0.09}$	$0.48^{+0.12}_{-0.16}$	-0.8^{+10}_{-10}	1.7000	5.7400	0.0500
M14-CC	64.4	11.4	$-1.0^{+0.9}_{-0.9}$	$10.5^{+1.3}_{-1.3}$	$14.29^{+0.09}_{-0.09}$	$0.48^{+0.12}_{-0.17}$	-2.1^{+11}_{-11}	2.3000	3.3400	0.2100

Table 3.2: Most likely parameters for a single SZ component, modeled with a gNFW (upper) and the empirical formalism (lower). Every row corresponds to a unique run in which we varied the parameters that are listed with uncertainties. The uncertainties on the derived parameters are given as the 16th and 84th quantiles. Corner plots of these runs are shown in the supplementary material. The coordinate centers ΔRA and ΔDec are given with respect to the BCG, which is located at an RA and Dec of $2^\circ17'44\farcs2128$, $-3^\circ45'31\farcs68$. † The effective significance is computed via Eq. (3.11).

latter section also discusses how adding zerospacing information changes the derived posterior distributions of the modeled parameters.

3.4.1 ALMA+ACA modeling

Table 3.2 presents the most likely parameters derived from the nested sampling routine for both formalisms. Because of the complex degeneracies between the different model parameters (especially in the case of the theoretical model), the error on the derived parameters is asymmetric. The posterior distributions of all model runs are shown in the supplementary material. In Table 3.2, the parameters which are unfrozen and hence modeled are indicated with error bars. The frozen parameters are set to the shape parameters for the A10 universal pressure profile (A10-

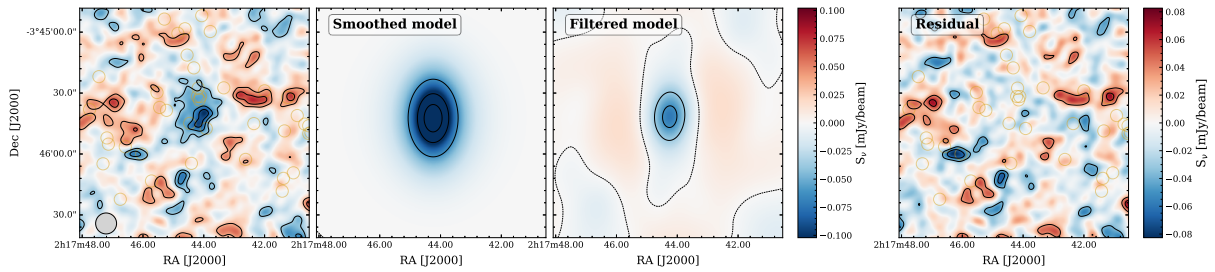

Figure 3.5: Most likely model from the theoretical formalism (based on the Bayes factor, row 5) of Table 3.2. In the left panel, we show the dirty image of the joined ACA+ALMA observations. The second panel is the likelihood-weighted model reconstruction from the nested sampling routine. The third panel shows the model corrected for the incomplete *uv*-coverage of the observations. On the right, we show the residuals by subtracting the model from the observed visibilities. The black contours are drawn at $[-4.5, -3.5, -2.5, -1.5, 1.5, 2.5, 3.5]-\sigma$ based on the noise in the residual map. The third panel also includes the 0σ level. The contours in the second panel are drawn at $[-6.5, -4.5, -2.5, 2.5, 3.5]-\sigma$. The model shows a clear resemblance to the data.

UPP) in the case of the theoretical formalism. For the empirical formalism runs, we froze the shape parameters to the averaged values found for the three different cluster classifications in Arnaud et al. (2010) and McDonald et al. (2014). The results on the theoretical formalism and the empirical formalism are provided in Sections 3.4.1 & 3.4.1, respectively. For all runs, we marginalized over the calibration and redshift uncertainties. All priors are given in Table 3.1.

The second column in Table 3.2 shows the Bayes factor $\mathcal{Z}$ which is the Bayesian evidence normalized by the evidence for the null model. Using Equation (3.11), we can conclude that we detect the SZ effect at $\sim 10.9 - 11.2\sigma$ in the ACA+ALMA data, depending on the model. In the next two sections, we will go into more depth on the results shown in Table 3.2.

The theoretical formalism

When modeling with the theoretical formalism (shown at the top of Table 3.2), we unfreeze the shape parameters one by one, thus systematically increasing the prior volume; as we do so, $|\Delta \ln \mathcal{Z}|$ systematically decreases (rows 1-4 in Table 3.2). Thus we conclude, via the Bayesian evidence, that we cannot robustly differentiate between runs that are modeled with more complexity (more unfrozen parameters) and the more simplistic ones because of the loss of large-scale information in the interferometric observations. This filtering removes the spatial scales which are sensitive to the total flux of the system and to the shape of the pressure profile in the outer regions, namely the β-parameter.[7] As the integrated pressure along the line of sight is degenerate with β, it becomes difficult to constrain the normalization of the profile and thus fit for P when β is unfrozen. This is especially clear when modeling with the empirical-model implementation

[7]We note that this is not due to a radial dependence of the filtering effect but rather due to the fact that the radial trend of the pressure profile in cluster outskirts is generally too shallow (i.e., described mostly by large-scale modes). Any small-scale feature in the outer regions with an extent matching the range of scales probed by ALMA would still be observed.

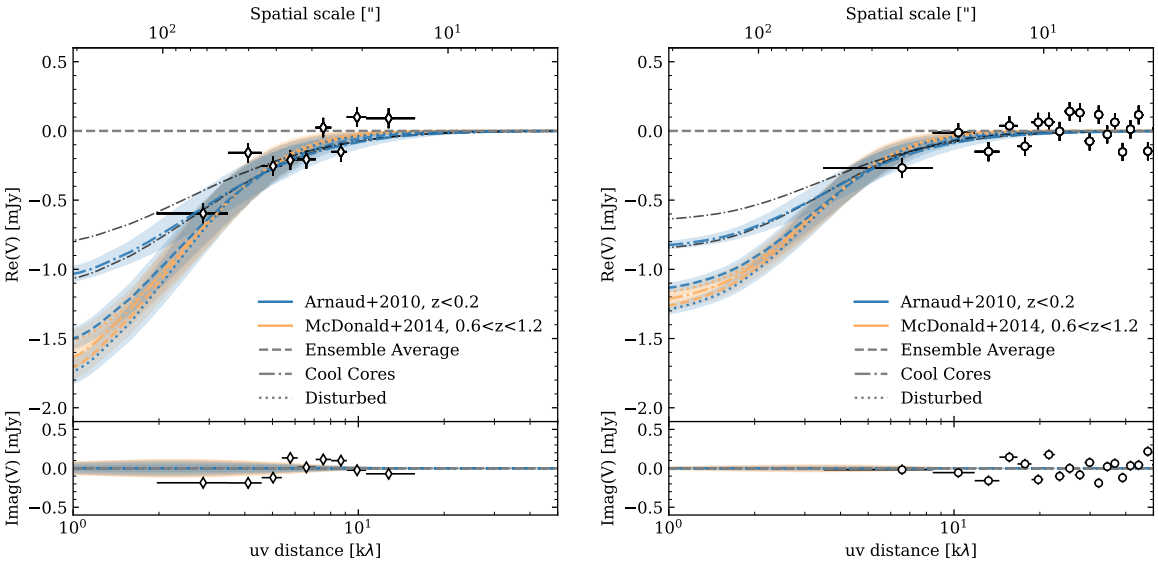

Figure 3.6: *uv*-radial distributions of the Band 3 ACA (left) and ALMA (right) observations in which the visibilities are phase-shifted to the center of the SZ decrement. The colored lines show the median primary beam-attenuated elliptical SZ models based on the empirical formalism which are reported in Table 3.2. The shaded regions indicate the standard deviation in the *uv*-radial bin of the model and are thus a direct consequence of the eccentricity of the cluster. To gauge the uncertainty, we show the 0.16-0.84 quantiles of the mean A10-cc profile with the gray dash-dotted lines. The divergence of the A10-CC profile from the rest of the models and the introduction of eccentricity to the modeling of the SZ signal shows that the data disfavors a local cool core cluster as the morphological state of XLSSC 122. Other classifications cannot be separated because of the limited capabilities of ALMA+ACA in constraining fluxes at scales larger than about $2\farcm0$ ($\sim 1\ k\lambda$).

described in the next section. However, in these single component fits, we do find overall higher evidence for elliptical models with an axis ratio of $\sim 50\%$ elongated nearly along the north-south axis.

Figure 3.5 shows the most likely model, based on the Bayesian evidence shown in Table 3.2, for the theoretical formalism. The model, shown in the second panel, is made by imaging each sample of the forward-modeling routine and weighting it by its likelihood when averaging them together and illustrates the high eccentricity of the system. The third panel shows the large-scale filtering by the incomplete *uv*-coverage on the images. The residuals in Figure 3.5 are obtained by subtracting the model in the visibility plane from the data. As the residuals indicate a good agreement between the observations and the modeled surface brightness, the base assumption that the bulk of the ICM is composed of a single pressure profile thus holds for this $z \sim 2$ cluster.

The modeling shows a preference for negative to flat γ solutions, indicating a disturbance of the pressure profile in the inner regions of the cluster. However, another plausible explanation for low γ-values would be that the positive continuum emission of the central galaxies balances

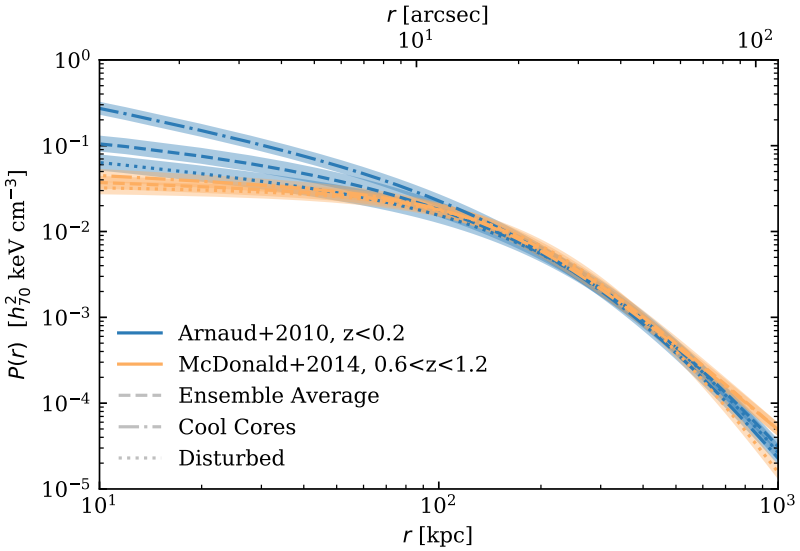

Figure 3.7: Derived radial pressure profiles of the best-fit elliptical models which follow the empirical formalism as shown in Table 3.2. The shape parameters of the A10-model parameters are frozen and set to the six classifications of Arnaud et al. (2010) and McDonald et al. (2014). The uncertainties are derived from the 0.16-0.84 quantiles of the sampled posterior distribution's mass (amplitude) parameter. The uncertainties are thus marginalized over the centroid position, eccentricity, redshift, and calibration uncertainties. These profiles are the image plane variants (Fourier transforms) of the ones shown in Figure 3.6.

the negative surface brightness of the SZ decrement. From the X-ray imaging (see Fig. 3.3), there is a small hint of possible AGN activity as a slight increase in emissions is found at the location of the BCG. However, we do not detect the BCG or any of the central galaxies in the ALMA and ACA data in either the continuum or any of the spectral lines (because of the spectral tuning of the observations). However, Figure 3.3 shows a decrease in the decrement around the central four galaxies, indicating a possible presence of continuum emission from the BCG. To test this, we reran the best-fitting gNFW model (row five in Table 3.2) with an additional point source component frozen at the location of the BCG (based on the HST imaging). We modeled (including the Band 4 data) both the amplitude and spectral slope of the central galaxy. We find that the amplitude of any point source at the location of the BCG is consistent with noise. Then, by resampling the parameter space through the nested sampling routine, we find no significant difference in the derived parameters of the gNFW profile, including the inner slope value, γ, when including a point source component. Through the Bayes factor, we can reject the presence of a point source at the location of the BCG in the ALMA+ACA data by 4.1σ. These results are similar to the findings of Kitayama et al. (2023) on the effect of low S/N contaminating sources when deriving pressure profiles from the SZ effect. Furthermore, the additional point source component did not affect the centroid position of the SZ effect.

ALMA+ACA+ACT: Single theoretical-model posterior values

Model Type	$\lvert\Delta \ln \mathcal{Z}\rvert$	$\sigma_{\rm eff}$	ΔRA	ΔDec	P_0	$r_{\rm s}$	e	PA	α	β	γ
–	–	–	[″]	[″]	[keV cm^{-3}]	[°]	-	[°]	–	–	–
gNFW	117.2	15.3	$-0.2^{+0.9}_{-0.9}$	$11.5^{+1.2}_{-1.2}$	$0.05^{+0.01}_{-0.01}$	$0.017^{+0.002}_{-0.001}$	0.00	0.0	1.0510	5.4905	0.3081
gNFW	115.5	15.2	$-0.1^{+0.9}_{-1.0}$	$11.5^{+1.3}_{-1.3}$	$0.04^{+0.07}_{-0.02}$	$0.018^{+0.005}_{-0.005}$	0.00	0.0	1.0510	5.4905	$0.41^{+0.26}_{-0.39}$
gNFW	115.5	15.2	$-0.2^{+1.0}_{-1.0}$	$11.3^{+1.2}_{-1.2}$	$0.10^{+0.26}_{-0.07}$	$0.009^{+0.010}_{-0.005}$	0.00	0.0	1.0510	$4.0^{+1.5}_{-0.8}$	$0.16^{+0.39}_{-0.66}$
gNFW	114.2	15.1	$-0.2^{+1.0}_{-1.0}$	$11.5^{+1.2}_{-1.2}$	$0.34^{+0.53}_{-0.25}$	$0.002^{+0.008}_{-0.001}$	0.00	0.0	$0.7^{+0.1}_{-0.1}$	$5.8^{+1.1}_{-1.0}$	$-0.01^{+0.37}_{-0.30}$
gNFW	118.8	15.4	$-0.3^{+0.9}_{-0.9}$	$11.3^{+1.3}_{-1.3}$	$0.06^{+0.01}_{-0.01}$	$0.020^{+0.002}_{-0.002}$	$0.47^{+0.12}_{-0.15}$	6^{+10}_{-10}	1.0510	5.4905	0.3081
gNFW	117.2	15.3	$-0.2^{+0.9}_{-0.9}$	$11.3^{+1.3}_{-1.3}$	$0.05^{+0.07}_{-0.02}$	$0.022^{+0.006}_{-0.006}$	$0.49^{+0.11}_{-0.14}$	6^{+10}_{-09}	1.0510	5.4905	$0.43^{+0.22}_{-0.35}$

ALMA+ACA+ACT: Single empirical-model posterior values

Model Type	$\lvert\Delta \ln \mathcal{Z}\rvert$	$\sigma_{\rm eff}$	ΔRA	ΔDec	log $M_{500,\rm c}$	e	PA	α	β	γ
–	–	–	[″]	[″]	[M$_\odot$]	–	[°]	–	–	–
A10-UPP	111.2	14.9	$-0.1^{+0.7}_{-0.8}$	$10.9^{+1.1}_{-1.1}$	$14.09^{+0.02}_{-0.02}$	0.00	0.00	1.0510	5.4905	0.3081
A10-MD	114.6	15.1	$-0.4^{+0.9}_{-0.8}$	$11.2^{+1.2}_{-1.2}$	$14.09^{+0.02}_{-0.03}$	0.00	0.00	1.4063	5.4905	0.3798
A10-CC	94.7	13.8	$0.6^{+0.8}_{-0.8}$	$10.1^{+1.1}_{-1.3}$	$13.98^{+0.03}_{-0.03}$	0.00	0.00	1.2223	5.4905	0.7736
M14-UPP	114.9	15.2	$-0.8^{+0.9}_{-0.9}$	$10.9^{+1.2}_{-1.1}$	$14.21^{+0.02}_{-0.03}$	0.00	0.00	2.2700	3.4800	0.1500
M14-MD	109.9	14.8	$-1.0^{+0.9}_{-0.9}$	$11.2^{+1.2}_{-1.3}$	$14.21^{+0.03}_{-0.03}$	0.00	0.00	1.7000	5.7400	0.0500
M14-CC	114.0	15.1	$-0.6^{+0.9}_{-0.9}$	$10.7^{+1.1}_{-1.2}$	$14.21^{+0.03}_{-0.03}$	0.00	0.00	2.3000	3.3400	0.2100
A10-UPP	110.9	14.9	$-0.0^{+0.8}_{-0.7}$	$10.7^{+1.1}_{-1.2}$	$14.18^{+0.08}_{-0.06}$	$0.32^{+0.18}_{-0.19}$	-2^{+13}_{-14}	1.0510	5.4905	0.3081
A10-MD	115.7	15.2	$-0.4^{+0.8}_{-0.7}$	$11.0^{+1.2}_{-1.2}$	$14.24^{+0.08}_{-0.08}$	$0.42^{+0.13}_{-0.17}$	1^{+10}_{-10}	1.4063	5.4905	0.3798
A10-CC	99.7	14.1	$0.7^{+0.6}_{-0.7}$	$10.4^{+1.3}_{-1.4}$	$14.37^{+0.11}_{-0.11}$	$0.71^{+0.07}_{-0.10}$	-3^{+5}_{-5}	1.2223	5.4905	0.7736
M14-UPP	116.4	15.3	$-0.8^{+0.8}_{-0.8}$	$10.8^{+1.3}_{-1.2}$	$14.37^{+0.08}_{-0.08}$	$0.45^{+0.12}_{-0.16}$	0^{+9}_{-9}	2.2700	3.4800	0.1500
M14-MD	111.0	14.9	$-1.0^{+0.8}_{-0.9}$	$10.9^{+1.2}_{-1.3}$	$14.35^{+0.08}_{-0.07}$	$0.42^{+0.13}_{-0.16}$	0^{+10}_{-10}	1.7000	5.7400	0.0500
M14-CC	115.8	15.2	$-0.6^{+0.8}_{-0.7}$	$10.6^{+1.2}_{-1.2}$	$14.38^{+0.09}_{-0.08}$	$0.48^{+0.12}_{-0.15}$	-1^{+8}_{-9}	2.3000	3.3400	0.2100

Table 3.3: Similar as Table 3.2 but modeled with ALMA+ACA+ACT observations.

The empirical formalism

For runs with the A10 (empirical) formalism, we did not model any of the shape parameters but set them to the values for each separate classification as described in Arnaud et al. (2010) and McDonald et al. (2014). In the modeling, we freed the centroid, eccentricity, position angle, and mass of the system, which is linked to the amplitude and scale radius of the pressure profile (see section 3.2.1). By freeing up the amplitude parameter, the forward modeling routine automatically corrected for the unequal Y-value of each classification. Hence, we find for the different model classifications a different mass estimate. However, the Bayesian evidence tells us (second column in Table 3.2) that the data cannot distinguish which model type is preferred when the total mass (or the total Compton-Y value) is unknown. Only the pressure profile that corresponds to the averaged local cool-core (A10-CC) profile is disfavored by the data ($\Delta \ln \mathcal{Z} > 2.3$).

When estimating the significance between various models, one cannot simply take the difference between two $\sigma_{\rm eff}$ values reported in the third column of Table 3.2. For example, the significance between the spherical symmetric A10-MD and A10-CC is, $\sigma_{\rm diff} = \sqrt{2 \times (62.3 - 59.5)} = 2.4$, meaning that the spherical A10-MD model is favored by the data with a significance of 2.4σ over the A10-CC one assuming a multivariate normal distribution for the posterior probability distribution, which is only a modest improvement. As the normal distribution is not a perfect fit for the posterior distribution, we can also look at the difference in the Bayes factor for the two

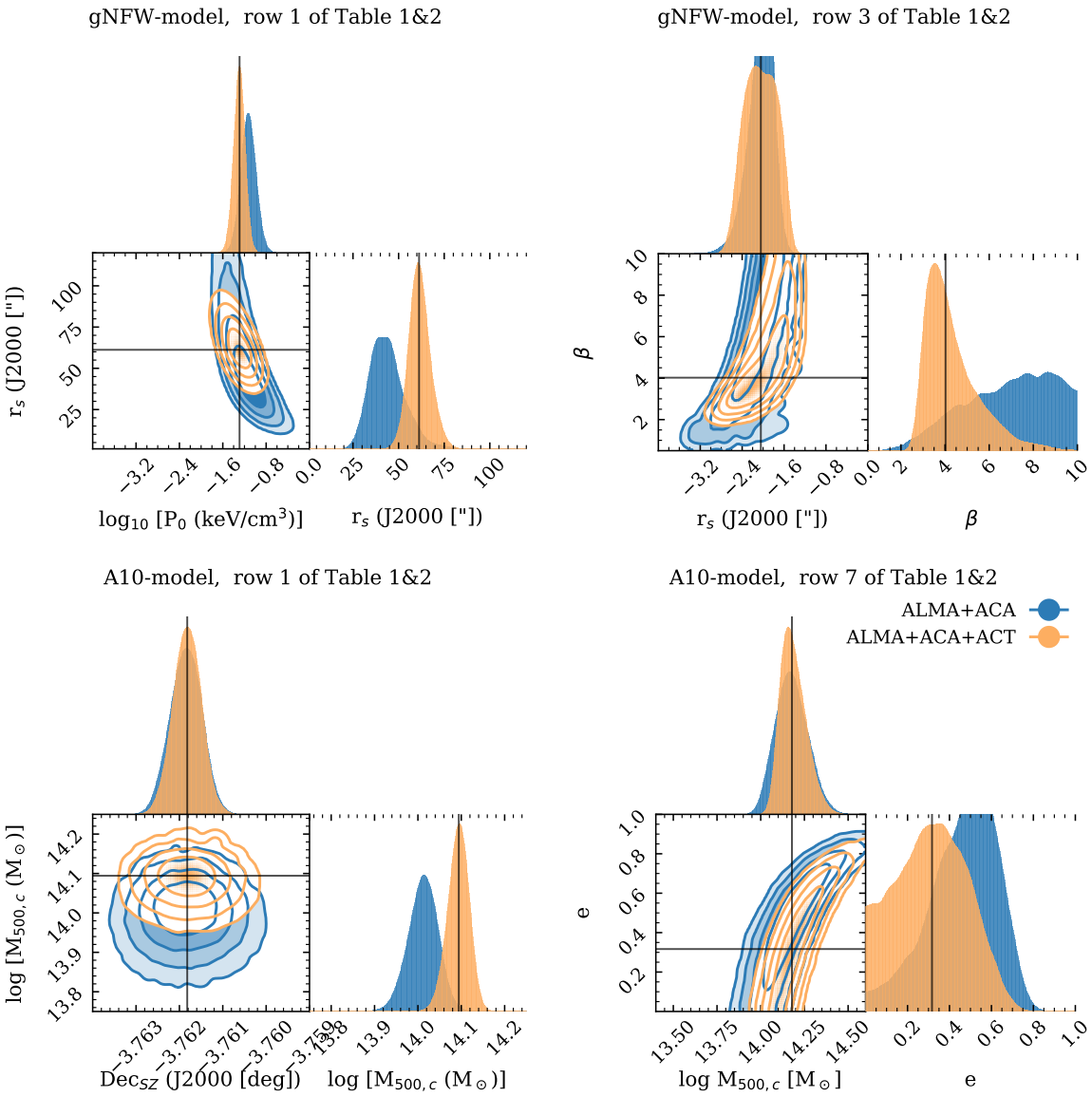

Figure 3.8: Comparison between modeling with ALMA+ACA (blue) and ALMA+ACA+ACT (orange) observations. The full posterior distributions of all runs can be found in the supplementary material. Here we highlight four marginalized posterior distributions to show the effect ACT observations have on the $P_0 - r_s$, $r_s - \beta$, Dec$-M_{500,c}$, and the $M_{500,c} - e$ relationships, shown from left to right, top to bottom. The weighted median values of the ALMA+ACA+ACT runs are highlighted with black lines. For a detailed description of the effect the ACT observations have on the sampled posterior distribution, we refer to the text in section 3.4.2.

classifications: $\Delta \ln \mathcal{Z} = 62.3 - 59.5 = 2.8$, which according to standard Bayesian inference is interpreted as a strong (but not definitive) evidence for preferring the A10-MD model over the A10-CC one (Dittrich et al., 2019). This is consistent with the finding from the theoretical

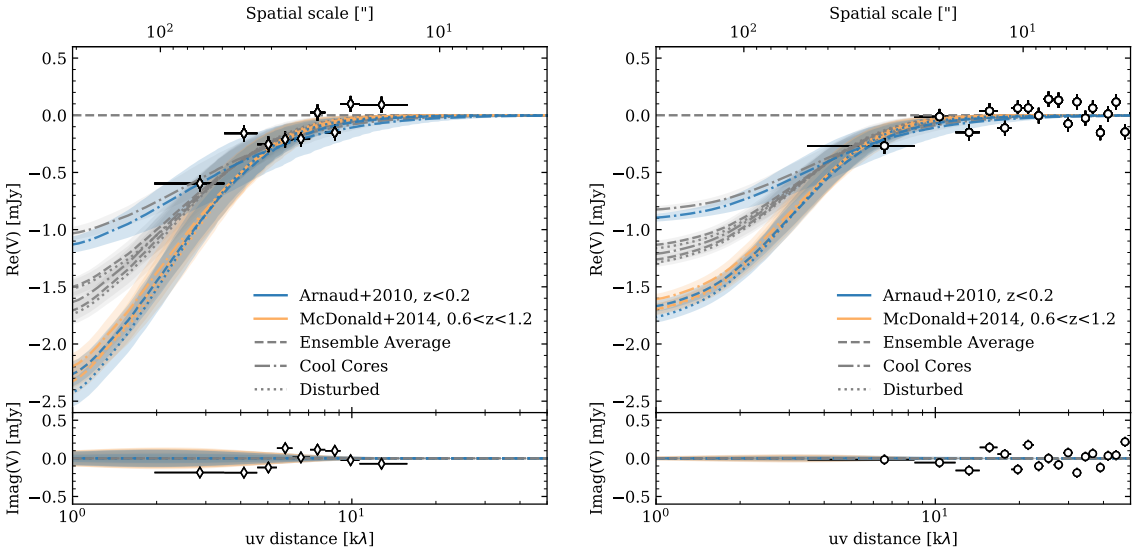

Figure 3.9: Same as Figure 3.6 (also shown here in gray), but including here the additional constraining power of the ACT data in the model fitting. We observe a tighter correlation at smaller *uv*-distances, an overall larger amplitude, and a smaller eccentricity. We note the ACT data are not shown due to the complexity of accurately representing the image space data in this domain.

formalism in the previous section that a small or negative γ solution is mildly preferred by the data.

Furthermore, the lack of short baselines in the ALMA+ACA observations explains why the mass estimates vary between models and why the data do not have a significant preference among the various templates. The latter statement is a consequence of the strong β–P_0 degeneracy which led to the inability to constrain β in the theoretical formalism. Figure 3.6 shows the constraining power of the ACA and ALMA observations together with the median models from Table 3.2 in the Fourier domain, the domain where the likelihood is estimated. Figure 3.6 is made by phase shifting the respective ALMA and ACA pointings to the centroid of the SZ decrement and then radially binning the uv-coordinates in spherically symmetric shells. The radial bins are spaced such that the statistical uncertainty in each bin is equal (i.e., each bin comprises an equal number of visibilities). The error bars show the mean and standard deviation for the real and imaginary parts of the visibilities for the stacked pointings. The ACA mosaic has no field pointing to the center of the mosaic. Therefore, we used the three ACA fields closest and with similar distances to the SZ centroid to combine the visibilities in *uv*-space. Adding other fields at a larger angular separation from the SZ centroid would cause discrepancies regarding the uv radial amplitude because of the primary beam attenuation of the antennas. For the ALMA observations, we show the central field in Figure 3.6. The same operation as done on the data is performed on the primary-beam attenuated SZ models shown in Table 3.2. We note that the modeling is performed on the unbinned two-dimensional visibilities, not these radially binned ones. The shaded regions

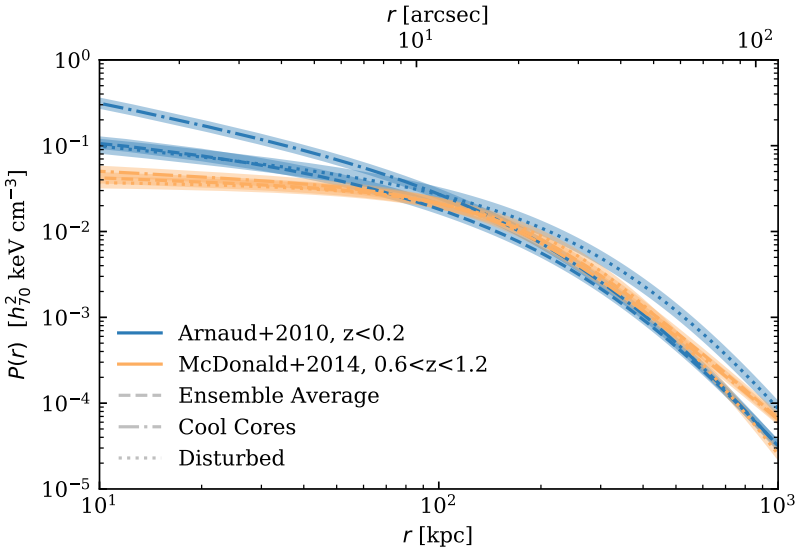

Figure 3.10: Same as Figure 3.7 but with the addition of ACT constraints, as in Figure 3.9.

in Figure 3.6 indicate the standard deviation in the *uv*-radial bin of the model, not the error provided in the posterior distribution, and are thus a direct consequence of the eccentricity of the cluster.

Figure 3.6 makes clear that we cannot distinguish between the different classifications when modeling for the projected eccentricity of the cluster. For intuition's sake, Figure 3.7 shows the image plane variant of Figure 3.6, namely the derived pressure profiles. Here we calculated the uncertainties based on the samples of the nested sampling routine. All in all, one needs to be careful when deriving pressure profiles when the total flux of the system is unknown. Hence, we turn in Section 3.4.2 to provide the results of the ALMA+ACA+ACT modeling.

3.4.2 ALMA+ACA+ACT joint likelihood modeling

By adding single-dish ACT observations, we get an additional constraint on the total flux of XLSSC 122. Even though XLSSC 122 is almost unresolved in ACT, as shown in Figure 3.1, we still propagate the full ICM model to the ACT frequency maps when forward modeling as described in section 3.2.2. The results for both the theoretical and empirical formalism are shown in Table 3.3. In Figure 3.8, we highlight four marginalized posterior distributions to show the effect that adding single-dish ACT observations to the forward-modeling routine has on the derived parameters. The full corner plots of the runs are included in the supplementary material.

Figures 3.9 and 3.10 show the *uv*-radial distributions of the modeled pressure profiles and its image-plane variant. We observe a tighter scatter at smaller *uv*-distances and a smaller eccentricity (also shown in Table 3.3 and the fourth panel of Fig. 3.8). In the ALMA+ACA runs, the eccentricity (defined as one minus the minor over major axis ratio) was, on average, $e = 0.50^{+0.12}_{-0.16}$. With the introduction of the ACT observations, we find that the eccentricity is

driven to lower values with a likelihood-weighted average of $e = 0.46^{+0.12}_{-0.16}$. This makes the eccentricity more consistent with 0, but regardless, Figure 3.8 shows that the modeling still has constraining power on e. Furthermore, the A10-CC profile model is disfavored by the data ($\Delta \ln \mathcal{Z} > 11.2$) and seems to compensate for the higher mass value with a larger minor over major axis ratio. The eccentricity is modeled by squeezing the grid on which the pressure distribution is mapped to the desired extent while assuming a nonzero eccentricity along the line of sight direction. This compression leads to a reduction in the integrated pressure along the line of sight, consequently decreasing the total flux. Hence, the eccentricity is degenerate with the amplitude and β-parameter of the pressure profile creating the wide posterior distribution shown in Figure 3.8.

Furthermore, with the inclusion of the ACT observations, we find higher halo mass estimates ($> 3\sigma$) for the spherically symmetric models, but the significance vanishes when the eccentricity is taken into account with the modeling. We do find systematically tighter uncertainties on the halo mass (by a factor of ~ 1.5) among the different models when modeling only to the ACA+ALMA observations. This is also shown in the third panel of Figure 3.8. This panel indicates that the inclusion of the ACT observations leads to a tighter constraint on $M_{500,c}$ while the centroid of the SZ effect is unaffected by the ACT-observation and driven by the ALMA+ACA observations which probe much smaller scales. Still, the McDonald et al. (2014) profiles consistently estimate higher masses; however, the discrepancy becomes insignificant ($< 2\sigma$) when the eccentricity is included in the modeling.

Furthermore, we still cannot significantly differentiate between the several profile classifications by adding ACT data. This is because of the high-dimensional parameter space, the complex degeneracies, the relatively low S/N in the spatial scales $3 - 10$ kλ of the ACA and ALMA observations, and the similarity between the different profiles. But guided by the Bayesian evidence ($\Delta \ln \mathcal{Z} > 4.7$), we can say that XLSSC 122 is similar to local morphologically disturbed clusters (A10-MD) and the more distant relaxed clusters (M14-UPP and M14-CC). The M14-MD model is disfavored ($\Delta \ln \mathcal{Z} > 4.8$) likely because of the relatively large β value, $\beta = 5.74$. From the ALMA+ACA+ACT modeling with the theoretical formalism, we find consistently lower beta values which is in line with the Bayes factor disfavoring the M14-MD model over the other ones.

Regarding the modeling based on the theoretical formalism, the first point to note is that the two gNFW runs in which we additionally unfroze the parameters γ, β and γ, β, and α for elliptical morphologies both resulted in highly unphysical solutions for the best-fit model parameters. For instance, the eccentricity parameter e converged to extreme values of $e > 0.9$. Similarly, the posterior distribution for the β slope saturated over the lower prior edge, corresponding to $\beta < 2$ and, in turn, to the impossibility of deriving a numerical solution to the line-of-sight pressure integral. Hence, these models are not reported in Table 3.3. For the remaining cases, the introduction of the ACT data significantly mitigated the $P_0 - r_\mathrm{s}$ degeneracy (see the first panel of Fig. 3.8). This translated to tighter constraints on the derived shape parameters of the gNFW-formalism: γ (the inner slope parameter) is now for all runs more consistent with zero and positive values, and the constraints on β (the outer slope parameter) are now consistent with derived values from hybrid analysis of observations and hydrodynamical simulations (Arnaud et al., 2010) and stacked *Chandra* observations (McDonald et al., 2014) while the corner plots from the ACA+ALMA only runs show that β was unconstrained (see the second panel of Fig. 3.8).

3.5 Two component ICM modeling

As the merger rate increases with redshift (Fakhouri et al., 2010) one might expect a more complex morphology of the pressure distribution in the ICM of XLSSC 122 than a single elliptical component. While Figure 3.5 indicates that a single component adequately describes the bulk of the ICM, there are still residual features that show negative deviations at $\sim -3\sigma$. Previous studies have demonstrated that on the occasion of a cluster fly-by or when the system is in a premerger or accretion phase, the pressure distribution can exhibit multiple peaks (see, for instance, Di Mascolo et al. 2021). Hence, these tentative negative features could be attributed to the presence of an infalling group or other kinds of complex morphologies, like filaments.

3.5.1 "Cleaned" image reconstruction

To better highlight possible asymmetric surface brightness distributions, we made a "cleaned" image reconstruction of the previously shown dirty images of XLSSC 122. The use of the clean algorithm has been the de facto standard in radio astronomy for half a century (e.g., Högbom, 1974). However, this routine assumes that the emission distribution is well described by an arbitrary set of point-like or multiscale Gaussian sources. Figure 3.6 directly shows that this assumption is invalid in our case, as our emission distribution is unevenly spread along the baselines and mainly concentrated at the smaller *uv*-distances (i.e., large angular scales). Therefore, we constructed our own deconvolution algorithm. Our routine is more analogous to the image reconstruction techniques used in optical interferometry, in which prior information about the source is exploited to deconvolve the dirty beam pattern from the true sky.

Our routine works as follows: If we assume the signal is well-described by a gNFW profile (instead of a combination of point sources), we can use our forward-modeling technique to find the best-described gNFW profile (think of this as a minor cycle of the deconvolution algorithm) and to subtract this from the visibilities (thus performing only one major cycle). Hence, we do not have an iterative approach but a Bayesian one in which we are guided by the evidence to find the most likely model rather than cleaning to an arbitrary threshold. By subtracting the model from the visibilities, the resulting residual image thus becomes freed of the dirty beam patterns originating from the convolution between the SZ effect and the incomplete *uv*-coverage. Then, similar to clean, we add the imaged residuals (shown on the right panel of Fig. 3.5) to the likelihood-weighted model, which is smoothed with the synthesized beam ($5''$) and attenuated by the primary beam, to create the image reconstruction. Hence, we employ the results of our forward-modeling routine presented above to get a clean-like reconstruction of XLSSC 122.

The deconvolved ACA+ALMA map of XLSSC 122 is shown in Figure 3.11. This image clearly shows two filamentary-like structures in the south which are co-spatial with the negative deviations at $\sim -3\sigma$ shown in the residual map of Figure 3.5.

3.5.2 Modeling asymmetric pressure distributions

After obtaining the cleaned interferometric image, we ran a two-component model to confirm via *uv*-based modeling that these filamentary-like structures are not an imaging artifact. The

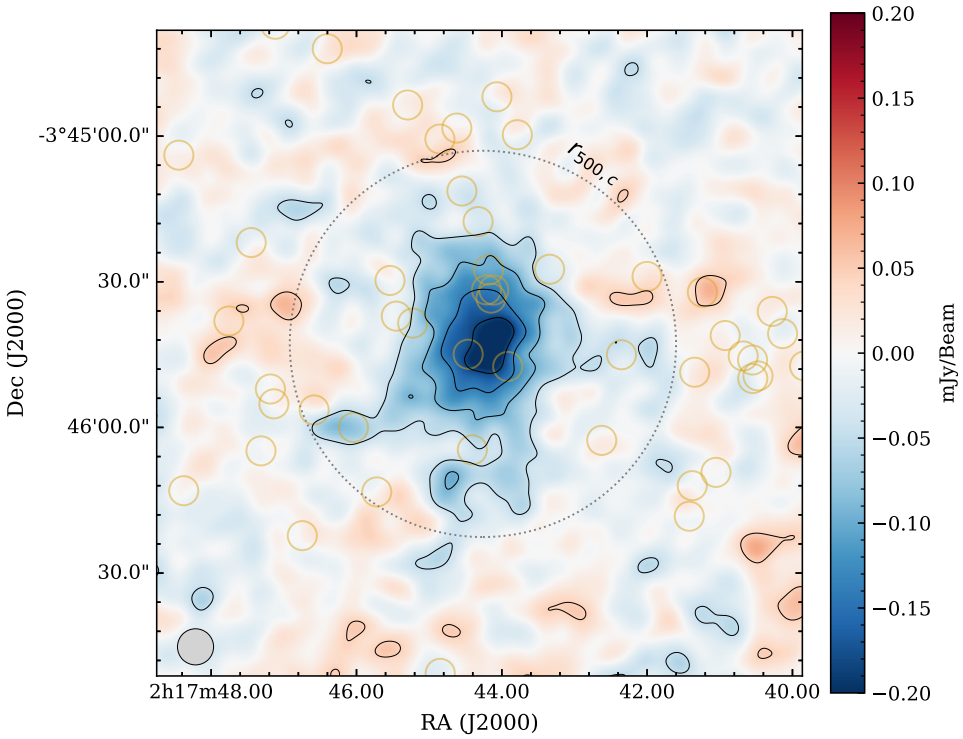

Figure 3.11: "Cleaned" ACA+ALMA image of XLSSC 122. Here we combined the likelihood-weighted reconstructed model of a single elliptical gNFW profile (see row five of Table 3.2), smoothed with the synthesized beam, together with the imaged residuals, computed in the *uv*-plane. Hence, we corrected for the dirty beam patterns visible in Figure 3.5. Contours are drawn from $[-10, -8, -6, -4, -2, 2, 4]-\sigma$ estimated on the residual map shown in Figure 3.5. We overlay the location of the cluster members and indicate $\mathrm{r}_{500,\mathrm{c}}$ centered on the peak of the SZ flux. We observe asymmetric features in the south, potentially indicating a morphological disturbance to the cluster.

empirical formalism is unsuitable for modeling faint elongated filamentary-like structures due to the constraint between the specific radius and the integrated flux. In contrast, the theoretical formalism decouples the specific radius r_s from the amplitude P_0, granting greater modeling flexibility for brighter but thinner surface brightness distributions. Hence, we ran the two-component models only with the theoretical formalism.

We consider both a spherical symmetric profile and one in which we freed the eccentricity. The shape parameters of the gNFW are frozen to the A10-UPP values, similar to what is done in Section 3.4.1. To let each run converge to a single solution, we used an ordered prior on the declinations of the centroids of the two SZ components which enforces that one model component has a declination that is always higher than the other. Similar to the single-component runs, we model the two-component runs twice: first is the likelihood computed with only the ACA+ALMA observations, and then with ACT+ACA+ALMA. Thus, in total, we perform four two-component model runs. The resulting four models are shown in Figure 3.12.

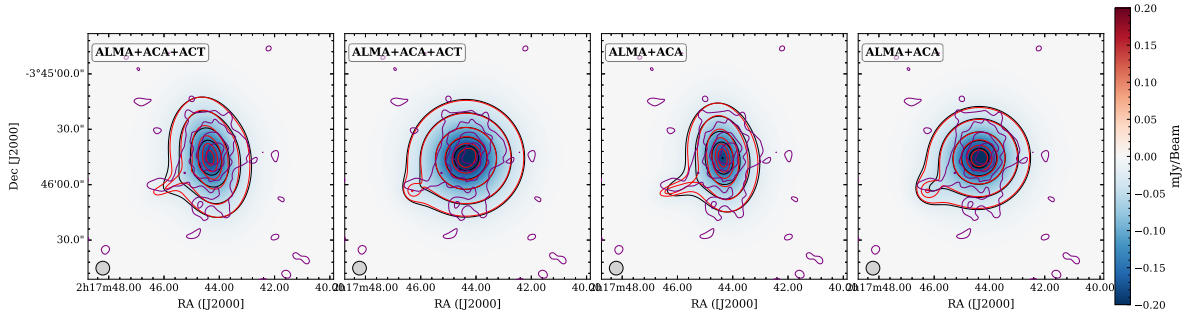

Figure 3.12: Results on the two-component modeling via the theoretical formalism for both the elliptical (columns one and three) and spherically symmetric implementations (columns two and four). Here, the shape parameters of the gNFW are frozen to the A10-UPP values. The first two columns are modeled to ALMA+ACA+ACT observations and the last two only to ALMA+ACA. In red, we show the unsmoothed model reconstruction. The color map and black contours are the same reconstruction but smoothed with $5''$ Gaussian taper to match the observations. The contours are drawn at the same levels in Figure 3.11. In purple, we show the contours of Figure 3.11. This figure indicates that the two-elliptical SZ components better resembles the surface brightness distribution of XLSSC 122 than the spherical one.

Regarding the ACA+ALMA-only modeling, both the spherically symmetric and elliptical models show in the likelihood-weighted image an extended feature along the southeastern filament (see the right two panels of Figure 3.12). For the spherically symmetric model, we observe an improvement of the Bayesian evidence of $|\Delta \ln \mathcal{Z}| = 62.3$ relative to the symmetrical one-component fit. For the elliptical one, we find $|\Delta \ln \mathcal{Z}| = 68.6$. The latter translates to a Bayesian evidence difference of 6.6 with respect to the best single elliptical gNFW model, indicating a tentative 3.6σ detection of the second component (see Eq. 3.11). A $\Delta \ln \mathcal{Z} = 6.6$ is considered as decisive evidence (Dittrich et al., 2019).

The likelihood-weighted model reconstructions of the ACT+ACA+ALMA runs are shown in the first two panels of Figure 3.12. When modeling with the additional ACT observations, only the elliptical implementation clearly shows the asymmetric feature along the southeastern direction. From the Bayesian evidence, we find $\Delta|\ln \mathcal{Z}| = 116.8$ and $\Delta|\ln \mathcal{Z}| = 121.8$, which corresponds to a difference of -0.4 and 3.0 (with the latter equivalent to a tentative 2.4σ preference) when compared with their respective single component gNFW model for the spherical and elliptical implementations. This implies that the observations require some degree of elongation in both the north-south and the cross-diagonal orientation. The absence of a secondary component in the spherically symmetric two-component ALMA+ACA+ACT run, as opposed to the ALMA+ACA run, and the lower significance of the ALMA+ACA+ACT run with respect to the ALMA+ACA run can be attributed to the flux constraint imposed by the ACT observations on the overall system. The ALMA+ACA observations lack short-baseline information, providing greater maneuverability for the model as demonstrated in Figure 3.12 where the integrated flux in the spherical symmetric ALMA+ACA run is larger when compared to the other.

Regarding the eccentricity, the modeling done on both the ACA+ALMA and ACA+ALMA+ACT

observations imply an eccentricity for the smaller component of ~ 0.8. This is extreme; however, the cause is most likely because of the model choice. Currently, there are no accurate models to describe these filamentary-like structures which were computationally feasible. However, to overcome a possible mismatch between the model implementation (a very eccentric gNFW profile) and the tentative filamentary-like structure, we weighted each sample of the nested sampling routine with its likelihood and computed the weighted average, which is the same as marginalizing over the posterior distribution. Then, we take into account all the complex degeneracies seen in the posterior distribution. Figure 3.12 shows each of the marginalized two-component gNFW models. By marginalizing over the posterior distribution, we get a smoother model which closely resembles the cleaned image, as indicated in Figure 3.12 where we plot the contours from the cleaned image reconstruction (see Fig. 3.11) on top of the models. We find that the southern filament is part of the bulk of the ICM, while the southeastern elongated structure is best described by the secondary, smaller component. The integrated flux of the secondary component is roughly twice as faint as the bulk of the ICM, and the projected centroids are separated by $\approx 33''$.

3.6 Mass estimates

Figure 3.13 shows an overview of halo masses ($M_{500,c}$) of XLSSC 122. Our SZ mass is calculated by taking the evidence-weighted average of the mass estimates from the empirical formalism runs utilizing ALMA+ACA+ACT observations as shown in Table 3.3, and is equal to $M_{500,c} = 1.66^{+0.23}_{-0.20} \times 10^{14}\ \mathrm{M}_{\odot}$. Here, we make use of local scaling relations from Arnaud et al. (2010) to convert $Y_{500,c}$ to an SZ-derived halo mass, as robust scalings derived from high$-z$ clusters do not exist.

The halo masses of XLSSC 122 from Mantz et al. (2018) are derived from X-ray imaging (*Chandra*) and CARMA measurements. First, the X-ray derived halo mass reported by Mantz et al. (2018) was obtained by integrating their radial density profile while using an X-ray spectroscopic temperature of $kT = 5.0$ keV and adopting a gas mass fraction of $f_{\rm gas}(r_{500,c}) = 0.125$. We made an independent estimate of the halo mass using these same data based on the $M_{500,c} - T_{\rm X}$ relationship of Vikhlinin et al. (2009). Adopting the temperate of $T_{\rm X} = 5.0 \pm 0.7$ keV, we obtain $\log_{10}(M_{500,c}\,[\,M_{\odot}]) = 14.19^{+0.09}_{-0.10}$ (also shown, in red, in Fig. 3.13). The errors are propagated from the temperature information and do not include any systematics. We note that this mass estimate is much more in line with the SZ-derived halo mass than converting the X-ray-derived gas mass to a halo mass as done by Mantz et al. (2018).

Further, we converted the $Y_{500,c}$ estimate from Mantz et al. (2018) – which was obtained by fitting an A10-UPP model to their CARMA observations – using the same methodology employed for our mass estimates; that result is shown as "CARMA 30 GHz" in Figure 3.13. We also quote the derived cluster mass of XLSSC 122 as reported in the ACT cluster catalog (Hilton et al., 2021). We show both the mass derived from the matched filter and one with an additional correction term (see Hilton et al., 2021, for details). Finally, we add estimates on the halo mass derived via the dispersion-velocity measurements of the cluster members XLSSC 122 dynamical mass.

To derive the dynamical mass, we adopt the methodology described in Aguado-Barahona

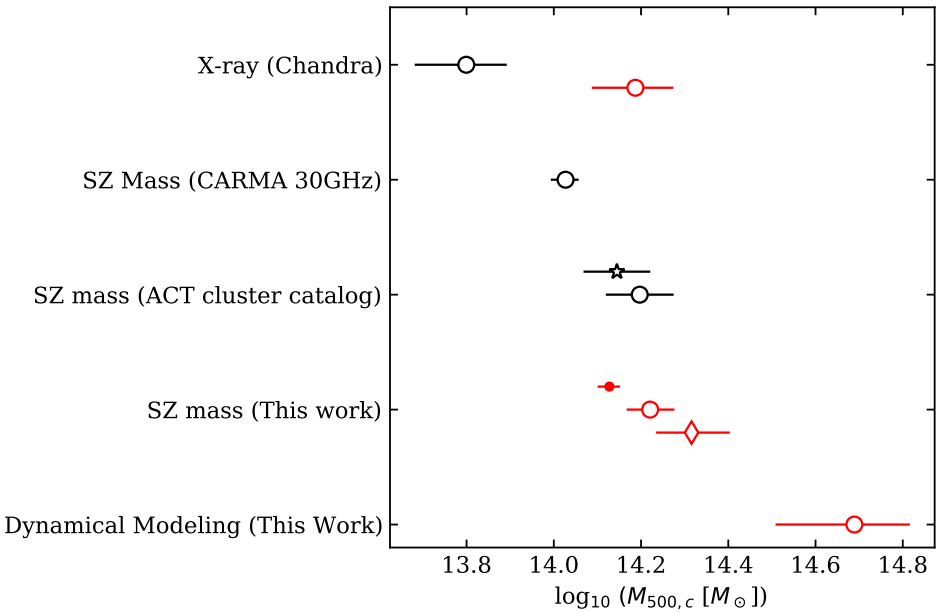

Figure 3.13: Overview of halo masses ($M_{500,c}$) of XLSSC 122. In red, we show the halo masses derived in this work. Regarding SZ measurements, the red open circle corresponds to the likelihood-weighted average of all masses derived from the empirical formalism (Table 3.3, lower table). The dot represents the mass estimates from the spherically symmetric model and the diamond that of elliptical ones. For the halo masses reported in the ACT cluster catalog, the star shows the calibrated mass estimate, and the circle the SZ mass obtained by matched filtering the frequency maps. The reported errors correspond to the $16^{\rm th} - 84^{\rm th}$ quantiles. This figure shows the discrepancies between the derived $M_{500,c}$ indicating that with forming clusters, one cannot reliably use one tracer or constant gas fraction to estimate the true halo mass.

et al. (2022). We used the cluster members in Willis et al. (2020) that were labeled as the "Gold" standard to derive the velocity dispersion. In total, we use the spectroscopic redshifts of 32 cluster members that fall within $r_{200,c}$. We found a $\sigma_{200,c} = 1014 \pm 169$ km s^{-1} by converting the redshift differences between cluster members and the median redshift to velocity offsets and estimating the biweight scale (Beers et al., 1990) and standard error over these velocities. Then, we used the scaling of Munari et al. (2013):

$$\frac{M^{\rm dyn}_{200,c}}{1 \times 10^{15}\ {\rm M}_\odot} = \left(\frac{\sigma_{200,c}}{A}\right)^{\frac{1}{\alpha}}, \tag{3.12}$$

with $A = 1177.0$ km s^{-1} and $\alpha = 0.364$ to convert the velocity dispersion to a dynamical mass estimate. To convert the halo mass to the $M_{500,c}$ definition we use the concentration parameter definition of Diemer & Joyce (2019) and the $M^{\rm dyn}_{200,c}$ to $M^{\rm dyn}_{500,c}$ conversion as implemented by the `colossus` package (Diemer, 2018). To estimate the uncertainty of the dynamical mass, we adopt the procedure of Ferragamo et al. (2020):

$$\Delta M^{\rm dyn}_{200,\rm c} = M^{\rm dyn}_{200,\rm c}\sqrt{\frac{\epsilon}{4(N_{\rm gal}-1)^{\beta}}}, \tag{3.13}$$

with $\epsilon = 16.2$ and $\beta = 1.13$. Here, we only propagated the statistical error on the velocity dispersion to the dynamical mass uncertainty as the redshift uncertainty was not given by Willis et al. 2020. All peculiar velocities were estimated with respect to the BCG, which was selected as the galaxy with the lowest magnitude. Following this procedure we find $\log_{10} M^{\rm dyn}_{500,\rm c} = 14.69^{+0.13}_{-0.18}\,\mathrm{M}_{\odot}$.

We find lower SZ-derived mass estimates than what is expected from the velocity-dispersion measurement ($\sim \times 2.5$). This finding is in line with that of other high-redshift SZ detections (Di Mascolo et al., 2023, Andreon et al., 2023). It suggests that the hot component of the ICM is still assembling and is actually part of several interacting substructures of lower-density gas. This hypothesis agrees with the lower X-ray derived mass estimate: because the X-ray emissivity is proportional to $\epsilon \propto n_{\rm e}^2$, it becomes decreasingly sensitive to lower dense regions, while the SZ effect is linearly proportional to the electron density, $n_{\rm e}$, and thus more sensitive to the hot gas component of the ICM in forming clusters. Hence, the lower halo mass estimates derived from X-ray observations are consistent with the picture that XLSSC 122 is still actively forming and largely composed of lower-density gas. If this is the case, the gas fraction of $f_{\rm gas} = 0.125$ used in Mantz et al. (2018) is most likely underestimating the true mass.

3.7 Discussion

3.7.1 Morphological implications

The main question of this paper is what phase of cluster assembly XLSSC 122 is in and, correspondingly, how disturbed it is. We provide an answer by combining high-resolution ALMA+ACA Band 3 observations with ACT data. By jointly modeling ALMA+ACA+ACT, we find that XLSSC 122 can be classified as a non cool-core when compared to local observations or as relaxed when compared to distant clusters. However, the difference between these two profile classifications can be attributed to the increasing merger rate at higher redshifts (Fakhouri et al., 2010), which logically explains the flattening of the profile. Even though the terminology used in McDonald et al. (2014) conveys the idea that XLSSC 122 can be interpreted as a "cool-core" cluster based on its pressure profile, it is actually undergoing some degree of morphological disturbance.

This morphological disturbance is consistent with the modeled eccentricity of $e = 0.46^{+0.12}_{-0.16}$. Even though the eccentricity strongly depends on the projection of the merger/post-merger on the sky (see, e.g., Cialone et al., 2018) that can make an elliptical structure look spherically symmetric, higher ellipticities must be caused by a morphological disturbance which is unresolved in the observations.

On slightly larger scales, we do resolve asymmetric features in the south of the cluster. By modeling these filamentary-like structures with a highly elliptical gNFW model, we tentatively confirm—at 3.6σ for ALMA+ACA and at 2.4σ when ACT is included (see Section 3.5.2)—the

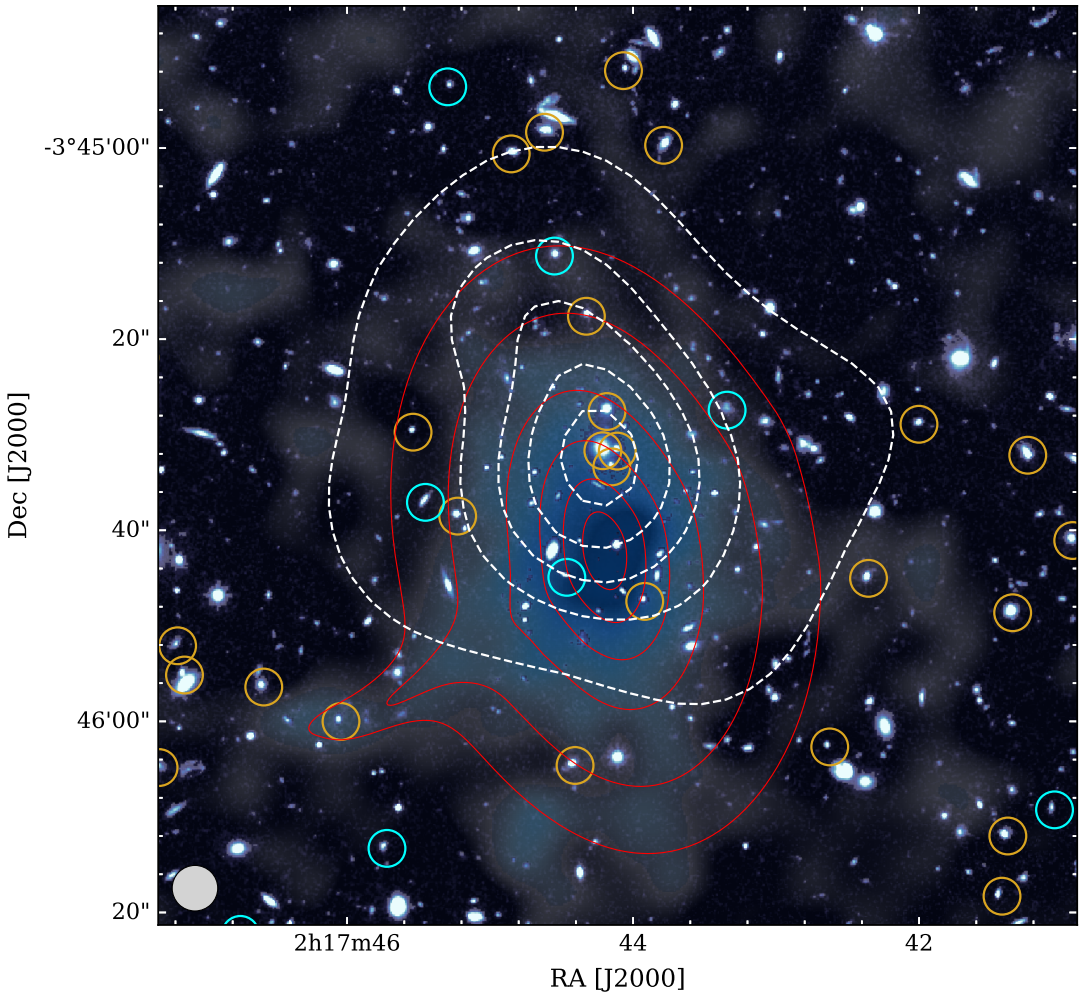

Figure 3.14: Complete multiwavelength view of XLSSC 122. We show adaptively smoothed *XMM-Newton* contours (white) overplotted on the HST F140W background. The cluster members are highlighted in gold and cyan, with the latter corresponding to star-forming and dusty galaxies based on the SED-fitting done by Trudeau et al. (2022). In between the cluster members, we visualize the SZ flux ($< -2\sigma$) as seen in the cleaned ALMA+ACA observations in blue. The beam size of the ALMA+ACA image (tapered to $5''$) is shown in the bottom left. The red contours represent our most likely model reconstruction obtained by forward modeling two gNFW components to the ALMA+ACA+ACT observations. The figure indicates a clear morphological difference between the equation of state parameters traced by X-ray and the SZ effect.

presence of a second component in the pressure distribution. We are aware that this specific model is not ideal for modeling filamentary-like structures, but it is sufficient to probe the significance of this feature in the native, *uv*-space of ACA and ALMA, rather than trying to infer a physical interpretation of the $\sim -3\sigma$ feature in the residual map. Future work should explore a wider variety of models that can capture the complexity of these asymmetric features, which will most

likely increase the detection inference of the second component. However, the tentative presence of this second component, which could be an infalling group, a filament, or a projection effect of an asymmetric assembling cluster, does strengthen the idea that this cluster is actively assembling and does not follow the definition of a relaxed cool-core-like structure.

By overlaying the cleaned SZ flux with X-ray emission and cluster member distribution, as shown in Figure 3.14, we notice two things: first, there is a large excess of gas in the south of the cluster where no X-ray emission is detected. This is in line with the difference in the reported mass estimates derived from X-ray and the SZ effect as mentioned in Section 3.6, again strengthening the idea that the hot ICM in XLSSC 122 is composed of low-density gas and is actively growing. Second, the peak of the pressure distribution, as mapped by the SZ signal, is offset from the BCG and the peak of the X-ray emission by $10'' \pm 1''$ (80 ± 7 kpc) when projected on the sky mainly along declination axis.[8]. The following section provides details on the possible implications.

3.7.2 Thermodynamical implications

To understand the offset between the SZ peak and the BCG, which is co-spatial with the X-ray imaging, as well as the excess of SZ flux in the southern part of the cluster, we can compare XLSSC 122 to the well-studied local cluster ($z = 0.451$) RX J1347.5-1145. This cluster is one of the brightest X-ray emitting galaxy clusters which has been studied extensively over the last decade in the mm-wave regime (see e.g. Komatsu et al. 2001, Kitayama et al. 2016, Ueda et al. 2018, and Di Mascolo et al. 2019). RX J1347.5-1145 hosts an excess of SZ flux in the southeast of the X-ray peak that is most likely a strong, shock-induced pressure perturbation caused by a major merger event. Similar to XLSSC 122, this excess is found at an offset of $27''$ ($\sim 109h^{-1}$ kpc) from the X-ray peak and is faint in the X-ray but bright in the SZ signal.

Since X-ray spectroscopy provides a temperature constraint that is essentially emission weighted, and the bulk of the X-ray emission is seen in the northern portion of the cluster, the global temperature constraint of $T_{\rm spec} = 5$ keV (Mantz et al., 2018) may not be valid in the southern portion of the cluster where the SZ signal peaks. Generally, merger events can temporarily boost the SZ flux on time scales much smaller than the virialization time of a massive cluster (Wik et al., 2008). Gas in an infalling substructure can be stripped by ram pressure of the main bulk of the ICM and create pressure perturbations induced by shock waves which boost the y-value locally. To investigate this further, we estimated temperature differences in XLSSC 122 by taking the ratio of the SZ flux over the square root of the X-ray surface brightness. Since the SZ effect traces the integrated pressure along the line of sight, and the X-ray emission traces roughly the density squared, combining them in this way results in a quantity proportional to the temperature of the ICM via the ideal gas law (under the assumption of constant temperature along the line of sight). One would expect a constant ratio if the gas is isothermal and both the X-ray and SZ observations have a similar point spread function (PSF). Figure 3.15 shows this ratio scaled to arbitrary units and indicates that XLSSC 122 is far from isothermal, with a pseudo

[8]We note that the ALMA measurements still contradict the CARMA results on the centroid position by $20'' \pm 1''$ (corresponding to a 3σ difference based on their derived uncertainty of the centroid, Mantz et al. 2018)

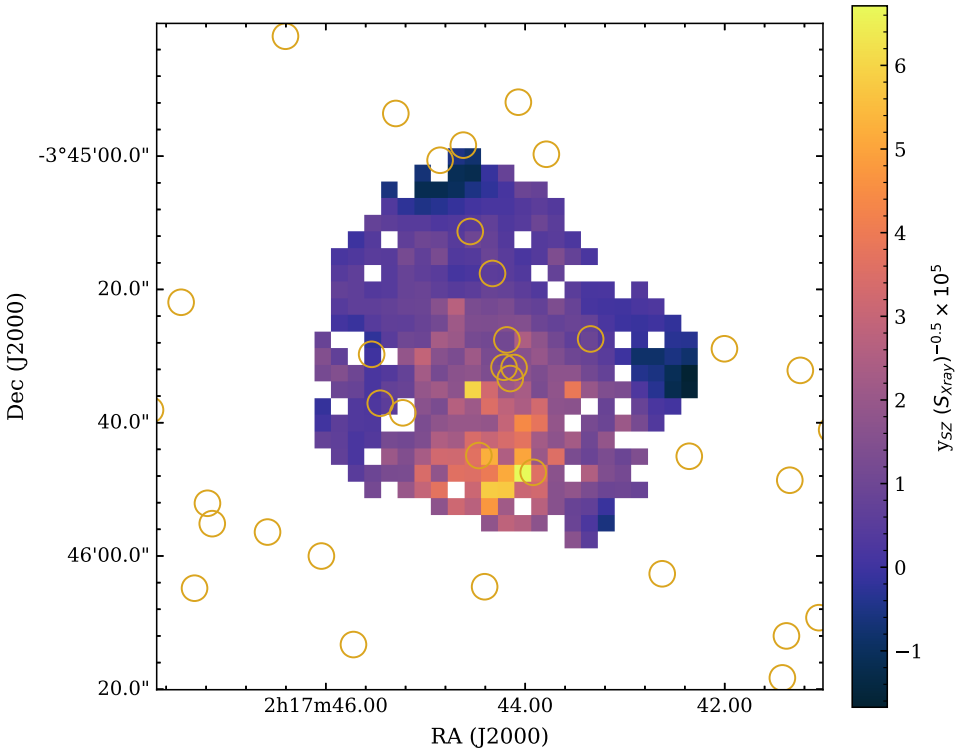

Figure 3.15: Pseudo-$k_B T_e$ ($y/\sqrt{S_X}$) map of XLSSC 122. It takes the ratio of the cleaned SZ map (Fig. 3.11) and the X-ray surface brightness (2nd panel of Fig. 3.3) within the 2σ adaptively smoothed X-ray contours (also shown in Fig. 3.3 and Fig. 3.14). The units are linearly scaled to an arbitrary value to show the relative pseudo temperature change in the south of XLSSC 122.

temperature increase of $\sim 3\times$ in the south, indicative of a disturbance. In Figure 3.15, both the *XMM-Newton* observations and the ALMA+ACA image reconstruction have a resolution of $\approx 5''$.

The pseudo temperature increase in the south is co-spatial with the tentative second SZ component and suggests gas stripping of an infalling subcluster which shock-heated the gas. This putative merger of an infalling group in the large-scale filamentary structure with the bulk of the already-formed ICM could temporarily boost the Y-value causing it to exceed the ACT detection threshold and thus be included in the catalog of (Hilton et al., 2021). However, other mechanisms may also contribute to explaining why XLSSC 122 is the only cluster detected by ACT during this epoch, despite having a halo mass well below the limit set by the hierarchical growth model of dark matter halos. For instance, bright radio galaxies are often located at the cores of (proto-)clusters (see, e.g., Di Mascolo et al., 2023) and reduce the amplitude of the SZ flux by infilling it with a positive signal, but XLSSC 122 lacks a radio-loud AGN in its BCG and thus its SZ signal is uncontaminated. Another possible explanation is the lack of optical confirmations of high$-z$ cluster candidates ($z > 1.3$), which would exclude them from the catalog of (Hilton et al., 2021).

In summary, our findings and interpretation on the forming ICM are: (1) we have tentative

evidence for a second pressure component with a flux ratio of $\sim 1{:}2$; (2) there is an offset between the pressure peak and the X-ray peak, which causes the enhancement of the pseudo temperature in the south; (3) the fact that XLSSC 122 is the only optically confirmed cluster of its epoch detected by ACT could be because of a merger event in which the substructure is going through its first core passage, temporarily boosting the y-value (Wik et al., 2008); and (4) the mismatch between X-ray and SZ-derived halo masses suggests that XLSSC 122 is undergoing a major merger that is heating the ICM, as opposed to heating coming from constant, small-scale accretion from the cosmic web.

3.7.3 Time scales

We estimate time scales to gauge the evolutionary stage of XLSSC 122. At any redshift, the masses of the largest gravitationally bound objects are sensitive to the underlying cosmology. The earliest objects of a given kind form at the rare, high peaks of the density distribution of the Universe (Press & Schechter, 1974). At a redshift of $z \sim 2$, the most massive and newly formed structures are (proto)clusters. From cosmology, we know that the density power spectra peaks at roughly $8h^{-1}$ Mpc. As a sphere with a radius of $8h^{-1}$ Mpc contains about the right amount of material to form a cluster (Peebles, 1980, Navas et al., 2024), we can find how far XLSSC 122 is in its assembly phase by estimating how large a sphere has already collapsed into the structure we observe.

If we assume the tentative detection of the colliding substructure in the south of the cluster as true, then by simply assuming a peculiar velocity of 1000 km s^{-1} $\simeq$ 1 Mpc Gyr^{-1}, we can estimate via standard Newtonian physics how large a sphere has already collapsed into what we know as XLSSC 122. If we treat the structures as point-like objects in which the infalling substructure accelerates constantly from $v_{\rm pec} = 0$ km s^{-1} to $v_{\rm pec} = 1 \times 10^3$ km s^{-1} within the expansion time of the Universe (which is $t = 3.3$ Gyr at $z = 1.98$), we find that the distance the substructure has traveled is

$$\Delta x = \frac{\Delta v \Delta t}{2} \simeq 1.8 \text{ Mpc},$$

which falls well within the σ_8-radius. Of course, observations cannot be fast-forwarded in time, and the only true indicator of whether XLSSC 122 can grow to become a local Coma-like cluster is its large scale surrounding (Remus et al., 2023). However, even though the above estimate is simplistic, it sketches the idea that XLSSC 122 still has the potential to grow.

Furthermore, we can estimate the virialization time and compare it to the lifetime of the Universe. The virialization time is roughly equal to three to ten times the sound crossing speed (Wik et al., 2008). Using the global ICM temperature form Mantz et al. (2018) we find the time to virialize

$$t_{\rm vir} = \frac{3R}{c_{\rm s}} = 3R \left(\sqrt{\gamma \frac{k_{\rm B} T}{m}} \right)^{-1} \simeq \frac{3R}{0.0038c} \simeq 0.5 \text{ Gyr},$$

for $c_{\rm s}$ the sound speed, c the speed of light, $\gamma = 5/3$, and $m = \mu m_{\rm p}$, which is the proton

mass multiplied by the mean molecular weight (or mass per particle). Thus a time scale fitting comfortably within the age of the Universe at that epoch provides sufficient time for the gas to convert its gravitational potential energy into thermal energy, which in turn enables one to detect it through observations of the SZ effect.

Even though XLSSC 122 is the most distant cluster detected in the ACT-cluster catalog, independent follow-ups of overdensities of galaxies around radio-bright AGN have found protoclusters at more distant redshifts. As an example, Di Mascolo et al. (2023) reports the first robust detection of the forming hot ICM component in a (proto-)cluster at $z > 2$, also using ALMA+ACA observations of the SZ effect. In that case, the target was the Spiderweb proto-cluster, which at $z = 2.156$ lies 300 Myr further back in cosmic time than XLSSC 122. Through modeling an A10-MD profile to the observations, Di Mascolo et al. (2023) found a $Y(< r_{500,\mathrm{c}}) = 0.76^{+0.19}_{-0.17} \times 10^{-6}$ Mpc^2. By fitting the same model to XLSSC 122, we find $Y(< r_{500,\mathrm{c}}) = 2.0^{+0.6}_{-0.4} \times 10^{-5}$ Mpc^2, approximately 20$\times$ the intrinsic $Y(< r_{500,\mathrm{c}})$ of the Spiderweb. Furthermore, XLSSC 122 exhibits a red sequence (Willis et al., 2020, Noordeh et al., 2021), while the Spiderweb proto-cluster is composed more of star-forming cluster members.

From the foregoing time scale estimates and by comparing with the Spiderweb protocluster, we propose that if the Spiderweb can be said to be in its "early childhood" phase, XLSSC 122 would be an "adolescent" cluster. It is still assembling and constitutes a bona fide yet immature galaxy cluster.

3.8 Conclusions

In this work, we add high-resolution ($\approx 5''$) ALMA (12m-array) and ACA (7m-array) Band 3 observations to augment an extensive collection of auxiliary data on XLSSC 122, the most distant cluster detected in recent cluster SZ catalogs. Through forward modeling analytical prescriptions of the pressure distribution to the interferometric ALMA+ACA observations jointly with those made by the single dish telescope ACT, we model the pressure distribution from the core ($\approx 5''$, ~ 40 kpc) to roughly half the virial radius. The results obtained from our forward modeling analysis lead us to the following conclusions:

1. We detect the SZ effect with a significance of 11σ in the ALMA+ACA data alone which increases to 15σ when ACT observations are included in the forward modeling routine. The significance is determined through the Bayesian evidence, as presented in Tables 3.2 & 3.3. Notably, in comparison to prior follow-up observations with CARMA, measurements using ALMA+ACA+ACT have higher resolution, sensitivity, and dynamic range, which both allow for higher fidelity imaging and improve the mitigation of contamination by compact sources. The result is that we find better agreement between the SZ decrement and the X-ray emission seen in archival *XMM-Newton* and *Chandra* observations.

2. Based on its radial pressure distribution, XLSSC 122 is classified as a noncool-core when compared with local observations (see Arnaud et al., 2010). In contrast, when compared to profiles of more distant clusters of galaxies (McDonald et al., 2014), XLSSC 122 exhibits a relatively relaxed state. However, via the Bayes factor, we cannot distinguish between the

two classifications, but we can distinguish them from the other pressure profile templates from Arnaud et al. (2010) and McDonald et al. (2014) with a significance of $\Delta \ln \mathcal{Z} \geq 4.5$ ($\geq 3\sigma$, see Table 3.3).

3. XLSSC 122 exhibits an eccentric structure, with $e = 0.46^{+0.12}_{-0.16}$, also indicating a morphologically disturbed nature of the cluster. Furthermore, our analysis leads to an improved precision of the SZ mass estimate to $M_{500,c} = 1.66^{+0.23}_{-0.20} \times 10^{14}$ $M_\odot$, though we note the overall accuracy could still be affected by the hydrostatic mass biases common to SZ mass estimates.

4. By reconstructing the interferometric image with the marginalized model reconstruction analog to the clean algorithm, we found an excess of SZ flux in the south with respect to the BCG and the X-ray surface brightness. Then, through modeling the SZ surface brightness with two components, we tentatively confirm the presence of a second source or filamentary-like structure to the southeast with $\Delta \ln \mathcal{Z} = 6.6$ ($\sigma_{\rm eff} = 3.6$) when modeling the ALMA+ACA observations alone and $\Delta \ln \mathcal{Z} = 3.0$ ($\sigma_{\rm eff} = 2.4$) when including ACT observations. We speculate that this second component could boost the Compton Y value locally as the gas is heated. As the cluster is still actively forming, the gas of the hot ICM is relatively low in density; hence the excess of gas in the south is detected with the SZ effect while going unnoticed in the X-ray wavelengths.

5. By comparing XLSSC 122 to local observations and even more distant clusters of galaxies, we posit the idea that XLSSC 122 is in its "adolescent" phase. Even though detected at $z \sim 2$, XLSSC 122 had time to virialize and attract matter over time, forming a bulk of hot but low-density gas in the ICM. Through our multiwavelength approach, we believe that XLSSC 122 is likely undergoing a major merger and that a major mechanism driving the heating of the ICM could be through this collision rather than constant small-scale accretion of matter from the cosmic web. This collision would have boosted the Y-value temporarily, causing it to exceed the ACT detection threshold, making it the only cluster around $z \sim 2$ that is optically confirmed and detected in the southern hemisphere by ACT.

Regarding future work in this field, we anticipate that ALMA imaging and characterization of the forming hot ICM via the SZ effect is only now beginning in earnest with the introduction of ALMA Band 1 (35-50 GHz; see Di Francesco et al., 2013, Huang et al., 2022). With 13 times the collecting area and a larger field of view, while sampling similar spatial scales as the ACA in Band 3, we can start to resolve the ICM in the most distant clusters of galaxies with only a fraction of the integration time. This is timely as Simons Observatory will come online next calendar year (Ade et al., 2019). This single-dish CMB survey telescope is expected to find more and more high-z clusters which can be followed up to begin building a statistical sample of resolved observations to understand ICM heating, cluster growth, and evolution. Looking to the further future, we can expect significant advances to be provided by major new (sub-)millimeter facilities, such as the 50-meter Atacama Large Aperture Submillimeter Telescope (AtLAST; Ramasawmy et al. 2022, Mroczkowski et al. 2023, Mroczkowski et al. 2024). AtLAST will feature a large 2° FOV with a $10''$ resolution at 150 GHz, providing a more complete, high spatial dynamic range

view of the SZ effect in clusters, bridging the detailed view provided by ALMA and the nearly all-sky view from CMB experiments.

Chapter 4,

Maria: a simulator for (sub-)mm single-dish observations

The content of this chapter is based on an article that is submitted to OJA as ***van Marrewijk*** *et al. (2024).*

“Way out west, they’ve got a name
For rain and wind and fire
The rain is Tess, the fire’s Joe
And they call the wind Maria
Maria blows the stars around
And sends the clouds a-flying”

- Alan J. Lerner

The most sensitive (sub-)millimeter (hereafter, (sub-)mm) user facility yet built is the Atacama Large Millimeter/submillimeter Array (ALMA), which outperforms current single-dish telescopes and other interferometers in terms of point source sensitivity due to its large collecting area and excellent site. However, interferometers like ALMA are optimized to achieve sub-arcsecond resolution in the (sub-)mm, but this comes at the expense of being unable to constrain large spatial scales, which are probed by short antenna spacings. This in turn is simply due to there being a minimum distance between two antennas that is needed to avoid collisions while tracking a source. This limit, known as the shadowing limit, prevents zero-spacing information and results in a biased recovery of the total integrated flux. Previous works have shown that even at scales the size of the synthesized beam (i.e., the interferometric resolution element), only a fraction of the true flux is recovered (see, e.g., Plunkett et al., 2023). Simulations indicate that to address the loss of information at larger angular scales and to provide good overlap in the Fourier domain, one should rely on single-dish telescopes with a dish size of at least three times the size of the interferometric array element. This is necessary to provide the complete Fourier sampling required for high spatial dynamic range and unbiased image reconstruction (Frayer, 2017, Plunkett et al., 2023).

On the other hand, large single-dish telescopes have their own observational limitations. For example, due to the faintness of the signal compared to the Earth's atmospheric emission, drifts in detector gain and response, and the fact most bolometer-based instruments are not set up to perform an absolute temperature calibration, bolometric arrays require differential measurements (e.g., going on and off source) to obtain an unbiased flux estimate. Single-dish user-facility telescopes like the Green Bank Telescope (GBT) therefore adopt a Lissajous daisy scanning pattern (e.g. Romero et al., 2020). These scanning trajectories impact the observed sky and introduce filtering effects, such as a higher sensitivity in the center compared to the outskirts.

Removing atmospheric contamination from differential measurements poses a significant challenge for ground-based telescopes. Simpler methods involve subtracting a common mode from the data or high-pass filtering the time-ordered data (TODs, also referred to as time streams) to exclude fluctuations below a certain threshold frequency. More sophisticated techniques may take into account non-trivial correlations between different detectors, how the fluctuations change over time, and how TODs cohere across time due to the periodicity of the scan pattern. Morris et al. (2022) has shown that the atmosphere exhibits these non-trivial correlations, which determine how effective any given mapmaking strategy will be. However, since the data comprise a superposition of astronomical signals, atmospheric influences, and detector noise, a faithful observation simulator can help inform us how different filtering and data reduction techniques impact mapmaking and the recovery of celestial signals.

In this work, we adapt `maria`[1] to perform as a virtual single-dish observational simulator, designed to closely mimic real-world conditions. We leveraged this tool to generate realistic synthetic TODs and maps from simulations, enabling a one-to-one comparison between simulated objects evolved in a cosmological environment, offering a more complex and accurate description than simple analytic models, and observational data. The tool is constructed as follows: we employ a predefined telescope and detector array design to scan in a daisy or back-and-forth azimuthal

[1]See https://thomaswmorris.com/maria/

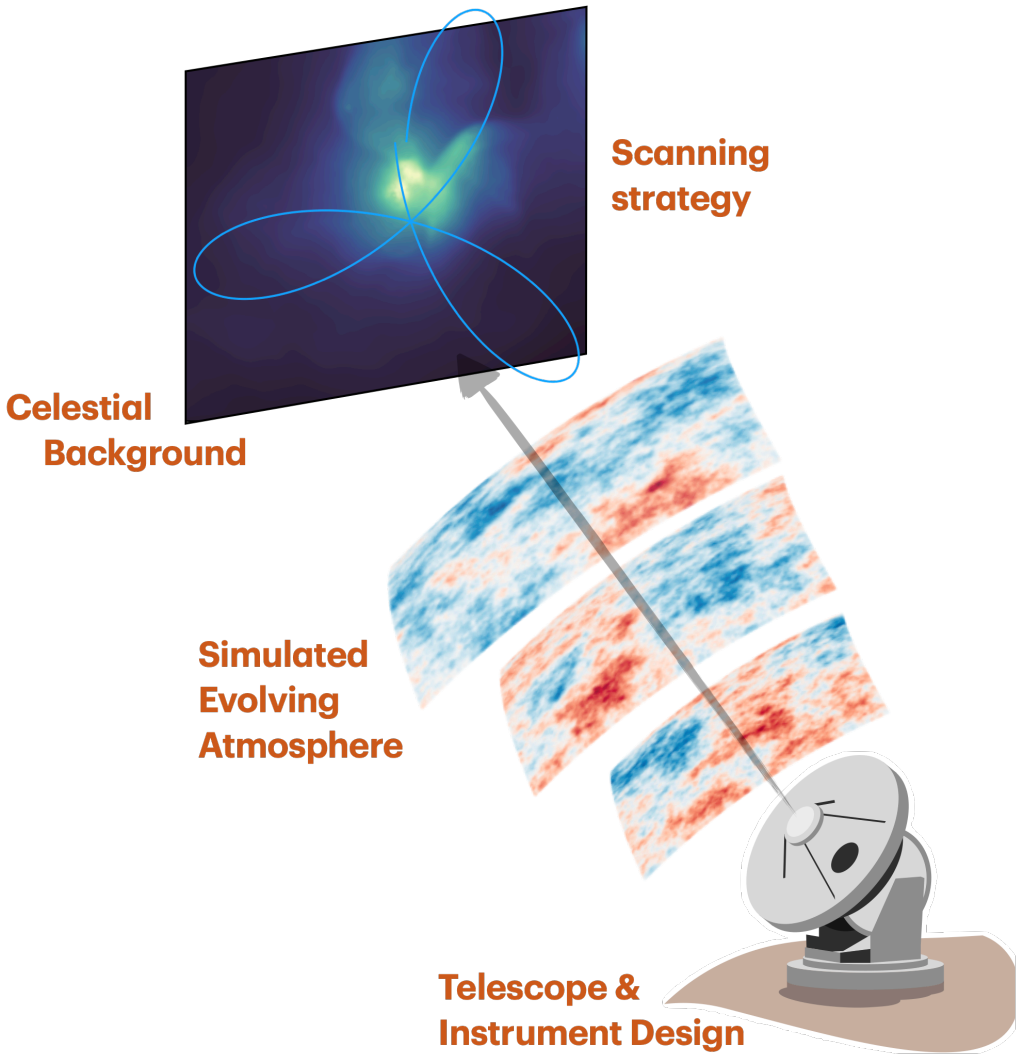

Figure 4.1: Schematic on how `maria` operates. The virtual telescope consists of four parts: A celestial background, a location and time-specific evolving atmosphere, a telescope and instrument design, and a scanning strategy.

scan pattern through the ever-changing atmosphere over a celestial body. We visualized these components in a sketch shown in Figure 4.1. This approach allows studies on optimizing telescope design and scanning strategies. Thus, `maria` functions similarly to codes such as `X-MAS` (Gardini et al., 2004, Rasia et al., 2008), `Phox` (Biffi et al., 2011), `pyXSIM` (ZuHone & Hallman, 2016), and `SOXS` (ZuHone et al., 2023) written to mimic X-ray observations, CASA `simobserve` (CASA Team et al., 2022) regarding interferometric observations, and TOAST (Puglisi et al., 2021) which is primarily used for Cosmic Microwave Background (CMB) survey forecasts.

The current implementation of `maria` is flexible and can be customized to various types

of instruments, such as heterodyne and integrated field units, to generate mock datacubes with spectral information. However, in this study specifically, we limit `maria` to generate synthetic broadband bolometric observations. In particular, we restrict `maria` three-fold: (i) We mimic only two facilities, of which one already exists (the GBT with the MUSTANG-2 instrument) which allows testing the `maria` output with real observations, and a future facility, namely the 50 meter Atacama Large Aperture Submillimeter Telescope (AtLAST; Ramasawmy et al. 2022, Mroczkowski et al. 2023, Booth et al. 2024, Mroczkowski et al. 2024, Reichert et al. 2024) with a possible bolometer instrument concept.[2] The tool itself includes configuration files to easily simulate more facilities, such as the Large Millimeter Telescope (LMT; Kaercher & Baars, 2000), as well as current CMB survey experiments such as the South Pole Telescope (SPT; Carlstrom et al., 2011, Bleem et al., 2015, 2020) and the Atacama Cosmology Telescope (ACT; Swetz et al., 2011, Thornton et al., 2016, Henderson et al., 2016), imminent ones like Simons Observatory (SO, Ade et al., 2019) and CCAT-prime (Fred Young Submm Telescope or FYST; CCAT-Prime Collaboration et al. 2023), and future ones like CMB-S4 (Abazajian et al., 2016). (ii) We focus on the $\nu \sim 100$ GHz regime, which is the high-frequency regime for the GBT, and the low-frequency regime for a telescope such as AtLAST. We note that `maria` can also simulate the atmosphere at higher frequencies up to where the atmosphere is still transmissive well into the submm. (iii) Finally, even though `maria` is generic and can be employed for a wide variety of science cases, we focus here on a specific one: the intracluster medium seen via the thermal Sunyaev-Zeldovich (SZ; Sunyaev & Zeldovich 1970, 1972b) effect. Briefly, the thermal SZ effect is a spectral distortion to the CMB, presents as a faint, extended decrement at frequencies $\nu \lesssim 218$ GHz, and is a probe of gas thermal energy (see, e.g., Mroczkowski et al. 2019 for a review, as well as Di Mascolo et al. (2024) for a more comprehensive overview of key AtLAST SZ science cases).

The remainder of this work is structured as follows: in Section 4.1 we provide a detailed description of the simulator's construction, elucidating its four constituent components. Section 4.2 demonstrates the simulator's ability to replicate existing MUSTANG-2 observations and offers an example of how it can be employed to assess the feasibility of scientific objectives. Moving forward, Section 4.3 delves into the specifics of forecasting for AtLAST. Lastly, Section 4.4 offers a comprehensive summary and discussion of our study.

4.1 A generic virtual single dish telescope

The simulator we built is a continuation of the atmospheric modeling work done by Morris et al. (2022, 2024). Therefore, we refer to those works and references therein for an in-depth discussion of atmospheric modeling. Here, we briefly describe how the `maria` simulation works. The simulator consists of five main components: 1) a telescope and instrument design, 2) a scanning strategy, 3) an input astronomical map, 4) a site and time location to generate atmospheric weather conditions, and 5) additional additive noise and detector inefficiencies. These components are visualized in Figure 4.1 and will be discussed separately in the following five subsections. For the full overview of all the parameters and corresponding tutorials, we refer to the `maria` website.[1]

[2] We note that AtLAST will host a multitude of different instruments, also including spectroscopic receivers.

With this setup, we can directly link fundamental design choices, such as primary size and the number of detectors, to a scientific output. Thus, we established a tool for communication between instrument scientists and observers, which is crucial for the development of future facilities.

4.1.1 Instrument configurations & Telescope designs

In `maria`, each simulation is characterized by a set of fundamental parameters regarding both the telescope and instrument design. Specifically, we use the primary size, the field of view (FoV), and the azimuthal and elevation bounds of the telescope for modeling the simulations. Further, `maria` positions detectors in the array evenly to fill the FoV in a hexagonally packed configuration. In the current implementation, each detector is specified with a default frequency band that has a flat response function (e.g., a flat passband from 140-160 GHz, centered at 150 GHz). `maria` also hosts the ability to import passbands.

In this study, we mimic two telescope and instrument designs: the operational MUSTANG-2 instrument (which uses bolometers) mounted on the GBT and a possible small-scale broadband continuum instrument concept for AtLAST. As noted in Section 4.3, the AtLAST concept presented here is limited by our own computational considerations rather than expected observatory capabilities. Table 4.1 provides an overview of the different designs of the two telescopes and instruments discussed in the next two subsections. It also includes parameters, which we will introduce in the remainder of this section.

MUSTANG-2 on the GBT

MUSTANG-2 is a 223-detector bolometer array on the 100 meter Green Bank Telescope (GBT), located in Green Bank, West Virginia at an elevation of 818 m above sea level. MUSTANG-2 achieves a $8\farcs5$ full width at half maximum (FWHM) resolution with an instantaneous FoV of $4\farcm2$ centered around 93 GHz, with a continuum bandwidth of $\approx$30 GHz. The detectors, which are horn-coupled, are spaced at $1.9\ f - \lambda$. For further information, see Dicker et al. (2014). The placement of MUSTANG-2 detectors on the sky is depicted in the left panel of Figure 4.2. `maria` includes a set of configuration files with hard-coded parameters to match MUSTANG-2 as well as other existing and upcoming telescope designs. However, as documented, any of these parameters can be reconfigured.

AtLAST

AtLAST (Klaassen et al., 2020, Ramasawmy et al., 2022) is a concept for a next-generation high-throughput submm telescope to be sited high in the Atacama Desert of Chile, on Llano de Chajnantor (i.e., the same plateau as that on which ALMA resides) at an elevation of approximately 5100 m above sea level. AtLAST is currently undergoing a design study funded by the European Commission.[3] Here, we define throughput, often referred to as *étendue*, as the collecting area of the primary mirror times the telescope FoV. With a surface accuracy of 20 μm, AtLAST will be capable of observations up to 950 GHz (i.e., in the 350 μm atmospheric window accessible in

[3] See https://cordis.europa.eu/project/id/951815.

Telescope Design	GBT	AtLAST
Primary size	100 m	50 m
Resolution at 90 GHz	$8\farcs5$	$16''$
Field of View†	$15'$	2°
Site location	Green Bank WV, USA	Atacama Desert Chile
Elevation	818 m	5100 m
Surface accuracy	230 μm	20 μm
Frequency coverage	1-116 GHz	$\approx 30 - 950$ GHz
Scanning speed	$\approx 50''/s$	$\approx 3^\circ/s$
Simulated instrument*		
Frequency coverage	78-108 GHz	66-118 GHz
Field of View	$4\farcm2$	0.25°
scanning radius	$4'$	0.25°
Read-out rate	100 Hz	225 Hz
Detector Count	223	3000
Optical efficiency	0.3	0.3
Illumination efficiency	0.8	0.8
White noise level	1.7 mK $\sqrt{\mathrm{s}}$	0.266 mK $\sqrt{\mathrm{s}}$
PWV RMS	0.5-5%	1-10%

Table 4.1: Instrument and telescope design differences between the Green Bank Telescope (GBT) and the 50 meter Atacama Large Aperture Submillimeter Telescope (AtLAST). * Here, we simulate MUSTANG-2 on the GBT and a small-scale plausible continuum receiver for AtLAST. For a more in-depth description of the used parameters for the latter design, we refer to Section 4.3. † Here, we estimate the full field of view of the GBT. The detector array FoV of MUSTANG-2 is limited by the cryostat size, which in turn is limited by its location in the GBT instrument turret. The full 2° FoV of AtLAST is accessible for two of the 6 planned instrument locations (see Mroczkowski et al., 2023, Mroczkowski et al., 2024).

top octile conditions there). AtLAST will include dedicated instrument spaces for six extremely large receivers, two of which can completely access the full 4.7-meter focal plane corresponding to the 2° FoV (see Mroczkowski et al., 2023, Mroczkowski et al., 2024).

4.1.2 Scanning strategies

After specifying the instrument configuration and telescope design in `maria`, we define a scanning strategy that determines the pointing of the virtual telescope throughout the observation. In this work, we use a double Lissajous daisy (or "daisy scan"). The double Lissajous daisy is defined as:

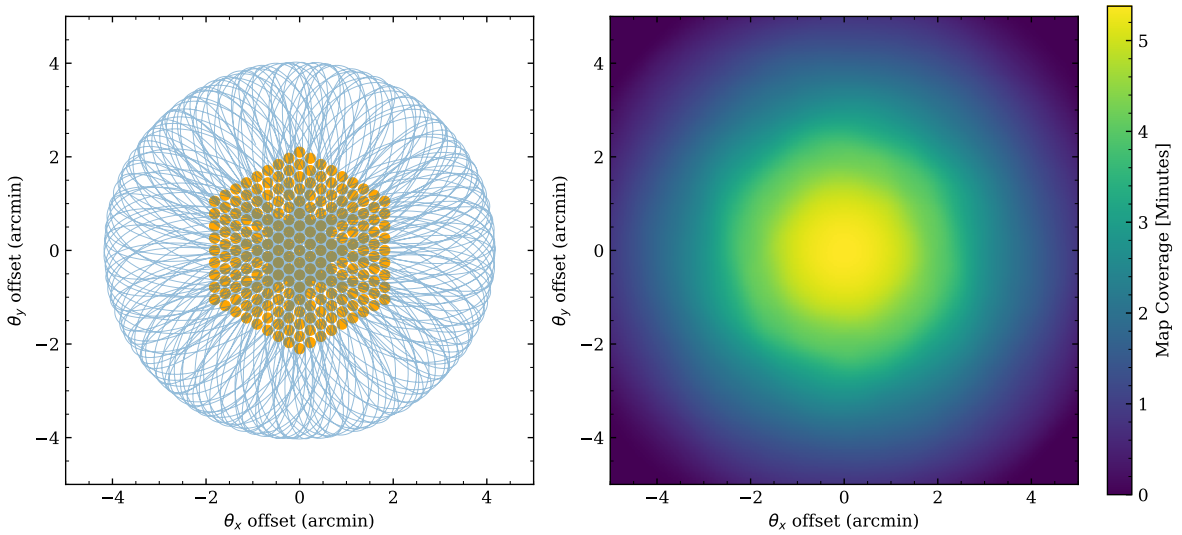

Figure 4.2: Example of a realistic scanning strategy used to mimic a MUSTANG-2 observation with `maria`. Here, we scan for 45 minutes with a read-out rate of 50 Hz and a maximum scan velocity of $51''\mathrm{s}^{-1}$, which occurs at the center of the Lissajous daisy scan. The left panel shows the instantaneous FoV of all detectors in the 93 GHz band. This array will be moved over the sky in the daisy pattern illustrated in blue. This scanning pattern leads to a higher sensitivity in the center than in the outskirts, as illustrated on the right panel, which shows how long each resolution element (a $8\farcs5$ beam) is covered by a detector. This hit map is smoothed with the diffraction-limited beam of the telescope. The pixel size of the map is set to $2''$, the value to Nyquist sample the MUSTANG-2 beam.

$$
\begin{aligned}
\vec{x_{\mathrm{outer}}} &= r_{\mathrm{outer}} \sin\left(\phi_{\mathrm{outer}}\right)\ \exp\left(i\ \phi_{\mathrm{outer}}/\mathrm{n_{petals}}\right), \\
\vec{x_{\mathrm{inner}}} &= r_{\mathrm{inner}} \sin\left(\phi_{\mathrm{outer}} + \pi/2\right)\ \exp\left(i\ \phi_{\mathrm{inner}}/\mathrm{n_{petals}}\right), \\
\vec{x_{\mathrm{scan}}} &= \vec{x_{\mathrm{outer}}} + \vec{x_{\mathrm{inner}}}, \\
\mathrm{RA},\ \mathrm{Dec} &= \mathbb{R}\left[\vec{x_{\mathrm{scan}}}\right],\ \mathbb{I}\left[\vec{x_{\mathrm{scan}}}\right],
\end{aligned}
\tag{4.1}
$$

with the r_{outer} the scanning radius of the daisy scan, ϕ_{outer} the phase which is defined as $\phi_{\mathrm{outer}} = t\ v_{\mathrm{scan}}/r_{\mathrm{outer}}$, where the t is the time stamp and v_{scan} the scanning velocity. We set $r_{\mathrm{inner}} = 0.15 r_{\mathrm{outer}}$ and $\phi_{\mathrm{innter}} = \sqrt{2}\phi_{\mathrm{outer}}$, and $\mathrm{n_{petals}} = 10/\pi$. We find this set of parameters to produce a daisy pattern which is ideal for MUSTANG-2-like observations. The resulting daisy scan is shown on the left panel of Figure 4.2. Using this scanning method, the detector array traverses the sky in a daisy pattern, passing close to the center after every pedal. This approach results in more frequent coverage in the middle of the field compared to the outskirts, leading to higher central sensitivity, as shown on the right side of Figure 4.2. That panel shows how long each pixel is covered by a detector during 45 minutes of scanning.

For the daisy scanning method, we specify the maximum scanning velocity (defined as the velocity at the center of the daisy scan), read-out rate, scanning radius, offset parameter, and pointing center. However, other scanning strategies, such as a simple 'stare' or a back-and-

forth azimuthal scan (e.g., a constant elevation scan), are also implemented in `maria`. Different scanning strategies lead to different types of sensitivity maps. For instance, when targeting clusters of galaxies, which are known as large extended objects, the GBT/MUSTANG-2 changes its scanning strategy by increasing the scanning radius of the daisy scan and changing the pointing in a box-like pattern after each scan by an arcminute to spread the sensitivity of the center to a wider area. These differences in scanning strategies can easily translate to a central sensitivity difference of a factor of ~ 1.5. Thus, one is free to choose how to optimize the observation strategies for a given science goal and can do so through `maria`.

4.1.3 Input astronomical map

The third component is the astronomical data from which we create a synthesized observation. We employ an approach similar to that of CASA `simobserve`, a tool used broadly for simulating interferometric observations. As an input file, `maria` requires a flexible image transport system (FITS; Wells et al. 1981) file in units of Jy/pixel or in Rayleigh-Jeans Kelvin ($\mathrm{K_{RJ}}$). Also, the pixel size must be specified in units of degrees or radians. The input file will be interpreted as the true background signal.

Often in the millimeter-wave regime, astronomical signals are contaminated by fore- and background sources, like the CMB, the Galaxy, and the Cosmic Infrared Background (CIB), where the latter is generally the unresolved confusion-limited submm/FIR emission dominated by dusty galaxies from different epochs, peaking between $z \sim 0.5 - 5$ (see, i.e., Devlin et al., 2009, MacCrann et al., 2024, Madhavacheril et al., 2024). In future implementations of `maria`, there will be an option to include these components through a power spectra modelization, which will be jointly mapped with the atmosphere. However, for the current version, we recommend manually adding these contamination sources to the input file when making forecasts for survey experiments, such as detecting the primary CMB or when performing line intensity mapping experiments.

4.1.4 Atmospheric modeling

The atmospheric modeling in `maria` is the backbone of the corruption model of the simulation. Therefore, this subsection details how the atmospheric modeling is set up and implemented. In particular, we discuss which weather data is used to generate local-and-time specific initial conditions (Section 4.1.4), how we generate atmospheric emission (Section 4.1.4) and corresponding turbulence from the initial conditions (Section 4.1.4), how we let the atmosphere evolve with time while scanning over it (Section 4.1.4), and how all this is implemented in `maria` (Section 4.1.4). For a more comprehensive overview of how the atmospheric model is built and how it compares with ACT observations, we refer to works of Morris et al. (2022, 2024).

Weather data

To simulate weather conditions at astronomical sites, `maria` uses reanalysis data from the European Centre for Medium-Range Weather Forecasts (ECMWF, Hersbach et al., 2020, where

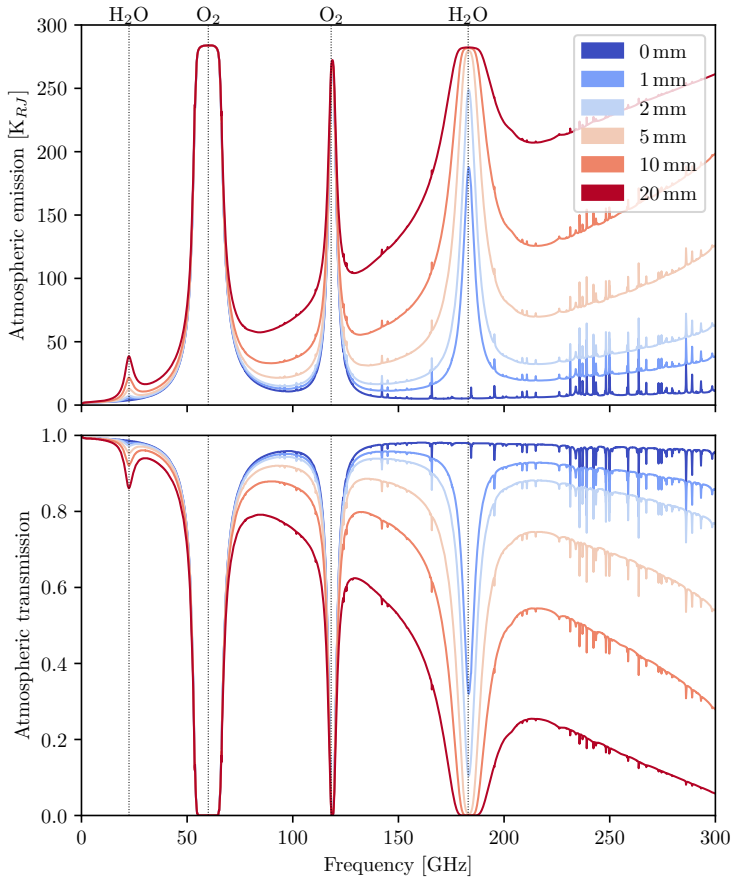

Figure 4.3: Emission and transmission spectra of the atmosphere at the Green Bank site for different levels of precipitable water vapor (PWV) computed using the `am` code (Paine, 2018). The four most significant spectral lines, due to water and molecular oxygen, are identified on the top axis. On time scales longer than a few seconds, the fluctuations in PWV due to spatial fluctuations in temperature and humidity generally dominate the noise temperature fluctuations observed (see Figs. 4.4 & 4.5.)

the fifth-generation atmospheric reanalysis is known as ERA5).[4] Reanalysis data is a mixture of weather observations with past short-range forecasts rerun with modern weather forecasting models from Hersbach et al. (2020). It further has the advantage of providing a characterization of the entire atmospheric column, which can often be quite different from ground-based weather measurements.

Atmospheric emission and opacity

As the dominant source of fluctuation in atmospheric emission and opacity for submillimeter telescopes is precipitable water vapor (PWV), we simulate atmospheric fluctuations by perturbing the line-of-sight water vapor of the receiver. We do this by generating a set of layers of turbulent fluctuations and scaling them appropriately according to site-specific weather data derived from ERA5. Typical minute-to-minute variations in PWV are on the order of a few percent of the total (Morris et al., 2024), though the relative fluctuation is a variable parameter in `maria`. We compute the atmospheric emission and opacity spectra using the vertical profiles of temperature, humidity, ozone, and wind velocity using the `am` atmospheric model (Paine, 2018) for a given site, altitude, and observing elevation. Samples of these spectra for different levels of PWV at

[4] See `https://thomaswmorris.com/maria/sites` for a list of supported sites.

the Green Bank site are shown in Figure 4.3.

Modeling turbulence

Atmospheric emission comprises a large, constant brightness from the atmosphere (which is almost always subtracted out of the timestream) but also a smaller time-dependent brightness, due mostly to fluctuations atmosphere temperature and water vapor density. Due to turbulent mixing between atmospheric layers of different temperature and humidity, local turbulent variations introduce spatial and temporal fluctuations in the atmosphere; see Tatarski 1961 for a statistical description of this phenomenon. For small angular separations, Morris et al. (2022) showed that the angular covariance of turbulent fluctuations in the line-of-sight atmospheric emission $\delta T(\theta)$ can be modeled as:

$$\Big\langle \delta T(\theta_0)\delta T(\theta_0+\theta)\Big\rangle \propto \int_0^\infty \sigma^2(z)\left(\frac{z\theta}{r_0}\right)^{5/6} K_{5/6}\left(\frac{z\theta}{r_0}\right)dz, \tag{4.2}$$

where θ is the angular separation on the sky, z is the distance from the observer, $K_\nu(\cdot)$ is the modified Bessel function of the second kind of order ν, and $\sigma^2(z)$ is the scaling of atmospheric brightness fluctuations as a function of distance from the observer, and r_0 is the turbulent outer scale.[5] This equation can be interpreted as a series of "integrated" layers of turbulence with a modified spectrum. For small angular separations, we recover a $5/3$ power law in the structure function which arises from:

$$\lim_{\theta\to 0}\Big[C(0)-C(\theta)\Big] \propto \theta^{5/3}, \tag{4.3}$$

where $C(\theta) = \langle \delta T(\theta_0)\delta T(\theta_0+\theta)\rangle$ is the turbulent covariance function in Eq. (4.2). This $5/3$ power law has been observed in, among others, Consortini & Ronchi (1972), Conan et al. (2000), Tokovinin (2002), and Morris et al. (2022). We use the value of 500 meters for the turbulent outer scale r_0, which comes from measurements done by Errard et al. (2015) and Morris et al. (2024). We further assume a "frozen-in" model for the turbulence (Lay, 1997), meaning that fluctuations are only induced by the motion along the line-of-sight with respect to the atmosphere as translated by the wind. For each detector i, we can compute its atmosphere-relative coordinates as

$$\theta_i(t) = \Delta\theta_i + \theta_{\text{scan}}(t) + \int_0^t \omega(t)dt, \tag{4.4}$$

where the first term is the detector offset from the boresight, the second is the motion of the boresight from the scan, and the third term represents the cumulative motion of the atmosphere. The angular wind velocities are derived from reanalysis profiles, which Morris et al. (2022) shows agree with what the telescope sees. Following this model, `maria` simulates layers of turbulence: for each depth of 10 layers between a height of $z = 500$ and $z = 5000$ meters away from the receiver, `maria` computes the angles that the beams will pass through and simulates turbulence to cover it.

[5] An analogous relation holds for opacity fluctuations.

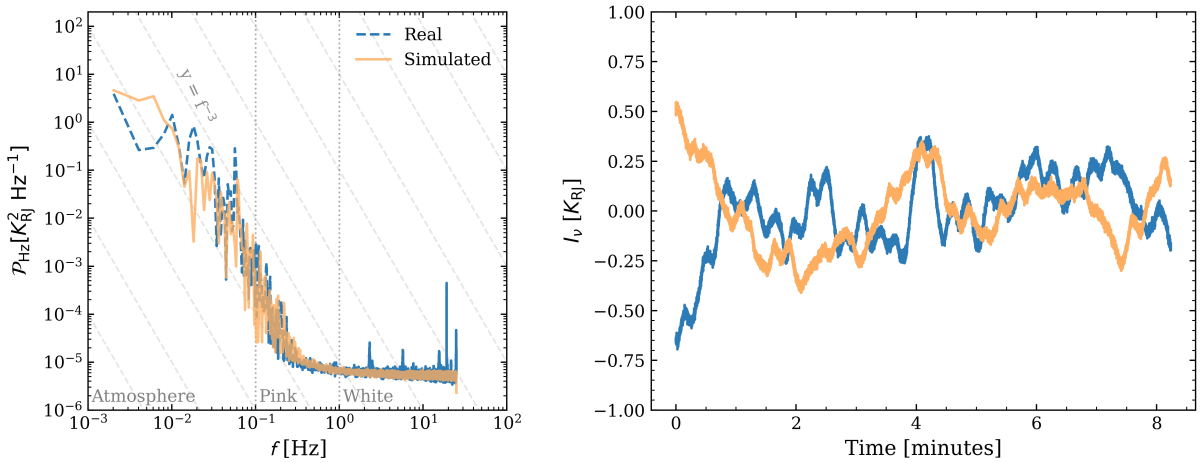

Figure 4.4: Comparison between the simulated mock TODs shown in orange with real MUSTANG-2 observations in blue. The weather resembles the atmospheric conditions of the Green Bank Telescope site, as seen in late November around 2 o'clock in the morning, local time. The left panel shows the corresponding mean power spectrum of all detectors. Here, we further highlight the frequency ranges where each noise contribution (atmospheric, pink, and white noise) dominates. The panel on the right shows a single detector's time-ordered data. This figure indicates a remarkable resemblance between real and mock data.

Modeling the evolving atmosphere

The `maria` code simulates turbulence using an auto-regressive version of the covariance matrix method (see e.g., Assémat et al. 2006). This method is preferred to Fourier-based methods (see e.g., Jia et al. 2015) for the simulations in this work, as they employ scans over a small area on the sky with long integration times. This means that the set of angular positions as described by Eq. 4.4 will comprise a long, thin strip of atmosphere which is much more efficiently generated with the former method. The covariance matrix method assumes that perturbations in atmosphere temperature and PWV due to turbulent mixing are described by a stationary Gaussian process with some covariance matrix. Generating a realization of such a process requires inverting the covariance matrix, which scales with cubic complexity in the number of points n and rapidly becomes computationally infeasible for $n \gtrsim 10^4$. We can instead generate a realization iteratively by conditioning a posterior on a sparse sampling of already-realized points and sampling from it. Considerations of sampling methods for balancing performance and realism are addressed in Morris et al. in prep., along with the trade-offs of different methods of turbulent generation. We compute the angular covariance as described by Eq. 4.2, and adjust the generated turbulent distribution to recover the mean and variance matching the simulation parameters.

Implementation in `maria`

In `maria`, generating an atmosphere necessitates specifying a date and time. `maria` then generates a random realization of a turbulent 3D atmosphere that evolves in accordance with the given

location and time settings. Subsequently, the previously defined instrument, telescope, and scanning pattern are used to scan through the evolving atmosphere. This scanning process creates TODs encompassing four variables: the position in Right Ascension (RA) and Declination (Dec), the time stamp, and the brightness temperature of the scan in units of $\mathrm{K_{RJ}}$. Furthermore, `maria` provides the option to overwrite the average PWV of the observation and the corresponding level of PWV fluctuations along the line-of-sight.

4.1.5 Additional contributions

Detector noise

`maria` provides the option to manually add noise with a power spectrum that scales as $1/f$ (also referred to as 'pink' noise) and spectrally flat noise (i.e., scale independent or 'white' noise). The additions of pink and white noise are meant to mimic detector and read-out amplifier and gain drift, and thermal and read-out noise, respectively. We note that $1/f$ noise often shares common modes over different detectors. Assuming detectors are completely independent, as done in our implementation, is thus conservative as common modes can often be removed when making maps.

Optical efficiencies

In order to account for the overall response of the detectors to astronomical and atmospheric signals, we included two different optical efficiency parameters for the coupling of the two components. The source of poor optical efficiency is generally dominated by Ruze scattering (Ruze, 1966), followed by a number of efficiency factors that impact the coupling of the instrument to the telescope optics.

In the case of the GBT, the optical efficiency for the main beam at $\nu = 89$ GHz is of order 40% (Frayer et al., 2019, White et al., 2022), while as much as twice that couples back to the atmosphere through scattering terms. To capture both systematics, we add a scalar multiplication to the amplitude of the input astronomical map. We adopt a default value of $\zeta = 0.3$ for coupling of the main beam (i.e., to the astronomical signal).

For the optical coupling of the atmospheric signal, we set the optical efficiency parameter higher, to $\epsilon = 0.8$, which we assume universally as the default in `maria`. The reason for a higher optical efficiency here than for the astronomical signal is that light scattered by the telescope, in general, is expected to couple back to the sky. We note that while improving the telescope surface accuracy will improve the coupling factor for the astronomical source, the coupling to the atmosphere should always be higher since it includes the efficiency of the main beam plus that which is Ruze scattered. $\epsilon \approx 0.8$ is derived from the ratio of total optical efficiency (i.e., $\zeta = 0.3$) over the Ruze scattering factor ($\approx 40\%$). However, we note that when modeling the atmosphere, the scaling ϵ is degenerate with the level of PWV fluctuations and its absolute value.

Finally, we need to consider the atmosphere's opacity, τ. Depending on the elevation of the source, the telescope site, the time of observing, and the observing frequency, the atmosphere absorbs parts of the astronomical background, typically varying from $e^{-\tau} = 0.7 - 0.9$ at 90 GHz.

The addition of the optical efficiencies and atmospheric absorption has two impacts. First, the astronomical response is no longer unity, so one must divide the resulting map by that same factor (i.e., $\zeta = 0.3 \cdot 0.85$) to "recalibrate". Second, it lowers the SNR of the observations by increasing the atmospheric and modeled detector noise (discussed in Sect. 4.1.5) at the time stream level with respect to the measured astronomical surface brightness. With all components combined, we can write a simplified antenna temperature equation for `maria`. This equation summarizes the various components that enter into the simulation and is written up as follows:

$$\mathrm{T_{scan}} = \frac{(\epsilon\ \mathrm{T_{atm}} + \zeta\ \mathrm{e}^{-\tau}\mathrm{T_{astro}} + \mathrm{T_{white}} + \mathrm{T_{pink}})}{\zeta \mathrm{e}^{-\tau}}. \tag{4.5}$$

With ζ and ϵ the optical efficiency parameters that couple to the atmosphere $\mathrm{T_{atm}}$ and the astronomical signal $\mathrm{T_{astro}}$, respectively. The resulting $\mathrm{T_{scan}}$ is a function of RA, Dec, and time of observing and is given in units of $\mathrm{K_{RJ}}$.

4.2 Validating `maria` with MUSTANG-2 observations

Previous work of Morris et al. (2022) demonstrated good agreement between reanalysis data and time-ordered data taken by telescopes at the Chajnantor site. However, this comparison has not been extended to other sites like Green Bank. This section compares time streams and noise maps between `maria` and actual MUSTANG-2 observations to benchmark how accurately `maria` mimics ground-based large single-dish facilities.

4.2.1 Comparing time streams

Figure 4.4 compares mock time streams with MUSTANG-2 observations, revealing a close resemblance between the modeled and actual time streams. The left panel shows the power spectra of the time streams depicted on the right. Prior to computing the power spectra, the time series are apodized with a tapered cosine window.

The power spectra reveal three different regimes where the atmosphere (left), pink (middle), and white noise (right) are dominant as a function of the sky sampling frequency. We found that a white noise level of T$= 1700\ \mu\mathrm{K}\sqrt{\mathrm{s}}$ (corrected for the calibration parameter ζ and the opacity of the atmosphere, see Eq. 4.5) was required to reproduce the real power spectrum. The $1/f$-term was also added in order to reproduce the real-time streams.

Regarding the atmospheric regime in the power spectra, Morris et al. (2022) derived that at angles below the outer scale, the power spectra should follow a frequency dependence of $\mathcal{P} \propto (f\,[\mathrm{Hz}])^{-8/3}$ when the beams propagating through the atmosphere do not heavily overlap (e.g., in the case of ACT). Conversely, at angles smaller than the near-field width of the beams, the angular atmospheric power spectra should follow a $\mathcal{P} \propto (f\,[\mathrm{Hz}])^{-3}$ dependency which is derived from the Fourier transform of the structure-function $C(0) - C(\theta) \propto \theta^2$; see the Appendix in Morris et al. 2022. In the case of the GBT/MUSTANG-2, the near field lies far above the atmosphere due to the large primary dish size. To illustrate, with the detectors being spaced $1.9f - \lambda$ apart, the angular separation would be approximately $15''$ on the sky. Consequently, the

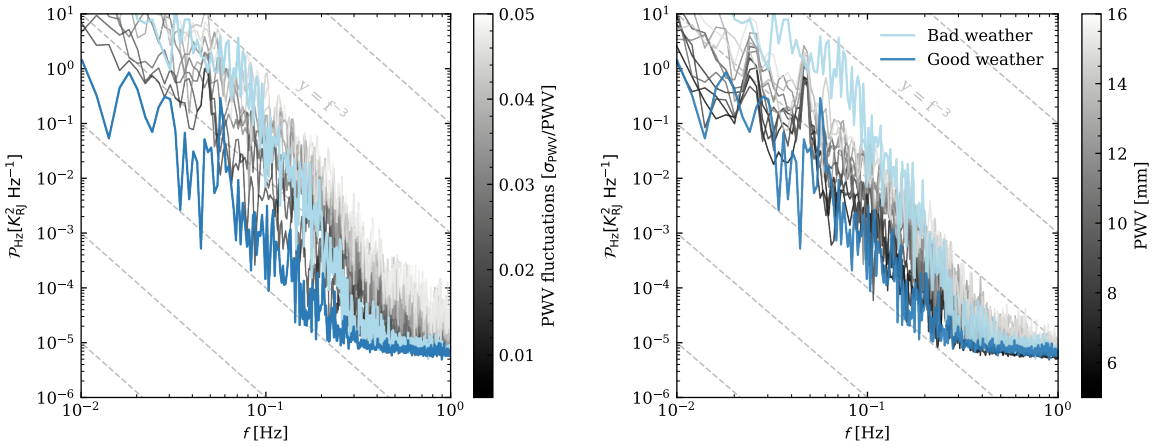

Figure 4.5: Shape dependence of the atmospheric mean power spectra derived from the synthetic time streams (gray lines) as a function of its simulated weather conditions. These are shown in comparison to real observations indicative of good weather (dark blue, also shown in Figure 4.4) and worse weather conditions (light blue). The top panel shows the effect of changing the turbulence along the line of sight, ranging from 0.5% to 5% of the total amount of PWV (7.7 mm). The bottom panel shows the behavior of the power spectra with increasing PWV given a constant level of PWV fluctuations of 0.5% of the total PWV.

two beams would only see a difference of $z\theta \approx 0.2$ m patch of the atmosphere at a distance of 3 km above the telescope while the whole beam is 100 m wide (following the primary dish size), indicating that the beams heavily overlap at the relevant scale heights. Therefore, we would expect the power law behavior of MUSTANG-2 data to follow the $\mathcal{P} \propto (f\,[\mathrm{Hz}])^{-3}$ trend as observed in the real data.

The shape of the power spectrum is also influenced by both the absolute level of PWV and its fluctuation strength along the line of sight, as illustrated in Figure 4.5. The top panel shows the power spectrum as a result of varying the turbulence, which is characterized here as the fractional PWV RMS along the line of sight. Here, we froze the PWV value to 7.7 mm. We plot the synthetic TODs along with real MUSTANG-2 observations, one of which is also shown in Figure 4.4, while the other is another real scan taken on the same day during worse weather conditions. The absolute level of PWV corresponds to the PWV level of the scan taken in worse weather conditions. In the bottom panel, we varied the overall PWV level while freezing its fluctuations scale to 0.5% (the level also used to reproduce the real time stream shown in Figure 4.4). In order to match the atmospheric power at small f for the scan taken in worse weather conditions, Figure 4.5 shows that not the level PWV, but rather a higher level of fluctuations (i.e., turbulence) is needed to reproduce the observations and is thus more indicative of observing bad weather.

The overall similarity between the mock and true time streams of Figure 4.4 is further confirmed by conducting a k-sample Anderson-Darling test between the two time streams depicted in Figure 4.4. The tests yield a p-value smaller than $p < 0.001$. This result strongly indicates a high level of agreement between the real and mock datasets.

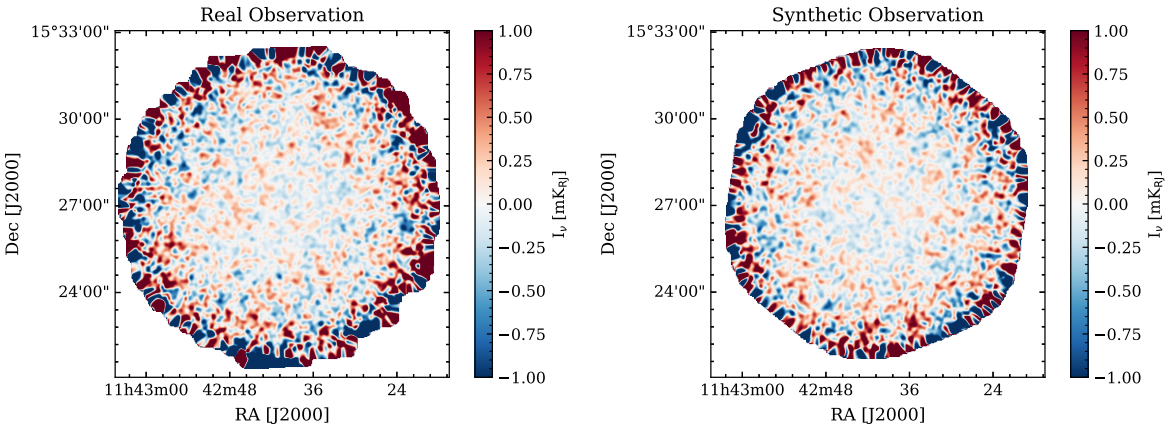

Figure 4.6: Noise maps, in units of Kelvin Raleigh-Jeans brightness temperature ($K_{\rm RJ}$), for a real (upper) and a mock (lower) observation. These maps are made using the 8.6 minute long scan shown in Figure 4.4 with the mapmaker implemented in `maria`. For both the real and synthetic maps, we find an RMS of 148 ± 3 $\mu{\rm K}_{\rm RJ}$ when estimated within the central $1'$ region. Here, we corrected the sensitivity of the mock observation with the square root of the ratio of the differences in detectors used. The real observations utilized only 170 detectors out of the 217 available.

4.2.2 Comparing noise maps

Transforming a synthetic time stream into a map of the sky is an art of its own. As `maria` is designed specifically for generating synthetic time streams, we also implemented a simple, easy-to-use Python-based mapmaking tool into the routine, which we based on MIDAS, the MUSTANG IDL Data Analysis System[6] (see Romero et al., 2020, and references therein). But as `maria` is a generic tool that can simulate various different telescopes and observation strategies, one might not always want to use the same mapmaker. Hence, we also made the TOD exportable to FITS tables and Hierarchical Data Format (HDF5) files so that one can use whichever mapmaker they prefer.

Briefly, the mapping tool we developed works as follows: Before binning the TODs into pixels (as also shown on the right panel of Figure 4.2), we Fourier filter the time streams to remove scales larger than the FoV (in the case for MUSTANG-2 this translates to $f = 0.08$) which we assume to be atmosphere dominated. Additionally, in `maria`, common modes arise solely from the modeled atmosphere (e.g., two adjacent detectors observing the same patch of the atmosphere). Thus, we remove the common mode before mapmaking by subtracting the first mode fit in a singular value decomposition (SVD) performed on the Fourier-filtered time streams. Then, we estimate the average amplitude of the signal measured by all detectors falling within a pixel to create a map. Finally, we smooth the map with the resolution of the telescope (defined as $\theta = 1.22\lambda/D$). The Fourier-filtered and common-mode subtracted maps for both the real and synthetic time streams are shown in Figure 4.6, revealing that the resulting noise maps are

[6]MIDAS when fully unraveled stands for the *MUltiplexed Superconducting Quantum Interface Device Transition Edge Sensor Array at Ninety Gigahertz Interactive Data Language Data Analysis System.*

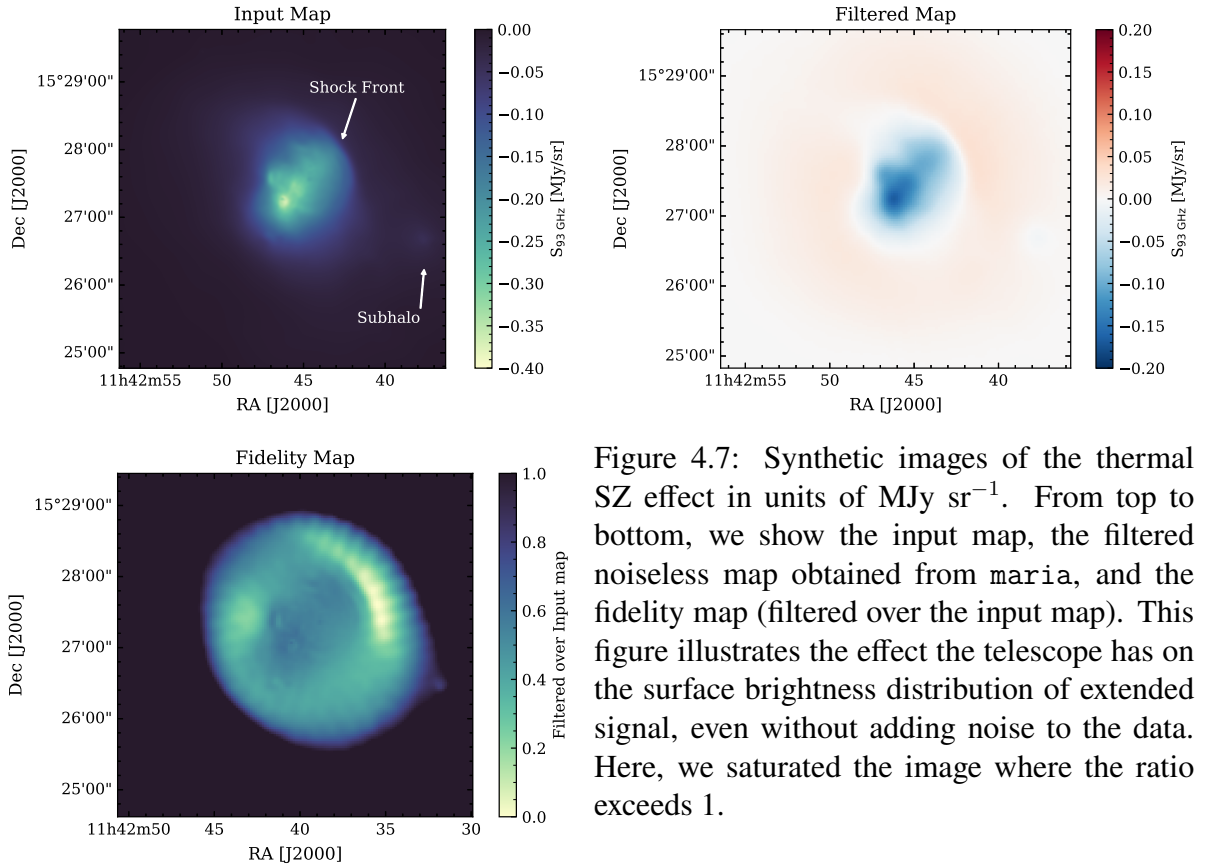

Figure 4.7: Synthetic images of the thermal SZ effect in units of MJy sr^{-1}. From top to bottom, we show the input map, the filtered noiseless map obtained from maria, and the fidelity map (filtered over the input map). This figure illustrates the effect the telescope has on the surface brightness distribution of extended signal, even without adding noise to the data. Here, we saturated the image where the ratio exceeds 1.

qualitatively similar.

Even though the fake and real scans show similar characteristics and sensitivities, we want to point out several second-order effects that can still cause minor differences between the real and mock data. The most notable one is that on timescales of an hour, the weather at the Green Bank site might vary, for instance, becoming cloudy. This can worsen or suddenly improve weather conditions, which might not be modeled in maria and lead to variations in the effective beam size. Additionally, surface deformations of MUSTANG-2's primary dish change the effective shape of the beam, which needs to be accurately calibrated. Further, the scanning strategy maria adopts is not exactly the same as that used by the GBT in MUSTANG-2 observations, as the real one features a less regular scanning trajectory.

Further, our model for the $(1/f)$ noise components is likely an oversimplification, as correlations in the instrumental $(1/f)$ noise are not fully accounted for in the maria simulations. A better characterization of which part of the optical/signal path (e.g., amplifiers, readouts, detector thermal drifts, optical loading due to spillover, or surface deformations) causes which noise contribution in the noise power spectra could help improve the noise model when making maps. Finally, the real observations include contamination in the form of spikes at high sampling frequencies ($f\ [\mathrm{Hz}] > 2$) that could originate from the pulse tube or other vibrating objects mounted on the GBT such as the feedarm.

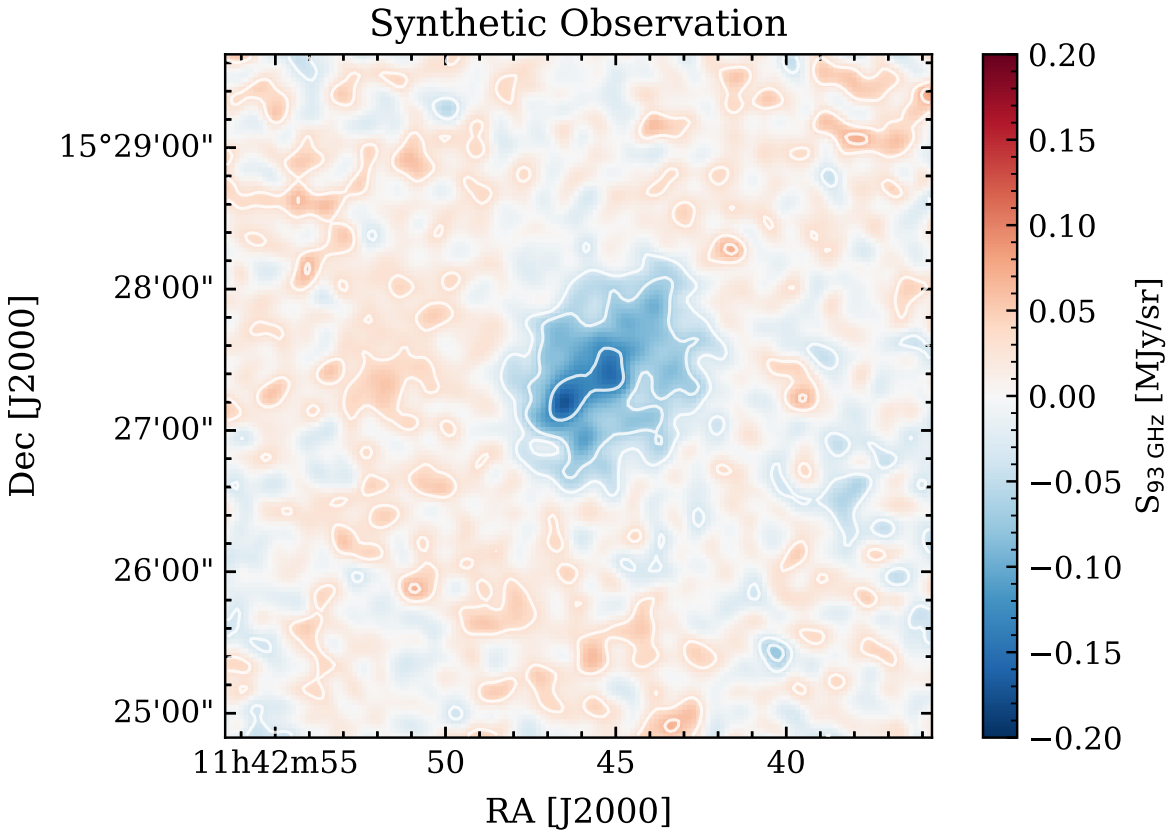

Figure 4.8: A 45-minute long mock observation of the thermal SZ effect as seen by MUSTANG-2 on the Green Bank Telescope generated with `maria`. The mock observation includes atmospheric and $1/f$ (pink) noise. The time streams are Fourier filtered and common-mode subtracted before imaged. The contours are drawn at $[-8, -4, -2, 2, 4] - \sigma$ with σ obtained from a circular aperture from the central region in a source-free run.

4.2.3 Forecasting MUSTANG-2 observations

As described in Section 4.1, `maria` offers the option to scan over a celestial object while traversing the atmosphere and as the noise properties `maria` derives are close to reality (as described above), we can consequently make mock observations for MUSTANG-2, akin to how CASA `simobserve` works for interferometric observations. To illustrate, we use a map of the thermal SZ effect from a galaxy cluster extracted from the "Dianoga" hydrodynamical zoom-in simulations (Rasia et al., 2015). Following the methodology employed by Di Mascolo et al. (2023), we transformed the particle information into a projected high-resolution Compton-y map of the hot gas within the intracluster medium (ICM) of a galaxy cluster. An example of such a map is shown on the top panel of Figure 4.7. This panel shows a cluster at $z = 1.0$ with a halo mass of $M_{500,c} = 8 \times 10^{14}$ $\mathrm{M}_\odot$. Here, we define $M_{500,c}$ as the mass of the system within a radius having an average density of 500$\times$ the critical density of the Universe at that redshift. This cluster is undergoing a merger, showing

features due to merger-driven shocks in the north and an additional faint subhalo component to the west of the main cluster.

To make mock MUSTANG-2 observations from this cluster, we used our mapmaking tool following the exact same procedure as described in section 4.2.2. We first ran maria without white, $1/f$, and atmospheric noise to show the effects the scanning, spatial resolution, filtering, processing, and common-mode subtraction have on the input map. The results of the "filtered" map are shown in the middle panel in Figure 4.7. Then, the ratio of the filtered map over the input map is shown in the bottom panel of Figure 4.7, which we will refer to as the fidelity map. We smoothed the input with the diffraction-limited beam before computing the fidelity map to prevent beam-smearing effects. We also shifted the flux of the filtered map so that the maximum pixel has a flux value of 0 to correct for any dc-offset between the two maps. We saturated the image where the ratio exceeds 1.

The common-mode subtraction and Fourier filtering cause the peak flux to drop by a factor ≈ 0.5. The fidelity map illustrates the difficulty in retrieving the astronomical signal. The two features described previously, namely the distinct shock front and the fainter subhalo, are visible in the fidelity map, meaning that they are suppressed in the filtered map and consequently in the observation itself. A peak flux reduction of $\approx 50\%$ can significantly impact the possibility of detection, as also seen in Figure 4.8. Figure 4.8 shows the full mock observation of the cluster in which we add the atmosphere, pink, and white noise to the time streams. This 45-minute long execution block clearly detects the tSZ effect with a peak SNR of -8σ; however, the shock front and the more extended, faint features of the cluster go undetected.

To further quantify the scale dependence of how information is lost due to filtering and processing, we compute the transfer function of the filtered map with respect to the input map (see Figure 4.9). Here, the transfer function is defined by taking the square root of the power spectra of both a noiseless and noisy 45-minute-long mock observation and dividing it by the power spectra of the input map. To prevent the power spectra from blowing up at large wave numbers (smaller scales), we added white noise to the image at a level of a tenth of the measured sensitivity in the central region in Figure 4.8. The power spectra are estimated by binning the Fourier transform of the map in log-spaced bins from $0\,\mathrm{k}\lambda < k < 40\,\mathrm{k}\lambda$ and taking the average of the amplitude of the Fourier transform per k-bin. The "noiseless" curve shows the ideal transfer function for the observations. It exhibits a flat k-dependence up to $\approx 30''$, after which it drops to ≈ 0.5 by $\approx 300''$, which is similar to what is derived from the fidelity map shown in Figure 4.7 and agrees well with real MUSTANG-2 observations (see e.g., Romero et al., 2020)

However, we note that the transfer function drops partially because of the Fourier filter applied to the streams before making maps. More advanced mapmakers, which adopt a maximum likelihood mapmaking approach, such as the mapmaker used with ACT observations (Dünner et al., 2013) and minkasi (Sievers et al., in prep), have indicated a more flat transfer function, e.g., being better equipped to recover larger angular modes at converged scales (see, e.g., Romero et al., 2020). Nevertheless, Figure 4.9 shows that regardless of the noise in the observations, scanning over a source reduces the recovered signal, and hence, the real observations must be corrected for such a transfer function. In future work, we will go into more depth on how well one can recover the input given the synthetic time streams. We will test current "observational" tools on how to retrieve radial surface brightness profiles and generic properties such as the halo

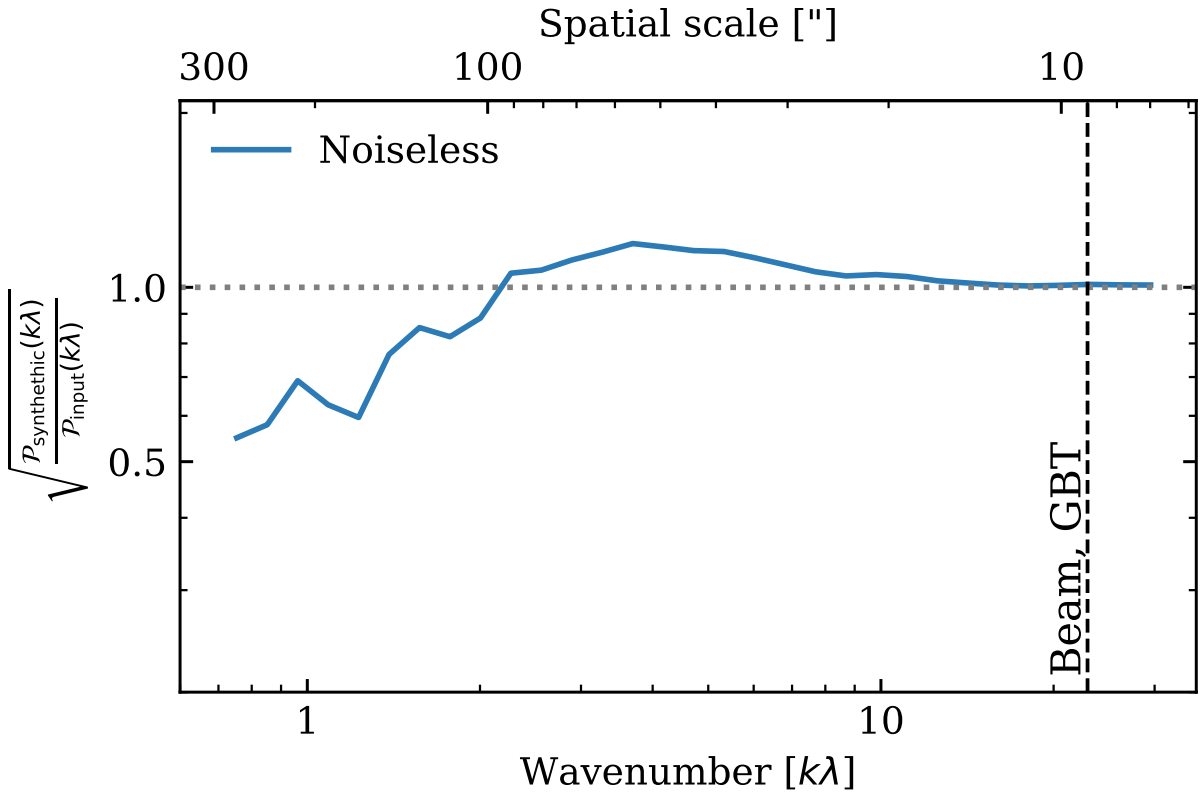

Figure 4.9: Transfer function of the mock MUSTANG-2 observation, derived from the power spectra of the filtered map shown in Figure 4.7. The transfer function is normalized by that of the input map shown in Figure 4.7 and smoothed with a top hat function.

mass of the cluster, as well as the feasibility of measuring features such as subhaloes and shock fronts. In this work, we focus on illustrating `maria` and how we can use it to create synthetic observations to study the feasibility of current, as illustrated in this section, and future facilities. We will further expand upon the latter in the next section.

4.3 AtLAST forecasts

To illustrate that `maria` can be used to evaluate science cases for future facilities, we provide a section on adjusting the simulation class for an AtLAST-like observation done with a relatively small-scale bolometer array design. We will also briefly discuss the performance of such a telescope in comparison with other single-dish facilities. In particular, we discuss the noise properties of the time streams and their level of common modes (see Section 4.3.2) as well as the sensitivity at beam scales (see Section 4.3.2). We will also make synthetic images of a galaxy cluster that comes from the Diagona hydrodynamical simulations for this simulated instrument and compare them and the resulting transfer function with that of MUSTANG-2 (see Section 4.3.3).

4.3.1 Simulation set up

AtLAST, as mentioned in Section 4.1.1, is an ongoing design study for a 50-meter single-dish facility to be located in the Atacama desert near ALMA. AtLAST's concept is that of a facility observatory hosting up to six massive instruments and serving a wide range of science cases. For the purpose of this work, we focus on a particular observing mode, class of instrumentation, and science goal, but we note that future works will explore AtLAST's observing capabilities more broadly as well as make forecasts for its scientific applicability. We note here that the telescope will have a 4.7-meter focal plane, corresponding to an instantaneous field of view of 2°, and will allow extremely fast scan velocities of up to $3^\circ\,\mathrm{s}^{-1}$ (e.g., in the middle of an azimuthal scan), and an acceleration of up to $1^\circ\,\mathrm{s}^{-2}$ as defined in Klaassen et al. (2020).

To Nyquist sample the beam, which has a FWHM $\theta = 1.22\lambda/D \approx 16''$ for a 50-meter telescope at 93 GHz and assuming an average scanning velocity of 1°/s, we need to scan with a read-out rate $90\times$ that of MUSTANG-2, resulting in a sampling of 900 Hz. AtLAST will also observe at high frequencies up to $\nu \approx 950$ GHz, increasing the rate to ≈ 9 kHz. Furthermore, to maintain the same sky sampling, the number of detectors increases with the frequency squared if the FoV size remains constant. For the 93 GHz band, we need $\approx 200,000$ detectors to fill the 2° FoV with the detectors placed at $1f - \lambda$. Hence, for the high-frequency ($\nu = 900$ GHz), AtLAST would need 20 million detectors to fill the FoV. Fortunately, as noted in Klaassen et al. (2020), the number of detectors increases by roughly a factor of ten every seven years, implying that instruments comprising of order 1 million detectors could be expected by 2030. However, both the high sampling rate and the number of detectors in the array result in stupendously large data rates. Simulating this with `maria` is thus computationally expensive and requires a large working memory ($>$ 1TB). The MUSTANG-2 mock observations can be run on a 2019 MacBook Pro with a 2.6 GHz 6-Core Intel Core i7 processor, but with the current implementation of `maria` (v1.0), an even bigger server (e.g., a 64-core workstation with 1 TB of random access memory) is not enough to mimic AtLAST-like configurations.

To temporarily overcome the data rate problem, we simulate here an instrument with a reduced FoV of only 0.25° ($15'$) and limit the maximum scanning velocity to $0.5^\circ\,\mathrm{s}^{-1}$, which occurs at the center of the daisy scan. This will limit the number of detectors to 3000 (a factor of 32 smaller than AtLAST could host) and lower the data rate by sampling at 225 Hz (12 times lower). These adjustments make the data rates feasible to run with `maria` as we continue to improve the efficiency of the code. For the remainder of this work, the observations are set to the following configuration: it will point at a source in the position of an RA and Dec of $(260.0^\circ, -10.0^\circ)$ at the date of 2022-08-01T23:00:00 which results in an average elevation of 57.3°. The default scanning radius of the daisy scan will be the size of the FoV. Furthermore, we will simulate one band for all detectors centered on 92 GHz with a bandwidth of 52 GHz, which is ideal for detecting the SZ effect at those frequencies. Finally, we will simulate the atmosphere to a scale height of 3000 meters above Chajnantor and use an RMS fractional variation in PWV of 5% to get a total temperature of around $T_{\mathrm{scan}} \approx 28\ K_{\mathrm{RJ}}$ which is a typical atmospheric value (Pardo et al., 2001) when observing at the APEX, ALMA, or future AtLAST site.

Further, we adopt the measured mean sensitivity of the PA6 array ($\mathrm{T} = 266\ \mu\mathrm{K}\ \sqrt{\mathrm{s}}$ at $\nu = 90$ GHz, Naess et al. in prep.) of ACT as a white noise level for each detector used in our

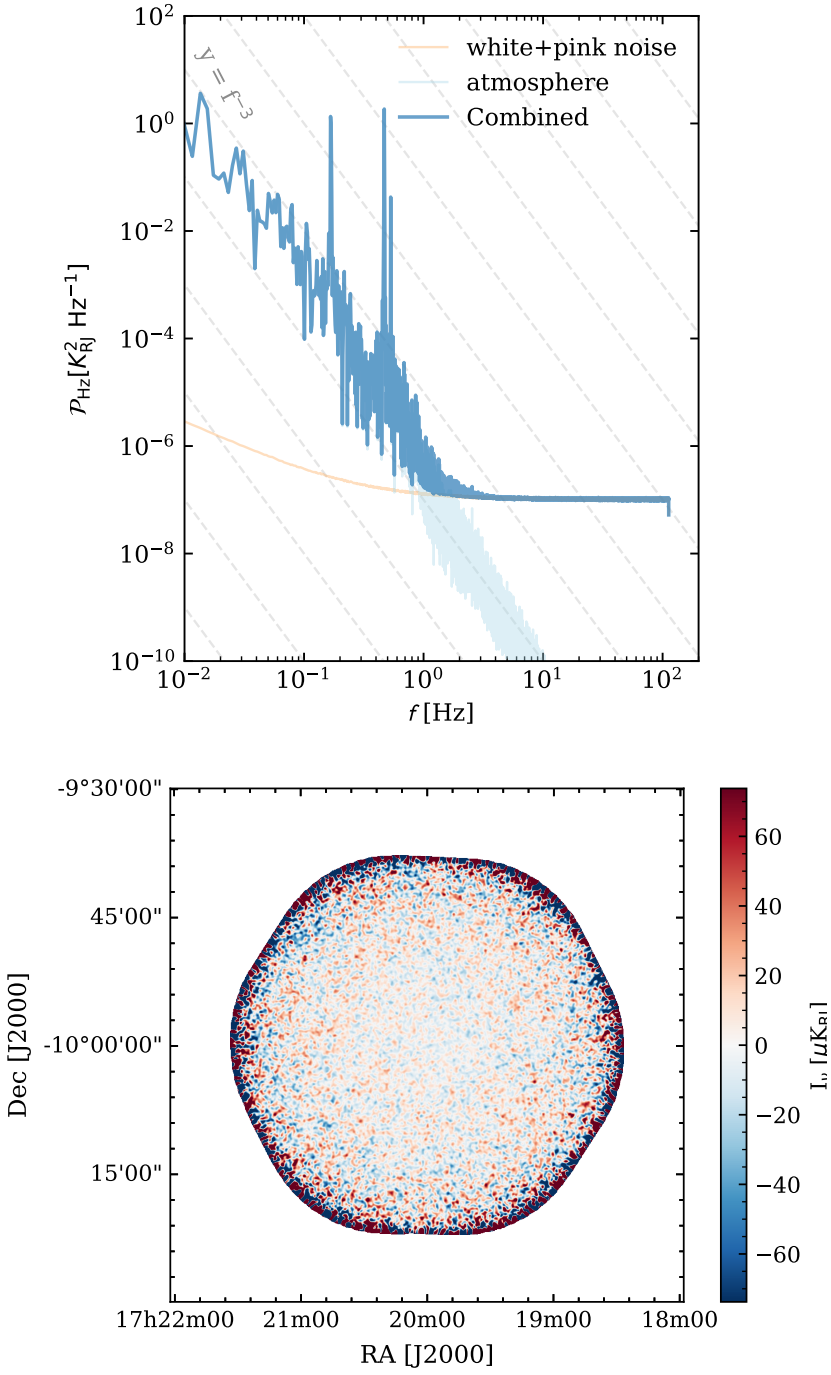

Figure 4.10: Simulated AtLAST noise power spectrum (upper panel) and the noise map (lower panel) resulting from an 8.6-minute long observing scan. The simulations are run assuming a broadband monochromatic imaging array centered at 93 GHz with 3000 detectors with a 0.25° instantaneous FoV. The time streams are common mode subtracted and Fourier filtered before imaged. More details of the observational setup can be found in Section 4.3. The resulting RMS of the noise map is 12.0 μJy/Beam which is equivalent to 12.2 $\mu{\rm K}_{\rm RJ}$.

setup. As the ACT detector noise performance is nearly background-limited, better sensitivities per detector per time stamp cannot easily be achieved. Further, we normalized the ACT sensitivity with the ratio of the different bandpasses and corrected for the optical efficiency we simulated; Here, we assume similar optical efficiencies as for the GBT and MUSTANG-2. The resulting white noise level is four times lower than that of MUSTANG-2. Then, we scaled the pink noise

level down from what we used in the MUSTANG-2 case with the same amplitude as the difference in the white noise levels. All this results in an antenna temperature of around $T_{\rm scan} \approx 72\ K_{\rm RJ}$ after correcting the time streams for the optical efficiency and the atmosphere's opacity. The resulting power spectrum and noise map are shown in Figure 4.10.

Before making this map, we highpass filter the time streams in Fourier space to remove scales larger than the field of view (i.e. $\lesssim 0.5$ Hz in the time domain, depending on the scanning speed). We then remove the first principal component, as is often done with real observations. The Fourier filtering removes the peaks caused by the scanning harmonics seen below 0.5 Hz in the upper panel of Figure 4.10. The Fourier filtering also removes most of the atmospheric contributions from the time streams.

4.3.2 Spatial scale considerations

When characterizing the noise properties of a telescope, two regimes need consideration. The first is regarding the recovery of large angular scales of the sky (low ℓ), crucial for applications such as CMB observations and line intensity mapping (LIM) experiments. The second regime involves the sensitivities at beam scales (high ℓ), which is essential for tasks like eliminating contaminating sources such as the cosmic infrared background or conducting targeted studies of, for instance, the circumgalactic medium in distant galaxies. In this section, we will briefly address both regimes.

Large spatial scales

In addition to collective area and resolution, one of the advantages of constructing a large ($\geq 30-$meter) single-dish telescope, such as AtLAST or CMB-HD (Sehgal et al., 2019, The CMB-HD Collaboration et al., 2022), turns out to be the enhanced correlation of atmospheric effects across beams of adjacent detectors, which facilitates better removal of the atmospheric signal.

In `maria`, we assume diffraction-limited beams, with a FWHM Gaussian beam defined as

$$\mathrm{FWHM}\ (z) = \mathrm{D}\sqrt{z^{-2} + z_r^{-2}}\ [\mathrm{rad.}]\,, \tag{4.6}$$

as a function of distance z perpendicular to the surface. Here, D is the size of the primary dish, and z_r is the Rayleigh height in meters which is defined as

$$z_r = \pi\,\frac{(\mathrm{D}/2)^2}{\lambda}\,, \tag{4.7}$$

where λ is the wavelength of the observation.

The Rayleigh height sets the boundary between the near and the far-field. From Eq. (4.7), we infer that in physical units (m), the near field beam behaves as a cylindrical column that transverses through the sky and diverges only at higher altitudes for larger dish sizes, as illustrated in Figure 4.11. Based on the geometry of the beam, we infer that a large dish sees more of the same atmosphere between two beams than a 6-m or a 42-cm aperture, which are the apertures sizes of the large aperture telescope (LAT) and small aperture telescope (SAT) used in Simons

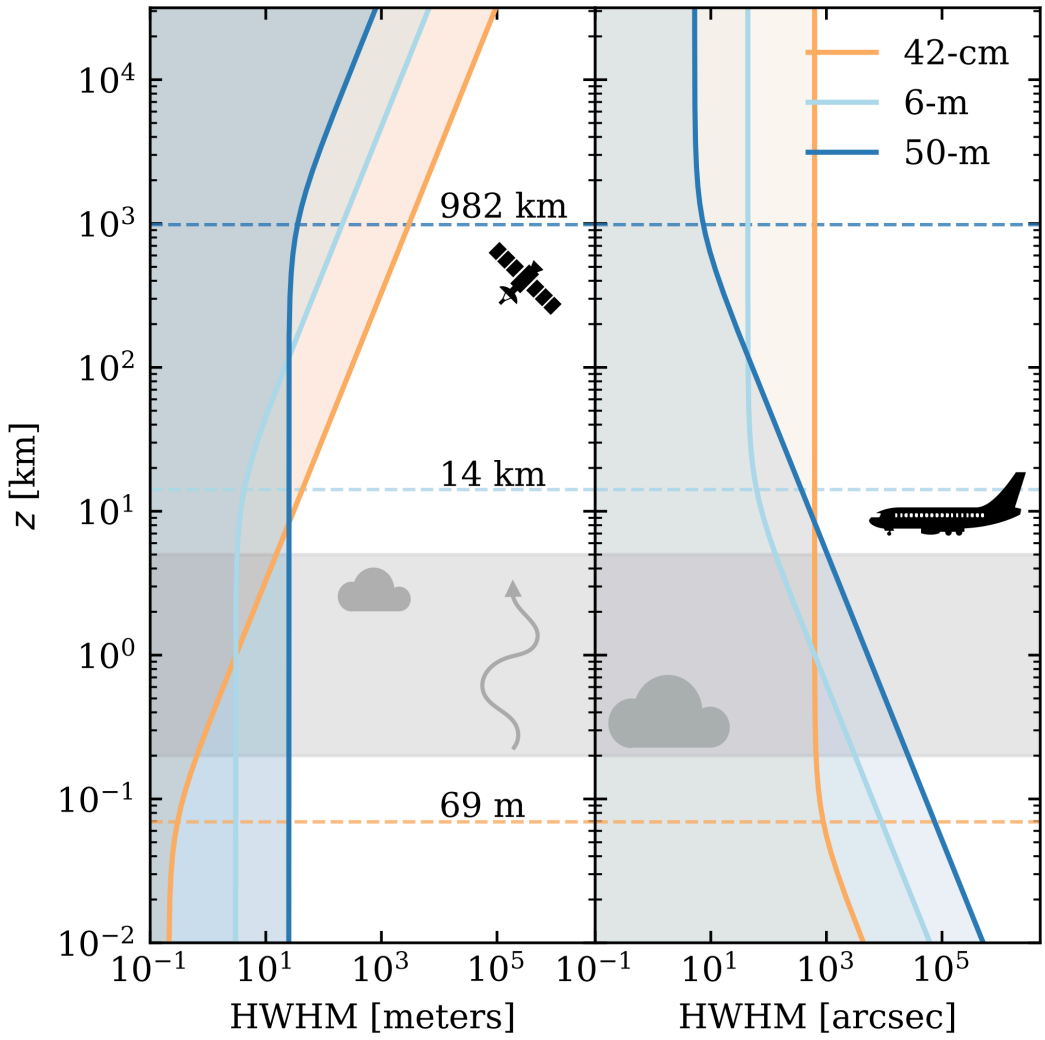

Figure 4.11: Illustration on how the geometry of how beams propagate through the atmosphere at a height z, perpendicular to the ground following Eqs. (4.6,4.7). The left panel shows the propagation in physical units (m), and the right panel shows it in angles (arcsec). We show three different beams corresponding to three different apertures, namely 42-cm (yellow), 6-m (light blue), and 50-m (dark blue). The Rayleigh heights of these beams are given at 150 GHz. In light gray, we show the heights where `maria` simulates the atmosphere ($z = 0.2-5$ km). For reference, we show the typical heights relative to Llano de Chajnantor of cumulus clouds, a passenger jet at cruising altitude, and the orbital radius of the International Space Station.

Observatory (SO, Ade et al., 2019). To illustrate, at a scale height of 1 km and adjacent detectors at 150 GHz spaced $1f - \lambda$ apart, with AtLAST, one detector's beam would be shifted only by 48 mm relative to the next adjacent beam (i.e. roughly one-thousandth of the 50 meter column of atmosphere probed in the near field). This implies that one detector sees 99.1% of the same

of the atmosphere as its neighbor. For the 6-m apertures, the same considerations imply the shift would be 87.9%, making time-lagged atmospheric signal removal more difficult. For the 42-cm, this would be even worse; however, as Figure 4.11 shows, a 42-cm aperture results in an extremely short near field, with the beams beginning to diverge around 69 meters, thus increasing the overlap in the instantaneous volumes of the atmosphere probed, which also should facilitate better atmospheric removal in post-processing.

With `maria`, we can test the trade-off between having a short near field with quickly diverging beams versus a more extended near field probing a larger column of common atmospheric signals. To quantify the observed degree of correlated atmosphere for different types of aperture sizes (42-cm, 6-m, and 50-m), we compare various eigenvalues of the first principal component using a principal component analysis (PCA) on time streams simulated with only atmospheric contributions. Since PCA is not scale-invariant, we standardized the time streams of various mock observations before estimating the eigenvectors. When setting up the arrays in `maria`, we placed 3000 detectors in a 2° FoV for all three aperture sizes. Therefore, the detectors in the array that correspond to an aperture size of 50-m will be spaced farther from each other in terms of $f - \lambda$ than the 6-m and 42-cm apertures because of the different beam sizes. Due to this sparseness, both the 50-m and 6-m cases have detectors in their array spaced beyond $2\ f - \lambda$, but the beams overlap for the 42-cm aperture. The detectors were then set up to stare through the atmosphere for a period of 60 seconds at the Llano de Chajnantor site. This experiment is thus set up similarly to the example outlined above.

Figure 4.12 shows a boxplot of the cumulative contribution rate of the first eigenvalues from 50 different atmospheric runs for two types of common modes: the time-lagged common mode and the instantaneous one. The instantaneous component measures the degree of common modes for all detectors in the 2° FoV integrated over half a second of integration time, which, as outlined above, should be larger for the 42-cm apertures. However, this is not significantly measured, as shown in Figure 4.12. This could be due to the low level of turbulence in the atmosphere at the Chajnantor site. In that case, even for non-overlapping beams, the observed atmosphere is still heavily correlated over the 2° FoV, thus reducing the advantage of overlapping beams for small apertures.

Regarding the time-lagged common mode, we performed the PCA on two neighboring detectors for all simulated time steps (1 minute of simulated TODs). From the back-of-the-envelope estimate above, the 50 m dish should detect more correlated atmosphere when it transverses through the cylindrical column than the smaller-sized apertures. The results shown in Figure 4.12 indicate that the 6 m and 42 cm scenarios perform less well than the 50 m dish by 1.6σ and 2.5σ, respectively, which is in line with the calculation outlined above. This suggests that the 50 m dish telescope has the highest level of measured common mode signal in the time streams.

A fundamental assumption here is that a higher level of common mode signal should allow for better mitigation of the atmosphere, leading to the recovery of lower ℓ. This simulation shows that a 50 m dish could better recover signals at lower ℓ than 6 m or 42-cm sized apertures for a similar FoV. ACT has already demonstrated with a 6 meter aperture and 1° FoV the ability to recover scales down to $\ell \approx 350$ (see, e.g., Coulton et al., 2024, Qu et al., 2024). Therefore, even if one assumes that the spatial scales one can recover are limited to scales less than or equal to the size of the FoV, this implies that AtLAST could also carry out CMB observations on similar

or larger angular scales than the current CMB experiments.

We note, however, that the comparison here limits all three aperture-sized telescopes with a FoV of 2°, while the SATs in SO will have $\approx 30^\circ$ FoV, which implies the recovery of even lower ℓ, although the atmosphere at these scales will not be as correlated. Regardless, this experiment highlights the need for techniques to mitigate atmospheric effects, both in hardware (for instance, by utilizing half wave plates) and in software (such as to improve upon the entire TOD to map pipeline). Additionally, the trade-off of having a large > 30 m single dish telescope is to be also sensitive to high-ℓ.

Small spatial scales

Regarding the sensitivity at beam scales (high ℓ), we can compare `maria` simulations with the predictions from the AtLAST sensitivity calculator.[7] There, the point source sensitivity is estimated by using the `CASA` corruption model set to *Total Power mode* (CASA Team et al., 2022) and scaling up the diameter of a single ALMA antenna to 50 meters. The sensitivity calculator is appropriate for maps of the line emission using state-of-the-art heterodyne instruments, which trade off a worse noise performance with respect to a bolometer to preserve phase coherence and achieve much higher spectral resolution ($R > 10^6$). However, this model does not account for correlated atmosphere, nor are scanning patterns implemented. Hence, using the sensitivity calculator to make forecasts for bolometric (e.g., broadband continuum) instruments is not ideal as it will act as if it has a single detector on the sky that will stare at the celestial object. Regardless, comparing the AtLAST sensitivity calculator with what `maria` outputs is a useful cross-check on results from `maria`.

The lower panel in Figure 4.10 displays the noise map for our simulated AtLAST observation, but with additional Fourier filtering and a common mode subtraction applied. Within the central $15'$ region, this map has a beam sensitivity of 12.0 μJy/Beam when assuming a diffraction-limited beam shape. In contrast to the AtLAST sensitivity estimator, which provides a sensitivity of 13.97 μJy/Beam for an 8.6 minute long observation scan[8], we find a slightly better per beam sensitivity (i.e., lower RMS) than theoretical predictions even without using the full AtLAST design specifics, and even though the 8.6-minute long integration time is distributed over the map, since the detector array moves on and off source as, for instance, it was for MUSTANG-2 (see Fig 4.2). Of course, the overall performance of `maria` depends somewhat on the actual instrument performance, and here we have conservatively adopted the same white and pink noise levels demonstrated by ACT. Regardless, the similar point source sensitivities appear to indicate that the two methodologies broadly agree.

4.3.3 Synthetic imaging

Without delving into the details of cluster astrophysics and the scientific advancements a telescope like AtLAST could bring to the field, we briefly demonstrate how to use `maria` to make forecasts

[7] See `https://senscalc.atlast.uio.no/`

[8] We used the average elevation of 57°, dual polarization mode, and a H_2O profile percentile of 25.

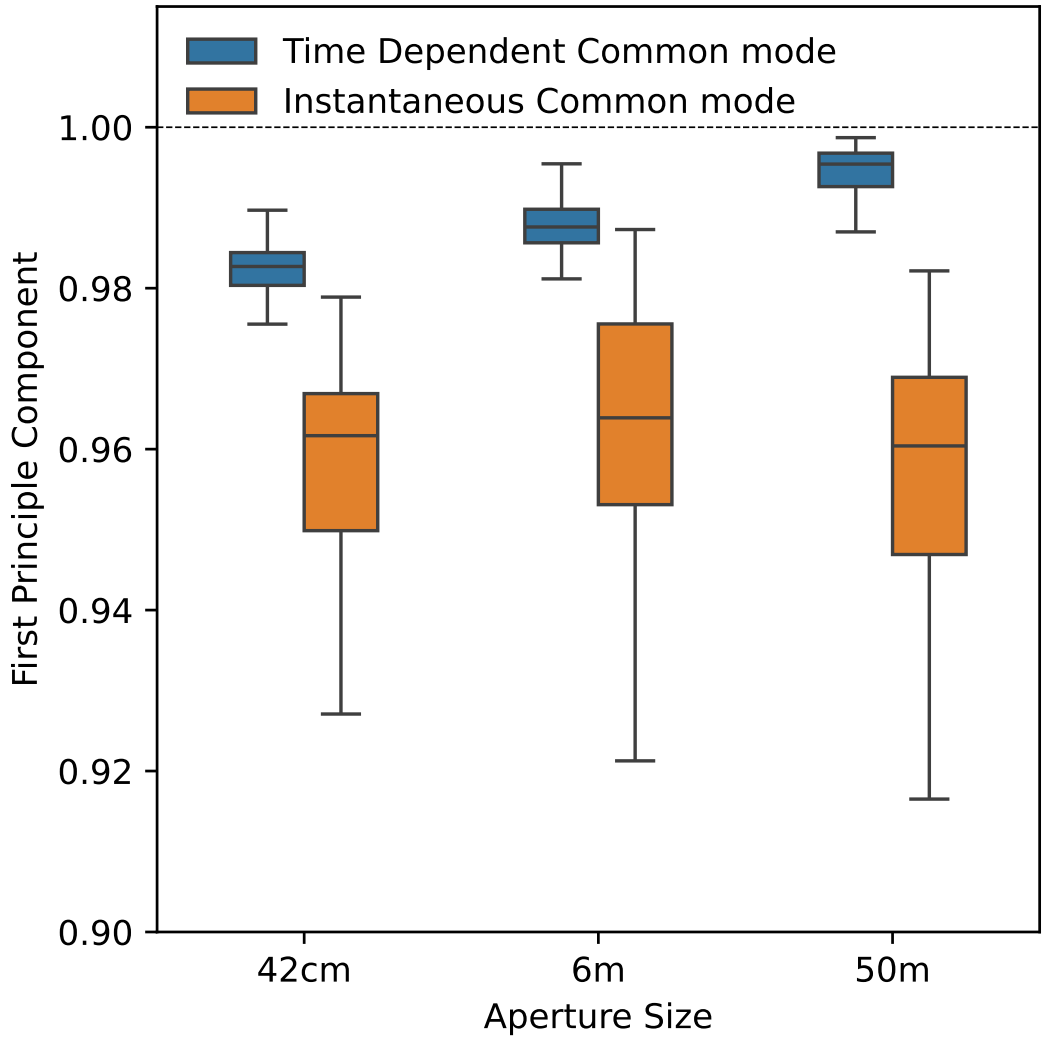

Figure 4.12: Estimated cumulative contribution rate of the eigenvalue of the first principal component of a time stream containing only atmospheric contributions simulated with a 42-cm, 6-m, and 50-m sized aperture. Here, we show the level of correlation between all the detectors for the whole 2° FoV for half a second of integration time (referred to as the Instantaneous Common mode) and for two neighboring detectors over a 60-second integration period (referred to as the Time Dependent Common mode). This figure indicates that the level of the correlated atmosphere is highest for the 50-m sized aperture.

for upcoming experiments like AtLAST and compare the resulting transfer function with that of MUSTANG-2 (see Section 4.2.3).

Using a similar approach as employed for the MUSTANG-2 case, Figure 4.13 shows the input map, the filtered map, and a synthetic observation of an output from the Diagona hydrodynamical simulation. The input maps represent the intracluster medium observed via the SZ effect from

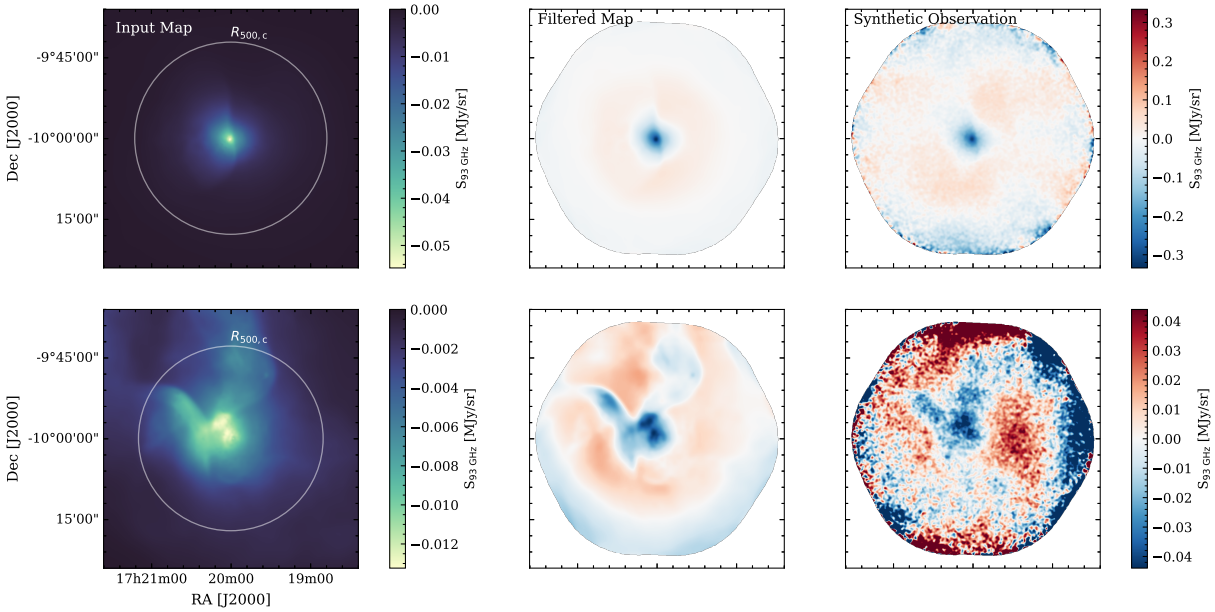

Figure 4.13: Simulated low redshift ($z = 0.0688$) clusters of galaxies, with masses $M_{500,c} = (8.8,\ 7.8) \times 10^{14}\ M_\odot$ (top to bottom), from the Dianoga suite of hydrodynamical simulations are shown on the left. The middle column shows an uncorrupted `maria` simulation of those clusters, highlighting the effects of an AtLAST-like transfer function. However, instead of simulating the complete $2°$ FoV, we mimic an instrument that only utilizes a $0.25°$ instantaneous FoV to facilitate simulation. The right column shows simulated observations, where atmospheric, white, and pink noise appropriate for 43 minutes of on-source integration time is added.

a cluster of galaxies. As an input, we used two clusters at $z = 0.0688$, with one exhibiting a more compact surface brightness distribution than the other, but both showing features due to cluster merger activities. The chosen redshift corresponds to a $1°$ FoV which corresponds to approximately 4.6 Mpc, roughly equivalent to $R_{200,c}$. The two clusters, with halo masses of $M_{500,c} = (8.8,\ 7.8) \times 10^{14}\ M_\odot$, are shown in that specific order in the first column of Figure 4.13.

Because of the low surface brightness and large projection on the sky, the only telescopes currently capable of detecting these clusters in the mm-wave regime are CMB-survey experiments, which typically have resolutions of $\approx 1 - 10'$ at 100 GHz. Thus, AtLAST-like observations with a resolution of $16''$ at 92 GHz could open new parameter spaces in cluster astrophysics. Such a telescope will be able to detect and resolve these objects as shown in the middle column of Figure 4.13. These filtered maps indicate that after applying the transfer function, the detailed structures are distinctly visible. Here, we lowered the frequency of the highpass filter in comparison to what we used to make the noise map in Figure 4.10, to not filter out the flux present at large scales. However, this led to a slight increase of predominantly atmospheric noise in the synthetic observation, as visible in the third and final column. These maps are made from 12 corrupted concatenated scans, each lasting 7.5 minutes, adding to 90 minutes of total integration time per cluster for the assumed instrument, which we emphasize is limited in detector count

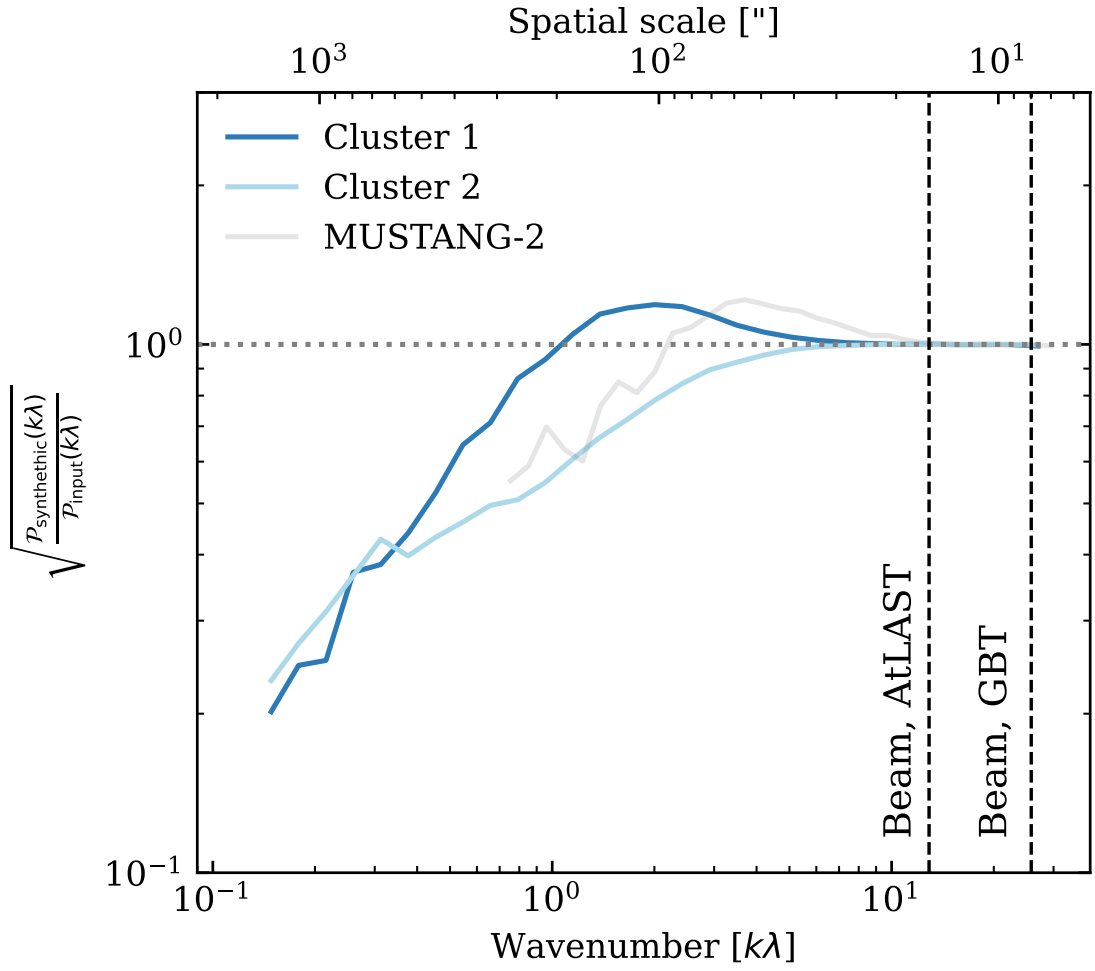

Figure 4.14: Resulting transfer functions of both clusters with cluster 1 corresponding to the first row in Figure 4.13. It is derived from the power spectra of the filtered map normalized by that of the input map. In gray, we show the equivalent function but from a MUSTANG-2 observation (see Figure 4.9).

compared to a future fully populated AtLAST focal plane (see Sect. 4.3.1). For both clusters, it is evident that the images are noisier than the map shown in Figure 4.10 because it is more difficult to separate the atmosphere from the extended signal at these scales ($> 15'$). However, both mock observations show clear detections of the interesting resolved features. This highlights the capabilities of a 50-meter single dish telescope like AtLAST with a $0.25°$ FoV equipped with 3000 detectors and a scanning velocity of $0.5°\mathrm{s}^{-1}$.

The contrast between the transfer function of these observations, shown in Figure 4.14, with respect to that of MUSTANG-2, also indicates how much better the larger FoV and higher mapping speed of AtLAST are at constraining larger spatial scales. The difference in transfer functions between both clusters comes from the difference in morphology and dynamical state.

4.4 Discussion and Summary

In this work, we utilized and further developed the atmospheric modeling tools that were first presented in Morris et al. (2022) to make forecasts for current and future single-dish facilities operating in the (sub-)mm-wave regime through bolometer arrays. We presented `maria`, now an open-source telescope simulator, and used it to generate synthetic time ordered data that recreate real observations. Furthermore, we built in a simplistic, Python-based mapmaker to facilitate interpretation for the broad user community.

The main drivers for this work were threefold. The first motivation is that the broader (sub-)mm community requires an easy-to-use, computationally efficient, and versatile simulator applicable to a variety of science cases, telescope sites, and designs. Section 4.1 provided the overview on how `maria` is set up to fulfill this goal. Second, `maria` enables a fair comparison between (sub-)mm observations with hydrodynamical simulations and other input models, as illustrated in Section 4.2. Henceforth, we can validate observational tools with these simulations. In particular, since the field of resolved SZ studies is now becoming more established, thanks to, for example, the wider bandwidth and sensitivity upgrades to ALMA (Carpenter et al., 2023) and the increased sensitivity of large single dish facilities, comparisons with hydrodynamical simulations are necessary to understand the systematic uncertainties in SZ analyses. The third and final motivation was to establish a connection between telescope designs, such as the number of detectors, field of view, and mapping speed, and the scientific goals for future facilities like the 50 meter Atacama Large Aperture Submillimeter Telescope (AtLAST). This objective was addressed in Section 4.3. However, regarding the latter goal, we simplified the instrument's capabilities to facilitate simulation. More comprehensive, large-scale forecasts will be presented in follow-up works, utilizing the AtLAST design's full field of view, polarization, and multichroic capabilities. For comparison, the data rates from mock observations will be $\approx 64\times$ larger when simulating a 2° FoV monochromatic instrument when simply filling AtLAST's focal plane. This highlights the fact that AtLAST, with instrumentation fully populating the field of view, will be firmly situated in the Big Data regime.

As this work illustrates in general the success of `maria`, it also has its limitations. Cosmic Microwave Background experiments or other single-dish simulators used for, for instance, the TolTEC Camera (see, e.g., Bryan et al., 2018) often refer to the Time-Ordered Astrophysics Scalable Tools package (`TOAST`, Puglisi et al., 2021, Kisner et al., 2023) or `BoloCalc` (Hill et al., 2018) to study systematic errors induced by the beam and calibration uncertainties. Apart from correlated atmospheric noise, `TOAST` and `BoloCalc` can also simulate cross-talk between detectors and scan-synchronous signals due to ground pickup as well as simulate leakage from total intensity to polarized light (Hill et al., 2018, Dachlythra et al., 2024). These noise contributions are not implemented in `maria`, nor are, for instance, surface deformations of the dish caused by gravity and thermal fluctuations. With `maria`, we simplistically assume diffraction-limited beams and uncorrelated pink and white noise. However, as demonstrated in Section 4.2, the noise corruption model implemented effectively replicates the noise characteristics observed in MUSTANG-2 data. Moreover, it's easily adaptable to other telescope configurations at different sites. Additionally, our implementation of the location-and-time-specific atmosphere in `maria`

stands out for its uniqueness while maintaining computational efficiency in computing the full evolving atmospheric volume.

Looking forward, we are working to increase the flexibility of `maria` as future versions will encompass the ability to observe in an interferometric mode where vector averaged phase delays can be computed as a function of baseline length. This could be relevant for ALMA long baseline and high-frequency campaigns done, for instance, since `maria` could function as an improved phase screen model required to reproduce the measured phase fluctuations (see e.g., Maud et al., 2023). Furthermore, future implementations of `maria` will be better equipped to simulate direct detection spectrometers as was done, for instance, in `TiEMPO` (Huijten et al., 2022). Currently, we advise creating "moment-0" maps with a small frequency width, while future versions will be able to generate mock observations to imitate observations using heterodyne and integrated field units with higher spectral resolution.

In closing, we emphasize that this work is meant to introduce a virtual (sub-)mm telescope simulation tool that is generic and applicable across several science fields, from observations of the Sun (M. Kirkaune et al., in prep) to the circumgalactic medium of galaxies (Schimek et al. 2024, Lee et al., in prep). Even though the synthetic observations in this work all show the intracluster medium as seen via the SZ effect, the tool is broadly applicable and will be featured in future work.

Chapter 5,

Conclusions & Future Outlook

The content of this chapter is partly based on the proposals I have written over the last three years, including one ALMA large program I PI'ed, and is inspired by the conferences I have attended.

Ik ken je het langst, jij kent mij het meest
Onderweg constant gevord door waar we zijn geweest
Met tijd gemeten groeiden we, maar jij iets meer dan ik
Waar je kijkt boven m'n hood zie ik de toekomst in je blik

De lucht gereflecteerd in de kleur van je ogen
Die lichten op wanneer je je verliest in hardop dromen
Uren tuurden we om het langst in de horizon
Waar je hem verbreedt, vergeet dan alsjeblieft niet waar hij ooit begon

Want, nu ben jij degene die gaat
Ik zeg je preventief ik heb je lief
Als ik je mis is het te laat
Maar afstanden zijn relatief
Want in jouw geval
Lees je wat in sterren staat geschreven
Je blik gericht op het heelal

We delen ons verleden, waarvan ik nooit zou vergeten
Hoe jij als enige zag dat tranen braken door m'n lach
In de vlucht waar ik me veel meer tegenkwam dan ik dacht
Eenmaal terug je vol geduld me met een knuffel had opgewacht

En vervolgens schreef je me wat jou was bijgebleven
Was dat je me kwam halen toen je kwijt was op het plein
Zoveel verhalen waar we elkaar nooit achterlaten
Want je maakt me de persoon die ik voor jou heb willen zijn

En nu ben jij degene die gaat
Ik zeg je preventief ik heb je lief
Als ik je mis is het te laat
Maar afstanden zijn relatief
Want in jouw geval
Lees je wat in sterren staat geschreven
Je blik gericht op het heelal

- Evina van Marrewijk

5.1 Summary

What objects form when overdensities first detach from the Hubble flow and emerge from the cosmic web? What characterizes them? And what impact do they have on the thermodynamical evolution of the Universe? In my thesis, I have studied the evolution of baryons, driven by a force that primarily acts on non-baryonic matter—gravity. I have examined this evolution within a small sample of objects that are the first to form in their respective epochs and lie at the edge of what is currently observable. In particular, I studied two redshift regimes at $z > 10$ and $z \sim 2$, which correspond to the epoch of reionization and thermalization of the Universe, respectively.

Chapter 2: At $z > 10$, the structures that are forming within the most massive overdensities are early-type galaxies. Together with my research group at ESO, I proposed new ALMA observations targeting a galaxy candidate thought to be at $z \sim 13$ to confirm its redshift and study the properties of the forming ISM. I analyzed the data using a novel technique I developed. By jackknifing the visibilities, we generated various noise realizations of the observation-specific ALMA measurement set. Then, by applying line-finding algorithms on the real and source-free image cubes, we sample the likelihood of a marginal detection being real without having to assume an underlying noise distribution. Through this method, I found no significant detection in the sub-mm for HD1 nor any of the other three galaxy candidates I studied that were posited to be at $z > 10$.

Determining whether faint astronomical sources are real is critical for many areas of astrophysics, where false-positive identifications of emission lines can lead to biases in derived physical properties. This is especially clear in cases of incorrect redshift solutions, which have profound implications for the number counts of the earliest galaxies, impacting our understanding of both cosmology and galaxy evolution. As technological advancements allow for the study of increasingly faint sources, the challenge of accurately characterizing those at the detection limit remains. To address this, I have made my analysis routine publicly available and easily accessible for others to use and applicable over a wide variety of science cases.[1]

Chatper 3: Moving along the history of the Universe to lower redshifts, $z \sim 2$, the most massive structures to form within overdensities are clusters/protoclusters of galaxies. At $z \sim 2$, these overdensities are massive enough to thermalize the gas to temperatures of $T > 10^7$ K. I studied the mechanisms driving the thermalization process, i.e., converting kinetic energy to thermal energy, in the most distant galaxy cluster detected in current wide-field surveys, XLSSC 122. High-resolution ALMA observations ($5''$, $\sim 15\times$ better than the initial observations identified it) revealed a subcomponent in the south of the cluster, where no X-ray emission was detected. Additionally, we found a temperature gradient with higher temperatures in the south of the cluster than in the north. This suggests the presence of a large bulk of low-density gas colliding with the main halo component, shock-heating the gas through a major merger.

Overall, we detected the SZ effect with 11σ significance in the ALMA+ACA+ACT observations and found a flattened inner pressure profile that is consistent with a noncool core classification with a significance of $\geq 3\sigma$. In addition to characterizing the dynamical state of the cluster, we provide an improved SZ mass estimate $M_{500,\mathrm{c}} = 1.66^{+0.23}_{-0.20} \times 10^{14}\ \mathrm{M}_\odot$. These

[1] See https://joshiwavm.github.io/jackknify/.

measurements are crucial for linking the cluster's thermodynamical parameters to cosmological parameters such as its halo mass. As upcoming CMB-survey experiments, like the Simons Observatory, are expected to find an order of magnitude more clusters at $z > 1.7$, these measurements can serve as templates to accurately convert the unresolved Compton-Y estimates to halo mass, pushing cluster cosmology to a previously unimagined regime.

Chapter 4: We introduce a versatile, user-friendly simulator to optimize scanning strategies and instrument designs to efficiently reduce atmospheric noise and filtering effects. We further use this tool to produce synthetic time streams and maps from hydrodynamical simulations, enabling a fair comparison between theory and reality. To generate synthetic time-ordered data, we developed a multi-purpose telescope simulator called `maria`, which implements a suite of telescope and instrument designs intended to mimic current and future facilities. Each mock observatory scans through the atmosphere in a configurable pattern over the celestial object. We generate evolving and location-and-time-specific weather for each of the fiducial sites using a combination of satellite and ground-based measurements. While `maria` is a generic virtual telescope, this study specifically focuses on mimicking broadband bolometers observing at ≈ 100 GHz.

To validate our virtual telescope, we compared the mock time streams with real MUSTANG-2 observations and find that they are quantitatively similar by conducting a k-sample Anderson-Darling test resulting in a $p-$value of $p < 0.001$. Subsequently, we image the time-ordered data to create noise maps and realistic mock observations of clusters of galaxies for both MUSTANG-2 and a small-scale instrument concept for the 50 m Atacama Large Aperture Submillimeter Telescope (AtLAST). Furthermore, using `maria`, we find that a 50 m dish provides the highest levels of correlation of atmospheric signals across adjacent detectors compared to smaller apertures (e.g., 42-cm and 6-m survey experiments), facilitating removal of atmospheric signal on large scales. This is because of the geometry of the beam: the transition between the near- and far-field is proportional to the dish size. Hence, for large single-dish facilities, the beams propagate as a single column through the sky, increasing the level of common modes measured between two readouts. This indicates that 50 m+ facilities, although more expensive to build, might be excellent for studying the CMB at both small and large angular scales. Additionally, the simulator is open source, and we provided tutorials to help the user community implement it in their own work.[2]

5.2 Future outlook

Returning to the initial questions posed, pushing (sub-)mm observations of objects to the redshift at which they are forming is challenging. All ALMA observations of $z > 10$ galaxy candidates are consistent with noise, leaving the corresponding ISM density and ionization parameter yet unconstrained. Regarding my studies on clusters of galaxies, observations like those I conducted with XLSSC 122 are unique. Clusters discovered in other works are often contaminated by bright galaxies (e.g., Gobat et al., 2019, Di Mascolo et al., 2023) or lack the spatial resolution and sensitivity to map the SZ effect from the core ($\sim 5''$, ~ 40 kpc) to beyond the virial radius

[2] See `https://thomaswmorris.com/maria/`.

($\gtrsim 4'$, $\gtrsim 2\,$Mpc). Therefore, our interpretation of what drives the reheating of the Universe is currently limited to a single source, which might not be representative of the population as a whole. Additionally, different hydrodynamical simulations vary in their predictions of how thermal energy evolves over time (Chen et al., 2024). So even though we now have the tools to compare apples with apples (mock observations of simulations with real observations), we do not have a large enough sample of clusters at high$-z$ to constrain the simulations.

Without being overly pessimistic about my own work, I believe I have presented in this thesis important first steps in the initial characterization of these objects, improving the set of tools available to study them, which are now ready when new observations or simulations arise. In the following and final section, I will conclude my thesis by outlining how I see the future evolving within my fields of interest. I will begin by discussing the near future and how I plan to continue my work before providing a broader perspective.

5.2.1 ALMA observations of z>10 galaxies (not candidates)

Given the rapid evolution of this research field as outlined in the introduction and Chapter 2, I based the following subsection on a simple archival search to identify upcoming observations related to EoR galaxies in the sub-mm wavelengths. The broader perspective provided is informed by discussions and interactions I hat at the ALMA WSU conference and the AtLAST conference.

As previously eluded to in the introduction, this field of research has grown massively over the last two years. For instance, the initial work we did focused on confirming the presence of these types of galaxies through observations executed in the sub-mm wavelengths, while in the following work, we already shifted to use ALMA as a targeted follow-up facility to JWST. JWST has now spectroscopically confirmed over 20 galaxies at $z > 10$, surpassing ALMA in its efficiency in confirming these objects through spectral line observations (Harikane et al., 2024b). The success of JWST, however, does not make ALMA (or any other(sub-)mm-wave facility) absolute. They are still key in deriving the physical properties of the ISM, such as their star formation history, gas metallicity, and total dust mass. These types of observations are key to determining how the first stars are formed and how strong the ionizing photon radiation is, the mechanism that drives the reionization of the Universe as a whole.

Regarding the near future, two additional DDT observations targeting $z > 10$ galaxy candidates have recently been completed.[3] The first project aims to confirm the redshifts of three massive objects through ALMA spectral line scans focusing on the [O III] 88 µm line. This approach follows similar attempts by Harikane et al. (2022), Kaasinen, **van Marrewijk** et al. (2023), Yoon et al. (2023), Fujimoto et al. (2023), Popping (2023), and Bakx et al. (2023), which were ultimately unsuccessful. According to the project abstract, these objects are among the brightest $z \sim 12$ candidates that JWST is expected to find. The masses of all three objects show a mild 2σ tension with the predictions of ΛCDM.

However, I find the latter two projects more exciting. The proposers aim to follow up on Glass-z12 (see also, Popping, 2023, Bakx et al., 2023, regarding 2023.A.00017.S) and Gl-z14

[3]They have project codes 2023.A.00003.S, 2023.A.00037.S, and 2023.A.00017.S.

(Carniani et al., 2024, regarding 2023.A.00037.S) with observations targeting [O III] 88 µm and [O III] 52 µm in Bands 6 and 8, respectively. As explained in Chapter 2, JWST/MIRI measurements of the Hα line have already constrained the redshift to the order of one ALMA spectral window. This significantly reduces the data volume by avoiding the need to search a full spectral scan eight times the size, thereby reducing the likelihood of a false detection. Moreover, observations of the [O III] 5007 Å line provide a lower limit on the electron density of the Strömgen sphere (Zavala et al., 2024), allowing for a more educated estimate of the sub-mm line fluxes. If detected, the combination of the various [O III] lines can accurately constrain the ionization parameter and density of the ISM through `Cloudy` modeling. This proposal thus aims to go beyond a simple redshift confirmation, enabling a deeper understanding of the physics that govern these EoR galaxies (see, e.g., Fujimoto et al., 2024, Zavala et al., 2024).

It is only a matter of time before ALMA achieves the first robust detection of a $z > 10$ galaxy. The non-detections reported so far have already provided valuable insights into ISM physics through the established upper limits, but if successful, the abovementioned observations could set the standard for future studies. However, this field of research will only come into its own with the introduction of ALMA's Widefield Sensitivity Upgrade (WSU; Carpenter et al. 2023). With the doubled correlated bandwidth, performing blind line searches will become approximately $4\times$ faster. Additionally, with quadrupled correlated bandwidth, there is even the possibility of detecting multiple lines simultaneously (Bakx & Dannerbauer, 2022, Carpenter et al., 2023), thus strengthening the redshift solution. Furthermore, the continuum mapping speed will increase by $3\times$ for a $2\times$ bandwidth and $6\times$ for the $4\times$ bandwidth due to the increased bandwidth and more efficient electronics (Carpenter et al., 2023). This improvement will hopefully enable continuum measurements of the thermal radiation emitted by dust grains. The latter is crucial for properly correcting optical and NIR measurements for dust attenuation, thereby providing more robust measurements of the stellar mass necessary for cosmological interpretations of the observations. Finally, when the ngVLA becomes operational, it will offer the ability to study molecular lines, such as CO(3-2) and CO(2-1), for galaxies at through absorption w.r.t. the CMB $z > 10$(da Cunha et al., 2013, Decarli et al., 2018) and [C II] 158 µm in emission for $z > 15$ (Carilli et al., 2018). These observations will be valuable for directly comparing EoR galaxies with their later counterparts using the same line diagnostics.

ALMA and ngVLA will be the optimal telescopes for targeted follow-up, but what they won't provide is an unbiased wide-field cosmological view of the (sub-)mm Universe. Due to the inherent nature of interferometers, they will have limited fields of view (FoV; $\approx 1'$), making blind line searches without any prior knowledge from the optical or NIR data extremely inefficient. Single-dish facilities can have a much larger instantaneous FoV. For instance, the Atacama Large Aperture Submillimeter Telescope (AtLAST; Booth et al. 2024) design study advocates for a 50m single-dish facility located in the Atacama Desert. It will have spectral coverage similar to ALMA but with a 2° FoV while maintaining approximately $1''$ resolution at the THz end of the spectrum, enabling unbiased surveys of cosmological volumes at high resolution in multiple bands (van Kampen et al., 2024). Depending on the underlying correlation function of EoR galaxies, AtLAST can optimize its scanning strategies between deep versus wide-field surveys, enabling a statistically significant sample of EoR galaxies and thus opening a completely new view of the processes of structure formation at the highest redshifts.

For all the above-described advancements in the field, as well as in general (see, e.g., González-López et al., 2019), proper noise characterization is essential. The WSU will provide twice (and later four times) the bandwidth, increasing the likelihood of false detections in blind line searches. Additionally, other interferometric facilities, such as the ngVLA and SKA, will, for instance, enable deep HI surveys, already revealing new HI detections up to $z \sim 0.4$ (e.g., Baker et al., 2024, Xi et al., 2024). As data volume increases with these new and upgraded facilities, so does the potential for spurious line detections. Therefore, it is, and will always be, crucial for the community to accurately assess the probability of false detections using statistically motivated approaches like the one I presented.

5.2.2 SZ observations of a protocluster at z=2.5?

This subsection is based on a DDT proposal I submitted requesting ACA Band 3 observations of the protocluster CL-J1001+0110. Using the tools described in Chapter 3, I conducted a preliminary analysis and found a 2.4σ detection of thermalized gas at $z = 2.501$, which would represent the highest redshift detection of the SZ effect in a protocluster to date. While the proposal was well-received, it was ultimately rejected as it was deemed unsuitable for a DDT. However, they strongly recommended resubmitting the proposal in the regular call of the proposals in 2025. Below, I summarize the proposal and the preliminary analysis. This work is representative of how future work regarding Chapter 3 will be continued and pushed to higher redshifts.

The intracluster medium (ICM) has been extensively studied in relatively nearby, mature galaxy clusters ($z \lesssim 1$). These observations have been crucial for the study of cosmology and galaxy evolution (see, e.g., Pratt et al., 2019, Donahue & Voit, 2022, for recent reviews). However, observations of the earliest phases of the formation of the ICM remained elusive. This rises a key question: *When do galaxy clusters first form?* The DDT observations we propose here will address this key question by pushing the detection of hot $T_e \gtrsim 10^7$ K gas in large-scale overdense environments to only 2 Gyr after the Big Bang. This limits their evolutionary pathways and will provide answers on when these overdensities first begin to resemble their lower-z counterparts.

Using ALMA, Di Mascolo et al. (2023) robustly detected—for the first time—a reservoir of hot ionized gas in a still-forming galaxy (proto-)cluster at $z > 2$. This hot gas around the Spiderweb galaxy (see Fig. 5.1) is fully consistent with being formed through the gravitational collapse of large-scale structures along the filamentary "cosmic web". Clusters — and presumably the densest cores of their distant counterparts — sit at the intersections in large-scale structures. Because of the large gravitational potential well of the dark matter halo, gas from the cosmic web flows through filaments to the center of a node, accreting onto the protocluster core. This accretion perturbs the gas via accretion shocks and mergers with other groups or clusters and heats the gas to temperatures beyond $T_e \gtrsim 10^7$ K, eventually providing thermal pressure support to the whole system over a process that takes a few Gyr (Wik et al., 2008).

The epoch of protocluster collapse — thought to be a few Gyr after the Big Bang ($z \simeq 2$) — is a particularly interesting era in cosmic history. Massive galaxies are assembling at the same moment when star formation peaks in cosmic time and when the first cluster-like halos appear

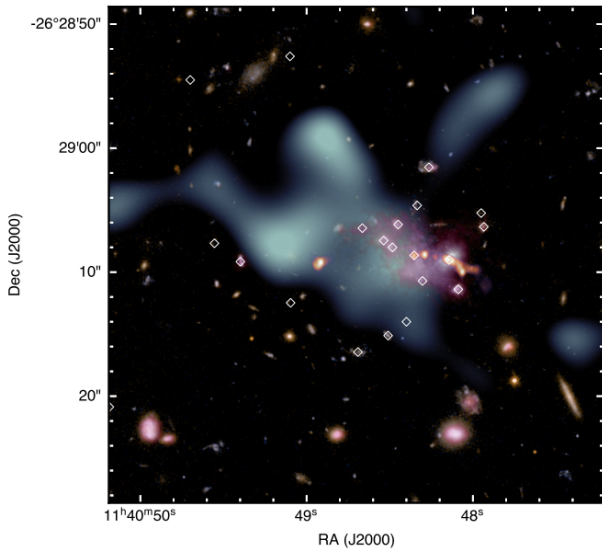

Figure 5.1: Multi-wavelength view of the Spiderweb complex from Di Mascolo et al. (2023) with the SZ effect in blue over an HST background. Purple shows the AGNs. This was the first robust detection (6σ) of the hot ICM in a forming galaxy cluster and was featured in an ALMA press release in March 2023.

(Fakhouri et al., 2010). Cosmological simulations (Olchanski & Sorce, 2018, Remus et al., 2023) predict the presence of hot gas in protoclusters already at $z \approx 2-4$. However, the amount of hot gas in the simulated protoclusters varies by a few orders of magnitude and depends on the resolution of the simulations and the specific feedback model implemented (see, e.g., Chen et al., 2024). Observational data is needed to constrain the simulations but has been minimal even though mock observations of these simulations indicate that the hot gas around the central galaxy should be detectable with X-ray or SZ observations (see, e.g., Castellani et al., 2024).

The confirmation of the presence of gravitationally collapsed objects beyond $z > 2$ is an important step towards corroborating so far untested theories. Pushing these observations to higher redshifts is essential to confront the theoretical predictions at their limits and further our understanding of the formation of the largest bound objects in the Universe. Therefore, we targeted with this proposal a protocluster that was formed half a Gyr earlier than the Spiderweb, namely CL-J1001 at $z = 2.501$. With our proposed observations of CL-J1001, we will have pushed further in cosmic time and, by doing so, limit the evolutionary pathways on which these objects evolve and be able to constrain better theories that have been around for decades.

CL-J1001+0220: the next Spiderweb

CL-J1001+0220 first came to our attention as it is part of a sample of protoclusters that all have detected giant (> 100 kpc) Lyα haloes in their core (Daddi et al., 2022). Of all these protoclusters, four have dedicated ALMA observations, of which only two are beyond $z > 2$, namely the Spiderweb (Di Mascolo et al., 2023) and CL-J1001. Both objects have similar halo masses ($M_{500,c} \approx 3 \times 10^{13}\ M_{\odot}$), but CL-J1001 is the most distant of the two. However, the hot gas has yet gone undetected.

There have been attempts to detect the forming hot gas in the X-ray with *Chandra*+*XMM-Newton* observations. Wang et al. (2016) combined *Chandra* and *XMM-Newton* surveys of the COSMOS field to get ~ 160 and ~ 60 ks on-source time per pointing, respectively. They found

4σ evidence of a $16''$-large extended X-ray source in the combined *Chandra+XMM-Newton* map. This is a factor ~ 2 smaller than the expected bulk extent of the proto-ICM (the $r_{500,c}$ for CL-J1001 is roughly $32''$), and the thermal origin of the emission is still highly debated (Champagne et al., 2021). At the same time, we note that even in the case of the more massive and more mature Spiderweb protocluster, the detection of the hot intracluster gas required a significant investment of 700 ksec on source (i.e., $7\times$ times as deep as the available data on CL-J1001; Tozzi et al. 2022). Still, only with the inclusion of SZ data was it possible to confirm that the hot gas in the Spiderweb complex is not associated with protocluster galaxies but with proto-ICM undergoing thermalization.

Luckily, there are archival but yet unpublished ACA Band 3 observations meant to detect the SZ effect in CL-J1001 (≈ 30 hours on source, see also Fig. 5.2). By forward modeling parametric profiles to the visibilities by means of a Bayesian analysis, we find that the data favors a SZ component at 2.4σ. Our preliminary analysis hints at the presence of hot thermal electrons in CL-J1001, which was formed half a Gyr earlier than the Spiderweb. If confirmed, this would be the highest redshift SZ detection in a protocluster to date. And most importantly, it will allow for peering into the thermodynamic structure of the system, adding yet another unprecedented piece in the thermalization history of cosmic structure.

Constraining the thermodynamic properties of forming proto-ICM in such a high-z is not relevant only in the context of SZ studies. In fact, laying in the COSMOS field, CL-J1001 has an extensive range of multi-wavelength coverage. Initially identified as a protocluster through *Herschel/SPIRE* observations (Wang et al., 2016) and confirmed through VLT-KMOS measurements (Smolčić et al., 2014), it has been followed up with NOEMA (Wang et al., 2016), ALMA Band 3 (Xiao et al., 2022) & 7 (Bussmann et al., 2015), and VLA Ka Band observations (Wang et al., 2016, 2018) targeting the cold molecular gas through multiple CO line transitions. Further in the optical/NIR, there are Subaru/MOIRCS NB (Wang et al., 2018) to target Hα, Keck/KCWI (Daddi et al., 2022) for the Lyα, and JWST (see also Fig. 5.3). All these works have been incremental in studying the effects of the environment on the 17 cluster members. However, again, a robust detection of the environment – the newly-formed ICM that dominates the system's baryonic mass budget– is still missing.

Why these observations should be taken sooner rather than later

One may ask, why does this relatively short (≈ 60 hours of on-source time) ACA Band 3 observation need to be executed now? Even though the detection of the SZ effect could be considered a strong stand-alone science case itself, we aim to provide a full characterization of the forming ICM. Therefore, we anticipate that X-ray follow-up observations will be needed once we are confident of the presence of hot ionized gas. The SZ effect probes the integrated pressure of the hot electrons in the ICM along the line of sight, while the X-ray emission traces the density of the ICM through free-free emission emitted by the same electrons. Thus, by jointly modeling X-ray emission with SZ measurements, we will gain temperature estimates of the ICM, an equation-of-state parameter crucial to understanding the formation of these types of structures, and will give the needed proof to interpret the mechanisms that drive other observational results, such as the giant (> 100 kpc) Lyα halo seen in the core of CL-J1001+0110.

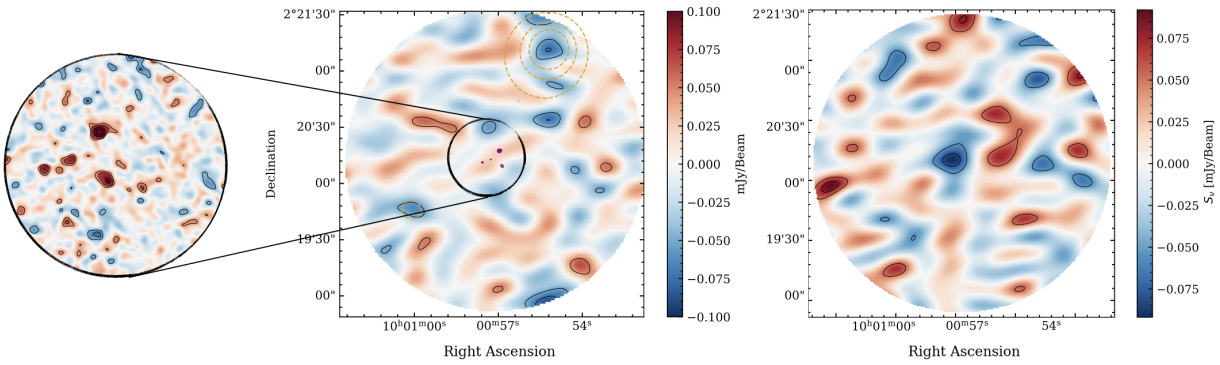

Figure 5.2: Archival ALMA Band 3 observations of CL-J1001+0220. **Left:** high-resolution (0.″2 at 100 GHz) Band 3 (100 GHz) observations showing the center of the protocluster core. **Middle:** Image reconstruction of the tentative SZ effect observed with ACA in Band 3. Here, we removed the emission from the central sources. The golden contours show the model reconstruction and are drawn at $(-0.015, -0.01, -0.005)$-mJy/Beam. The black contours, which correspond to the ACA map, are drawn at $(-3, -2, +2, +3)$-σ. **Right:** A mock observation where we injected a toy model of the SZ effect to the jack-knifed visibilities. Contours are drawn at $(-3, -2, +2, +3, +5, +7)$-σ. We tentatively detect a SZ component with 2.4σ through forward modeling to the uv-plane (middle panel), which shows similar significance as the simplistic toy model.

Launched in 1999, *Chandra* is the only X-ray telescope with sufficient spatial resolution to separate point source contaminants from the diffuse ICM. However, it is experiencing a rapid loss of sensitivity at low photon energies (where the majority of the signal should be redshifted). More crucially, the proposed budget of the US Congress entails severe budget cuts to *Chandra*, and this valuable resource will likely be entirely decommissioned soon. A DDT *Chandra* proposal to follow on the ALMA proposal here must be submitted within the next year, as this will be the last chance. Another opportunity to detect the forming ICM in protoclusters will not present itself from the X-ray perspective in the next two decades as new missions are still under development and experience massive budget costs. There will not be another opportunity for the next 20 years to get a full picture of the thermodynamical properties of the newly formed ICM.

Description of observations

To robustly detect the SZ effect in CL-J1001+0220, we propose increasing the on-source time to triple that of the original observation. This extended integration, when combined with the existing archival data, would double the S/N of our analysis, enabling a robust detection of the SZ effect 2.5 Gyr after the Big Bang.

To show the feasibility of our setup, we jack-knife the visibilities (by randomly multiplying half of all visibilities with -1 and rebin after; see Chapter 2) to make a noise map of the archival ACA Band 3 observation. To this noise map, we add a toy model of the SZ effect, built from the average radial pressure distribution of McDonald et al. (2014) using the halo-mass and redshift

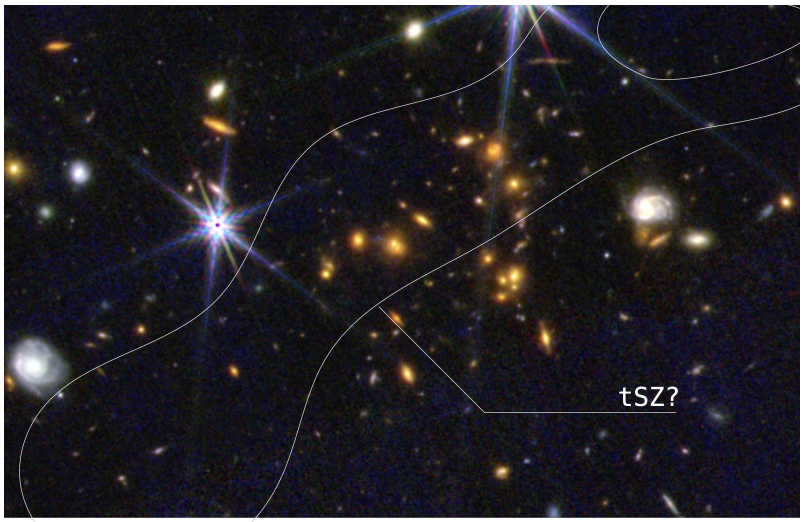

Figure 5.3: JWST/NIRCam observations of the COSMOS field centered on CL-J1001+0220. This figure clearly indicates a galaxy overdensity at $z = 2.501$, predominately made out of star-forming dusty galaxies. We added a sketch on where the hot gas – seen through the SZ effect – would fall based on our model. Deeper observations are needed to confirm.

reported in Daddi et al. (2022). We then correct the resulting surface brightness distribution of the toy model for the sampling function of the archival observations. The results are shown on the right panel of Fig. 5.2. This panel shows that if uncontaminated and if CL-J1001 follows the self-similarity principle, we should detect the SZ effect with a peak S/N of 3σ. In the real data, as stated above, we detect the SZ effect at 2.4σ via the Bayesian evidence, although slightly off-centered from the center of the protocluster (notably also the case for the Spiderweb protocluster, Di Mascolo et al., 2023). As both the toy model and analysis done on the real observation indicate a tentative detection, we are confident that with twice the depth, we can robustly confirm the presence of hot gas in this protocluster core.

To conclude and summarize:

- With the proposed observation, we aim to confirm the presence of hot $T_e \gtrsim 10^7$ K gas in CL-J1001+0220 via the SZ effect. Preliminary modeling showed that the current archival ACA Band 3 data prefers a SZ component with a significance of 2.4σ. By quadrupling the integration time, we can boost the significance by a factor of 2, thus robustly confirming the presence of the forming ICM, making it the most distant detection of the SZ effect to date.
- Hydrodynamical simulations predict that hot gas in protocluster cores should be present at $z = 2 - 4$ (see, e.g., Remus et al., 2023, Di Mascolo et al., 2023). However, the amount of hot gas in the simulated protoclusters varies by a few orders of magnitude and depends on the resolution of the simulations and the specific feedback model implemented (see, e.g., Chen et al., 2024). Pushing observations to higher redshifts is thus essential to confront the theoretical predictions at their limits and further our understanding of the formation of the largest bound objects in the Universe.
- We aim to get a full thermodynamical characterization of the forming ICM. For this, X-ray observations are necessary in conjunction with SZ observations. However, *Chandra* – currently the most sensitive telescope to detect the diffuse ICM in the X-ray – is rapidly losing sensitivity

at the lower energy bands and might be decommissioned next year. All, while newer missions, will not be deployed for the next two decades. Therefore, detection of the hot gas via this measurement is needed sooner rather than later to get a chance to characterize this forming structure fully.

- As CL-J1001+0220 lies within the COSMOS field, a wide range of multi-wavelength data is accessible (see also Fig 5.3). This enables environmental studies on the cluster members in this epoch in which star formation and AGN feedback are much more prominent than in the local universe. However, proper detection of the hot gas – the environment in which these galaxies evolve in – remains elusive and is needed to cross-correlate the environment with cluster member properties. Only ACA observations can provide such crucial confirmation (or rejection) of the putative SZ signal.

5.2.3 Resolved SZ observations at the epoch of most rapid cluster growth

This subsection is based on a work that started as an ALMA Large Program I PI'ed to resolve the morphology of clusters at the epoch of the most rapid cluster growth ($1.25 < z < 1.5$). Although initially rejected, after several revisions and rebrandings, I eventually got 80 hours of MUSTANG-2, 80 hours of ACA, and 5 hours of ALMA/12m-array observations awarded. Most of the observations have not yet been conducted, but in this subsection, I show the initial proposal and preliminary results.

During cluster assembly, shocks due to mergers and accretion heat the ICM to temperatures $T_e > 10^7$ K, making merging clusters prominent X-ray and thermal Sunyaev-Zeldovich sources. Since 2009, SZ surveys such as ACT (Hilton et al., 2018, 2021) and SPT (Carlstrom et al., 2011, Bleem et al., 2015, 2020, 2024) have cataloged thousands of massive clusters, though only ≈ 50 of them are currently detected beyond $z > 1.25$. These surveys, however, do not provide sufficient resolution to reveal the nature and structure of clusters, and often detailed follow-up reveals what was thought to be a single cluster is, in fact, a dramatic merger (Di Mascolo et al., 2021).

Importantly, the merger rate of clusters increases steadily with z, peaking around $z \sim 1.6$ (Fakhouri et al., 2010, Olchanski & Sorce, 2018). Meanwhile, typical merger trees leading to a simulated cluster with a mass and dynamical state similar to Virgo at $z = 0$ show the thermal energy growth is most rapid between $1.2 < z < 2.0$ (Dolag et al., 2016, Chiang et al., 2020, Young et al., 2021, Chen et al., 2024). With the Universe only $\sim 3.5-4$ Gyr old at these redshifts, the time since cluster formation began ($\sim 1.5-3$ Gyr after the Big Bang) is close to the dynamical time scale for the virialization of massive clusters (~ 1 Gyr). Observations of the properties of clusters – such as their morphology – in this redshift range thus provide particularly important clues to the early evolution of clusters and their members. ALMA and MUSTANG-2 provide better angular resolution than CMB surveys, making them ideal for studying the morphology of the ICM. As a consequence, characterizing the SZ signal in clusters has been an important scientific driver for ALMA since ALMA memo #1 (Owen et al., 1980) and MUSTANG-2. To date, however, most high-resolution follow-up studies are limited to a small number of objects or individual systems (e.g., Di Mascolo et al., 2020, Kitayama et al., 2023). There has never been a statistically significant survey of SZ sources involving both ALMA and MUSTANG-2 to

study the thermodynamical properties of the ICM in a carefully selected sample of clusters. This survey, the Representative Cluster Evolution Sunyaev-Zeldovich Survey (ReCESS), is the first step towards this goal.

The goal of Representative Cluster Evolution Sunyaev-Zeldovich Survey

To provide an indication of the scope of ReCESS, it is important to note the current limitations in observational data. Resolved measurements beyond $z > 1$ of a sample of clusters that directly probe the pressure distribution are notably absent from the literature (e.g., Ruppin et al., 2019, probes $0.5 < z < 1$). Most existing observations rely on X-ray measurements (see, e.g., McDonald et al., 2014), which primarily trace the ICM through free-free emission, $\epsilon_{ff} \propto n_e^2$. This method, however, only indirectly probes the pressure of the thermalized gas. Furthermore, studies at $z > 1$ that utilize the thermal SZ effect generally consist of individual objects or pilot programs with a limited number of clusters. As a result, these studies lack a well-defined selection criterion, complicating efforts to estimate the selection bias in current wide-field surveys.

As discussed in Section 1.4.2, pressure is the fundamental physical parameter measured by the SZ effect. The shape of the radial pressure profile is crucial for the reliability of cluster counts and the cosmological conclusions drawn from them. Since the pressure profile directly influences the 2D surface brightness distribution of the SZ effect, its overall shape, when averaged over a large population, significantly affects the completeness of clusters detected in wide-field SZ surveys. Incorrect assumptions about pressure profiles thus lead to biases in the completeness function, which in turn introduce biases in the cosmological constraints (Gallo et al., 2024). Additionally, contamination from point sources blended with the SZ flux can distort the reconstructed Compton-Y values by approximately $1\% - 2\%$, with potential biases reaching up to 50% in extreme cases (Dicker et al., 2021, 2024).

ReCESS will resolve clusters of galaxies at $\approx 10''$, enabling the characterization of the radial pressure distribution and the separation of contaminating point sources for all ACT-selected clusters within the $1.25 < z < 1.5$ range, initially detected with an SNR> 4.5 in ACT DR5 (Hilton et al., 2021). Consequently, ReCESS will provide critical data to better understand the systematic uncertainties that arise when extending cluster-based cosmological measurements to higher redshifts. With ReCESS, we will also identify merging systems and explore the characteristics of adolescent clusters, revealing their morphology across a range of scales—from the inner regions to beyond the virial radius—when combined with single-dish frequency maps from ACT (akin to the technique presented in Chapter 3).

Preliminary results

Here, we present preliminary work on the first four observations I conducted with MUSTANG-2 from a combined sample of 19 SZ-selected clusters observed with MUSTANG-2 and ALMA+ACA. Maps of the first four observations are shown in Figure 5.4. Our full sample, in relation to the overall cluster population, is shown in Figure 5.5.

At this stage, it is still too early to derive a "Universal Pressure Profile" at $z \simeq 1.5$, given that we only have four clusters available, so I have omitted that analysis from the thesis. However,

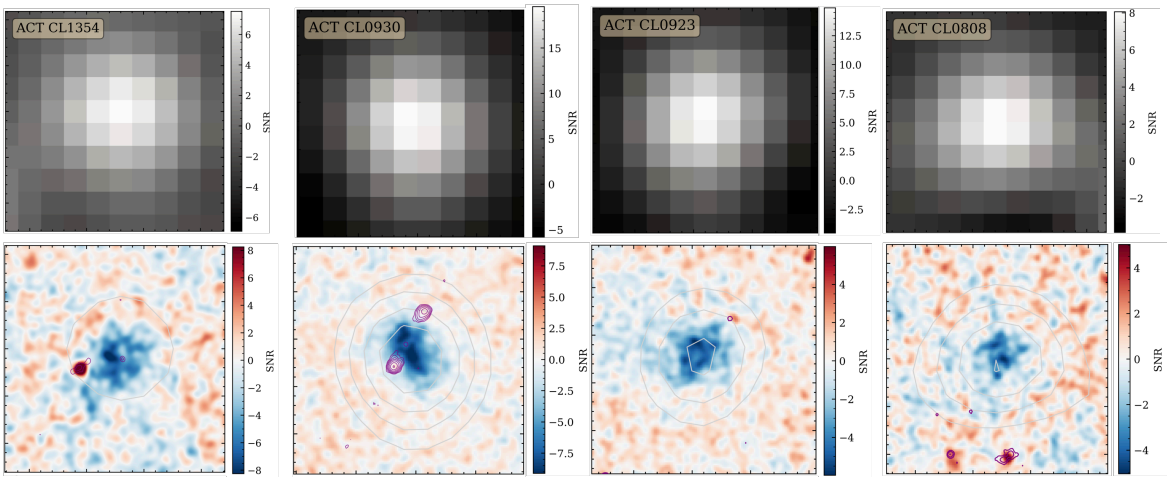

Figure 5.4: Mustang-2 observations of the four clusters from the ReCESS sample. From left to right, we show the four different clusters. The top row shows the four ACT observations that are used to select the clusters. The bottom row shows their corresponding GBT/MUSTANG-2 observations that add resolution to the data ($15\times$ better resolution). Overlayed in purple, we show VLA observations from the FIRST survey. The VLA contours are drawn at [0.6, 1.4, 3.1, 7.1, 16.2, 37.0, 84.3] mJy/Beam.

the SZ maps show promising results. All observations indicate a clear detection of the SZ effect. Additionally, we identified five point-like objects across the four maps, along with one giant radio jet. Notably, the number of galaxies contaminating the SZ signal seems higher than what is typically observed in SZ-selected clusters at lower redshifts (Dicker et al., 2024). Sources located more than $104''$ from a cluster's center can bias the SZ signal, with some sources introducing a bias exceeding 50%, while the average bias level remains around $1\% - 2\%$ (Dicker et al., 2024). Given that sources tend to be dustier at higher redshifts (Zavala et al., 2021), the contamination level for ReCESS sources might be generally higher. The upcoming observations will be necessary to confirm whether the derived halo masses from the integrated Compton-Y measurements are indeed biased high across the entire sample and are needed to assess the impact this might have on the completeness function of clusters at $1.25 < z < 1.5$ for ACT.

Furthermore, the morphology of the cluster ACT-CL0930 is particularly noteworthy. Similar to the findings of Orlowski-Scherer et al. (2022), it exhibits radio jets at the cluster's outskirts. If the suppression of SZ flux is not merely due to the filling in of positive flux from the radio lobes, these observations could help determine the nature of the pressure supporting the cavities (e.g., thermal vs. non-thermal). If confirmed, these measurements would be only the second of their kind, providing valuable insights into mechanical feedback from AGN, which plays a key role in quenching cooling flows and regulating star formation in galaxy cluster cores.

Future directions following ReCESS

ReCESS will provide a systematic study of cluster formation by resolving clusters during the epoch of the most rapid cluster growth. This study will deliver the statistical sample needed

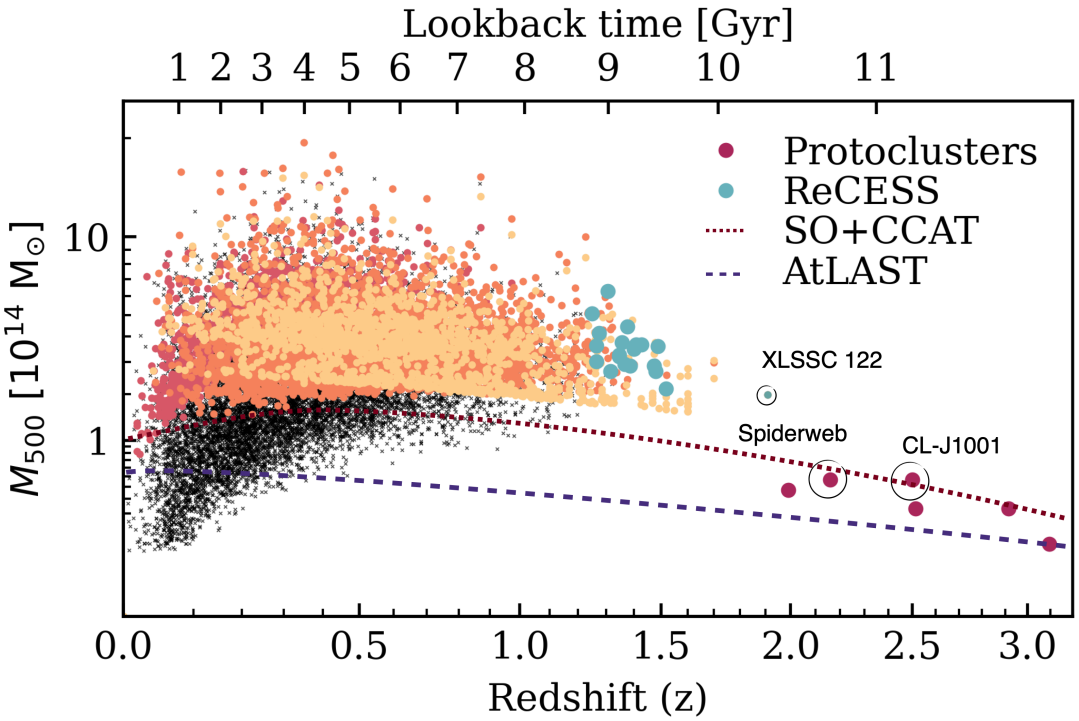

Figure 5.5: Redshift–mass distribution of clusters from *Planck*, SPT, ACT, and eRASS. We further highlight the ReCESS sample (blue) and a sample of protoclusters, selected on having giant > 100 kpc Ly$-\alpha$ haloes, which include XLSSC 122, the Spiderweb, and CL-J1001+0110. We further indicate the expected sensitivity of future surveys S0 when combined with CCAT observations (red-dotted CCAT-Prime Collaboration et al., 2023) and AtLAST (Di Mascolo et al., 2024).

to make significant advancements in understanding high-z galaxy clusters and linking them to simulations, as discussed in Section 5.2. By probing a previously unexplored epoch of cluster evolution, ReCESS will reveal the mechanisms driving the thermalization of the intracluster medium up to $z \simeq 1.7$. However, since the full sample is still being observed, completing the various research goals will require time. In the interim, new CMB-survey telescopes, such as the Simons Observatory (SO), will begin delivering their first datasets. SO is expected to discover an order of magnitude more clusters at $z > 1.5$ than ACT and SPT by probing lower halo masses, potentially extending into the realm of protoclusters ($z \gtrsim 2$, see Figure 5.5).

With the introduction of the WSU, ALMA is positioning itself as a premier telescope for following up on data from CMB surveys or other tracers of overdensities, such as giant Lα haloes (Daddi et al., 2022, as well as Fig. 5.5). Additionally, single-dish facilities are making significant advancements. Various telescopes, such as the Sardinia Radio Telescope, have successfully implemented the use of kinetic inductance detectors (KIDs; Day et al. 2003). KIDs enable the focal plane to be filled with thousands of detectors while minimizing readout loss, significantly improving the surface brightness sensitivity of single-dish facilities that use bolo-

metric broadband instruments. One notable proposed project involves replacing MUSTANG-2 with a new instrument called WIKID (Romero, 2024), which would be built using KIDs. This upgrade would drastically enhance the surface brightness sensitivity of the GBT at 93 GHz, allowing it to outperform ALMA even after the WSU. My point is that the future for resolved SZ science looks promising. Planned technological advancements are on the horizon and will soon be commissioned, enabling the study of galaxy clusters with precision and resolution comparable to what X-rays have achieved for decades, but at redshifts previously unobservable by X-ray instruments. This progress is particularly important as *Chandra*, the leading instrument for high-resolution X-ray observations, will soon be decommissioned, and new X-ray missions are still under development and facing significant budget challenges.

While waiting for the observations to come in, the new CMB surveys to come online, and the technological advancements to kick in, we can refer to hydrodynamical simulations to study the thermalization processes of the Universe and evaluate how well we can recover this information using tools such as `maria`. Current cosmological hydrodynamical simulations, such as Flamingo (Schaye et al., 2023) and Magenticum (Marini et al., In prep.), start to approach volumes the size of the observable Universe. Applying similar selection functions as used for the ReCESS sources to the simulated haloes, we can start to compare the real with simulated populations. Going one step further, with tools like `maria` and interferometric simulators such as `simobserve`, we can create mock observations from these simulations, analyzing synthetic observations as if real. Such analysis will not only confirm the robustness of our tools but also provide the theoretical/simulation-based context within which observations are compared and, in turn, validate the robustness of the simulations when these observations eventually are taken.

5.2.4 How to solve a problem like `maria`

The following subsection discusses the future development of `maria` *and is an extension of the discussion provided in Chapter 4. Parts of it are inspired by a new collaboration that began based on the work presented in Chapter 4 with the "Origins Data Science Laboratory" here in Munich, which specializes in analysis methods, algorithms, and computer-aided tools to better understand and exploit multidimensional, complex data.*

In the forthcoming era of big data and the global shift towards more sustainable alternatives, there is an urgent need to develop green telescopes that prioritize energy efficiency in both hardware and software. As mentioned in Chapter 4, facilities like AtLAST, along with SKA, ngVLA, and DSA-2000, will generate high data rates and require substantial storage and supercomputing resources to process and calibrate the data. One straightforward method to reduce computation time and storage requirements is to discard data, such as visibilities (a strategy that the SKA is considering), or to down-sample time streams (as already done with MUSTANG-2 observations). However, these approaches could impact the reproducibility of research and limit the effectiveness of tools designed to extract the maximum scientific value from datasets.

The above considerations underscore the need for more efficient code implementations. In the case of `maria`, we have already made significant improvements to the code infrastructure since the initial publication (Chapter 4). We have enhanced parallelization using `dask`, significantly

reducing the RAM required for making mock observations for AtLAST by a factor of ten. Additionally, we plan to further optimize the code by utilizing Python's `jax` for GPU acceleration. However, I believe that the most significant software developments will be through the usage of neural networks. Applying simplistic analysis tools, such as the naive mapmaking used in Chapter 4, is not only computationally inefficient but also suboptimal for retrieving scientific information and distinguishing the astronomical source from noise components.

Denoising timestreams from millions of detectors on a large single-dish telescope is well-suited to information field theory methods, particularly using the Numerical Information Field Theory tool (`NIFTy`; Selig 2014, Enßlin 2019, Edenhofer et al. 2024). Single-dish facilities face significant challenges in separating atmospheric and astronomical signals, especially at large scales. This difficulty arises due to the large dynamic range in amplitudes—approximately seven orders of magnitude—between the atmosphere and the astronomical signal, as well as the fact that they share common modes across detectors, thus plausibly confusing CMB signal for a common mode measured in the atmosphere. Additionally, the nonlinearity caused by sky scanning with a non-constant velocity further complicates the transformation from time-domain data to map-domain data. Traditional mapmaking methods assume a stationary, flat sky and pointing matrix creating a linear, invertible operation from time streams to sky coordinates (see, Dünner et al., 2013, section 11 for a more thorough description of mapmaking). However, this assumption is not valid at, for instance, the turnaround of a back-and-forth scan, eventually leading to loss at large scales (Naess & Louis, 2023). `NIFTy` can learn these nonlinear operations by training on simulated `maria` observations, accounting for sky-scanning nonlinearity, while solving for a time-evolving atmosphere using Gaussian processes.

A final application of `maria` to discuss is its potential for studying phase delays caused by the ever-changing turbulent atmosphere. This is particularly relevant for long-baseline, high-frequency campaigns conducted with ALMA, as `maria` could serve as an improved phase screen model, adding realism to replicate the empirical findings on measured phase stabilities reported in Maud et al. (2023). These findings are significant not only for ALMA but also for the ngVLA. There is an ongoing discussion about having two or three antennas continuously monitor the phase screen at multiple points, which could be essential for achieving the goal of 1 micro-arcsecond astrometry. Although these studies are not yet integrated into the ngVLA baseline design, and the associated cost for additional antennas may present challenges, it is valuable to quantitatively assess this proposal. Addressing these issues is strategically important for ngVLA development and ideally suited for study with `maria`.

5.2.5 AtLAST: the future (sub-)mm observatory

The discussion presented here is primarily based on the recent works published by Di Mascolo et al. (2024), to which I contributed.

Throughout this thesis, I have utilized various (sub-)mm telescopes to cover the full range of spatial scales relevant to my research. This approach was necessary because CMB surveys, such as ACT, lack the spatial resolution and point source sensitivity needed to map the calorimetry in clusters or detect the most distant galaxies. On the other hand, interferometers filter out flux

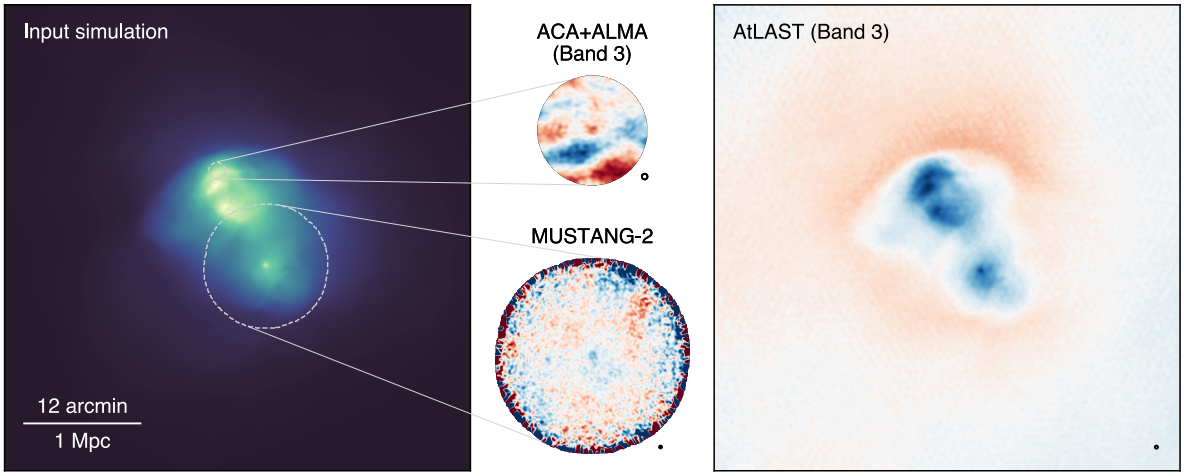

Figure 5.6: Simulated nearby galaxy cluster ($M_{500} = 1.28 \times 10^{15}$ $M_{\odot}$, $z = 0.0688$; left) as observed by ALMA+ACA in Band 3 (top center), MUSTANG-2 (bottom center), and by AtLAST in Band 3 (right). The respective beams are shown in the bottom right corner of each panel. The input simulation is extracted from the Dianoga cosmological simulation suite (Rasia et al., 2015, Bassini et al., 2020). Overlaid as dashed white circles are the ACA+ALMA and MUSTANG-2 footprints. We note that the respective panels on the central column are scaled up arbitrarily with the goal of highlight any observed features, and do not reflect the relative angular sizes of the fields. For all cases, we consider an on-source time of 8 hours. The mock AtLAST and MUSTANG-2 observations are generated using `maria` (see Chapter 4), assuming an AtLAST setup with minimal detector counts of 50,000. For ACA+ALMA, we employed `simobserve`. Figure comes from Di Mascolo et al. (2024).

at large spatial scales, making it challenging to constrain the thermal energy and halo mass of a system, and they – as well as current large-single dish facilities – have a limited FoV. Ideally, I would have preferred to work with a (sub-)mm telescope that combines a large FoV with $\approx 1-10''$ resolution (at 1000 and 100 GHz, respectively) while maintaining high fidelity on large spatial scales. In this final section of my thesis, I will conclude with a brief overview of a telescope design that meets these criteria – the 50-meter Atacama Large Aperture Submillimeter Telescope (AtLAST; Ramasawmy et al. 2022, Mroczkowski et al. 2023, Booth et al. 2024, Mroczkowski et al. 2024, Reichert et al. 2024) – and how I would like to use it.

As discussed in Chapter 4, AtLAST is a concept for a next-generation, high-throughput (sub-)mm telescope to be located in the Atacama Desert. Throughput, often referred to as *étendue*, is defined here as the product of the primary mirror's collecting area and the telescope's FoV. With a surface accuracy of 20 μm, AtLAST will be capable of observations from 40 GHz up to 950 GHz. The telescope will feature dedicated spaces for six extremely large receivers, two of which will have full access to the 4.7-meter focal plane corresponding to the 2° FoV (see Mroczkowski et al., 2024).

With its large FoV, it can probe proper cosmological volumes as, for instance, current ALMA large programs such as ASPECS (Walter et al., 2016) will be covered within a single pointing.

This will uncover an optically unbiased Universe, for instance, crucial for understanding the evolution of galaxies overall (e.g., Lee et al., 2024, van Kampen et al., 2024). In this last section, however, I will focus on the study of high-z clusters of galaxies.

AtLAST will offer a new perspective on the SZ effect from the warm/hot gas in the Universe. The 50-meter aperture will enable high angular resolution (especially at high frequencies), enabling the measurement of the SZ signal across a broad dynamic range of spatial scales, from a few arcseconds to degrees (Di Mascolo et al., 2024, as well as Figure 5.6). These technological advances will enable the combined study of the thermal, kinetic, and relativistic SZ effects, providing a fresh perspective on the growth and thermalization of cosmic structures (Di Mascolo et al., 2024). AtLAST will also have the capability to scan the entire southern hemisphere, offering a complete census of the cluster population (Figure 5.5). This comprehensive coverage will help overcome the biases inherent in current cluster selection strategies (Section 5.2.3) by not only detecting but simultaneously resolving structures as well as contaminants. As a result, AtLAST will play a pivotal role in establishing galaxy clusters as key cosmological probes at $z > 1.5$

By resolving the multi-faceted SZ footprint of galaxy (proto-)clusters, AtLAST will trace the full evolution of their thermodynamic properties from the local Universe to the start of the Universe's reheating ($z \simeq 5$) up to the epoch of reionization through kSZ measurements. Its ability to resolve clusters at low-surface brightness will open an SZ window on the low-density warm/hot gas within the cosmic large-scale structure, including the characterization of the largely unexplored properties of assembling ICM seeds within protocluster overdensities. These environments are ideal for studying how deviations from thermalization, gas accretion, and dynamic processes impact the thermal history of the Universe, cementing its place as an essential tool for future cosmological research.

My publications

Below is a complete list of publications to which I contributed during my PhD. Publications marked with (★) form the science chapters of this thesis. Those marked with (■) are works I contributed to that are related to the content of this thesis. The (•) symbols denote other works in which I was involved.

Main works:

★ Kaasinen, **van Marrewijk**, Popping, Ginolfi, Di Mascolo, Mroczkowski, Concas, Di Cesare, Killi, & Langan, 2023, A&A, 671, A29
To see or not to see a z $\sim$ 13 galaxy, that is the question. Targeting the [C II] 158 μm emission line of HD1 with ALMA.

★ **van Marrewijk**, Kaasinen, Popping, Mroczkowski, Di Mascolo, Boogaard, Valentino, Bakx, & Yoon, 2024, A&A, Submitted
Quantifying the detection likelihood of faint peaks in interferometric data through jackknifing. Test application on finding $z > 10$ galaxy candidates.

★ **van Marrewijk**, Di Mascolo, Gill, Battaglia, Battistelli, Bond, Devlin, Doze, Dunkley, Knowles, Hincks, Hughes, Hilton, Moodley, Mroczkowski, Naess, Partridge, Popping, Sifón, Staggs, & Wollack, 2024, A&A, Accepted
XLSSC 122 caught in the act of growing up: Spatially resolved SZ observations of a z=1.98 galaxy cluster.

★ **van Marrewijk**, Morris, Mroczkowski, Cicone, Dicker, Di Mascolo, Haridas, Orlowski-Scherer, Rasia, & Romero, 2024, OJAA, Submitted
maria: A novel simulator for forecasting (sub-)mm observations.

Contributed works:

■ Di Mascolo, Perrott, Mroczkowski, Andreon, Ettori, Simionescu, Raghunathan, **van Marrewijk**, Cicone, Lee, Nelson, Sommovigo, Booth, Klaassen, Andreani, Cordiner, Johnstone, van Kampen, Liu, Maccarone, Morris, Saintonge, Smith, Thelen, & Wedemeyer, 2024, A&A, Submitted

Atacama Large Aperture Submillimeter Telescope (AtLAST) Science: Resolving the Hot and Ionized Universe through the Sunyaev-Zeldovich effect.

- Madhavacheril, Qu, Sherwin, MacCrann, Li, Abril-Cabezas, Ade, Aiola, Alford, Amiri, Amodeo, An, Atkins, Austermann, Battaglia, Battistelli, Beall, Bean, Beringue, Bhandarkar, Biermann, Bolliet, Bond, Cai, Calabrese, Calafut, Capalbo, Carrero, Challinor, Chesmore, Cho, Choi, Clark, Córdova Rosado, Cothard, Coughlin, Coulton, Crowley, Dalal, Darwish, Devlin, Dicker, Doze, Duell, Duff, Duivenvoorden, Dunkley, Dünner, Fanfani, Fankhanel, Farren, Ferraro, Freundt, Fuzia, Gallardo, Garrido, Givans, Gluscevic, Golec, Guan, Hall, Halpern, Han, Harrison, Hasselfield, Healy, Henderson, Hensley, Hervías-Caimapo, Hill, Hilton, Hilton, Hincks, Hložek, Ho, Huber, Hubmayr, Huffenberger, Hughes, Irwin, Isopi, Jense, Keller, Kim, Knowles, Koopman, Kosowsky, Kramer, Kusiak, La Posta, Lague, Lakey, Lee, Li, Limon, Lokken, Louis, Lungu, MacInnis, Maldonado, Maldonado, Mallaby-Kay, Marques, McMahon, Mehta, Menanteau, Moodley, Morris, Mroczkowski, Naess, Namikawa, Nati, Newburgh, Nicola, Niemack, Nolta, Orlowski-Scherer, Page, Pandey, Partridge, Prince, Puddu, Radiconi, Robertson, Rojas, Sakuma, Salatino, Schaan, Schmitt, Sehgal, Shaikh, Sierra, Sievers, Sifón, Simon, Sonka, Spergel, Staggs, Storer, Switzer, Tampier, Thornton, Trac, Treu, Tucker, Ullom, Vale, Van Engelen, Van Lanen, **van Marrewijk**, Vargas, Vavagiakis, Wagoner, Wang, Wenzl, Wollack, Xu, Zago, & Zheng, 2024, ApJ, 962, 113
  The Atacama Cosmology Telescope: DR6 Gravitational Lensing Map and Cosmological Parameters.

- Coulton, Madhavacheril, Duivenvoorden, Hill, Abril-Cabezas, Ade, Aiola, Alford, Amiri, Amodeo, An, Atkins, Austermann, Battaglia, Battistelli, Beall, Bean, Beringue, Bhandarkar, Biermann, Bolliet, Bond, Cai, Calabrese, Calafut, Capalbo, Carrero, Chesmore, Cho, Choi, Clark, Rosado, Cothard, Coughlin, Crowley, Devlin, Dicker, Doze, Duell, Duff, Dunkley, Dünner, Fanfani, Fankhanel, Farren, Ferraro, Freundt, Fuzia, Gallardo, Garrido, Givans, Gluscevic, Golec, Guan, Halpern, Han, Hasselfield, Healy, Henderson, Hensley, Hervías-Caimapo, Hilton, Hilton, Hincks, Hložek, Ho, Huber, Hubmayr, Huffenberger, Hughes, Irwin, Isopi, Jense, Keller, Kim, Knowles, Koopman, Kosowsky, Kramer, Kusiak, La Posta, Lakey, Lee, Li, Li, Limon, Lokken, Louis, Lungu, MacCrann, MacInnis, Maldonado, Maldonado, Mallaby-Kay, Marques, **van Marrewijk**, McCarthy, McMahon, Mehta, Menanteau, Moodley, Morris, Mroczkowski, Naess, Namikawa, Nati, Newburgh, Nicola, Niemack, Nolta, Orlowski-Scherer, Page, Pandey, Partridge, Prince, Puddu, Qu, Radiconi, Robertson, Rojas, Sakuma, Salatino, Schaan, Schmitt, Sehgal, Shaikh, Sherwin, Sierra, Sievers, Sifón, Simon, Sonka, Spergel, Staggs, Storer, Switzer, Tampier, Thornton, Trac, Treu, Tucker, Ullom, Vale, Van Engelen, Van Lanen, Vargas, Vavagiakis, Wagoner, Wang, Wenzl, Wollack, Xu, Zago, & Zheng, 2024, Phys. Rev. D, 109, 063530
  The Atacama Cosmology Telescope: High-resolution component-separated maps across one third of the sky.

- Qu, Sherwin, Madhavacheril, Han, Crowley, Abril-Cabezas, Ade, Aiola, Alford, Amiri, Amodeo, An, Atkins, Austermann, Battaglia, Battistelli, Beall, Bean, Beringue, Bhandarkar, Biermann, Bolliet, Bond, Cai, Calabrese, Calafut, Capalbo, Carrero, Carron, Challinor, Chesmore, Cho, Choi, Clark, Córdova Rosado, Cothard, Coughlin, Coulton, Dalal, Darwish, De-

vlin, Dicker, Doze, Duell, Duff, Duivenvoorden, Dunkley, Dünner, Fanfani, Fankhanel, Farren, Ferraro, Freundt, Fuzia, Gallardo, Garrido, Gluscevic, Golec, Guan, Halpern, Harrison, Hasselfield, Healy, Henderson, Hensley, Hervías-Caimapo, Hill, Hilton, Hilton, Hincks, Hložek, Ho, Huber, Hubmayr, Huffenberger, Hughes, Irwin, Isopi, Jense, Keller, Kim, Knowles, Koopman, Kosowsky, Kramer, Kusiak, La Posta, Lague, Lakey, Lee, Li, Li, Limon, Lokken, Louis, Lungu, MacCrann, MacInnis, Maldonado, Maldonado, Mallaby-Kay, Marques, McMahon, Mehta, Menanteau, Moodley, Morris, Mroczkowski, Naess, Namikawa, Nati, Newburgh, Nicola, Niemack, Nolta, Orlowski-Scherer, Page, Pandey, Partridge, Prince, Puddu, Radiconi, Robertson, Rojas, Sakuma, Salatino, Schaan, Schmitt, Sehgal, Shaikh, Sierra, Sievers, Sifón, Simon, Sonka, Spergel, Staggs, Storer, Switzer, Tampier, Thornton, Trac, Treu, Tucker, Ullom, Vale, Van Engelen, Van Lanen, **van Marrewijk**, Vargas, Vavagiakis, Wagoner, Wang, Wenzl, Wollack, Xu, Zago, & Zheng, 2024, ApJ, 962, 112
The Atacama Cosmology Telescope: A Measurement of the DR6 CMB Lensing Power Spectrum and Its Implications for Structure Growth.

- Kitayama, Ueda, Okabe, Akahori, Hilton, Hughes, Ichinohe, Kohno, Komatsu, Lin, Miyatake, Oguri, Sifón, Takakuwa, Takizawa, Tsutsumi, **van Marrewijk**, & Wollack, 2023, PASJ, 75, 311
Galaxy clusters at z $\sim$ 1 imaged by ALMA with the Sunyaev-Zel'dovich effect.
- Mroczkowski, Donahue, **van Marrewijk**, Clarke, Hoffer, Intema, Di Mascolo, Popping, Pratt, Sun, & Voit, 2022, A&A, 665, A48
The strongest cool core in REXCESS: Missing X-ray cavities in RXC J2014.8-2430.

- Rybak, **van Marrewijk**, Hodge, Andreani, Calistro Rivera, Graziani, McKean, Viti, & van der Werf, 2023, A&A, 679, A119
PRUSSIC. II. ALMA imaging of dense-gas tracers in SDP.81: Evidence for low mechanical heating and a sub-solar metallicity in a z = 3.04 dusty galaxy.
- Rybak, Hodge, Greve, Riechers, Lamperti, **van Marrewijk**, Walter, Wagg, & van der Werf, 2022, A&A, 667, A70
PRUSSIC. I. A JVLA survey of HCN, HCO^+, and HNC (1-0) emission in z $\sim$ 3 dusty galaxies: Low dense-gas fractions in high-redshift star-forming galaxies.

Bibliography

Abazajian, K., Addison, G., Adshead, P., et al. 2019, arXiv e-prints, arXiv:1907.04473

Abazajian, K. N., Adshead, P., Ahmed, Z., et al. 2016, arXiv e-prints, arXiv:1610.02743

Adam, R., Ricci, M., Eckert, D., et al. 2024, A&A, 684, A18

Adamo, A., Atek, H., Bagley, M. B., et al. 2024, The First Billion Years, According to JWST

Ade, P., Aguirre, J., Ahmed, Z., et al. 2019, J. Cosmology Astropart. Phys., 2019, 056

Aguado-Barahona, A., Rubiño-Martín, J. A., Ferragamo, A., et al. 2022, A&A, 659, A126

Alberts, S. & Noble, A. 2022, Universe, 8, 554

Alpher, R. A. & Herman, R. 1948, Nature, 162, 774

Andreon, S., Maughan, B., Trinchieri, G., & Kurk, J. 2009, A&A, 507, 147

Andreon, S., Romero, C., Aussel, H., et al. 2023, Monthly Notices of the Royal Astronomical Society, 522, 4301

Andreon, S., Romero, C., Castagna, F., et al. 2021, Monthly Notices of the Royal Astronomical Society, 505, 5896

Arnaud, M., Pratt, G. W., Piffaretti, R., et al. 2010, A&A, 517, A92

Assémat, F., Wilson, R. W., & Gendron, E. 2006, Optics express, 14, 988

Astronomisches Jahrbuch. 1823, Astronomisches Jahrbuch: 1826 (1823) (Dümmler)

Baker, A., Blyth, S., Holwerda, B., et al. 2024, in American Astronomical Society Meeting Abstracts, Vol. 243, American Astronomical Society Meeting Abstracts, 346.07

Bakx, T. J. L. C. & Dannerbauer, H. 2022, MNRAS, 515, 678

Bakx, T. J. L. C., Tamura, Y., Hashimoto, T., et al. 2020, Monthly Notices of the Royal Astronomical Society, 493, 4294

Bakx, T. J. L. C., Zavala, J. A., Mitsuhashi, I., et al. 2023, Monthly Notices of the Royal Astronomical Society, 519, 5076

Baronchelli, I., Bonato, M., De Zotti, G., et al. 2024, Galaxies, 12, 26

Baronchelli, I., Scarlata, C. M., Rodríguez-Muñoz, L., et al. 2021, ApJS, 257, 67

Bassini, L., Rasia, E., Borgani, S., et al. 2020, A&A, 642, A37

Battaglia, N., Bond, J. R., Pfrommer, C., & Sievers, J. L. 2012, ApJ, 758, 75

Battistelli, E. S., Barbavara, E., de Bernardis, P., et al. 2023, in The Sixteenth Marcel Grossmann Meeting. On Recent Developments in Theoretical and Experimental General Relativity, 1542–1556

Beers, T. C., Flynn, K., & Gebhardt, K. 1990, AJ, 100, 32

Bertin, E. & Arnouts, S. 1996, A&AS, 117, 393

Biffi, V., Dolag, K., Boehringer, H., & Lemson, G. 2011, PHOX: X-ray Photon Simulator, Astrophysics Source Code Library, record ascl:1112.004

Bleem, L. E., Bocquet, S., Stalder, B., et al. 2020, ApJS, 247, 25

Bleem, L. E., Klein, M., Abbot, T. M. C., et al. 2024, The Open Journal of Astrophysics, 7, 13

Bleem, L. E., Stalder, B., de Haan, T., et al. 2015, ApJS, 216, 27

Bond, J., Cole, S., Efstathiou, G., & Kaiser, N. 1991, The Astrophysical Journal, 379, 440

Bond, J. R., Kofman, L., & Pogosyan, D. 1996, Nature, 380, 603

Boogaard, L., Meyer, R. A., & Novak, M. 2021

Booth, M., Klaassen, P., Cicone, C., et al. 2024, arXiv e-prints, arXiv:2405.20140

Bouwens, R. J., Smit, R., Schouws, S., et al. 2022, ApJ, 931, 160

Bower, R. G. 1991, Monthly Notices of the Royal Astronomical Society, 248, 332

Brodwin, M., Gonzalez, A. H., Stanford, S. A., et al. 2012, ApJ, 753, 162

Bromm, V., Coppi, P. S., & Larson, R. B. 1999, The Astrophysical Journal, 527, L5

Bryan, S., Austermann, J., Ferrusca, D., et al. 2018, in Society of Photo-Optical Instrumentation Engineers (SPIE) Conference Series, Vol. 10708, Millimeter, Submillimeter, and Far-Infrared Detectors and Instrumentation for Astronomy IX, ed. J. Zmuidzinas & J.-R. Gao, 107080J

Bulbul, E., Liu, A., Kluge, M., et al. 2024, A&A, 685, A106

Bussmann, R. S., Riechers, D., Fialkov, A., et al. 2015, ApJ, 812, 43

Böhringer, H., Schuecker, P., Pratt, G. W., et al. 2007, A&A, 469, 363

Calvi, V., Trenti, M., Stiavelli, M., et al. 2016, ApJ, 817, 120

Carilli, C. L., Murphy, E. J., Ferrara, A., & Dayal, P. 2018, in Astronomical Society of the Pacific Conference Series, Vol. 517, Science with a Next Generation Very Large Array, ed. E. Murphy, 557

Carlstrom, J. E., Ade, P. A. R., Aird, K. A., et al. 2011, PASP, 123, 568

Carniani, S., Ferrara, A., Maiolino, R., et al. 2020, Monthly Notices of the Royal Astronomical Society, 499, 5136

Carniani, S., Hainline, K., D'Eugenio, F., et al. 2024, arXiv e-prints, arXiv:2405.18485

Carpenter, J., Brogan, C., Iono, D., & Mroczkowski, T. 2023, in Physics and Chemistry of Star Formation: The Dynamical ISM Across Time and Spatial Scales, ed. V. Ossenkopf-Okada, R. Schaaf, I. Breloy, & J. Stutzki, 304

CASA Team, Bean, B., Bhatnagar, S., et al. 2022, PASP, 134, 114501

Castellani, F., Clerc, N., Pointecouteau, E., et al. 2024, A&A, 682, A23

Castellano, M., Fontana, A., Treu, T., et al. 2022, ApJ, 938, L15

Castellano, M., Napolitano, L., Fontana, A., et al. 2024, arXiv e-prints, arXiv:2403.10238

Cavaliere, A. & Fusco-Femiano, R. 1976, A&A, 49, 137

CCAT-Prime Collaboration, Aravena, M., Austermann, J. E., et al. 2023, ApJS, 264, 7

Cen, R. & Ostriker, J. P. 1999, ApJ, 514, 1

Champagne, J. B., Casey, C. M., Zavala, J. A., et al. 2021, ApJ, 913, 110

Chen, Z., Jamieson, D., Komatsu, E., et al. 2024, Phys. Rev. D, 109, 063513

CHEX-MATE Collaboration, Arnaud, M., Ettori, S., et al. 2021, A&A, 650, A104

Chiang, Y.-K., Makiya, R., Komatsu, E., & Ménard, B. 2021, ApJ, 910, 32

Chiang, Y.-K., Makiya, R., Ménard, B., & Komatsu, E. 2020, The Astrophysical Journal, 902, 56

Chiang, Y.-K., Overzier, R., & Gebhardt, K. 2013, ApJ, 779, 127

Churazov, E., Vikhlinin, A., & Sunyaev, R. 2015, MNRAS, 450, 1984

Cialone, G., De Petris, M., Sembolini, F., et al. 2018, Monthly Notices of the Royal Astronomical Society, 477, 139

Conan, R., Borgnino, J., Ziad, A., & Martin, F. 2000, JOSA A, 17, 1807

Consortini, A. & Ronchi, L. 1972, Applied Optics, 11, 1205

Copernicus, N. 1543, De revolutionibus orbium coelestium

Coulton, W., Madhavacheril, M. S., Duivenvoorden, A. J., et al. 2024, Phys. Rev. D, 109, 063530

Curti, M., D'Eugenio, F., Carniani, S., et al. 2023, Monthly Notices of the Royal Astronomical Society, 518, 425

Curti, M., Maiolino, R., Curtis-Lake, E., et al. 2024, A&A, 684, A75

Curtis-Lake, E., Carniani, S., Cameron, A., et al. 2023, Nature Astronomy, 7, 622

Czekala, I., Loomis, R. A., Teague, R., et al. 2021, ApJS, 257, 2

da Cunha, E., Groves, B., Walter, F., et al. 2013, ApJ, 766, 13

Dachlythra, N., Duivenvoorden, A. J., Gudmundsson, J. E., et al. 2024, ApJ, 961, 138

Daddi, E., Rich, R. M., Valentino, F., et al. 2022, ApJ, 926, L21

Davis, M., Efstathiou, G., Frenk, C. S., & White, S. D. M. 1985, ApJ, 292, 371

Day, P. K., LeDuc, H. G., Mazin, B. A., Vayonakis, A., & Zmuidzinas, J. 2003, Nature, 425, 817

Dayal, P. & Ferrara, A. 2018, Phys. Rep., 780, 1

de Bernardis, P., Ade, P. A. R., Bock, J. J., et al. 2000, Nature, 404, 955

De Looze, I., Cormier, D., Lebouteiller, V., et al. 2014, A&A, 568, A62

De Rossi, M. E. & Bromm, V. 2023, ApJ, 946, L20

de Sitter, W. 1917, MNRAS, 78, 3

Decarli, R., Carilli, C., Casey, C., et al. 2018, in Astronomical Society of the Pacific Conference Series, Vol. 517, Science with a Next Generation Very Large Array, ed. E. Murphy, 565

Devlin, M. J., Ade, P. A. R., Aretxaga, I., et al. 2009, Nature, 458, 737

Dewdney, P. E., Hall, P. J., Schilizzi, R. T., & Lazio, T. J. L. W. 2009, IEEE Proceedings, 97, 1482

Di Francesco, J., Johnstone, D., Matthews, B. C., et al. 2013, arXiv e-prints, arXiv:1310.1604

Di Mascolo, L., Churazov, E., & Mroczkowski, T. 2019, Monthly Notices of the Royal Astronomical Society, 487, 4037

Di Mascolo, L., Mroczkowski, T., Churazov, E., et al. 2020, A&A, 638, A70

Di Mascolo, L., Mroczkowski, T., Perrott, Y., et al. 2021, A&A, 650, A153

Di Mascolo, L., Perrott, Y., Mroczkowski, T., et al. 2024, arXiv e-prints, arXiv:2403.00909

Di Mascolo, L., Saro, A., Mroczkowski, T., et al. 2023, Nature, 615, 809

Dicke, R. H., Peebles, P. J. E., Roll, P. G., & Wilkinson, D. T. 1965, ApJ, 142, 414

Dicker, S. R., Ade, P. A. R., Aguirre, J., et al. 2014, in Society of Photo-Optical Instrumentation Engineers (SPIE) Conference Series, Vol. 9153, Millimeter, Submillimeter, and Far-Infrared Detectors and Instrumentation for Astronomy VII, ed. W. S. Holland & J. Zmuidzinas, 91530J

Dicker, S. R., Battistelli, E. S., Bhandarkar, T., et al. 2021, Monthly Notices of the Royal Astronomical Society, 508, 2600

Dicker, S. R., Perez Sarmiento, K., Mason, B., et al. 2024, ApJ, 970, 84

Diemer, B. 2018, ApJS, 239, 35

Diemer, B. & Joyce, M. 2019, ApJ, 871, 168

Dittrich, D., Leenders, R. T. A. J., & Mulder, J. 2019, Sociological Methods & Research, 48, 642

Dolag, K., Borgani, S., Murante, G., & Springel, V. 2009, MNRAS, 399, 497

Dolag, K., Komatsu, E., & Sunyaev, R. 2016, MNRAS, 463, 1797

Donahue, M. & Voit, G. M. 2022, Phys. Rep., 973, 1

Donnan, C. T., McLeod, D. J., Dunlop, J. S., et al. 2023, Monthly Notices of the Royal Astronomical Society, 518, 6011

Duffy, R. T., Logan, C. H. A., Maughan, B. J., et al. 2022, Monthly Notices of the Royal Astronomical Society, 512, 2525

Dünner, R., Hasselfield, M., Marriage, T. A., et al. 2013, ApJ, 762, 10

Eddington, A. S. 1919, The Observatory, 42, 119

Edenhofer, G., Frank, P., Roth, J., et al. 2024, The Journal of Open Source Software, 9, 6593

Einstein, A. 1916, Annalen der Physik, 354, 769

Eisenstein, D. J. & Hu, W. 1998, ApJ, 496, 605

Endo, A., Werf, P., Janssen, R. M. J., et al. 2012, Journal of Low Temperature Physics, 167, 341

Enßlin, T. A. 2019, Annalen der Physik, 531, 1800127

Enßlin, T. A. & Kaiser, C. R. 2000, A&A, 360, 417

Errard, J., Ade, P. A. R., Akiba, Y., et al. 2015, ApJ, 809, 63

Fakhouri, O., Ma, C.-P., & Boylan-Kolchin, M. 2010, Monthly Notices of the Royal Astronomical Society, 406, 2267

Ferland, G. J., Chatzikos, M., Guzmán, F., et al. 2017, Rev. Mexicana Astron. Astrofis., 53, 385

Ferragamo, A., Rubiño-Martín, J. A., Betancort-Rijo, J., et al. 2020, A&A, 641, A41

Finkelstein, S. L., Bagley, M. B., Ferguson, H. C., et al. 2023, ApJ, 946, L13

Fixsen, D. J. 2009, ApJ, 707, 916

Fixsen, D. J., Cheng, E. S., Gales, J. M., et al. 1996, ApJ, 473, 576

Frayer, D. T. 2017, arXiv e-prints, arXiv:1706.02726

Frayer, D. T., Maddalena, R. J., White, S., et al. 2019, Calibration of Argus and the 4mm Receiver on the GBT, Green Bank Telescope Memorandum 302, June 5, 2019, 21 pages

Friedmann, A. 1922, Zeitschrift fur Physik, 10, 377

Fudamoto, Y., Oesch, P. A., Walter, F., et al. 2024, Monthly Notices of the Royal Astronomical Society, 530, 340

Fujimoto, S., Finkelstein, S. L., Burgarella, D., et al. 2023, ApJ, 955, 130

Fujimoto, S., Ouchi, M., Nakajima, K., et al. 2024, ApJ, 964, 146

Fukugita, M. & Peebles, P. J. E. 2004, ApJ, 616, 643

Gallo, S., Douspis, M., Soubrié, E., & Salvati, L. 2024, A&A, 686, A15

Gardini, A., Rasia, E., Mazzotta, P., et al. 2004, MNRAS, 351, 505

Gobat, R., Daddi, E., Coogan, R. T., et al. 2019, A&A, 629, A104

Gobat, R., Daddi, E., Onodera, M., et al. 2011, A&A, 526, A133

González-López, J., Decarli, R., Pavesi, R., et al. 2019, ApJ, 882, 139

González-López, J., Novak, M., Decarli, R., et al. 2020, ApJ, 897, 91

Gruzinov, A. & Hu, W. 1998, ApJ, 508, 435

Gunn, J. E. & Gott, J. Richard, I. 1972, ApJ, 176, 1

Gunn, J. E. & Peterson, B. A. 1965, ApJ, 142, 1633

Gupta, N., Saro, A., Mohr, J. J., Dolag, K., & Liu, J. 2017, Monthly Notices of the Royal Astronomical Society, 469, 3069

Gutkin, J., Charlot, S., & Bruzual, G. 2016, Monthly Notices of the Royal Astronomical Society, 462, 1757

Harikane, Y., Inoue, A. K., Ellis, R. S., et al. 2024a, arXiv e-prints, arXiv:2406.18352

Harikane, Y., Inoue, A. K., Mawatari, K., et al. 2022, ApJ, 929, 1

Harikane, Y., Nakajima, K., Ouchi, M., et al. 2024b, ApJ, 960, 56

Harikane, Y., Ouchi, M., Inoue, A. K., et al. 2020, ApJ, 896, 93

Harikane, Y., Ouchi, M., Oguri, M., et al. 2023, ApJS, 265, 5

Harrison, E. R. 1970, Phys. Rev. D, 1, 2726

Hashimoto, T., Inoue, A. K., Mawatari, K., et al. 2019, PASJ, 71, 71

Hashimoto, T., Laporte, N., Mawatari, K., et al. 2018, Nature, 557, 392

Hatziminaoglou, E., Zwaan, M., Andreani, P., et al. 2015, The Messenger, 162, 24

Henderson, S., Allison, R., Austermann, J., et al. 2016, Journal of Low Temperature Physics, 184, 772

Hersbach, H., Bell, B., Berrisford, P., et al. 2020, QJRMS, 146:730, 1999

Hill, C. A., Bruno, S. M. M., Simon, S. M., et al. 2018, in Society of Photo-Optical Instrumentation Engineers (SPIE) Conference Series, Vol. 10708, Millimeter, Submillimeter, and Far-Infrared Detectors and Instrumentation for Astronomy IX, ed. J. Zmuidzinas & J.-R. Gao, 1070842

Hilton, M., Hasselfield, M., Sifón, C., et al. 2018, ApJS, 235, 20

Hilton, M., Sifón, C., Naess, S., et al. 2021, ApJS, 253, 3

Högbom, J. A. 1974, A&AS, 15, 417

Huang, Y.-D., Hwang, Y.-J., Chiong, C.-C., et al. 2022, in Society of Photo-Optical Instrumentation Engineers (SPIE) Conference Series, Vol. 12190, Millimeter, Submillimeter, and Far-Infrared Detectors and Instrumentation for Astronomy XI, ed. J. Zmuidzinas & J.-R. Gao, 121900K

Hubble, E. 1929, Proceedings of the National Academy of Science, 15, 168

Hubble, E. P. 1922, ApJ, 56, 162

Huijten, E., Roelvink, Y., Brackenhoff, S. A., et al. 2022, Journal of Astronomical Telescopes, Instruments, and Systems, 8, 028005

Inoue, A. K., Tamura, Y., Matsuo, H., et al. 2016, Science, 352, 1559

Isobe, Y., Ouchi, M., Tominaga, N., et al. 2023, ApJ, 959, 100

Itoh, N., Kohyama, Y., & Nozawa, S. 1998, ApJ, 502, 7

Jia, P., Cai, D., Wang, D., & Basden, A. 2015, Monthly Notices of the Royal Astronomical Society, 447, 3467

Jiang, L., Kashikawa, N., Wang, S., et al. 2021, Nature Astronomy, 5, 256

Jorsater, S. & van Moorsel, G. A. 1995, AJ, 110, 2037

Kaasinen, **van Marrewijk**, J., Popping, G., Ginolfi, M., et al. 2023, A&A, 671, A29

Kaercher, H. J. & Baars, J. W. 2000, in Society of Photo-Optical Instrumentation Engineers (SPIE) Conference Series, Vol. 4015, Radio Telescopes, ed. H. R. Butcher, 155–168

Keating, G. K., Bower, G. C., Marrone, D. P., et al. 2015, ApJ, 814, 140

Kéruzoré, F., Mayet, F., Pratt, G. W., et al. 2020, A&A, 644, A93

Killi, M., Watson, D., Fujimoto, S., et al. 2023, Monthly Notices of the Royal Astronomical Society, 521, 2526

Kisner, T., Keskitalo, R., Zonca, A., et al. 2023, TOAST: Time Ordered Astrophysics Scalable Tools, Astrophysics Source Code Library, record ascl:2307.022

Kitayama, T., Ueda, S., Akahori, T., et al. 2020, PASJ, 72, 33

Kitayama, T., Ueda, S., Okabe, N., et al. 2023, PASJ, 75, 311

Kitayama, T., Ueda, S., Takakuwa, S., et al. 2016, PASJ, 68, 88

Klaassen, P. D., Mroczkowski, T. K., Cicone, C., et al. 2020, in Society of Photo-Optical Instrumentation Engineers (SPIE) Conference Series, Vol. 11445, Society of Photo-Optical Instrumentation Engineers (SPIE) Conference Series, 114452F

Knox, L., Scoccimarro, R., & Dodelson, S. 1998, Phys. Rev. Lett., 81, 2004

Kohandel, M., Ferrara, A., Pallottini, A., et al. 2023, Monthly Notices of the Royal Astronomical Society, 520, L16

Komatsu, E., Dunkley, J., Nolta, M. R., et al. 2009, ApJS, 180, 330

Komatsu, E., Matsuo, H., Kitayama, T., et al. 2001, PASJ, 53, 57

Kravtsov, A. V. & Borgani, S. 2012, ARA&A, 50, 353

Lacey, C. & Cole, S. 1993, Monthly Notices of the Royal Astronomical Society, 262, 627

Lacy, M., Baum, S. A., Chandler, C. J., et al. 2020, PASP, 132, 035001

Laporte, N., Ellis, R. S., Boone, F., et al. 2017, ApJ, 837, L21

Larson, R. B. 1972, MNRAS, 157, 121

Larson, R. B. 2003, Reports on Progress in Physics, 66, 1651

Lau, E. T., Hearin, A. P., Nagai, D., & Cappelluti, N. 2021, Monthly Notices of the Royal Astronomical Society, 500, 1029

Lay, O. P. 1997, A&AS, 122

Le Brun, A. M. C., McCarthy, I. G., & Melin, J.-B. 2015, Monthly Notices of the Royal Astronomical Society, 451, 3868

Lee, M. M., Schimek, A., Cicone, C., et al. 2024, arXiv e-prints, arXiv:2403.00924

Lemaître, G. 1927, Annales de la Société Scientifique de Bruxelles, 47, 49

Li, Q., Cui, W., Yang, X., et al. 2023, MNRAS, 523, 1228

Loomis, R. A., Öberg, K. I., Andrews, S. M., et al. 2018, AJ, 155, 182

Lovell, C. C., Harrison, I., Harikane, Y., Tacchella, S., & Wilkins, S. M. 2023, MNRAS, 518, 2511

Low, F. J., Rieke, G. H., & Gehrz, R. D. 2007, ARA&A, 45, 43

MacCrann, N., Sherwin, B. D., Qu, F. J., et al. 2024, ApJ, 966, 138

Madhavacheril, M. S., Hill, J. C., Næss, S., et al. 2020, Physical Review D, 102, 023534

Madhavacheril, M. S., Qu, F. J., Sherwin, B. D., et al. 2024, ApJ, 962, 113

Maiolino, R. & Mannucci, F. 2019, A&A Rev., 27, 3

Maiolino, R., Scholtz, J., Witstok, J., et al. 2024, Nature, 627, 59

Mantz, A. B., Abdulla, Z., Allen, S. W., et al. 2018, A&A, 620, A2

Mantz, A. B., Abdulla, Z., Carlstrom, J. E., et al. 2014, The Astrophysical Journal, 794, 157

Marini et al., I. In prep., A&A

Mather, J. C. 1982, Appl. Opt., 21, 1125

Maud, L. T., Asaki, Y., Nagai, H., et al. 2023, ApJS, 267, 24

Mauerhofer, V. & Dayal, P. 2023, Monthly Notices of the Royal Astronomical Society, 526, 2196

McDonald, M., Benson, B. A., Vikhlinin, A., et al. 2014, ApJ, 794, 67

McMullin, J. P., Waters, B., Schiebel, D., Young, W., & Golap, K. 2007, Astronomical Society of the Pacific Conference Series, Vol. 376, CASA Architecture and Applications (ASPBooks), 127

Miley, G. & De Breuck, C. 2008, A&A Rev., 15, 67

Mingozzi, M., James, B. L., Berg, D. A., et al. 2024, ApJ, 962, 95

Morris, T. W., Bustos, R., Calabrese, E., et al. 2022, Phys. Rev. D, 105, 042004

Morris, T. W., Page, L. A., & ACT Collaboration. 2024, in prep.

Mroczkowski, T. 2011, ApJ, 728, L35

Mroczkowski, T., Bonamente, M., Carlstrom, J. E., et al. 2009, ApJ, 694, 1034

Mroczkowski, T., Cicone, C., Reichert, M., et al. 2023, in 2023 XXXVth General Assembly and Scientific Symposium of the International Union of Radio Science (URSI GASS), 1–4

Mroczkowski, T., Donahue, M., **van Marrewijk**, J., et al. 2022, A&A, 665, A48

Mroczkowski, T., Gallardo, P. A., Timpe, M., et al. 2024, arXiv e-prints, arXiv:2402.18645

Mroczkowski, T., Nagai, D., Basu, K., et al. 2019, Space Sci. Rev., 215, 17

Munari, E., Biviano, A., Borgani, S., Murante, G., & Fabjan, D. 2013, Monthly Notices of the Royal Astronomical Society, 430, 2638

Naess, S., Aiola, S., Austermann, J. E., et al. 2020, J. Cosmology Astropart. Phys., 2020, 046

Naess, S. & Louis, T. 2023, The Open Journal of Astrophysics, 6, 21

Nagai, D., Vikhlinin, A., & Kravtsov, A. V. 2007, ApJ, 655, 98

Naidu, R. P., Oesch, P. A., Dokkum, P. v., et al. 2022, ApJ, 940, L14

Nakajima, K., Ouchi, M., Isobe, Y., et al. 2023, ApJS, 269, 33

Nakazato, Y., Yoshida, N., & Ceverino, D. 2023, ApJ, 953, 140

Navas, S., Amsler, C., Gutsche, T., et al. 2024, Phys. Rev. D, 110, 030001

Nelson, D., Pillepich, A., Ayromlou, M., et al. 2024, A&A, 686, A157

Newman, A. B., Ellis, R. S., Andreon, S., et al. 2014, ApJ, 788, 51

Noordeh, E., Canning, R. E. A., Willis, J. P., et al. 2021, Monthly Notices of the Royal Astronomical Society, 507, 5272

Nozawa, S., Itoh, N., & Kohyama, Y. 1998, ApJ, 508, 17

Nussbaumer, H. & Bieri, L. 2011, The Observatory, 131, 394

Oesch, P. A., Bouwens, R. J., Illingworth, G. D., et al. 2014, ApJ, 786, 108

Oesch, P. A., Brammer, G., van Dokkum, P. G., et al. 2016, ApJ, 819, 129

Olchanski, M. & Sorce, J. G. 2018, A&A, 614, A102

Orlowski-Scherer, J., Di Mascolo, L., Bhandarkar, T., et al. 2021, A&A, 653, A135

Orlowski-Scherer, J., Haridas, S. K., Di Mascolo, L., et al. 2022, A&A, 667, L6

Overzier, R. A. 2016, A&A Rev., 24, 14

Owen, F. N., Spangler, S. R., & Cotton, W. D. 1980, The Astronomical Journal, 85, 351

Padin, S., Cartwright, J. K., Mason, B. S., et al. 2001, ApJ, 549, L1

Paine, S. 2018, The am atmospheric model

Pandey, S., Baxter, E. J., Xu, Z., et al. 2019, Phys. Rev. D, 100, 063519

Pardo, J., Cernicharo, J., & Serabyn, E. 2001, IEEE Transactions on Antennas and Propagation, 49, 1683

Park, H., Shapiro, P. R., Komatsu, E., et al. 2013, The Astrophysical Journal, 769, 93

Pavesi, R., Sharon, C. E., Riechers, D. A., et al. 2018, ApJ, 864, 49

Peebles, P. J. E. 1965, ApJ, 142, 1317

Peebles, P. J. E. 1972, Comments on Astrophysics and Space Physics, 4, 53

Peebles, P. J. E. 1980, The large-scale structure of the universe (Princeton Press)

Peebles, P. J. E. 1993, Principles of Physical Cosmology (Princeton University Press)

Peebles, P. J. E. & Yu, J. T. 1970, ApJ, 162, 815

Penzias, A. A. & Wilson, R. W. 1965, ApJ, 142, 419

Petry, D., Stanke, T., Biggs, A., et al. 2020, The Messenger, 181, 16

Pierre, M., Valtchanov, I., Altieri, B., et al. 2004, J. Cosmology Astropart. Phys., 2004, 011

Planck Collaboration, Ade, P. A. R., Aghanim, N., et al. 2014, A&A, 571, A1

Planck Collaboration, Ade, P. A. R., Aghanim, N., et al. 2013, A&A, 550, A131

Planck Collaboration, Ade, P. A. R., Aghanim, N., et al. 2016, A&A, 594, A27

Plunkett, A., Hacar, A., Moser-Fischer, L., et al. 2023, PASP, 135, 034501

Pointecouteau, E., Santiago-Bautista, I., Douspis, M., et al. 2021, A&A, 651, A73

Popping, G. 2023, A&A, 669, L8

Pratt, G. W., Arnaud, M., Biviano, A., et al. 2019, Space Sci. Rev., 215, 25

Press, W. H. & Schechter, P. 1974, ApJ, 187, 425

Puglisi, G., Keskitalo, R., Kisner, T., & Borrill, J. D. 2021, Research Notes of the American Astronomical Society, 5, 137

Qu, F. J., Sherwin, B. D., Madhavacheril, M. S., et al. 2024, ApJ, 962, 112

Raghunathan, S., Whitehorn, N., Alvarez, M. A., et al. 2022, ApJ, 926, 172

Ramasawmy, J., Klaassen, P. D., Cicone, C., et al. 2022, in Society of Photo-Optical Instrumentation Engineers (SPIE) Conference Series, Vol. 12190, Millimeter, Submillimeter, and Far-Infrared Detectors and Instrumentation for Astronomy XI, ed. J. Zmuidzinas & J.-R. Gao, 1219007

Rasia, E., Borgani, S., Murante, G., et al. 2015, ApJ, 813, L17

Rasia, E., Mazzotta, P., Bourdin, H., et al. 2008, ApJ, 674, 728

Readhead, A. C. S., Myers, S. T., Pearson, T. J., et al. 2004, Science, 306, 836

Reichardt, C. L., Patil, S., Ade, P. A. R., et al. 2021, ApJ, 908, 199

Reichert, M., Timpe, M., Kaercher, H., et al. 2024, arXiv e-prints, arXiv:2406.08611

Remijan, A., Biggs, A., Cortes, P., et al. 2019, ALMA doc, 7

Remus, R.-S., Dolag, K., & Dannerbauer, H. 2023, ApJ, 950, 191

Ren, Y. W., Fudamoto, Y., Inoue, A. K., et al. 2023, ApJ, 945, 69

Ricci, M., Adam, R., Eckert, D., et al. 2020, A&A, 642, A126

Robertson, H. P. 1933, Reviews of Modern Physics, 5, 62

Romero, C. 2024, arXiv e-prints, arXiv:2405.06489

Romero, C., McWilliam, M., Macías-Pérez, J. F., et al. 2018, A&A, 612, A39

Romero, C. E., Sievers, J., Ghirardini, V., et al. 2020, ApJ, 891, 90

Rowland, L. E., Hodge, J., Bouwens, R., et al. 2024, arXiv e-prints, arXiv:2405.06025

Rubin, V. C., Ford, W. K., J., & Thonnard, N. 1980, ApJ, 238, 471

Ruppin, F., Mayet, F., Macías-Pérez, J. F., & Perotto, L. 2019, Monthly Notices of the Royal Astronomical Society, 490, 784

Ruppin, F., Mayet, F., Pratt, G. W., et al. 2018, A&A, 615, A112

Ruppin, F., McDonald, M., Hlavacek-Larrondo, J., et al. 2023, ApJ, 948, 49

Ruze, J. 1966, Proceedings of the IEEE, 54, 633

Rybak, M., Hodge, J. A., Greve, T. R., et al. 2022, A&A, 667, A70

Rybak, M., **van Marrewijk**, J., Hodge, J. A., et al. 2023, A&A, 679, A119

Ryden, B. 2003, Introduction to cosmology (Cambridge University Press)

Sachs, R. K. & Wolfe, A. M. 1967, ApJ, 147, 73

Sarazin, C. L. 1986, Reviews of Modern Physics, 58, 1

Saro, A., Mohr, J. J., Bazin, G., & Dolag, K. 2013, ApJ, 772, 47

Saxena, A., Bunker, A. J., Jones, G. C., et al. 2024, A&A, 684, A84

Sayers, J., Montaña, A., Mroczkowski, T., et al. 2019, ApJ, 880, 45

Sayers, J., Mroczkowski, T., Zemcov, M., et al. 2013, ApJ, 778, 52

Schaye, J., Kugel, R., Schaller, M., et al. 2023, Monthly Notices of the Royal Astronomical Society, 526, 4978

Schimek, A., Decataldo, D., Shen, S., et al. 2024, A&A, 682, A98

Schmidt, M. 1968, ApJ, 151, 393

Sehgal, N., Aiola, S., Akrami, Y., et al. 2019, in Bulletin of the American Astronomical Society, Vol. 51, 6

Selig, M. 2014, in American Institute of Physics Conference Series, Vol. 1636, Bayesian Inference and Maximum Entropy Methods in Science and Engineering (AIP), 68–73

Sereno, M., Umetsu, K., Ettori, S., et al. 2018, ApJ, 860, L4

Serra, P., Westmeier, T., Giese, N., et al. 2014

Sharp, M. K., Marrone, D. P., Carlstrom, J. E., et al. 2010, ApJ, 713, 82

Shirasaki, M., Sifón, C., Miyatake, H., et al. 2024, arXiv e-prints, arXiv:2407.08201

Silich, E. M., Bellomi, E., Sayers, J., et al. 2024a, in European Physical Journal Web of Conferences, Vol. 293, mm Universe 2023 - Observing the Universe at mm Wavelengths, 00050

Silich, E. M., Bellomi, E., Sayers, J., et al. 2024b, ApJ, 968, 74

Singh, A., Mohr, J. J., Davies, C. T., et al. 2024, arXiv e-prints, arXiv:2407.10961

Slipher, V. M. 1917, Proceedings of the American Philosophical Society, 56, 403

Smith, K. M. & Ferraro, S. 2016, arXiv e-prints, arXiv:1607.01769

Smolčić, V., Ciliegi, P., Jelić, V., et al. 2014, MNRAS, 443, 2590

Speagle, J. S. 2020, Monthly Notices of the Royal Astronomical Society, 493, 3132

Spergel, D. N., Verde, L., Peiris, H. V., et al. 2003, ApJS, 148, 175

Springel, V., White, S. D. M., Jenkins, A., et al. 2005, Nature, 435, 629

Stanford, S. A., Brodwin, M., Gonzalez, A. H., et al. 2012, ApJ, 753, 164

Stanway, E. R. & Eldridge, J. J. 2018, Monthly Notices of the Royal Astronomical Society, 479, 75

Stefanon, M., Labbé, I., Bouwens, R. J., et al. 2019, ApJ, 883, 99

Steidel, C. C., Adelberger, K. L., Shapley, A. E., et al. 2000, ApJ, 532, 170

Strömgren, B. 1939, ApJ, 89, 526

Sunyaev, R. A. & Zeldovich, I. B. 1980, MNRAS, 190, 413

Sunyaev, R. A. & Zeldovich, Y. B. 1970, Ap&SS, 7, 3

Sunyaev, R. A. & Zeldovich, Y. B. 1972a, A&A, 20, 189

Sunyaev, R. A. & Zeldovich, Y. B. 1972b, Comments on Astrophysics and Space Physics, 4, 173

Swetz, D. S., Ade, P. A. R., Amiri, M., et al. 2011, The Astrophysical Journal Supplement Series, 194, 41

Tamura, Y., C. Bakx, T. J. L., Inoue, A. K., et al. 2023, ApJ, 952, 9

Tamura, Y., Mawatari, K., Hashimoto, T., et al. 2019, ApJ, 874, 27

Tatarski, V. I. 1961, Wave Propagation in a Turbulent Medium (McGraw-Hill, NY)

The CMB-HD Collaboration, :, Aiola, S., et al. 2022, arXiv e-prints, arXiv:2203.05728

Thompson, A. R., Moran, J. M., & Swenson, George W., J. 2017, Interferometry and Synthesis in Radio Astronomy, 3rd Edition

Thongkham, K., Gonzalez, A. H., Brodwin, M., et al. 2024, ApJ, 967, 123

Thornton, R. J., Ade, P. A. R., Aiola, S., et al. 2016, The Astrophysical Journal Supplement Series, 227, 21

Tinker, J., Kravtsov, A. V., Klypin, A., et al. 2008, ApJ, 688, 709

Tokovinin, A. 2002, Publications of the Astronomical Society of the Pacific, 114, 1156

Tozzi, P., Gilli, R., Liu, A., et al. 2022, A&A, 667, A134

Trudeau, A., Willis, J. P., Rennehan, D., et al. 2022, Monthly Notices of the Royal Astronomical Society, 515, 2529

Tsukui, T., Iguchi, S., Mitsuhashi, I., & Tadaki, K. 2022, in Society of Photo-Optical Instrumentation Engineers (SPIE) Conference Series, Vol. 12190, Millimeter, Submillimeter, and Far-Infrared Detectors and Instrumentation for Astronomy XI, ed. J. Zmuidzinas & J.-R. Gao, 121901C

Tsukui, T., Iguchi, S., Mitsuhashi, I., & Tadaki, K. 2023

Ueda, S., Kitayama, T., Oguri, M., et al. 2018, ApJ, 866, 48

Ura, R., Hashimoto, T., Inoue, A. K., et al. 2023, ApJ, 948, 3

van Albada, T. S., Bahcall, J. N., Begeman, K., & Sancisi, R. 1985, ApJ, 295, 305

van Kampen, E., Bakx, T., De Breuck, C., et al. 2024, arXiv e-prints, arXiv:2403.02806

van Marrewijk, J. & Di Mascolo, L. 2024

van Marrewijk, J., Di Mascolo, L., Gill, A. S., et al. 2023, arXiv e-prints, arXiv:2310.06120

van Marrewijk, J., Kaasinen, M., Popping, G., et al. Sub., A&A, submitted for publication

van Marrewijk, J., Morris, T. W., Mroczkowski, T., et al. 2024, arXiv e-prints, arXiv:2402.10731

Venemans, B. P., Röttgering, H. J. A., Miley, G. K., et al. 2007, A&A, 461, 823

Vikhlinin, A., Burenin, R. A., Ebeling, H., et al. 2009, ApJ, 692, 1033

Vio, R. & Andreani, P. 2016, A&A, 589, A20

Voit, G. M. 2021, Galactic Atmospheres, https://galacticatmospheres.pubpub.org/pub/oqgzyzh0

Walker, A. G. 1937, Proceedings of the London Mathematical Society, 42, 90

Walter, F., Decarli, R., Aravena, M., et al. 2016, ApJ, 833, 67

Wang, T., Elbaz, D., Daddi, E., et al. 2016, ApJ, 828, 56

Wang, T., Elbaz, D., Daddi, E., et al. 2018, ApJ, 867, L29

Weiß, A., Kovács, A., Coppin, K., et al. 2009, ApJ, 707, 1201

Wells, D. C., Greisen, E. W., & Harten, R. H. 1981, A&AS, 44, 363

Westmeier, T., Kitaeff, S., Pallot, D., et al. 2021, MNRAS, 506, 3962

White, E., Ghigo, F. D., Prestage, R. M., et al. 2022, A&A, 659, A113

White, S. D. M. & Rees, M. J. 1978, MNRAS, 183, 341

Wik, D. R., Sarazin, C. L., Ricker, P. M., & Randall, S. W. 2008, ApJ, 680, 17

Wilkins, S. M., Lovell, C. C., Vijayan, A. P., et al. 2023, Monthly Notices of the Royal Astronomical Society, 522, 4014

Willis, J. P., Canning, R. E. A., Noordeh, E. S., et al. 2020, Nature, 577, 39

Willis, J. P., Clerc, N., Bremer, M. N., et al. 2013, Monthly Notices of the Royal Astronomical Society, 430, 134

Wilson, T. L., Rohlfs, K., & Hüttemeister, S. 2009, Tools of Radio Astronomy

Witstok, J., Smit, R., Maiolino, R., et al. 2022, Monthly Notices of the Royal Astronomical Society, 515, 1751

Xi, H., Peng, B., Staveley-Smith, L., et al. 2024, ApJ, 966, L36

Xiao, M. Y., Wang, T., Elbaz, D., et al. 2022, A&A, 664, A63

Yang, S., Lidz, A., Smith, A., Benson, A., & Li, H. 2023, Monthly Notices of the Royal Astronomical Society, 525, 5989

Yoon, I., Carilli, C. L., Fujimoto, S., et al. 2023, ApJ, 950, 61

Yoshida, N., Springel, V., White, S. D. M., & Tormen, G. 2000, ApJ, 544, L87

Young, S., Komatsu, E., & Dolag, K. 2021, Phys. Rev. D, 104, 083538

Zavala, J. A., Casey, C. M., Manning, S. M., et al. 2021, ApJ, 909, 165

Zavala, J. A., Castellano, M., Akins, H. B., et al. 2024, arXiv e-prints, arXiv:2403.10491

Zeimann, G. R., Stanford, S. A., Brodwin, M., et al. 2012, ApJ, 756, 115

Zeldovich, Y. B. 1972, Monthly Notices of the Royal Astronomical Society, 160, 1P

Zeldovich, Y. B. & Sunyaev, R. A. 1969, Ap&SS, 4, 301

Zhao, J. & Furlanetto, S. R. 2024, arXiv e-prints, arXiv:2401.07893

Ziparo, F., Ferrara, A., Sommovigo, L., & Kohandel, M. 2023, Monthly Notices of the Royal Astronomical Society, 520, 2445

ZuHone, J. A. & Hallman, E. J. 2016, pyXSIM: Synthetic X-ray observations generator, Astrophysics Source Code Library, record ascl:1608.002

ZuHone, J. A., Vikhlinin, A., Tremblay, G. R., et al. 2023, SOXS: Simulated Observations of X-ray Sources, Astrophysics Source Code Library, record ascl:2301.024

Zwicky, F. 1933, Helvetica Physica Acta, 6, 110

Zwicky, F. 1937, ApJ, 86, 217

Acknowledgments

Tony and Gergö, my greatest gratitude goes to you. Thank you so much for taking me on and introducing me to the world of science. You showed me what a wonderful, human, and joyful place it can be. Tony, you have always said it takes a village to raise a scientist; thank you for creating that village. It was a wonderful and constructive environment in which I could grow. I have learned so much from you both. From your enthusiasm, calmness, patience, expertise, and the ability to always see the bigger picture. Thank you again.

Luca, thank you for macheteing your way through the crazy jungle of resolved SZ science and letting me follow in your footsteps. You are like a big academic brother to me. Thank you for all the random chats and always being available. See you in the Netherlands!

Melanie, I love your drive, enthusiasm, and pure honesty. I am super grateful that we worked together and for not always chatting about work. You are a wonderful human being. Best of luck down under!

GESO, Alice, Claudia, Francesco, Ilaria, Ivanna, Michele, and Roman, thank you all for brightening my week every week. Thank you for putting up with my silly questions and letting me babble on for the whole meeting. Thank you for the vegan sushi, the great trips, the science discussions, and for being generally great colleagues, collaborators, and friends.

My correctors, thank you, Bruno, Eiichiro, and Jason, for always showing interest in my work and your enthusiasm. Thank you for reviewing the thesis, sharing your thoughts on the Universe, and supporting me in trying to make sense of it all. I have learned a great deal from you and hope to continue learning from you for many more years.

All my co-authors and collaborators, none of the work presented here could have been done without you. Thank you for your feedback and your attention to detail. You have shown me that I love to collaborate and work in teams. I especially want to thank Thomas for being my weather guru, the ACT Collaboration, the MUSTANG-2 Team, and the AtLAST consortium. Thank you Adam, Ajay, Bruce, Charles, Claudia, Emily, Jack, Jo, Jonas, Matus, Simon, and Tetsu.

My ESO friends, moving abroad is always scary, but making new friends makes it worth it. Thank you for brightening my day every day. For all the coffees, for all the little walks, for the many tablefootballtabletournaments, for the beer Fridays, for being there for each other, for the board games, for opening a sandwich shop, for having science coffee, for the volleyball, for the football, for the Nerf gun fights, for the dinners, for the hikes, for the traveling, for an unforgettable three years. Thank you all!

Ivanna, I am super grateful we met. You and I quickly became best friends and best of roommates. I think by living together, we become all the closer. I will miss having you around 24/7. I will miss our little gratitude walks in the morning, the little coffees in the afternoon, and me beating you with the dice game. We will stay in touch. I will take good care of your plants, and best of luck in Madrid.

Nelma, I cannot stress how important you are for all ESO students. You were the backbone of the OfS; always quick to point out that I forgot to add my receipts to the travel request, but more importantly, you were always there to listen when people needed it. Thank you for all the help you have given. I already miss saying good morning every day. Take care!

Mijn vrienden over de grens, bedankt voor het behouden van contact. Voor het lachen over de app. Voor het langs komen. Dat jullie me uitzwaaide en nu mij weer met open armen opgevangen. Voor het vertrouwen dat onze relatie goed zit. Dank je Max, Ier, Ceet, Pim, Rut, en Yoni.

Mam en Pap, dankjewel voor al jullie support en de vrijheid die jullie mij altijd gegeven hebben. Door jullie heb ik deze droom kunnen verwerkelijken. Bedankt voor alle de hulp. Voor met 200 km/uur en volle wagen naar München te rijden. Voor de vele belletjes. Voor de vitamines. En voor alles voor wat vanzelfsprekend voelt.

Finie, jij kent mij het langst en ik ken jou het meest. Onderweg constant gevormd door waar we zijn geweest. Nu kom ik terug en ben jij degene die gaat. Dus ik zeg preventief, ik heb je lief.

Marjolijn, naar jouw gaat mijn hart. Het is niet altijd even makkelijk geweest de laatste drie jaar, maar toch hebben wij onze weg gevonden en zijn wij ook samen door dit avontuur heen gegaan. Dank je wel voor al je liefde. Dank je dat je met twee benen in twee steden wilde staan en dat je nu met me verder wilt gaan.

- München, Augustus 2024